MODELING AND CONTROL OF SINGLE-TRACK VEHICLES: A HUMAN-MACHINE-ENVIRONMENT INTERACTIONS PERSPECTIVE

BY YIZHAI ZHANG

A dissertation submitted to the

Graduate School—New Brunswick

Rutgers, The State University of New Jersey

in partial fulfillment of the requirements

for the degree of

Doctor of Philosophy

Graduate Program in Mechanical and Aerospace Engineering

Written under the direction of

Dr. Jingang Yi

and approved by

_____

_____

_____

_____

New Brunswick, New Jersey

January, 2014

ABSTRACT OF THE DISSERTATION

Modeling and Control of Single-Track Vehicles: A Human-Machine-Environment Interactions Perspective

by Yizhai Zhang

Dissertation Director: Dr. Jingang Yi

Single-track vehicles, such as motorcycles and bicycles, not only provide an everyday transportation means and recreational sport, but also offer an excellent platform to study physical human-machine-environment (HME) interactions. The main goal of this dissertation is to present a modeling and control system design framework for HME interactions in single-track vehicle systems.

The dissertation focuses on three aspects: autonomous vehicle design, vehicle-environment interaction, and human-vehicle interaction. First, we propose novel modeling and control designs for riderless single-track vehicle to achieve agile maneuver navigation and stationary balancing. To achieve agile maneuver, the zero lateral velocity nonholonomic constraint at the tire contact point is relaxed. An empirical tire-road friction model is explicitly considered in the dynamic model. An external/internal convertible (EIC) model-based controller is designed for both trajectory tracking and path following strategies. Two different control designs are then presented to balance

the stationary bicycle through steering control and gyroscopic actuator control, respectively. To capture the vehicle-environment interaction, the second part of the dissertation focuses on the study of the tire-road interaction. A high-fidelity tire model is proposed and built on the calculation of the deformation and friction force distributions in stick-slip transition. An in-situ sensing technique is also developed to directly measure the friction force distribution. The model and the sensing development can be further used for facilitating real-time friction parameter estimation and vehicle safety control. The third part of the dissertation mainly discusses the human-vehicle interaction. A dynamic model is first proposed to capture the physical rider-bicycle interaction. A novel pose estimation approach is developed to integrate the wearable inertial sensors with on-board force sensors. A balancing design is finally presented to control the stationary rider-bicycle interaction. All the modelings and control designs in the dissertations are validated through extensive simulations and experiments.

The outcomes of the dissertation provide not only a modeling and control framework but also a physical experimental platform to study the unstable HME interactions. We discuss the future research direction at the end of the dissertation.

Acknowledgements

I would like to first thank my advisor, Dr. Jingang Yi, for all of his support, encouragement and guidance throughout my years study at Rutgers and for my professional career development. It is him who led me into the robotics and mechatronics field. During my four years study, no matter what I experienced with the successes and failures, Dr. Yi always helped and encouraged and provided endless support. Without his support, encouragement and guidance, I would not be able to complete this dissertation.

Thanks go to my committee members, Dr. Haym Benaroya, Dr. Zoran Gajic, and Dr. Qingze Zou, for their constructive comments and suggestions to improve this dissertation. I would also be grateful to thank many labmates at Rutgers including Mitja, Fei, Kuo, Kaiyan, Pengcheng and many of them. Their support, suggestion, and encouragement help me complete my PhD study.

Dedication

This dissertation is dedicated to my wife Jing Xu, and my parents.

Table of Contents

List of Tables

List of Figures

Nomenclature

X, Y, Z	A ground-fixed coordinate system.
x, y, z	A wheel-base line moving coordinate system.
x_w, y_w, z_w	A front wheel plane coordinate system.
x_b, y_b, z_b	A rear frame body coordinate system.
C_1, C_2	Front and rear wheel contact points on the ground.
F_{tx}, F_{ty}, F_{tz}	The front wheel contact forces in the x, y, z-axis directions.
F_{rx}, F_{ry}, F_{rz}	The rear wheel contact forces in the x, y, z directions.
$\boldsymbol{v}_f, \boldsymbol{v}_r$	Velocity vectors of the front and rear wheel contact points, respectively.
v_{fx}, v_{fy}	Front wheel contact point C_1 velocities along the x- and y-axis directions, respectively.
v_{rx}, v_{ry}	Rear wheel contact point C_2 velocities along the x- and y-axis directions, respectively.
v_{fx_w}, v_{fy_w}	Front wheel contact point C_1 velocities along the x_w- and y_w-axis directions, respectively.
v_X, v_Y	Rear wheel contact point C_2 velocities along the X- and Y-axis directions, respectively.
ω_f, ω_r	Wheel angular velocities of the front and rear wheels, respectively.
$\boldsymbol{v}_B$	Velocity vector of the bicycle's or motorcycle's main frame (with rear wheel set).

γ_f, γ_r	Slip angles of the front and rear wheels, respectively.
λ_f, λ_r	Longitudinal slip values of the front and rear wheels, respectively.
φ_b, ψ	Rear frame roll and yaw angles of main frame, respectively.
φ_h	Human rider roll angle.
φ_f	The front steering wheel plane camber angle.
ϕ_s	Motorcycle steering angle.
ϕ_g	Motorcycle kinematic steering angle (projected steering angle on the ground plane).
σ	The front kinematic steering angle variable.
m	The total mass of the main frame and wheel.
m_h	The total mass of rider's trunk.
J_s	The mass moment of rotation of the steering fork (with the front wheel set) about its rotation axis.
l	Motorcycle wheel base, i.e., distance between C_1 and C_2.
l_t	The front steering wheel trail.
h_b	The height of the motorcycle center of mass.
R_t	The front and rear wheel radius.
δ	The rear frame rotation angle from its vertical position.
ξ	The front steering axis caster angle.
C_d	The aerodynamics drag coefficient.
k_λ, k_γ, k_{φ_b}	Longitudinal, lateral, and camber stiffness coefficients of motorcycle tires, respectively.
$L(L_c)$	The (constrained) Lagrangian of the motorcycle systems.

$\mathcal{P}, \partial\mathcal{P}, \mathcal{P}^\circ$	Tire-road contact patch, the boundary and the interior region of the contact patch
$\mathbf{F}_f$	Total tire-road friction force
F_{fx}, F_{fy}	Total friction forces along the x- and y-axis directions
$\mathbf{P}_f$	Local friction stress on $\mathcal{P}$
P_{fx}, P_{fy}	Local friction stresses along the x- and y-axis directions
F_z	Total tire-road normal contact force
P_n	Local normal contact pressure on $\mathcal{P}$
P_{air}	Tire inflation air pressure
$\mathbf{f}_f^i$	Friction force on beam i
$\mathbf{f}_b^i$	Bending force on beam i
$\mathbf{f}_e^i$	Net elastic force on beam i
$\mathbf{F}_{\partial\mathcal{P}}$	Total boundary force
$F_{\partial\mathcal{P}x}, F_{\partial\mathcal{P}y}$	Total boundary forces along the x- and y-axis directions
$\mathbf{f}_{\partial\mathcal{P}}^i$	Boundary force on beam i on $\partial\mathcal{P}$
$f_{\partial\mathcal{P}x}^i, f_{\partial\mathcal{P}y}^i$	Boundary forces on beam i on $\partial\mathcal{P}$ along the x- and y-axis directions
$\sigma_{\mathcal{P}x}, \tau_{\mathcal{P}x}$	Spatially normalized $\mathbf{f}_e^i$ and $\mathbf{f}_b^i$ along the x-axis direction
$2h$	Thickness of the tire rubber layer
R_o, R_i	Outer and inner radii of the tire rubber layer cross the tire center line ($R_o = R_i + 2h$)
E, G, ν	Young's module, shear modulus and Poisson's ratio of the tire rubber materials

Chapter 1
Introduction

1.1 Motivation

Human with trained motor skills can flexibly interact with machines while smart machines can also provide motor assistance and enhancement to facilitate human motor skills learning. However, we currently lack theories and design tools to model and control the interaction due to the complex human-machine-environment (HME) interactions. In this dissertation, single-track vehicle such as motorcycle and bicycle is used as a paradigm to study the modeling, sensing and control of HME interactions.

Single-track vehicles provide an everyday transportation means and recreational sport. In comparison with double-track vehicles such as passenger cars, single-track vehicles have attractive characteristics. Single-track vehicles have high maneuverability and strong off-road capabilities. In the environments such as deserts, forests, and mountains, the mobility of single-track vehicles significantly outperforms that of double-track vehicles.

Single-track vehicles such as bicycles also offer an excellent platform to study HME interactions. When riding a bicycle, the rider-bicycle interactions are through multiple contacts at the handlebar, the seat and the pedals. The rider not only controls the steering and speed through limbs, but also uses body movements to engage forceful physical interactions with the bicycle for maintaining balance. Understanding and modeling such dynamic and energetic interactions are challenging. Moreover, recent studies demonstrate promising results of treating Parkinson's disease patients through

bicycle riding [2–4]. Thus, bicycles can be used as a potential rehabilitation device for recovering human postural control for disabilities patients [2].

The main goal of this dissertation is to propose a novel modeling and control framework for single-track vehicles from the human-machine-environment interactions perspective. Serving as a corner stone, the research outcome of this dissertation will further enable to study the neuro control and sensorimotor mechanism in HME interactions. It is of the hope that the research outcome will also be potentially useful to study other types of HME interactions.

1.2 Background

The HME interactions for single-track vehicles include two aspects: human-machine interaction and machine-environment interaction. From the human-machine interaction aspect, how the rider actually controls and balances the bicycle or motorcycle is still an open question. In this dissertation, we focus on rider-bicycle interactions and propose a modeling framework for these dynamic interactions. On the vehicle-environment interaction perspective, tire-road interactions provide the major thrust/braking forces for the vehicle system and play a critical role in HME system. Thus, understanding, modeling and control of the tire-road interaction are the main foci in this dissertation for safe and efficient operations of the single-track vehicles.

In the following, we first review the related work in literature.

1.2.1 Modeling and control of riderless single-track vehicle

The mechanical structure of bicycle or motorcycle consists of four rigid components: two wheels, a steering mechanism and a rear frame. Therefore, the single-track vehicle is a typical multi-body system. Bicycles and motorcycles share same structures and properties from dynamic and control aspects. Thus, we do not differentiate them

throughout the dissertation. Since the last century, many studies are reported to model the bicycle or motorcycle motions [5, 6]. The simplest model is the one degree of freedom model that only produces the roll motion and the representative work for the models are discussed in [7–9]. The first linear model that is able to predict the non-minimal phase behavior and the speed dependent stability is the "Whipple Model" [10]. The Whipple Model is bechmarked and derived through four independent methods in [5]. Many other non-linear models are also derived by using multi-body dynamic analysis [6, 11, 12]. However, due to the complexity of intrinsic nonlinear characteristics, some high-fidelity models are complicated such that a closed-form model for balancing and motion control design cannot be easily obtained [6]. Computer-aid tools are also used to simulate the extremely complex models. Sharp and Cossalter separately extended the bicycle models by considering the tire frictional interactions for motorcycles [13–17].

Control of an autonomous single-track vehicle only using the steering and velocity as control inputs is challenging due to the platform's non-minimum phase and underactuation properties. For such systems, there is no analytical casual compensator for *exactly* output (trajectory) tracking while keeping the internal (balancing) stability [18]. With an additional rider lean (i.e., weight shifting) as a control input, it has been shown that maneuvering a bicycle becomes easier because adding this extra control input essentially eliminates the right half-plane zeros [19]. In [20], an autonomous bicycle is designed and balanced using gyroscopic actuators. The controller in [20] is based on a linearized bicycle model. In [21], a nonlinear control method is designed for a trajectory tracking and balancing. A nonlinear controller based on maneuver regulation and inverse optimal control is presented in [22]. In [12], sliding-mode control is successfully implemented on an autonomous bicycle in laboratory. In [23], a balancing and tracking control mechanism is designed by on-board shifting weights. In [24, 25], a simplified inverted pendulum model is utilized for bicycle balancing. A proportional

derivative (PD) controller with a disturbance observer is employed to design a controller to balance the bicycle. The studies in [24, 25] however focus on balancing the bicycle on a straight-line motion.

Despite of the abovementioned studies, modeling and control of single-track vehicle for agile maneuvers, such as those maneuvers by professional racing riders, still remain a challenging task due to intrinsic unstable platform and complex tire-road interaction. Professional motorcycle riders can actually leverage the safety limits of the tire-road interaction, and maintain the vehicles at high performance while preserving safety. The previous reported modeling framework assume the nonholonomic constraint of the rear wheel contact point. In this dissertation, we relax such zero lateral velocity constraint to achieve agile maneuvers as those of the professional riders. In order to fully capture the tire/road slippage, we also consider an empirical tire friction model in the dynamic model of riderless single-track vehicle. An external/internal convertible (EIC) model-based control is used to design the autonomous agile maneuvers.

Compared to autonomous single-track vehicle with a certain forward velocity, balancing stationary single-track vehicle is much more challenging, especially for only using the front tire steering control. It is known that the single-track vehicle has "self-balance" ability at high speed. Nevertheless, the stationary single-track vehicles do not possess such property. In [26, 27], simulation results demonstrate the possibility to use only steering control to balance the stationary bicycle. However, no experiments are reported for such a control scheme. In [20, 23], additional actuated inputs such as weight-shifting or gyroscopic forces are used to reduce the difficulty of stationary balancing. In the dissertation, we present two different control designs based on steering control and gyroscopic actuator control, respectively. Experiments are also conducted on the developed instrumented bicycle called "bikebot" to validate the control designs.

1.2.2 Modeling and sensing of tire-road interaction

On the vehicle-environment interaction perspective, tire-road interactions provide the major thrust/braking forces for the vehicle system and play a critical role in HME system. Thus, understanding, modeling and control of the tire-road interaction are one of the main focuses in this dissertation. Tire-road interactions and real-time tire sensing play an extremely important role in vehicle dynamics and safety control. However, analytically modeling of the tire-road interactions is challenging because these interactions are complex, highly nonlinear, and depend on various tire and road conditions. Further challenges arise because of lack of effective, non-intrusive, inexpensive sensing technology to obtain in-situ tire-road contact information [28]. Most friction force models are obtained empirically, such as Pacejka "magic" formula [29] that capture the phenomenological relationships between the total friction forces and tire kinematics (e.g., slip ratios and slip angles etc.) Although the physical and LuGre dynamical friction models [30–35] try to capture and interpret the total friction forces through the rubber deformation and the friction force distributions, several critical modeling assumptions on the deformation and force distributions are made *a prior* for these distributions without experimental validations.

Various tire sensors are also developed to measure the rubber tread deformation and stresses. In [36,37], a tire sensor has been developed to measure the tire tread deformation. There is however no further reported evaluation on tire-road friction forces from the measured tread deflection. Surface acoustic wave (SAW) sensors are proposed for the "smart tire" application in [38]. Strain and capacitance sensors have been developed for monitoring the tire tread deformation [39, 40]. In [41, 42], accelerometers are placed inside tires for friction force estimations. Optical sensors are also developed for measuring tire deformation [43]. The optical sensing system is complicated and might not be very robust for varying tire running environments and for real-time applications. Piezoelectric sensors such as polyvinylidene fluoride (PVDF) has been

proposed and used for measuring the stresses on the inlet surface of the tire [44]. The stress measurements are interpreted through a friction force model. The results in [44] demonstrate the feasibility of the PVDF-based tread deformation sensor. In [45], a differently configured PVDF-based deformation sensor is designed to measure the tire sidewall deformation and then to estimate the tire slip angle. Built on these measurements, the tire lateral friction force is estimated using an analytical force model. A similar PVDF-based deformation sensor is also reported in [46]. Although the above discussed tire sensors provide measurements of the forces and the deformations, few results are reported to capture the local friction forces and their distributions. Moreover, these tire sensors cannot capture all aspects of the tire-road interaction forces. For example, the piezoelectric tire sensors such as PVDF cannot capture the static loading and forces.

From the above discussion, it is desirable to have a high-fidelity tire-road contact model and a novel sensing technique to capture the vehicle-environment interactions. The deformation and friction force distributions are particularly attractive and useful for real-time estimation of the tire frictional parameters for vehicle dynamics and control. We develop a modeling and sensing approach to obtain the deformation and force distribution in stick-slip transition on the contact patch in this dissertation.

1.2.3 Pose estimation, modeling and control of physical rider-bicycle interaction

Understanding the human-vehicle interaction such as physical rider-bicycle interaction is challenging. The difficulties are mainly due to the non-rigid rider body, the multiple contacts physical interaction, the complicated sensorimotor control mechanism, and lack of effective, non-intrusive motion sensors.

Simple inverted pendulum models and multi-body dynamic models are used for

the study of physical rider-bicycle interaction; see [19, 47] and references therein. In those studies, human riders are considered as a rigid part of the motorcycle, or only a riderless system is discussed. In [48], a human-bicycle model and comparison with experiments are presented for maneuver simulation. The human is considered as a point mass connected to the bicycle and only linearized models are obtained. Nonlinear human-bicycle physical models are complex because of high-dimensional human movements [47]. Moore [6] mainly uses the engineering and experimental approach to identify the interaction parameters between the rider and the bicycle. In this dissertation, we present a physical dynamic model which can reveal the physical dynamic interaction between the rider's trunk and the bicycle.

To precisely capture the rider-bicycle physical interaction, a robust pose estimation scheme is necessary. Existing motion capture systems, such as optical-, acoustic-, or magnetic-based tracking systems, are limited to indoor usage within a confined space and cannot be used for tracking human movement in natural environment. Because of small size, low cost and low power consumption, MEMS-based inertial sensors such as accelerometers, gyroscopes, or inertial measurement units (IMU) are widely used as wearable sensors for human motion and gait estimation. The orientation or the position of a body segment can be obtained by integration of gyroscope or acceleration signals. However, the results of such strapdown IMU integration have severe drifting problem due to the sensor measurement biases and noises. To overcome this problem, other complementary sensors, such as magnetic and ultrasonic sensors, are usually fused with inertial sensors to eliminate the drifting effect [49–54]. Human anatomical constraints are also used to enhance the fusion accuracy [55]. In [56], multiple accelerometers are used to estimate the gait without directly integrating IMU measurements. For walking gait estimation, a "resetting" technique is used in [57, 58] to initialize the integration at the beginning of each stride. In this dissertation, a computational scheme is proposed to estimate both the rider trunk pose and the bicycle roll

angle only using body-mounted inertial and force sensors. The scheme is based on the developed rider-bicycle dynamic model.

In addition, a balancing control design is presented to control the rider-bicycle interaction. The control design is based on a hierarchical sliding-model control approach with an integrated disturbance observer to estimate the interaction torques between the rider and the bicycle. Furthermore, we explore the rider's sensorimotor skill in bicycle riding. Moore [6] uses system identification to obtain an empirical model of the relationship between the steering angle and bicycle stability. Cain [59] has proposed a linear model to describe the steady-state turning and verified the model by vast experiments. A proportion integration differentiation (PID) controller is presented to mimic human steering control and a time-delay controller is used to model the rider trunk effect without experimental validations in [60]. A systematic review of the rider control up to the date can be referred to [61]. However, none of the aforementioned work investigated the human active reactions to external disturbances. In the last part of this dissertation, preliminary experimental results and observations are presented to show how the rider reacts external disturbances. To study the rider's sensorimotor skill for balancing, we build an instrumented and actuated autonomous bicycle "bikebot". The experimental platform and preliminary discovery can be further extended to study the human sensorimotor skill in future research.

1.3 Dissertation outline and contributions

The dissertation contains seven chapters. Chapter 1 is the introduction. In Chapter 2, the modeling and control of riderless single-track vehicle for agile maneuver navigation are first presented. In Chapter 3, two different control strategies are discussed for stationary balancing. To enhance the understanding of tire-road interaction, a sensor-enabled high-fidelity tire model is presented in Chapter 4. In Chapter 5, we consider

to model and estimate the rider-bicycle interaction in real time. A novel pose estimation scheme is proposed based on the fusion of force/inertial sensors. In Chapter 6, a controller is designed to control the physical rider-bicycle interactions. Preliminary experiments are also presented to study the human sensorimotor skill. Finally, conclusions and future work are discussed in Chapter 7. We describe the main content of each chapter as follows.

In Chapter 2, we first relax the commonly-used zero lateral velocity nonholonomic constraint for the real wheel contact point of the single-track vehicle system. Such nonholonomic constraint is not realistic for vehicle modeling, particularly for the vehicle dynamics in agile maneuvers. Second, we explicitly consider the tire-road interaction in the modeling framework because of the importance of the interaction on vehicle dynamics. With the new model, an external/internal convertible (EIC) model-based control design is presented. The control system design takes advantages of the control actuation flexibility and reduces the design complexity than those in [21] and [26]. The simulation examples of the trajectory tracking and path following demonstrate the effectiveness and efficacy of the modeling and control design.

In Chapter 3, we present two control designs to balance stationary bicycle. In the first design, we consider front-wheel steering as the control input. The design is based on the sliding mode control approach. We reveal and explicitly identify the attraction region of the control design. In the second design, a gyroscopic balancer mounted on the rear rack of the bicycle is used as the control actuator for stationary bicycle. An energy-shaping based control design is proposed to stabilize the bicycle to the orbital trajectory around the vertical equilibrium position. The effectiveness of both the control designs are validated by experiments.

We present the modeling, analysis and experimental studies of the stick-slip interactions between the tire and the firm road in Chapter 4. A semi-analytical model is first proposed to predict the normal force distribution on the tire contact patch. A

beam-spring network modeling approach is then used to capture and compute the friction force and rubber deformation distributions on the contact patch. To validate the contact models and analyses, a pressure-sensitive, electric conductive rubber sensor is embedded inside the tire rubber layer to extract the three-dimensional forces on the contact patch. Both the analytical and experimental results show that the friction force and rubber deformation distributions are dependent on the contact normal force distribution and the tire structural properties.

In Chapter 5, a novel pose estimation scheme is presented to obtain both the rider trunk pose and the bicycle roll angle only using body-mounted inertial and force sensors. The proposed estimation scheme is built on a rider-bicycle dynamic model and the integration of the wearable inertial and bicycle force sensors. We take advantages of the attractive properties of robust force measurements and motion-sensitive inertial measurements. The rider-bicycle dynamic model provides the underlying relationship between the force and the inertial measurements. The sensor fusion design fully incorporates the dynamic effects of the force measurements. The effectiveness of the estimation scheme is demonstrated through extensive bicycle riding experiments.

To control the rider-bicycle interactions, we first propose a hierarchical sliding-mode control approach in Chapter 6. Multiple coupled sliding surfaces are used to design the controller. The human trunk action is considered as an unknown disturbance and a nonlinear disturbance observer (NDOB) is used to estimate its value. The stability of the combined control and NDOB systems is guaranteed. The performance of the control systems is demonstrated through numerical simulations. In this chapter, we also present preliminary experimental results to study the human sensorimotor control using the bikebot. The external perturbation torques are generated by the gyroscopic actuator. Both straight line riding and circle trajectory riding are conducted in the experiments. The experiments conclude that the human rider mainly use steering rather than trunk motion to overcome external disturbances.

The main contribution of the dissertation is the development of a novel modeling and control framework of single-track vehicle from the HME interactions perspective. The detailed contributions of the dissertation are listed as follows.

1. Novel riderless single-track vehicle modeling and control design are proposed with considering the tire dynamics and relaxing the nonholonomic constraints. The new modeling and control design are able to realize the aggressive motions of agile maneuvers. Such a modeling and control framework can be further extended to study other machine-environment interactions.

2. The stationary balancing control of single-track vehicle is studied. A new steering model is proposed to capture the relationship between steering angle and center of mass change. Two different controllers are designed to implement the stationary balancing of single-track vehicle via steering control and gyroscopic balancer control, respectively. Experiments are conducted to validate the control designs.

3. A high fidelity tire model and a new in-situ sensing technique are introduced to tire-road interaction. Unlike empirical models, the new tire model is to investigate the friction force and deformation distributions on the tire-road contact patch with experimental validations and analyses. The understanding and modeling of the tire-road interactions potentially provide new knowledge and methods for flexible thin-layer/rigid contacts in other mechanical systems.

4. An in-situ human pose sensing scheme is proposed for the complex physical rider-bicycle interaction. The novel pose estimation scheme is built by integrating the dynamic model and the wearable inertial and bicycle force sensors together. These modeling and control approaches for rider-bicycle interaction can be applied to other HME systems.

5. A novel bicycle platform is developed for studying human balancing motor skills. Preliminary experiments are conducted on the bikebot to study and demonstrate the

rider sensorimotor control. The platform development provides a new tool to study human sensorimotor control in human-machine interactions.

Chapter 2

Modeling and Control of Autonomous Riderless Single-Track Vehicle

2.1 Introduction

Single-track vehicles, such as motorcycles and bicycles, have high maneuverability and strong off-road capabilities. In environments such as deserts, forests, and mountains, mobility of single-track vehicles significantly outperforms that of double-track vehicles. The recent demonstration of the Blue Team's autonomous motorcycle (Fig. 2.1(a)) in the 2005 DARPA Grand Challenge autonomous ground vehicles competition has shown an example of the high-agility of the single-track platform [62].

Although the extensive study of the motorcycle dynamics have revealed some knowledge of motorcycle platform under steady motions, however, modeling and control of motorcycles for agile maneuvers, such as those by professional racing riders, still remains a challenging task due to motorcycle's intrinsic unstable platform and complex tire-road interaction. Professional motorcycle riders can leverage the safety limits of the tire-road interaction, and maintain the vehicles at high performance while preserving safety. The objective of this chapter is to develop a new modeling and control scheme for an autonomous motorcycle of agile maneuvers. Comparing with existing study on the motorcycle dynamics and control, the main contribution of this study is the new modeling and control system design with integrated motorcycle dynamics with tire-road interaction. First, we relax the common zero lateral velocity nonholonomic constraint for the wheel contact points of the motorcycle system. Such

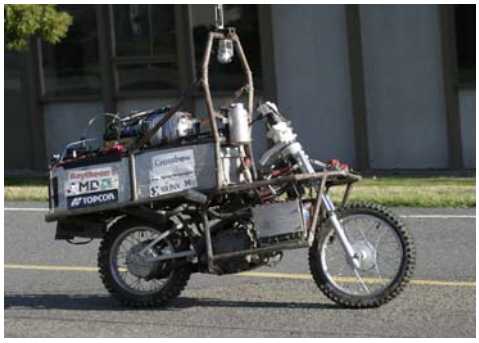

(a)

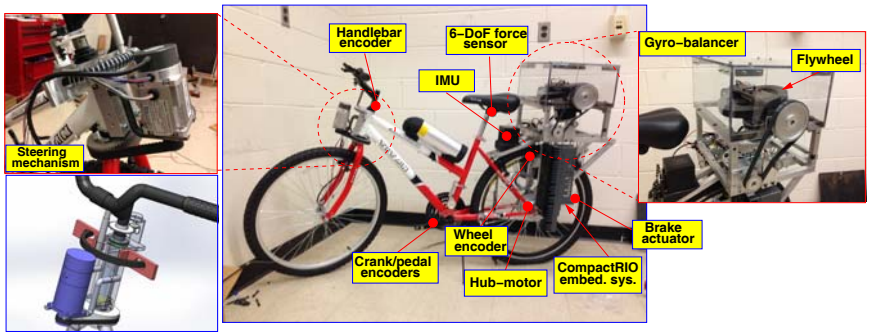

(b)

Figure 2.1: (a) The Blue team autonomous motorcycle. (b) Rutgers autonomous bicycle "bikebot".

nonholonomic constraint is not realistic for high-fidelity vehicle modeling [47]. The existence of non-zero lateral velocity is particular useful for capturing motorcycle dynamics in agile maneuvers. Second, we explicitly consider the tire-road interaction for designing control algorithms because of the importance of the tire-road interaction on motorcycle dynamics. To our knowledge, there is no study that explicitly considers such kinds of tire dynamics into the motorcycle control system design.

Control of an autonomous motorcycle only using the steering and moving velocity as inputs is challenging due to the platform's non-minimum phase and underactuation properties [1]. For such systems, there does not exist an analytical casual compensator

[1] An underactuated mechanical system is referred to a mechanical dynamic system in which the number of control inputs is less than the number of the generalized coordinates [63]. Readers can also refer to [64] for an overview of control of nonlinear non-minimum phase systems.

for *exactly* output (trajectory) tracking while keeping the internal (balancing) stability [18]. With an additional rider lean (i.e., weight shifting) as an control input, it has been shown that maneuvering a bicycle becomes easier because adding the extra control input essentially eliminates the right half-plane zeros [19]. In [20], an autonomous bicycle is designed and balanced using gyroscopic actuators. The controller in [20] is based on a linearized bicycle model. In [21], a nonlinear control method is designed for a trajectory tracking and balancing. In [23], a balancing and tracking control mechanism is designed by on-board shifting weights. In [24,25], a simplified inverted pendulum model is utilized for bicycle balancing. A proportional derivative (PD) controller with a disturbance observer is employed to design a controller to balance the bicycle. They however focus on balancing the bicycle on a straight-line motion.

In [21], an external/internal convertible (EIC) dynamical system is presented and the motorcycle dynamics are of an example of the EIC system. A nonlinear tracking control design is also discussed for the non-minimum phase bicycle dynamic systems. In [26], we have extended the dynamic models to consider motorcycle geometric and steering mechanism properties. In both [21] and [26], nonholonomic constraints of zero lateral velocity at the rear wheel contact point are enforced and only rear wheel friction force is considered for traction/braking forces. We relax the nonholonomic constraint assumption and consider that both wheels can produce braking actuation though the traction is only from the rear wheel. With the new model, the EIC model-based control design is presented in this chapter. The control systems design takes advantages of the control actuation flexibility and reduces the design complexity than those in [21] and [26]. Two simulation examples demonstrate the effectiveness and efficacy of the control systems design.

We also present a path-following design to overcome the large errors shown in the trajectory tracking. For autonomous vehicles, particularly the underactuated mechanical systems, maneuver regulation or path following control has demonstrated a

superior performance comparing with the trajectory tracking design [65–69]. In those path-following control design, the desired velocity profile along the trajectory is obtained either using Lyapunov-based approach or requiring online solving an optimization problem, which is non-causal for non-minimum phase dynamical systems such as motorcycle dynamics. We use a velocity field concept to generate the desired velocity profile for motorcycle systems. Our approach is inspired by the work in [70] of passivity-based control of fully-actuated robot manipulators. We integrate the velocity field concept with the EIC control design of underactuated non-minimum phase motorcycle dynamics.

2.2 Geometry and kinematics relationships

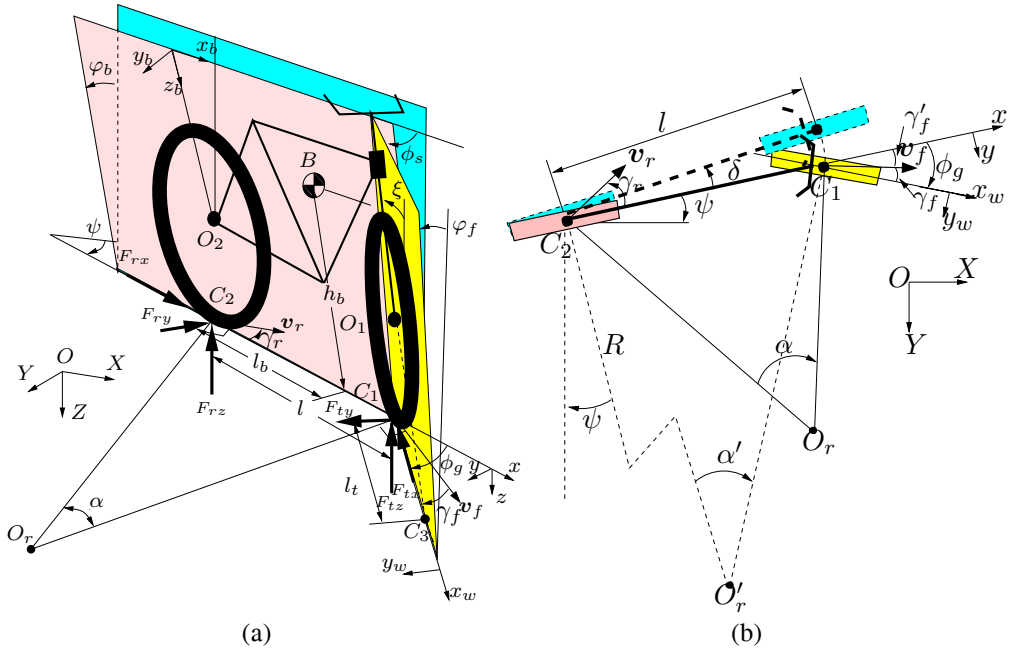

Figure 2.2: A schematic of the riderless motorcycle-bicycle. (a) Kinematic and dynamic modeling schematic. (b) Top view of the motorcycle-bicycle kinematic steering mechanism.

The riderless motorcycle is considered as as a two-part platform: a rear frame and a steering mechanism. Figure 6.1 shows a modeling schematic of the vehicle. We consider the following modeling assumptions: (1) the wheel/ground is a point contact

and thickness and geometry of the motorcycle tire are neglected; (2) The motorcycle body frame is considered a point mass; and (3) the motorcycle moves on a flat plane and vertical motion is neglected, namely, no suspension motion.

We denote C_1 and C_2 as the front and rear wheel point points with the ground, respectively. As illustrated in Fig. 6.1(a), three coordinate systems are used: the navigation frame $\mathcal{N}$ (X, Y, Z-axis fixed on the ground), the wheel base moving frame (x, y, z-axis fixed along line C_1C_2), and the rear body frame $\mathcal{B}$ (x_b, y_b, z_b-axis fixed on the rear frame). For the frame $\mathcal{B}$, we use (3-1-2) Euler angles and represent the motion by yaw angle ψ and roll angle φ_b. We denote unit vector sets for the three coordinate systems as $(\boldsymbol{I}, \boldsymbol{J}, \boldsymbol{K})$, $(\boldsymbol{i}, \boldsymbol{j}, \boldsymbol{k})$, and $(\boldsymbol{i}_B, \boldsymbol{j}_B, \boldsymbol{k}_B)$, respectively. We consider the trajectory of point C_2, denoted by its coordinates (X, Y) in $\mathcal{N}$, as motorcycle position. The orientation of the coordinate systems and the positive directions for angles and velocities follow the conversion of the SAE standard [5].

We consider the instantaneous rotation center of the motorcycle motion on the horizontal plane. Let O_r denote the instantaneous rotation center and O_r' denote the neutral instantaneous rotation center which is the intersection point of the perpendicular lines of the front and rear wheel planes; see Fig. 2.2. Under the neutral turning condition [71], the slip angles of the front and rear wheels are the same, that is, $\lambda_f = \lambda_r$, and then the rotation center angles for O_r and O_r' are equal to the kinematic steering angle ϕ_g, namely, $\alpha = \alpha' = \phi_g$. Let R denote the instantaneous radius of the trajectory of point C_2 under neutral turning conditions. We define σ as the kinematic steering variable as

$$\sigma := \tan\phi_g = \frac{l}{R}\,. \tag{2.1}$$

From the geometry of the front wheel steering mechanism [71], we find the following relationship,

$$\tan\phi_g\,\mathrm{c}_{\varphi_b} = \tan\phi_s\,\mathrm{c}_\xi\ . \tag{2.2}$$

, where $\mathrm{c}_\xi := \cos\xi$, $\mathrm{s}_\xi := \sin\xi$ for angle ξ. If we assume a small roll and steering

angles, then from (2.2) we obtain an approximation

$$\dot{\sigma}\, \mathrm{c}_{\varphi_b} = \dot{\phi}_s\, \mathrm{c}_{\xi}\,. \tag{2.3}$$

The motion of the motorcycle on the XY plane can be captured by the generalized coordinates $(X, Y, \psi, \varphi_b, \sigma)$. Note that the use of variable σ is to capture the steering impact on the motorcycle dynamics. The nonholonomic constraint of the rear wheel and the motion trajectory geometry imply the yaw kinematics equality

$$v_{rx} = R\dot{\psi} = \frac{l}{\sigma}\dot{\psi}\,. \tag{2.4}$$

From a differential geometry viewpoint [2], we can partition the generalized velocities of the motorcycle as base velocities $\dot{\boldsymbol{r}} = [\dot{\varphi}_b,\, v_{rx},\, v_{ry},\, \dot{\sigma}]^T$ and fiber velocities $\dot{\boldsymbol{s}} = \dot{\psi}$. We then write the constraints in (2.4) simply as

$$\dot{\boldsymbol{s}} + A(\boldsymbol{r}, \boldsymbol{s})\dot{\boldsymbol{r}} = 0, \tag{2.5}$$

where $A(\boldsymbol{r}, \boldsymbol{s}) = \begin{bmatrix} 0 & -\frac{\sigma}{l} & 0 & 0 \end{bmatrix}$.

Due to the steering mechanism and caster angle, the height of the mass center of gravity of the motorcycle is changing under steering. As shown in Fig. 6.1(b), the height change Δh_B of the center of gravity B due to the steering action can be calculated as [26]

$$\Delta h_B = \approx \frac{l_b l_t \sigma\, \mathrm{c}_{\xi}}{l}\, \mathrm{s}_{\varphi_b}\,, \tag{2.6}$$

where we use a small angle approximation $\sigma \approx \phi_g$ from the relationship (5.9).

Remark 2.1. *The height change Δh_B of the gravity center B due to steering given in (2.6) is an approximation. A more accurate modeling of Δh_B with experimental validation is given in [73]. The model of Δh_B given in [73] considers the effect of the tire size without using a small angle approximation and the resultant relationship*

[2] We here take a description of the base-fiber structure of nonholonomic dynamical systems with symmetry in [72].

between Δh_B and s_{φ_b} is not linear as shown in (2.6). However, we still use the simplified model (2.6) to design the trajectory tracking and path-following controllers and the results can be readily extended to the realistic steering model in [73].

Remark 2.2. *In [21] and [74], the steering axis is assumed to be vertical. This assumption simplifies the motorcycle dynamics and neglects a significant geometric stabilization mechanism, which is the "motorcycle trail" (denoted as l_t in Fig. 2.2) discussed in [75–77] and [71]. The resulting model of the motorcycle dynamics cannot capture the influence of the steering angle ϕ_s on the roll dynamics when $v_{rx} = 0$. Namely, one cannot use steering to stabilize the motorcycle. Such an observation is also pointed out in [19].*

Given the roll angle φ_b and the steering angle ϕ_s, the camber angle of the front wheel is approximated as

$$\varphi_f = \varphi_b + \phi_s \, \mathrm{s}_\xi \, . \tag{2.7}$$

We consider the relationship between velocities of point C_2 and the front wheel center O_1. We write the position vector $\boldsymbol{r}_{O_1} = \boldsymbol{r}_{C_2} + \boldsymbol{\rho}_{C_2O_1}$, where $\boldsymbol{r}_{C_2}$ is the position vector of point C_2 and $\boldsymbol{\rho}_{C_2O_1} = l\boldsymbol{i}_B - r\boldsymbol{k}_B = l\boldsymbol{i} + r\,\mathrm{s}_{\varphi_b}\boldsymbol{j} - r\,\mathrm{c}_{\varphi_b}\boldsymbol{k}$ is the relative position vector of B. The angular velocity of the rear frame is represented as $\boldsymbol{\omega} = \dot{\varphi}_b\boldsymbol{i} + \dot{\psi}\boldsymbol{k}$. Thus, we obtain

$$\boldsymbol{v}_{O_1} = \dot{\boldsymbol{r}}_{C_2} + \boldsymbol{\omega} \times \boldsymbol{\rho}_{C_2O_1} = (v_{rx} - r\dot{\psi}\,\mathrm{s}_{\varphi_b})\boldsymbol{i} + (v_{ry} + l\dot{\psi} + r\dot{\varphi}_b\,\mathrm{c}_{\varphi_b})\boldsymbol{j} + r\dot{\varphi}_b\,\mathrm{s}_{\varphi_b}\boldsymbol{k}. \tag{2.8}$$

2.3 Motorcycle dynamics

We use the constrained Lagrangian method in [72] to obtain the dynamic equation of the motion of the riderless motorcycle. We consider the motorcycle as two parts: one rear frame with mass m and one steering mechanism with the mass moment of inertia

J_s. The Lagrangian L of the motorcycle is calculated as

$$L = \frac{1}{2} J_s \dot{\phi}_s^2 + \frac{1}{2} m \boldsymbol{v}_B \cdot \boldsymbol{v}_B - mg \left(h_b \, \mathrm{c}_{\varphi_b} - \Delta h_B \right) \tag{2.9}$$

To calculate the mass center velocity, we take a similar approach as in (2.8) and obtain

$$\boldsymbol{v}_B = (v_{rx} - h_b \dot{\psi} \, \mathrm{s}_{\varphi_b}) \boldsymbol{i} + (v_{ry} + l_b \dot{\psi} + h_b \dot{\varphi}_b \, \mathrm{c}_{\varphi_b}) \boldsymbol{j} + h_b \dot{\varphi}_b \, \mathrm{s}_{\varphi_b} \, \boldsymbol{k}.$$

Plugging the above equations and (2.3)-(2.6) into (2.9), we obtain

$$\begin{aligned} L = & \frac{J_s}{2 \, \mathrm{c}_\xi^2} \dot{\sigma}^2 + \frac{1}{2} m \left[(v_{rx} - h_b \dot{\psi} \, \mathrm{s}_{\varphi_b})^2 + (v_{ry} + l_b \dot{\psi} + h_b \dot{\varphi}_b \, \mathrm{c}_{\varphi_b})^2 + {h_b}^2 \dot{\varphi}_b^2 \, \mathrm{s}_{\varphi_b}^2 \right] \\ & - mg \left(h_b \, \mathrm{c}_{\varphi_b} - \frac{l_b l_t \, \mathrm{c}_\xi}{l} \sigma \, \mathrm{s}_{\varphi_b} \right) . \end{aligned} \tag{2.10}$$

Incorporating the constraints (2.5), we obtain the constrained Lagrangian L_c as [3]

$$\begin{aligned} L_c = & \frac{J_s}{2 \, \mathrm{c}_\xi^2} \, \mathrm{c}_{\varphi_b}^2 \, \dot{\sigma}^2 + \frac{1}{2} m \Bigg\{ \left[\left(1 - \frac{h_b}{l} \sigma \, \mathrm{s}_{\varphi_b} \right)^2 + \frac{{l_b}^2}{l^2} \sigma^2 \right] v_{rx}^2 + v_{ry}^2 + \frac{2 l_b}{l} \sigma v_{rx} v_{ry} + \\ & \frac{2 l_b h_b \sigma}{l} \, \mathrm{c}_{\varphi_b} \, \dot{\varphi}_b v_{rx} + 2 h_b \, \mathrm{c}_{\varphi_b} \, \dot{\varphi}_b v_{ry} + {h_b}^2 \dot{\varphi}_b^2 \Bigg\} - mg \left(h_b \, \mathrm{c}_{\varphi_b} - \frac{l_b l_t \sigma \, \mathrm{c}_\xi}{l} \, \mathrm{s}_{\varphi_b} \right) \end{aligned} \tag{2.11}$$

The moment M_s on the rotating axis is obtained as

$$M_s = \frac{l_t}{\sqrt{1 + (l_t / r)^2}} \left(F_{ty} \, \mathrm{c}_{\varphi_f} - F_{tz} \, \mathrm{s}_{\varphi_f} \right) . \tag{2.12}$$

The detailed calculation of (2.12) is given in Appendix A.

The equations of motion using the constrained Lagrangian are obtained as [72] [4]

$$\frac{d}{dt} \frac{\partial L_c}{\partial \dot{r}^i} - \frac{\partial L_c}{\partial r^i} + A_i^k \frac{\partial L_c}{\partial s^k} = - \frac{\partial L}{\partial \dot{s}^l} C_{ij}^l \dot{r}^j + \tau^i, \; i, j = 1, \ldots, 4, \tag{2.13}$$

[3] Readers can refer to [72] for the definition of the constrained Lagrangian L_c and also Chapter 5 of [72] for the Lagrange-d'Alembert principle for nonholonomic constrained dynamical systems.

[4] Here the summation convention is used where, for example, if s is of dimension m, then $A_i^k \frac{\partial A_j^l}{\partial s^k} \equiv \Sigma_{k=1}^m A_i^k \frac{\partial A_j^l}{\partial s^k}$.

where τ^i are the external forces/torques, A_i^k is the element of connection $A(\boldsymbol{r}, \boldsymbol{s})$ at the kth row and ith column, and C_{ij}^l denote the components of the curvature of $A(\boldsymbol{r}, \boldsymbol{s})$ as

$$C_{ij}^l = \frac{\partial A_i^l}{\partial r^j} - \frac{\partial A_j^l}{\partial r^i} + A_i^k \frac{\partial A_j^l}{\partial s^k} - A_j^k \frac{\partial A_i^l}{\partial s^k}. \tag{2.14}$$

From state variable σ, from (2.13), we obtain the steering dynamics as

$$\frac{d}{dt}\left(\frac{J_s}{\mathrm{c}_\xi^2}\,\mathrm{c}_{\varphi_b}^2\,\dot{\sigma}\right) - \frac{mgl_t l_b\,\mathrm{c}_\xi}{l}\,\mathrm{s}_{\varphi_b} = \tau_s + M_s\,. \tag{2.15}$$

Considering a position feedback control of the steering angle directly, we can reduce the dynamic equation (2.15) by a kinematic steering system as

$$\dot{\sigma} = \omega_\sigma, \tag{2.16}$$

where the input ω_σ is considered as the virtual steering velocity and given by dynamic extension

$$\dot{\omega}_\sigma = \frac{\mathrm{c}_\xi^2}{J_s\,\mathrm{c}_{\varphi_b}^2}\,(\tau_s + M_s) - 2\tan\varphi_b\dot{\varphi}_b\dot{\sigma} + \frac{mgl_t l_b\,\mathrm{c}_\xi^3}{lJ_s}\,\mathrm{s}_{\varphi_b}\,.$$

Similarly, we obtain the roll dynamics equation

$$\begin{aligned}&\frac{l_b h_b\sigma}{l}\mathrm{c}_{\varphi_b}\,\dot{v}_{rx} + h_b\,\mathrm{c}_{\varphi_b}\,\dot{v}_{ry} + {h_b}^2\ddot{\varphi}_b + \left(1 - \frac{h_b\sigma}{l}\,\mathrm{s}_{\varphi_b}\right)\frac{h_b\sigma\,\mathrm{c}_{\varphi_b}}{l}v_{rx}^2\\ &\quad -g\left(h_b\,\mathrm{s}_{\varphi_b} + \frac{l_t l_b\,\mathrm{c}_\xi}{l}\sigma\,\mathrm{c}_{\varphi_b}\right) = -\frac{l_b h_b}{l}\,\mathrm{c}_{\varphi_b}\,v_{rx}\omega_\sigma,\end{aligned} \tag{2.17}$$

longitudinal dynamics equation

$$\begin{aligned}&\left[\left(1 - \frac{h_b\sigma}{l}\,\mathrm{s}_{\varphi_b}\right)^2 + \frac{{l_b}^2\sigma^2}{l^2}\right]\dot{v}_{rx} + \frac{l_b\sigma}{l}\dot{v}_{ry} + \frac{l_b h_b\sigma}{l}\,\mathrm{c}_{\varphi_b}\,\ddot{\varphi}_b\\ &-2\left(1 - \frac{h_b\sigma}{l}\,\mathrm{s}_{\varphi_b}\right)\frac{h_b\sigma}{l}\,\mathrm{c}_{\varphi_b}\,\dot{\varphi}_b v_{rx} - \frac{l_b h_b\sigma}{l}\,\mathrm{s}_{\varphi_b}\,\dot{\varphi}_b^2 = -\left[-2\left(1 - \frac{h_b\sigma}{l}\,\mathrm{s}_{\varphi_b}\right)\frac{h_b}{l}\,\mathrm{s}_{\varphi_b}\,v_{rx}\right.\\ &\left.+\frac{2{l_b}^2\sigma}{l^2}v_{rx} + \frac{l_b}{l}v_{ry} + \frac{l_b h_b}{l}\,\mathrm{c}_{\varphi_b}\,\dot{\varphi}_b\right]\omega_\sigma + \frac{1}{m}F_{rx}\\ &-\frac{1}{m\sqrt{1+\sigma^2}}\,(F_{tx} + \sigma F_{ty}) - \frac{1}{m}C_d v_{rx}^2,\end{aligned} \tag{2.18}$$

and lateral dynamics equation

$$\frac{l_b\sigma}{l}\dot{v}_{rx}+\dot{v}_{ry}+h_b\,\mathrm{c}_{\varphi_b}\,\ddot{\varphi}_b-h_b\,\mathrm{s}_{\varphi_b}\,\dot{\varphi}_b^2=-\frac{l_b v_{rx}}{l}\omega_\sigma-\frac{1}{m}F_{ry}+\frac{1}{m\sqrt{1+\sigma^2}}\left(F_{ty}-\sigma F_{tx}\right). \tag{2.19}$$

In (2.18), C_d is the aerodynamic drag coefficient.

Let $\dot{\boldsymbol{q}} := [\dot{\varphi}_b \;\; v_{rx} \;\; v_{ry}]^T$ denote the generalized velocity of the motorcycle and we rewrite the dynamic equations (2.17)-(2.19) in a compact matrix form as

$$\mathbf{M}\ddot{\boldsymbol{q}}=\mathbf{K}_m+\mathbf{B}_m\begin{bmatrix}\omega_\sigma\\F_{tx}\\F_{ty}\\F_{rx}\\F_{ry}\end{bmatrix}, \tag{2.20}$$

where matrices

$$\mathbf{M}=\begin{bmatrix}M_{11}&M_{12}\\M_{21}&M_{22}\end{bmatrix}=\left[\begin{array}{c|cc}{h_b}^2&\frac{l_bh_b\sigma}{l}\,\mathrm{c}_{\varphi_b}&h_b\,\mathrm{c}_{\varphi_b}\\\hline\frac{l_bh_b\sigma}{l}\,\mathrm{c}_{\varphi_b}&\left(1-\frac{h_b\sigma}{l}\,\mathrm{s}_{\varphi_b}\right)^2+\frac{{l_b}^2\sigma^2}{l^2}&\frac{l_b\sigma}{l}\\h_b\,\mathrm{c}_{\varphi_b}&\frac{l_b\sigma}{l}&1\end{array}\right], \tag{2.21}$$

$$\mathbf{K}_m=\begin{bmatrix}-\left(1-\frac{h_b\sigma}{l}\,\mathrm{s}_{\varphi_b}\right)\frac{h_b\sigma\,\mathrm{c}_{\varphi_b}}{l}v_{rx}^2+g\left(h_b\,\mathrm{s}_{\varphi_b}+\frac{l_tl_b\,\mathrm{c}_\xi}{l}\sigma\,\mathrm{c}_{\varphi_b}\right)\\2\left(1-\frac{h_b\sigma}{l}\,\mathrm{s}_{\varphi_b}\right)\frac{h_b\sigma}{l}\,\mathrm{c}_{\varphi_b}\,\dot{\varphi}_bv_{rx}+\frac{l_bh_b\sigma}{l}\,\mathrm{s}_{\varphi_b}\,\dot{\varphi}_b^2-\frac{1}{m}C_dv_{rx}^2\\h_b\,\mathrm{s}_{\varphi_b}\,\dot{\varphi}_b^2\end{bmatrix},$$

and

$$\mathbf{B}_m=\begin{bmatrix}-\frac{l_bh_b}{l}\,\mathrm{c}_{\varphi_b}\,v_{rx}&0&0&0&0\\B_\omega&-\frac{1}{m\sqrt{1+\sigma^2}}&-\frac{\sigma}{m\sqrt{1+\sigma^2}}&\frac{1}{m}&0\\-\frac{l_bv_{rx}}{l}&-\frac{\sigma}{m\sqrt{1+\sigma^2}}&\frac{1}{m\sqrt{1+\sigma^2}}&0&-\frac{1}{m}\end{bmatrix}.$$

In the above matrix $\mathbf{B}_m$,

$$B_\omega=2\left[\left(1-\frac{h_b\sigma}{l}\,\mathrm{s}_{\varphi_b}\right)\frac{h_b}{l}\,\mathrm{s}_{\varphi_b}-\frac{{l_b}^2\sigma}{l^2}\right]v_{rx}-\frac{l_b}{l}v_{ry}-\frac{l_bh_b}{l}\,\mathrm{c}_{\varphi_b}\,\dot{\varphi}_b.$$

It is clear that the control inputs in (2.16) and (2.20) are the virtual steering velocity ω_σ and the wheel traction/braking forces $\boldsymbol{F}_f$ and $\boldsymbol{F}_r$.

2.4 Tire dynamics models

In this section, to make the modeling process trackable, we integrate an empirical and simple tire-road interaction into motorcycle dynamics. In Chapter 4, we will propose a high fidelity model for real-time tire-road sensing applications.

2.4.1 Tire kinematics relationships

Figure 2.3 illustrates the kinematics of the tire-road contact. Let $\boldsymbol{v}_c = v_{cx}\boldsymbol{i}+v_{cy}\boldsymbol{j}+v_{cz}\boldsymbol{k}$ and $\boldsymbol{v}_o = v_{ox}\boldsymbol{i} + v_{oy}\boldsymbol{j} + v_{oz}\boldsymbol{k}$ denote the velocities of the contact point and the wheel center in frame $\mathcal{B}$, respectively. We define the longitudinal slip ratio λ_s and the lateral side slip ratio λ_γ, respectively, as

$$\lambda_s := \frac{v_{cx} - R_t\omega_w}{v_{cx}},\ \lambda_\gamma := \tan\gamma = -\frac{v_{cy}}{v_{cx}}, \tag{2.22}$$

where ω_w is the wheel angular velocity and γ is the side slip angle.

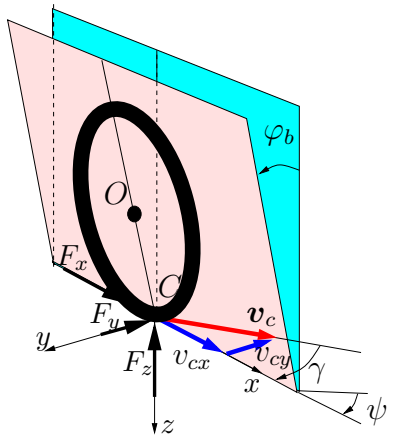

Figure 2.3: Schematic of the tire kinematics.

For the front wheel, the camber angle is different (2.7), and the velocity relationship

between C_1 and the wheel center O_1 in $\mathcal{B}$ is then

$$v_{fx} = v_{fox} + R_t\dot{\psi}\,\mathrm{s}_{\varphi_b},\ v_{fcy} = v_{foy} - R_t\dot{\varphi}_f\,\mathrm{c}_{\varphi_f},\ v_{fz} = v_{foz} - R_t\dot{\varphi}_f\,\mathrm{s}_{\varphi_b}\,. \tag{2.23}$$

Using the relationship (2.8) and (2.7), we simplify the above velocity calculation and obtain

$$v_{fx} = v_{rx},\ v_{fy} = v_{ry} - R_t\dot{\phi}_s\,\mathrm{s}_\xi\,\mathrm{c}_{\varphi_b} + l\dot{\psi}. \tag{2.24}$$

From the side slip ratio (2.22) of the rear wheel, we have

$$\lambda_{r\gamma} = \tan\gamma_r = -\frac{v_{ry}}{v_{rx}} = -\frac{v_{fy}}{v_{fx}} - \frac{R_t\dot{\phi}_s\,\mathrm{s}_\xi\,\mathrm{c}_{\varphi_b} - l\dot{\psi}}{v_{rx}} = \tan\gamma_f' - \frac{R_t\tan\xi\,\mathrm{c}^2_{\varphi_b}}{v_{rx}}\omega_\sigma + \sigma, \tag{2.25}$$

where $\gamma_f' := \phi_g - \gamma_f$ and $\tan\gamma_f' = -\frac{v_{fy}}{v_{fx}}$. We also use relationships (2.3) and (2.4) in the last step above. Moreover, from (5.9) and the geometry and kinematics of the front wheel (Fig. 6.1), we have

$$\sigma = \tan\phi_g = \tan(\gamma_f' + \gamma_f) \approx \tan\gamma_f' + \tan\gamma_f = \lambda_{r\gamma} + \frac{R_t\tan\xi\,\mathrm{c}^2_{\varphi_b}}{v_{rx}}\omega_\sigma - \sigma + \lambda_{f\gamma}.$$

Therefore, we obtain the relationship between the front and rear wheel side slip ratios as follows.

$$\lambda_{f\gamma} = 2\sigma - \frac{R_t\tan\xi\,\mathrm{c}^2_{\varphi_b}}{v_{rx}}\omega_\sigma - \lambda_{r\gamma}. \tag{2.26}$$

Similarly, we can obtain the slip ratio calculation of the front wheel as follows. We obtain the longitudinal velocity of point C_1 as

$$v_{fx_w} \approx v_{rx}\,\mathrm{c}_{\phi_g} + (v_{ry} + \sigma v_{rx})\,\mathrm{s}_{\phi_g} = \frac{1}{\sqrt{1+\sigma^2}}\left[\left(1+\sigma^2\right)v_{rx} + \sigma v_{ry}\right].$$

Then, by the definition (2.22), we obtain the front wheel longitudinal slip ratio

$$\lambda_{fs} = 1 - \frac{R_t\omega_f}{v_{fx_w}} = 1 - \frac{R_t\sqrt{1+\sigma^2}}{(1+\sigma^2)v_{rx} + \sigma v_{ry}}\omega_f. \tag{2.27}$$

2.4.2 Empirical frictional force model

We focus on modeling of the longitudinal force F_x and lateral force F_y because of their importance in motorcycle dynamics and motion control.

The tire-road frictional forces depend on many factors, such as slip and slip angles, vehicle velocity, normal load, and tire and road conditions, etc. It is widely accepted that the pseudo-static relationships, namely, the mathematical models of the longitudinal force F_x and slip λ, and the lateral force F_y and slip angle γ, are the most important characteristics to capture the tire-road interaction. We propose to approximate the friction forces by a piecewise linear relationship shown in Fig. 2.4. Let $F(x)$ denote the frictional force as a function of independent variable x. The piecewise linear function $F(x)$ captures the property of the tire-road forces: when $0 \leq x \leq x_m$, $F(x) = kx$, where k is the stiffness coefficient, and when $x_m < x \leq x_{\max}$, $F = \frac{(1-\alpha_x)F_m}{x_m - x_{\max}}(x - x_m) + F_m$, where $0 \leq \alpha_x \leq 1$ is a constant that represents the fraction of the force at $x_{\max}$ of the maximum force F_m. We thus write the force $F(x)$ as follows.

$$F(x) = k(a_1 + a_2 x), \tag{2.28}$$

where

$$a_1 = \begin{cases} 0 & 0 \leq x \leq x_m \\ \frac{(x_{\max} - x_m)x_m}{x_{\max} - x_m} & x_m < x \leq x_{\max}, \end{cases} \quad a_2 = \begin{cases} 1 & 0 \leq x \leq x_m \\ \frac{-(1-\alpha_x)x_m}{x_{\max} - x_m} & x_m < x \leq x_{\max}. \end{cases}$$

With the force model (2.28), we write the longitudinal force as

$$F_x(\lambda_s) = k_\lambda \left[a_{1\lambda} + a_{2\lambda} \operatorname{sgn}(\lambda_s)\lambda_s \right], \tag{2.29}$$

where the function $\operatorname{sgn}(x) = 1$ for $x \geq 0$ and -1 otherwise is used to capture both positive (braking) and negative (traction) forces for $F_x(\lambda_s)$. For the lateral force, due to the large camber angle of the motorcycle tires, we have

$$F_y(\lambda_{eq}) = k_\gamma \left[a_{1\gamma} + a_{2\gamma} \operatorname{sgn}(\lambda_{eq})\lambda_{eq} \right], \tag{2.30}$$

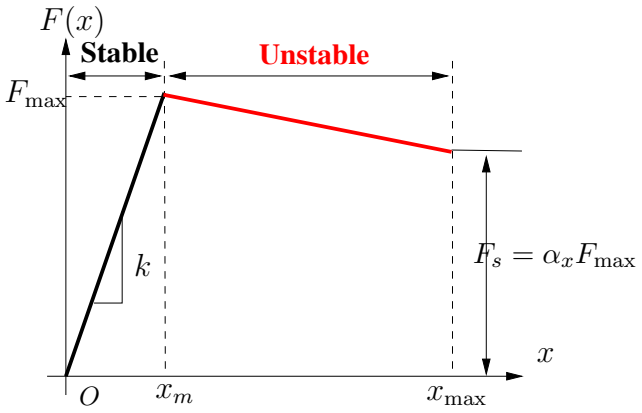

Figure 2.4: Linear approximation of the tire-road frictional force $F(x)$.

where we define the equivalent side slip ratio

$$\lambda_{eq} = \tan\gamma_{eq} = \tan\left(\gamma + \frac{k_{\varphi_b}}{k_\gamma}\varphi_b\right) \approx \lambda_\gamma + \frac{k_{\varphi_b}}{k_\gamma}\tan\varphi_b.$$

The values of the longitudinal, corning, and cambering coefficients, k_λ, k_γ, k_{φ_b}, depend on the normal load F_z. Due to the acceleration and deceleration, the normal load F_z often changes during motion. For front and rear wheels, the normal loads F_{tz} and F_{rz} are obtained respectively as

$$F_{tz} = \frac{l_b}{l}mg - \frac{h_b}{l}m\dot{v}_{Bx},\ F_{rz} = \frac{l-l_b}{l}mg + \frac{h_b}{l}m\dot{v}_{Bx}, \tag{2.31}$$

where $\dot{v}_{Bx}$ is the longitudinal acceleration of the motorcycle at the mass center B. The relationship between $\dot{v}_{Bx}$ and the acceleration of point C_2 is obtained as

$$\dot{v}_{Bx} = \dot{v}_{rx} - v_{ry}\dot{\psi} - h_b\ddot{\psi}\,\mathrm{s}_{\varphi_b} - l_b\dot{\psi}^2 - 2h_b\dot{\psi}\dot{\varphi}_b\,\mathrm{c}_{\varphi_b}\,.$$

The calculation of the above relationship is given in Appendix B. In this chapter, we use the tire models in [1] to calculate the dependence of the stiffness coefficients on the normal load.

2.4.3 Combined tire and motorcycle dynamics models

We combine the motorcycle dynamics (2.16) and (2.20) with the tire dynamics. The controlled input variables are the front and rear wheel angular velocities, namely, ω_f

and ω_r, respectively, and the steering angle ϕ_s. Note that the driving wheel is the rear wheel and we can apply braking for the front wheel, namely, $F_{tx} \geq 0$. For the control system design, we consider the pseudo-static friction models (2.29) and (2.30), and therefore we write the longitudinal at the front and rear wheels as

$$F_{tx} = F_{1f} + F_{2f}\lambda_{fs}, \quad F_{rx} = F_{1r} + F_{2r}\lambda_{rs} \tag{2.32}$$

and lateral forces

$$F_{ty} = F_{3f} + F_{4f}\left(\lambda_{f\gamma} + \frac{k_{f\varphi_b}}{k_{f\gamma}}\tan\varphi_f\right), \; F_{ry} = F_{3r} + F_{4r}\left(\lambda_{r\gamma} + \frac{k_{r\varphi_b}}{k_{r\gamma}}\tan\varphi_b\right), \tag{2.33}$$

where $F_{1i} = k_{i\lambda}a_{1i\lambda}$, $F_{2i} = k_{i\lambda}a_{2i\lambda}\operatorname{sgn}(\lambda_{is})$, $F_{1i} = k_{i\lambda}a_{1i\lambda}$, $F_{2i} = k_{i\lambda}a_{2i\lambda}\operatorname{sgn}(\lambda_{is})$, $i = f, r$, and $a_{ji\lambda}$, $a_{ji\gamma}$, $j = 1, 2$, are the longitudinal and lateral force model parameters defined in (2.28), respectively.

Plugging (2.32) and (2.33) into (2.20) and using the relationship (2.26), we obtain

$$\mathbf{M}(\boldsymbol{q}, \sigma)\ddot{\boldsymbol{q}} = \mathbf{K}(\dot{\boldsymbol{q}}, \boldsymbol{q}, \sigma) + \mathbf{B}\boldsymbol{u}, \tag{2.34}$$

where input $\boldsymbol{u} := \begin{bmatrix} \omega_\sigma & \boldsymbol{u}_\lambda^T \end{bmatrix}^T$, $\boldsymbol{u}_\lambda = \begin{bmatrix} \lambda_{fs} & \lambda_{rs} \end{bmatrix}^T$, matrix

$$\mathbf{K} = \begin{bmatrix} K_1 \\ \hdashline K_2 \end{bmatrix} = \begin{bmatrix} (K_m)_1 \\ \hdashline (K_m)_2 - \dfrac{F_{1f}}{m\sqrt{1+\sigma^2}} - \dfrac{\sigma}{m\sqrt{1+\sigma^2}}F_{34} + \dfrac{F_{1r}}{m} \\ (K_m)_3 - \dfrac{\sigma F_{1f}}{m\sqrt{1+\sigma^2}} + \dfrac{1}{m\sqrt{1+\sigma^2}}F_{34} - \dfrac{F_{ry}}{m} \end{bmatrix}, \tag{2.35}$$

$(K_m)_i$ is the ith row of matrix $\mathbf{K}$, $F_{34} = F_{3f} + F_{4f}\left(\lambda_{f\gamma} + \frac{k_{f\varphi_b}}{k_{f\gamma}}(2\sigma - \lambda_{r\gamma})\right)$, and

$$\mathbf{B} = \left[\begin{array}{c:cc} B_{11} & B_{12} \\ \hdashline B_{21} & B_{22} \end{array}\right] = \left[\begin{array}{c:cc} -\dfrac{l_b h_b}{l}\,\mathrm{c}_{\varphi_b}\, v_{rx} & 0 & 0 \\ \hdashline B_\omega + \dfrac{R_t\sigma F_{4f}\tan\xi\,\mathrm{c}^2_{\varphi_b}\,k_{f\varphi_b}}{m v_{rx} k_{f\gamma}\sqrt{1+\sigma^2}} & -\dfrac{F_{2f}}{m\sqrt{1+\sigma^2}} & \dfrac{F_{2r}}{m} \\ -\dfrac{l_b v_{rx}}{l} - \dfrac{R_t F_{4f}\tan\xi\,\mathrm{c}^2_{\varphi_b}\,k_{f\varphi_b}}{m v_{rx} k_{f\gamma}\sqrt{1+\sigma^2}} & -\dfrac{\sigma F_{2f}}{m\sqrt{1+\sigma^2}} & 0 \end{array}\right]. \tag{2.36}$$

Remark 2.3. *We assume that the motorcycle is rear-wheel driven and thus the front wheel cannot produce the traction force. We consider the following distribution rule for braking and traction strategy among two wheels. The rear tire can produce both traction and braking forces, while the front tire can only produce braking force. If a braking force is needed, the front tire would first be used to brake and produce the amount of needed braking force. If the needed braking force cannot be fully generated by the front tire after the slip ratio reaches λ_{sm}, the rear tire will then brake to produce the necessarily extra braking forces.*

2.5 Trajectory tracking control systems design

2.5.1 External/Internal convertible dynamical systems

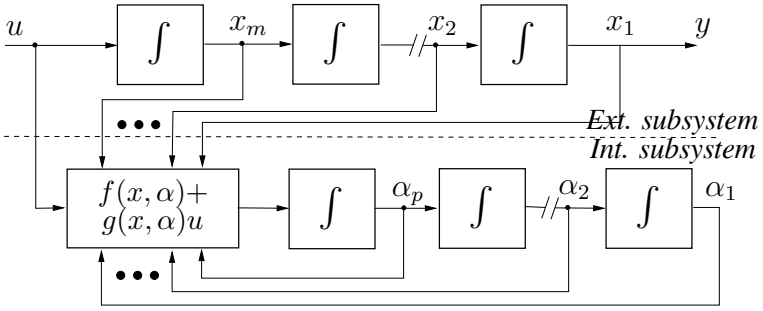

Figure 2.5: An external/internal convertible system.

The motorcycle dynamics with tire models are presented by (2.34). We now consider to put such a system into the form of an external/Internal convertible (EIC) dynamical systems. The EIC form of a nonlinear dynamical system can be viewed as a special case of the normal form.

Definition 2.1 ([21])**.** *A single-input, single-output, n $(= m + p)$-dimensional time-invariant nonlinear control system is called in an* external/internal convertible form *if*

the system is of the form

$$\Sigma(u)\begin{cases}\dot{x}_i = x_{i+1}, & i = 1, \cdots, m-1,\\ \dot{x}_m = u,\\ \dot{\alpha}_i = \alpha_{i+1}, & i = 1, \cdots, p-1,\\ \dot{\alpha}_p = f(x,\alpha) + g(x,\alpha)u,\\ y = x_1,\end{cases} \tag{2.37}$$

with input $u \in \mathbb{R}$*, output* $y \in \mathbb{R}$*, state variables* (x, α)*, with* $x := (x_1, \cdots, x_m) \in \mathbb{R}^m$ *and* $\alpha := (\alpha_1, \cdots \alpha_p) \in \mathbb{R}^p$*. The coordinates* (x, α) *are assumed to be defined on the open ball* $\mathbf{B}_r \subset \mathbb{R}^n$ *around the origin. The origin is assumed to be an equilibrium of the system, namely,* $f(0, 0) = 0$*. The functions* $f(x, \alpha)$ *and* $g(x, \alpha)$ *are* C^n *in their arguments, and* $g(x, \alpha) \neq 0$ *for all* $(x, \alpha) \in \mathbf{B}_r$*. Moreover, we refer to the* external subsystem *of* $\Sigma(u)$ *as*

$$\Sigma_{\text{ext}}(u)\begin{cases}\dot{x}_i = x_{i+1}, & i = 1, \cdots, m-1,\\ \dot{x}_m = u\end{cases} \tag{2.38}$$

and the internal subsystem *of* $\Sigma(u)$ *as*

$$\Sigma_{\text{int}}(u)\begin{cases}\dot{\alpha}_i = \alpha_{i+1}, & i = 1, \cdots, p-1,\\ \dot{\alpha}_p = f(x,\alpha) + g(x,\alpha)u.\end{cases} \tag{2.39}$$

Figure 2.5 shows the structure of an EIC system. An EIC system is *convertible* because under a simple state-dependent input and an output transformation, the internal system is converted to an external system, and the external system is converted to an internal system (*dual* structure). To see such a property, let

$$u = g(x,\alpha)^{-1}\left[v - f(x,\alpha)\right] \tag{2.40}$$

define a state-dependent input transformation, $u \mapsto v$. Define $\xi = \alpha^1$ as the *dual output.* Apply transformation (2.40) to the EIC system (2.37) and the resulting system

is referred to as the *dual* of $\Sigma(u)$.

$$\Sigma_d(v) \begin{cases} \dot{x}_i = x_{i+1}, & i = 1, \cdots, m-1, \\ \dot{x}_m = -g(x,\alpha)^{-1} f(x,\alpha) + g(x,\alpha)^{-1} v, & \\ \dot{\alpha}_i = \alpha_{i+1}, & i = 1, \cdots, p-1, \\ \dot{\alpha}_p = v, & \\ \xi = \alpha_1. & \end{cases} \tag{2.41}$$

Thus the use of input transformation (2.40) and the output assignment $\xi = \alpha_1$ converts the internal dynamics of $\Sigma(u)$ to the external dynamics of $\Sigma_d(v)$, and the external dynamics of $\Sigma(u)$ to the internal dynamics of $\Sigma_d(v)$.

Since the EIC form is a special normal form of nonlinear dynamical systems, we can apply the input-output linearization method [64, 78] to convert (2.34) into an EIC form. Let $B_{22} \in \mathbb{R}^{2\times 2}$, $B_{22} \in \mathbb{R}^{2\times 2}$, and $K_2 \in \mathbb{R}^2$ denote the block elements of matrices $\mathbf{M}$, $\mathbf{B}$, and $\mathbf{K}$, given by (2.21), (2.36), and (2.35), respectively. Using the input transformation

$$\boldsymbol{u}_\lambda = B_{22}^{-1} M_{22} \left[M_{22}^{-1} \left(M_{21} \ddot{\varphi}_b - K_2 - B_{21} \omega_\sigma \right) + \boldsymbol{u}_a \right], \tag{2.42}$$

Eq. (2.34) becomes

$$\begin{cases} M_{11} \ddot{\varphi}_b = K_1 - M_{12} \boldsymbol{u}_a + B_{11} \omega_\sigma \,, \\ \begin{bmatrix} \dot{v}_{rx} \\ \dot{v}_{ry} \end{bmatrix} = \begin{bmatrix} a_{rx} \\ a_{ry} \end{bmatrix} =: \boldsymbol{u}_a, \end{cases} \tag{2.43}$$

where $\boldsymbol{u}_a$ is the controlled acceleration of point C_2 in the xyz coordinate system. We also define the controlled linear acceleration of point C_2 and yaw acceleration as

$$\boldsymbol{u}_j := \begin{bmatrix} u_{rx} \\ u_{ry} \\ u_\psi \end{bmatrix} = \begin{bmatrix} \dot{a}_{rx} \\ \dot{a}_{ry} \\ \ddot{\psi} \end{bmatrix} = \begin{bmatrix} \dot{\boldsymbol{u}}_a \\ \frac{v_{rx}\omega_\sigma + \sigma a_{rx}}{l} \end{bmatrix}, \tag{2.44}$$

where we use kinematics $l\dot{\psi} = \sigma v_{rx}$ in the calculation. Let (X, Y) denote the coordinates of the contact point C_2 and then we have

$$\begin{bmatrix} v_X \\ v_Y \end{bmatrix} = \begin{bmatrix} \dot{X} \\ \dot{Y} \end{bmatrix} = \begin{bmatrix} \mathrm{c}_\psi & -\mathrm{s}_\psi \\ \mathrm{s}_\psi & \mathrm{c}_\psi \end{bmatrix} \begin{bmatrix} v_{rx} \\ v_{ry} \end{bmatrix}.$$

Differentiating the above equation twice (dynamic extension), we obtain

$$\begin{bmatrix} \ddot{v}_X \\ \ddot{v}_Y \end{bmatrix} = \mathbf{U} + \boldsymbol{u}_J, \tag{2.45}$$

where

$$\mathbf{U} = \begin{bmatrix} -2\dot{v}_{rx}\,\mathrm{s}_\psi - 2\dot{v}_{ry}\,\mathrm{c}_\psi - v_{rx}\dot{\psi}\,\mathrm{c}_\psi + v_{ry}\dot{\psi}\,\mathrm{s}_\psi \\ 2\dot{v}_{rx}\,\mathrm{c}_\psi - 2\dot{v}_{ry}\,\mathrm{s}_\psi - v_{rx}\dot{\psi}\,\mathrm{s}_\psi - v_{ry}\dot{\psi}\,\mathrm{c}_\psi \end{bmatrix} \dot{\psi}$$

and

$$\boldsymbol{u}_J := \begin{bmatrix} \mathrm{c}_\psi & -\mathrm{s}_\psi \\ \mathrm{s}_\psi & \mathrm{c}_\psi \end{bmatrix} \begin{bmatrix} u_{rx} \\ u_{ry} \end{bmatrix} + \begin{bmatrix} -v_{rx}\,\mathrm{s}_\psi - v_{ry}\,\mathrm{c}_\psi \\ v_{rx}\,\mathrm{c}_\psi - v_{ry}\,\mathrm{s}_\psi \end{bmatrix} u_\psi. \tag{2.46}$$

We define the new inputs u_X and u_Y such that

$$\boldsymbol{u}_J = -\mathbf{U} + \begin{bmatrix} u_X \\ u_Y \end{bmatrix} \tag{2.47}$$

and then the motorcycle dynamics (2.43) are in the EIC form as

$$\Sigma_{\text{ext}}: \begin{cases} \begin{bmatrix} \ddot{v}_X \\ \ddot{v}_Y \end{bmatrix} = \begin{bmatrix} u_X \\ u_Y \end{bmatrix}, \end{cases} \tag{2.48a}$$

$$\Sigma_{\text{int}}: \ \ddot{\varphi}_b = \frac{g}{h_b}\left(\mathrm{s}_{\varphi_b} + \frac{l_b l_t\,\mathrm{c}_\xi\,\dot{\psi}}{h_b v_{rx}}\,\mathrm{c}_{\varphi_b}\right) - \frac{1}{h_b}\left(1 - \frac{h_b\dot{\psi}}{v_{rx}}\,\mathrm{s}_{\varphi_b}\right)\dot{\psi} v_{rx}\,\mathrm{c}_{\varphi_b} - \frac{1}{h_b}\,\mathrm{c}_{\varphi_b}\,u_{\psi y}, \tag{2.48b}$$

where

$$u_{\psi y} := l_b u_\psi + a_{ry}. \tag{2.49}$$

Remark 2.4. *When the motorcycle runs along a straight-line, $\sigma = 0$ and matrix B_{22} becomes singular and we cannot use input transformation (2.42). In this case, we*

calculate the total braking force from the second equation of the motions and split two the front and rear wheels in a way not producing any net moments around mass center B. A similar approach is discussed in [79]. If the resultant total force is traction, then it must be produced by the rear wheel.

2.5.2 Trajectory tracking control

Control system overview

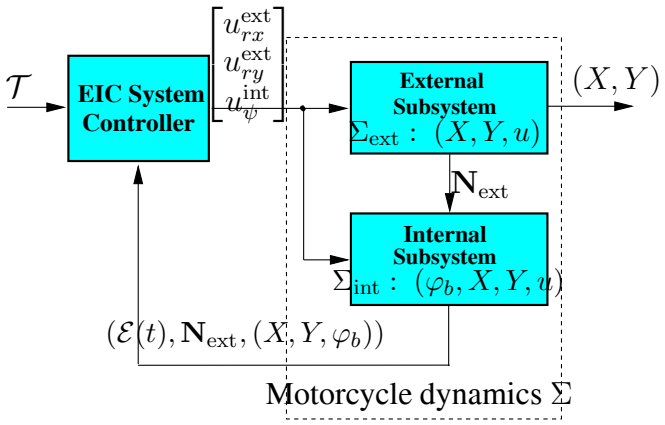

Figure 2.6: EIC-based approximate output tracking control of the autonomous motorcycle dynamics.

The trajectory control system then guides the motorcycle to follow the desired trajectory $\mathcal{T}$: $(X_d(t), Y_d(t))$ while keeping the platform balanced and stable. We here employ and extend the control design approach in [21]. Figure 2.6 illustrates such a control scheme. The trajectory control design consists of two steps. The first step to design a tracking control $\mathbf{u}_{\text{ext}}$ of the external subsystem Σ_{ext} for the desired trajectory $\mathcal{T}$. The second step is to design a balancing controller for the internal subsystem Σ_{int} around the internal equilibrium manifold, denoted as $\mathcal{E}(t)$. The internal equilibrium manifold $\mathcal{E}(t)$ is an embedded sub-manifold in the state space and dependent on the external control $\mathbf{u}_{\text{ext}}$ and the external subsystem. Estimations of internal equilibrium $\mathcal{E}(t)$ and its derivatives are obtained by a dynamic inversion technique [21]. The final casual control system is a combination of external and internal design.

Approximate tracking control

We assume that the desired trajectory $\mathcal{T} : (X_d(t), Y_d(t))$ is differentiable at least up to fourth order, that is C^4 [5]. This is feasible since the motion planning algorithm can usually generate a set of piecewise circular curves (C^∞) for $\mathcal{T}$ [80].

We design a controller $\mathbf{u}_{\text{ext}}$ to track the desired trajectory $(X_d(t), Y_d(t))$ for the external subsystem Σ_{ext} (2.48a) disregarding, for the moment, the evolution of the internal subsystem Σ_{int} (2.48b).

$$\boldsymbol{u}^{\text{ext}} := \begin{bmatrix} u_X^{\text{ext}} \\ u_Y^{\text{ext}} \end{bmatrix} = \begin{bmatrix} X_d^{(3)} \\ Y_d^{(3)} \end{bmatrix} - \sum_{i=1}^{3} b_i \begin{bmatrix} X^{(i-1)} - X_d^{(i-1)} \\ Y^{(i-1)} - Y_d^{(i-1)} \end{bmatrix}, \tag{2.50}$$

where constants b_i, $i = 1, 2, 3$, are chosen such that the polynomial equation $s^3 + b_3 s^2 + b_2 s + b_1 = 0$ is Hurwitz. Under such a control, we define a nominal external vector field $\mathbf{N}_{\text{ext}}$ as

$$\mathbf{N}_{\text{ext}} := \begin{bmatrix} \dot{X}(t) \\ \ddot{X}(t) \\ X_d^{(3)} - \sum_{i=1}^{3} b_i \left(X^{(i-1)} - X_d^{(i-1)} \right) \\ \dot{Y}(t) \\ \ddot{Y}(t) \\ Y_d^{(3)} - \sum_{i=1}^{3} b_i \left(Y^{(i-1)} - Y_d^{(i-1)} \right) \end{bmatrix}, \tag{2.51}$$

By external control (2.50) and the input transformation (2.47), we find the input $\boldsymbol{u}_J^{\text{ext}} = -\mathbf{U} + \boldsymbol{u}^{\text{ext}}$. From (2.46), we obtain $\boldsymbol{u}_j^{\text{ext}}$ as

$$\begin{bmatrix} u_{rx} \\ u_{ry} \end{bmatrix} + \begin{bmatrix} -v_{ry} \\ v_{rx} \end{bmatrix} u_\psi = \begin{bmatrix} \mathrm{c}_\psi & \mathrm{s}_\psi \\ -\mathrm{s}_\psi & \mathrm{c}_\psi \end{bmatrix} \boldsymbol{u}_J. \tag{2.52}$$

Note that $\boldsymbol{u}_J \in \mathbb{R}^2$ and $\boldsymbol{u}_j \in \mathbb{R}^3$ and the above equation is under-determined. There are many options to determine $\boldsymbol{u}_j$ by (2.52). Here we propose to choose $u_\psi = \ddot{\psi} = 0$

[5] For the external subsystem control, we only need $\mathcal{T}$ to be C^3. The requirement for C^4 is due to the estimation of the internal (roll angle) equilibrium and its derivatives by a dynamic inversion technique.

because such a choice significantly reduces the complexity of the control design as shown in the following.

$$\boldsymbol{u}_j^{\text{ext}} = \begin{bmatrix} u_{rx}^{\text{ext}} \\ u_{ry}^{\text{ext}} \\ u_{\psi}^{\text{ext}} \end{bmatrix} = \begin{bmatrix} \boldsymbol{R}(\psi)\boldsymbol{u}_J^{\text{ext}} \\ 0 \end{bmatrix} = \begin{bmatrix} \boldsymbol{R}(\psi)\left(-\mathbf{U} + \boldsymbol{u}^{\text{ext}}\right) \\ 0 \end{bmatrix}. \tag{2.53}$$

Next, we consider the internal (roll angle) equilibrium, denoted as φ_e, by substituting u_{ψ}^{ext} and u_{ry}^{ext} above into the internal subsystem dynamics (2.48b). We define the implicit function F_{φ_b} of φ_b as

$$F_{\varphi_b} := g\left(\tan\varphi_b + \frac{l_b l_t \dot{\psi}\, \mathrm{c}_{\xi}}{h_b v_{rx}}\right) - \left(1 - \frac{h_b \dot{\psi}\, \mathrm{s}_{\varphi_b}}{v_{rx}}\right)\dot{\psi} v_{rx} - u_{\psi y}^{\text{ext}}, \tag{2.54}$$

$u_{\psi y}^{\text{ext}} = l_b u_{\psi}^{\text{ext}} + a_{ry} = a_{ry}$, and the roll angle equilibrium $\varphi_e := \varphi_e(\dot{\psi}, v_{rx}, \boldsymbol{u}_j^{\text{ext}})$ is a solution of the algebraic equation $F_{\varphi_e} = 0$. We define an internal (roll angle) equilibrium manifold $\mathcal{E}(t)$ as

$$\mathcal{E}(t) = \left\{ \left(X^{(0,2)}, Y^{(0,2)}, \varphi_b^{(0,1)}\right) \;\middle|\; \varphi_b = \varphi_e,\ \ \dot{\varphi}_b = 0 \right\}. \tag{2.55}$$

The internal equilibrium manifold $\mathcal{E}(t)$ can be viewed as a time-dependent graph over the 6-dimensional (X, Y)-subspace in $\mathbb{R}^6$ of the external subsystem (2.48a) that is evolved with the external nominal vector field $\mathbf{N}_{\text{ext}}$ (2.51) under the external subsystem control $\boldsymbol{u}^{\text{ext}}$.

For the motorcycle balance systems, we like to control the roll angle φ_b around $\mathcal{E}(t)$ while the external subsystem is tracking $\mathcal{T}$ under the control of $\boldsymbol{u}^{\text{ext}}$. Note that $\dot{\varphi}_e \neq 0$ and $\ddot{\varphi}_e \neq 0$ in general and here we approximate the derivatives $\dot{\varphi}_e$ and $\ddot{\varphi}_e$ by using directional derivatives [64, 78] along the vector field $\mathbf{N}_{\text{ext}}$. We define the directional derivative (or Lie derivative) as $\bar{L}_{\mathbf{N}_{\text{ext}}}\varphi_e := L_{\mathbf{N}_{\text{ext}}}\varphi_e + \frac{\partial \varphi_e}{\partial t}$ and $\bar{L}^2_{\mathbf{N}_{\text{ext}}}\varphi_e := \bar{L}_{\mathbf{N}_{\text{ext}}}\bar{L}_{\mathbf{N}_{\text{ext}}}\varphi_e$. With the above approximations for $\dot{\varphi}_e$ and $\ddot{\varphi}_e$, the stabilizing control of the internal subsystem Σ_{int} (2.48b) around $\mathcal{E}(t)$ is then given by the following feedback

linearization

$$u_{\psi y}^{\text{int}} = \left(\frac{\mathrm{c}_{\varphi_b}}{h_b}\right)^{-1} \left[\frac{g}{h_b}\left(\mathrm{s}_{\varphi_b} + \frac{l_b l_t\, \mathrm{c}_\xi\, \dot{\psi}}{h_b v_{rx}}\, \mathrm{c}_{\varphi_b}\right) - \frac{1}{h_b}\left(1 - \frac{h_b \dot{\psi}}{v_{rx}}\, \mathrm{s}_{\varphi_b}\right) \dot{\psi} v_{rx}\, \mathrm{c}_{\varphi_b} - v_{\psi y}\right], \tag{2.56a}$$

$$v_{\psi y} = \bar{L}^2_{\mathbf{N}_{\text{ext}}} \varphi_e - \sum_{i=1}^{2} a_i (\varphi_b^{(i-1)} - \bar{L}^{i-1}_{\mathbf{N}_{\text{ext}}} \varphi_e). \tag{2.56b}$$

where constants a_1 and a_2 are chosen such that the polynomial equation $s^2 + a_2 s + a_1 = 0$ is Hurwitz. Therefore, the internal control is obtained from (2.49) as

$$u_\psi^{\text{int}} = \frac{1}{l_b}\left(u_{\psi y}^{\text{int}} - a_{ry}\right) \tag{2.57}$$

The *final* control system design of the motorcycle balance system (2.45) combines the above development in (2.57) and (2.53) as

$$\boldsymbol{u}_j = \begin{bmatrix} u_{rx}^{\text{ext}} \\ u_{ry}^{\text{ext}} \\ u_\psi^{\text{int}} \end{bmatrix} \tag{2.58}$$

It is noted that the coupling between the external- and internal-subsystem control designs is through the introduction of the internal equilibrium manifold $\mathcal{E}(t)$. By defining $\mathcal{E}(t)$, we approximately decouple the external and internal subsystems using the EIC dual structural properties of the motorcycle system.

We define $\boldsymbol{\vartheta}(t) = [X(t)\ v_X(t)\ \dot{v}_X(t)\ Y(t)\ v_Y(t)\ \dot{v}_Y(t)]^T$ as the state variables of the external subsystem and $\boldsymbol{\varrho}(t) = [\varphi_b(t)\ \dot{\varphi}_b(t)]^T$ as the state variables of the internal subsystem. We also define the output $\boldsymbol{\zeta}(t) = [X(t)\ Y(t)]^T$ and desired output $\boldsymbol{\zeta}_d(t) = [X_d(t)\ Y_d(t)]^T$. We assume that the desired trajectory $\boldsymbol{\zeta}_d(t)$ and its derivatives (up to the fourth order) are bounded by a positive number $\epsilon > 0$, namely, $\boldsymbol{\zeta}_d(t) \in \mathbf{B}_\epsilon^{(4)} := \{\boldsymbol{x}(t) \mid \|\boldsymbol{x}^{(0,4)}(t)\|_\infty < \epsilon\}$, where $\|\boldsymbol{x}^{(0,n)}(t)\|_\infty := \sup_{t\geq 0} \|\boldsymbol{x}^{(0,n)}(t)\|_\infty$. We also define the tracking errors $e_i^\vartheta = \boldsymbol{\vartheta}_i - X_d^{(i-1)}$, $e_{i+3}^\vartheta = \boldsymbol{\vartheta}_{i+3} - Y_d^{(i-1)}$, $i = 1, 2, 3$, $e_j^{\varphi_b} = \varphi_b{}^{(j)} -$

$\varphi_e^{(j)}$, $j = 0, 1$, and $\boldsymbol{e} := [e_1^{\vartheta},\ \cdots,\ e_6^{\vartheta},\ e_1^{\varphi_b},\ e_2^{\varphi_b}]^T$. We also define the perturbation error p_{φ_b} ($= O(\|\boldsymbol{\zeta}_d^{(0,4)}(t)\|, \|\boldsymbol{e}\|)$ as the approximation errors by using the directional derivatives for $\dot{\varphi}_e$ and $\ddot{\varphi}_e$ in the internal subsystem control design (2.56b), namely,

$$p_{\varphi_b} = \bar{L}^2_{\mathbf{N}_{\text{ext}}}\varphi_e - \ddot{\varphi}_e + \sum_{i=1}^{2} a_i(\varphi_{b_e}^{(i-1)} - \bar{L}^{i-1}_{\mathbf{N}_{\text{ext}}}\varphi_e).$$

We similarly define another two perturbation errors p_X ($= O(\|\boldsymbol{\zeta}_d^{(0,4)}(t)\|, \|\boldsymbol{e}\|)$ and p_Y ($= O(\|\boldsymbol{\zeta}_d^{(0,4)}(t)\|, \|\boldsymbol{e}\|)$ due to the resulting errors in the external subsystem state $\boldsymbol{\vartheta}(t)$ using the internal subsystem control $u_{\psi y}^{\text{int}}$ in the external subsystem (2.58). An explicit formulation for p_X and p_Y can be similarly found by the dual structure of EIC system [21]. We consider the perturbation vector for the error dynamics of $\Sigma(u)$ (2.47) under control (2.58) as

$$p(\boldsymbol{\zeta}_d^{(0,4)}(t), \boldsymbol{e}) = [0,\ 0,\ p_X,\ 0,\ 0,\ p_Y,\ 0,\ p_{\varphi_b}]^T.$$

We assume an affine perturbation for $p(y_d^{(0,4)}(t), e)$, namely, there exist constants $k_1 > 0$ and $k_2 > 0$ such that $\|p(\boldsymbol{\zeta}_d^{(0,5)}(t), \boldsymbol{e})\|_\infty \leq k_1\epsilon + k_2\|\boldsymbol{e}\|_\infty$.

We only state the convergence properties of the approximate tracking control design. The proof of these properties follows directly from Proposition 6.7.4 and Theorem 6.7.6 in [21] and we omit here.

Theorem 2.1. *For the balance system (2.47), assuming that the desired trajectory $\boldsymbol{\zeta}_d(t) \in \mathbf{B}_\epsilon^{(4)}$ for some $\epsilon > 0$ and if the affine perturbation constant $k_2 > 0$ is a sufficiently small real number, then there exists a $t_1 > 0$, and a class-$\mathcal{K}$ function $r(\epsilon)$ such that for all $(\boldsymbol{e}^{\vartheta}(0), \boldsymbol{e}_b^{\varphi}(0)) \in \mathbf{B}_{r(\epsilon)}$, $(\boldsymbol{e}^{\vartheta}(t), \boldsymbol{e}_b^{\varphi}(t))$ converges to zero exponentially until $(\boldsymbol{e}^{\vartheta}(t), \boldsymbol{e}_b^{\varphi}(t))$ enters $\mathbf{B}_{r(\epsilon)}$. Once $(\boldsymbol{e}^{\vartheta}(t), \boldsymbol{e}_b^{\varphi}(t))$ enters $\mathbf{B}_{r(\epsilon)}$, it will stay in $\mathbf{B}_{r(\epsilon)}$ thereafter.*

Estimation of the internal equilibrium manifold

A dynamic inversion technique approach in [21] is used to estimate the internal equilibrium state φ_e in (2.56b). To illustrate the dynamic inversion technique, we differentiate

$F_{\varphi_b} = 0$ with time, and using the fact that $u_\psi^{\text{ext}} = \ddot{\psi} = 0$ we obtain

$$\begin{aligned}\dot{\varphi}_e &= \frac{1}{g\sec^2\varphi_e + h_b\dot{\psi}\,\mathrm{c}_{\varphi_e}}\left(\frac{gl_bl_t\,\mathrm{c}_\xi\,\dot{\psi}\dot{v}_{rx}}{h_bv_{rx}^2} + \dot{\psi}\dot{v}_{rx} + u_{ry}^{\text{ext}}\right)\\ &=: E(\varphi_e, \dot{\psi}, v_{rx}, \dot{v}_{rx}, u_{ry}^{\text{ext}}).\end{aligned} \tag{2.59}$$

A dynamic inverter for an estimate $\hat{\varphi}_e$ of the internal equilibrium φ_e is designed as

$$\dot{\hat{\varphi}}_e = -\beta F_{\hat{\varphi}_b} + E(\hat{\varphi}_e, \dot{\psi}, v_{rx}, \dot{v}_{rx}, u_{ry}^{\text{ext}}), \tag{2.60}$$

where $F_{\hat{\varphi}_e}$ is given by (2.54) and $\beta > 0$ is the inverter gain. The proof of the exponential convergence of the estimation (2.60) follows directly from the development of the dynamic inversion technique in [21].

The estimate of the directional derivative $\bar{L}_{\mathbf{N}_{\text{ext}}}\varphi_e$ in (2.56b) is obtained by (2.60).The estimate of $\bar{L}^2_{\mathbf{N}_{\text{ext}}}\varphi_e$ is obtained by directly taking one more directional derivative of $\bar{L}_{\mathbf{N}_{\text{ext}}}\varphi_e$ along $\mathbf{N}_{\text{ext}}$. For brevity, we give the derivation in Appendix C. We also list the calculation of $\bar{L}_{\mathbf{N}_{\text{ext}}}u_{rx}^{\text{ext}}$ and $\bar{L}_{\mathbf{N}_{\text{ext}}}u_{ry}^{\text{ext}}$ in Appendix C. Such calculations are needed for computing $\bar{L}^2_{\mathbf{N}_{\text{ext}}}\varphi_e$. The approximation errors in estimating φ_e (by $\hat{\varphi}_e$) and its directional derivatives $\bar{L}_{\mathbf{N}_{\text{ext}}}\varphi_e$ and $\bar{L}^2_{\mathbf{N}_{\text{ext}}}\varphi_e$ (by $\bar{L}_{\mathbf{N}_{\text{ext}}}\hat{\varphi}_e$ and $\bar{L}^2_{\mathbf{N}_{\text{ext}}}\hat{\varphi}_e$, respectively) are considered as additional terms in the perturbation $p(\boldsymbol{\zeta}_d^{(0,4)}(t), \boldsymbol{e})$. Therefore, the stability results of the approximate control design in the previous section are still held.

Remark 2.5. *Although the above control system design is similar to those in [21], the final form is much simpler because we have chosen $u_\psi^{\text{ext}} = 0$ in (2.53). We have such a flexibility by (2.52) to determine $\boldsymbol{u}_j$ because we have three control input variables now while in [21] only the rear wheel driving torque and the steering angle are controlled. Because of this difference, we only require the trajectory $\mathcal{T}$ is at least C^4 rather than C^5 as the requirement of the controller in [21]. Using optimization techniques by considering the input constraints for determining $\boldsymbol{u}_j$ by (2.52) is an extension of the control design and currently ongoing research.*

2.5.3 Simulation results

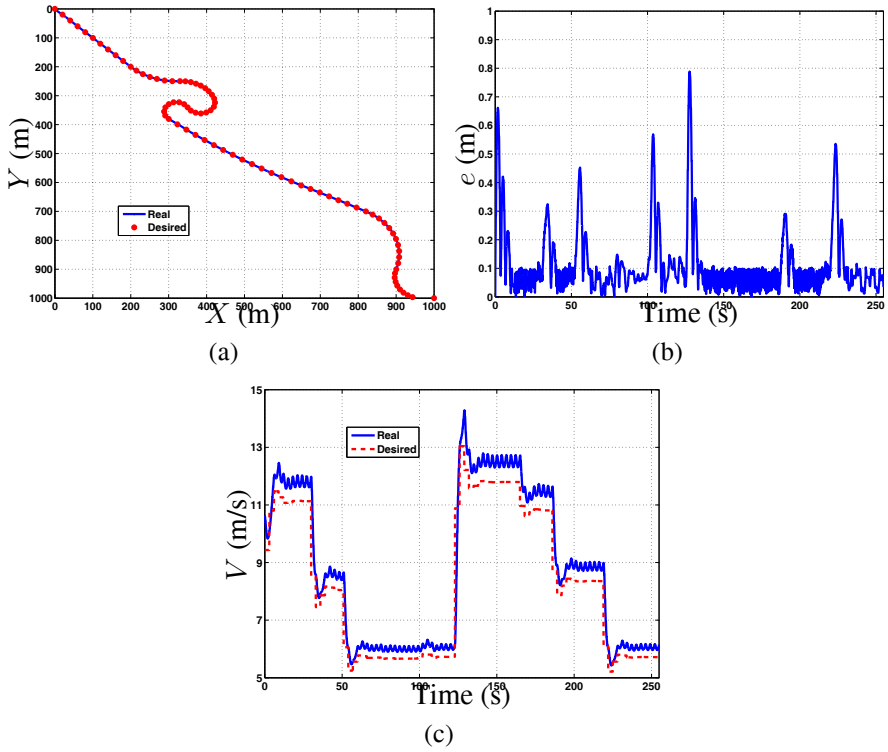

Figure 2.7: Tracking performance of a general trajectory. (a) Trajectory positions. (b) Tracking position error. (c) Rear wheel contact point velocity magnitude.

In this section, we demonstrate the control systems design through two numerical examples. The first example is taken from [26] for showing a general motorcycle trajectory while the second example to illustrate an aggressive maneuvers with a large side slip angles.

We use a racing motorcycle prototype in [1] and [81] in our simulation. The motorcycle parameters are listed in Table 5.1. We use the tire 160/70 in [1] for the racing motorcycle since the testing data are available. The tire stiffness coefficients listed in Table 5.1 are calculated under the nominal load $F_z = 1600$ N.

Figure 2.7 shows the trajectory tracking performance of a general trajectory. The position errors under the control system in Fig. 2.7(b) are within 1 meter with the center line of the track throughout the entire course. The desired velocity in Fig. 2.7(c) is

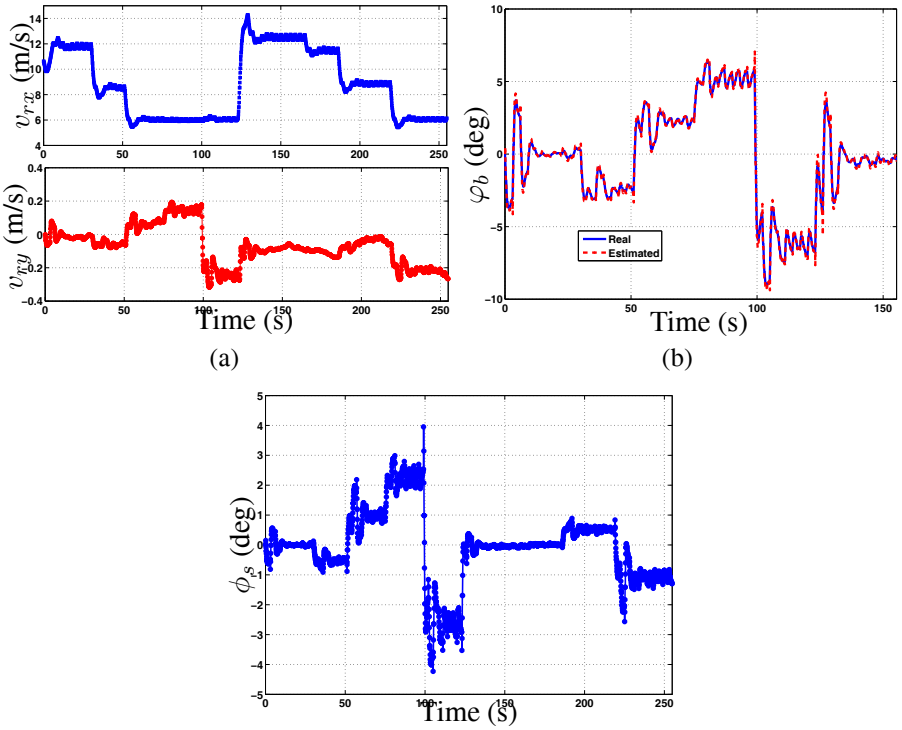

Figure 2.8: Roll angle and steering angle of the general trajectory tracking. (a) Rear wheel contact point body-frame velocities v_{rx} and v_{ry}. (b) Roll angle φ_b. (b) Steering angle ϕ_s.

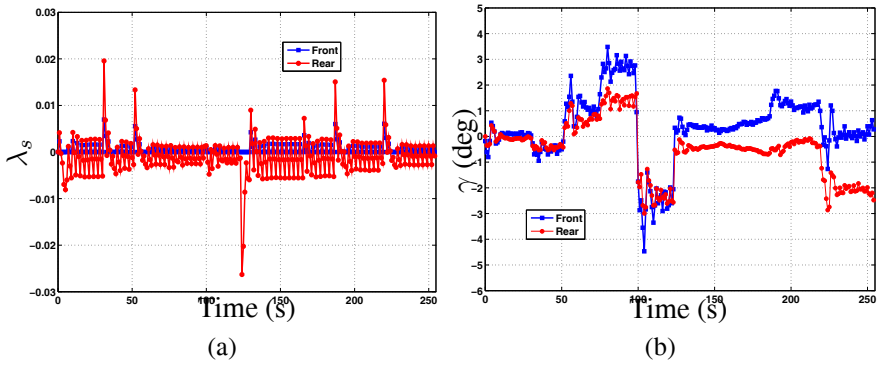

Figure 2.9: Longitudinal slips and slip angles at the front and rear wheels. (a) Slip ratio λ_{fs} and λ_{rs}. (b) Slip angles γ_f and γ_r.

determined by the curvature of the trajectory. In Fig. 2.8, we have shown the roll angle φ_b, the body-frame velocities v_{rx} and v_{ry} of rear wheel contact point C_2, and steering angle ϕ_s. From Fig. 2.8(a) we clearly see that the lateral velocity v_{ry} is quite small most time because the motorcycle is running along a straight-line at most time. At turning

m(kg)	l_b(m)	l(m)	l_t(m)	h_b(m)	ξ(deg)	R_t(m)	λ_{sm}	$\lambda_{\gamma m}$(deg)	μ_m	k_λ(N)	k_{φ_b}(N/rad)	k_γ(N)
274.2	0.81	1.37	0.15	0.62	26.1	0.3	0.1	6	3	41504	23968	1227

Table 2.1: Motorcycle model parameters

locations, the longitudinal velocity is reduced and the lateral velocity increases. The roll angle and steering angle are small for such a small-curvature trajectory.

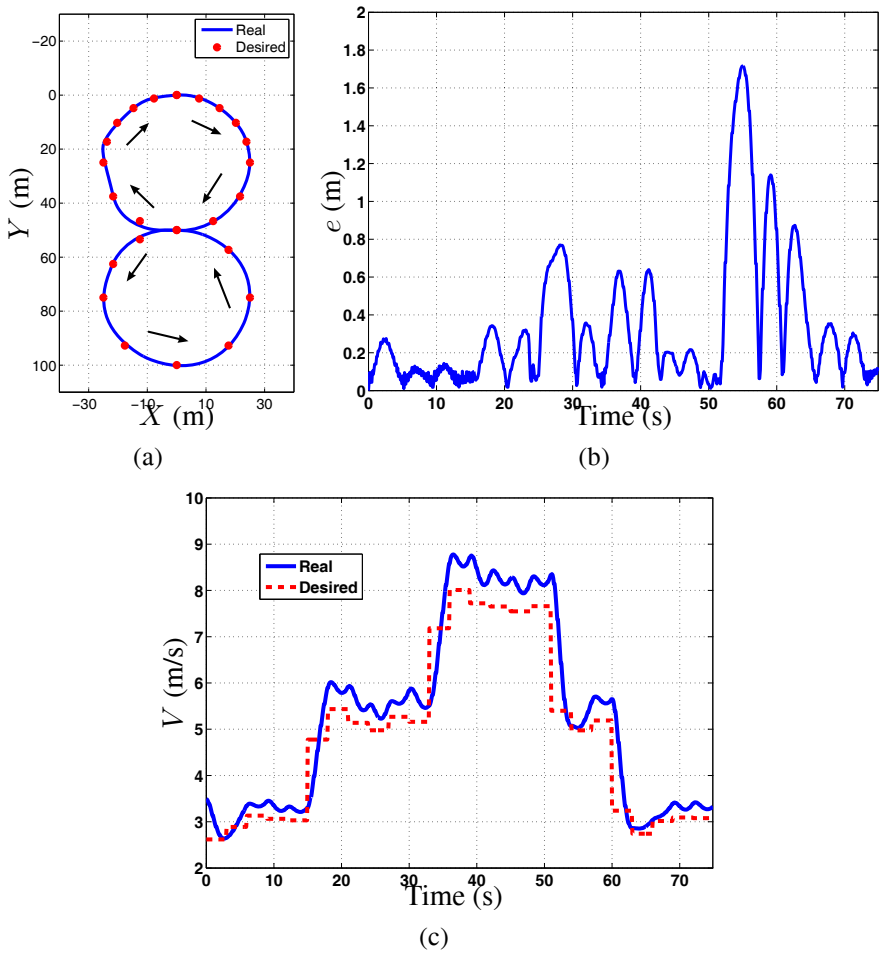

Figure 2.10: An "8"-shape trajectory tracking. (a) Trajectory positions. (b) Tracking position error. (c) Rear wheel contact point velocity magnitude.

Figure 2.9 shows the longitudinal slips and side slip angles of the front and rear wheels. Again, it is clear that the slip values at both wheels are small. The front wheel only brakes and the rear wheel generates traction or braking forces. For example, when the motorcycle accelerates around 120 s, the rear wheel slip has a large negative spike to produce the traction force. When the vehicle needs to reduce velocity, both wheels

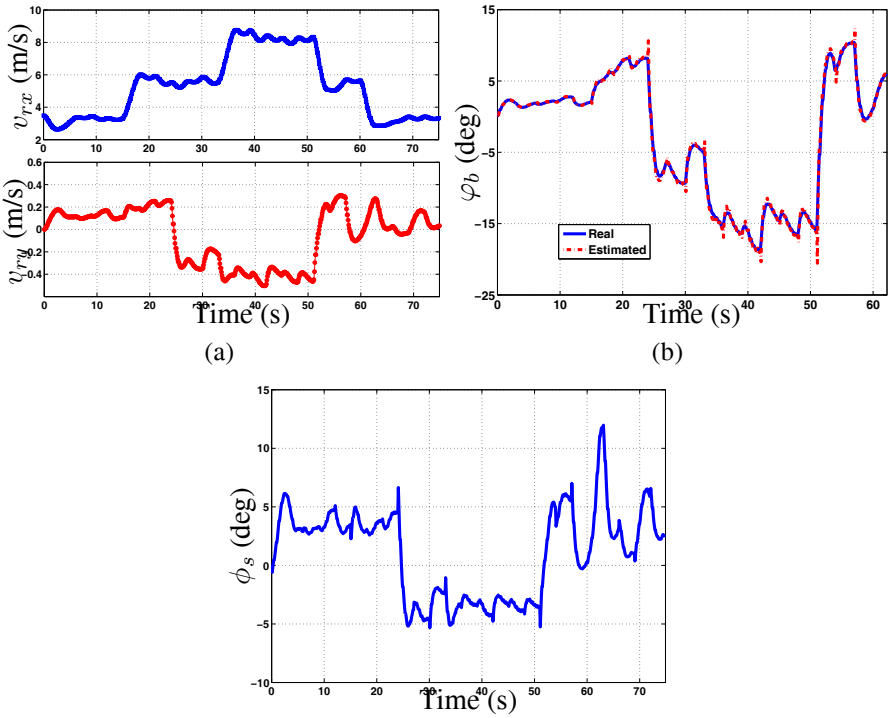

Figure 2.11: Roll angle and steering angle of the "8"-shape trajectory tracking. (a) Rear wheel contact point body-frame velocities v_{rx} and v_{ry}. (b) Roll angle φ_b. (c) Steering angle ϕ_s.

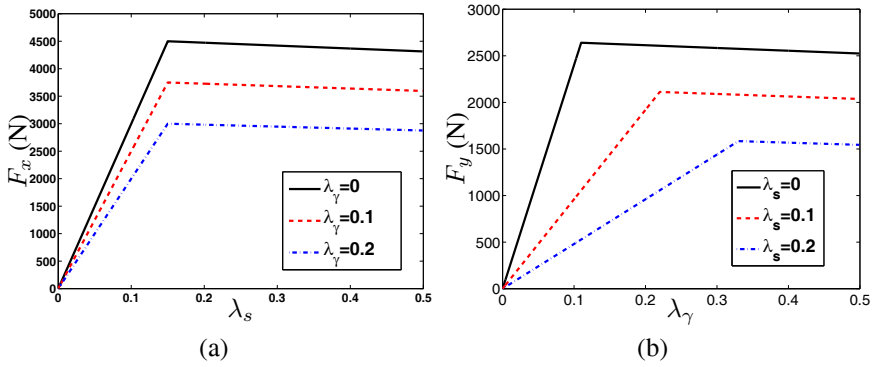

Figure 2.12: Approximate piecewise linear tire forces characteristics. (a) Longitudinal force with various tire slip angle ratios λ_γ. (b) Lateral force with various tire slip ratios λ_s. The tire stiffness parameters are taken from [1].

brake with a set of large positive slip spikes shown in Fig. 2.9(a). The side slip angles shown in Fig. 2.9(b) clearly illustrate that at large-curvature locations, the side slip angles are increased to produce the lateral forces for turning. Typically, the rear side slip angles are small and close to zero.

The second example shows that the motorcycle runs under a more aggressive maneuver. The desired trajectory is "8"-shape with circular radius of 25 meters; see Fig. 2.10(a). In Fig. 2.10(a), the motorcycle starts from the origin and moves along the direction indicated by the arrows in the figure. The desired velocity of the motorcycle moving along the "8"-shape trajectory is designed to be varying significantly as shown in Fig. 2.10(c). Comparing with the previous example, the tracking errors of the "8"-shape trajectory are much larger; see Fig. 2.10(b). This is mainly due to the quick change of the desired velocity profile.

Figure 2.11 shows the body-frame velocity, roll angle, and steering angle for the "8"-shape trajectory. We clearly see the change of the lateral velocity during each circle of the "8"-shape trajectory. The lateral velocity magnitude is large due to the smaller turning radius. The maximum roll angle is around 15 degs and that is much larger than that of the previous example. The steering angle is large as well to make the motorcycle turn in a tighter and small circle. The oscillations in both the roll angle (Fig. 2.11(b)) and the steering angle (Fig. 2.11(c)) are probably due to the variations in the desired velocity.

2.6 Path-following control system design

In this section, we extend the modeling approach by considering of the coupling effect of the longitudinal and the lateral friction forces. We then introduce a velocity-field maneuver regulation control in which the goal of the control system design is to follow the trajectory path, while the desired velocity is self-tuned online.

2.6.1 Coupled empirical friction force model

In the previous sections, we presented a piecewise linear model of the motorcycle tire-road friction forces. However, the dependency and coupling effects between the

longitudinal and the lateral forces are not considered. We extend the previous results and present a coupled friction force model here.

We consider the pseudo-static friction model of the longitudinal force F_x and longitudinal slip ratio λ_s, and the lateral force F_y and side slip ratio λ_γ ($\lambda_\gamma = \tan\gamma$, γ is slip angle). We propose to approximate the friction forces by a piecewise linear relationship given by (2.28). To capture the coupling effects between F_x and F_y, we consider the model parameters k and x_m along the x and y directions are dependent on each other. For example, the values of the longitudinal stiffness k_x (k value in (2.28) for F_x) and the maximum slip ratio λ_{sm} (x_m value in (2.28) for F_x) are functions of tire slip angle ratio λ_γ. Similarly, tire corning stiffness k_y (k value in (2.28) for F_y) and the maximum side slip ratio $\lambda_{\gamma m}$ (x_m value in (2.28) for F_y) also depend on the longitudinal slip ratio λ_s. Denoting k_{0x} and λ_{sm0} (k_{0y} and $\lambda_{\gamma m0}$) as the parameter values of longitudinal (lateral) force F_x (F_y) when coupling effects with F_y (F_x) are not considered, we use the following equations to update parameters k_x and λ_{sm} (parameters k_y and $\lambda_{\gamma m}$.) For the longitudinal direction, we have

$$k_x = k_{0x}(a_1\lambda_\gamma + 1), \quad \lambda_{sm} = \lambda_{sm0} \tag{2.61}$$

and for the lateral direction force,

$$k_y = k_{0y}\frac{a_2\lambda_s + 1}{a_3\lambda_s + 1}, \quad \lambda_{\gamma m} = (a_3\lambda_s + 1)\lambda_{\gamma m0}, \tag{2.62}$$

where a_1, a_2, and a_3 are three parameters in the coupled tire model. We use (2.61) and (2.62) to capture the coupling effects because such relationships have been observed in experiments.

Figure 2.12 shows the property of the coupled tire mode when $k_{x0} = 30000$ N and $k_{y0} = 24000$ N. In this example, we use $a_1 = -\frac{5}{3}$, $a_2 = -2$, and $a_3 = 10$ for the motorcycle tires. For slip ratio λ_s, we set $\lambda_{sm0} = 0.15$, $\lambda_{\max} = 0.5$, $\alpha_x = 0.8$; and for side slip ratio λ_γ, we set $\lambda_{\gamma m0} = 0.11$, $x_{\max} = 1$,$\alpha_x = 0.9$. In the following, we

use the coupled coefficients (2.61) and (2.62) in the dynamic model (2.34) to design a path-following controller.

2.6.2 Path-following maneuvering design

We propose to use velocity field-based approach to design the path-following control of the motorcycle system. We assume that the motorcycle motion planning modules such as the one in [80] generate the desired trajectory $\mathcal{T}$: $(X_d(\tau), Y_d(\tau))$. Note that the trajectory $\mathcal{T}$ is parameterized by τ, which is not necessarily the same as time t. Therefore, the desired outcome of the control design design is to follow the trajectory path without specifying the velocity trajectory associated with the path. Instead, the desired velocity profile is a part of the control design process using a time-suspension technique.

Time suspension and velocity field design

We use a time suspension technique to design the desired velocity profile. The basic idea of time suspension is to use self-placing technique to adjust the desired rate of the progression of the parameter τ related to $\mathcal{T}$. In other word, we do not need to assign any desired velocity profile in advance and the motorcycle will instantaneously adjust its velocity according to the changes of the path-following errors. One obvious advantage of using the time suspension technique in our design is to reduce tracking error and thus to improve tracking performance.

We also use a velocity field design concept. The adopted velocity field approach is to define a reference input as a vector of velocities in the moving plane, rather than directly in terms of a reference-parameterized path. The main benefit of using a velocity field design is to further improve tracking performance [70]. To construct the velocity field, we use a potential function-based approach that is similar to those in [70]. We

define the following potential function to capture the position errors along the path.

$$U(X,Y) = \frac{1}{2}\beta_1 \left[(1-\cos(X-X_d)) + (1-\cos(Y-Y_d))\right], \tag{2.63}$$

where $\beta_1 > 0$ is a constant gain. At any position, we design the velocity vector by

$$\begin{bmatrix} V_x(\tau) \\ V_y(\tau) \end{bmatrix} = \lambda_1(X,Y) \begin{bmatrix} \frac{dX_d}{d\tau} \\ \frac{dY_d}{d\tau} \end{bmatrix} - \lambda_2(X,Y) \begin{bmatrix} h\sin(X-X_d) \\ h\sin(Y-Y_d) \end{bmatrix}, \tag{2.64}$$

where $\lambda_1(X,Y) = e^{-\beta_2 U(X,Y)}$, $\lambda_2(X,Y) = 2 - e^{-\beta_2 U(X,Y)}$, and $\beta_2 > 0$ is a self-pacing parameter. The time suspension level is defined by the following dynamics of τ

$$\dot{\tau} = \frac{d\tau}{dt} = \lambda_1(X,Y). \tag{2.65}$$

Remark 2.6. *We consider the time suspension parameter dynamics (2.65) as a part of augmented motorcycle dynamics (2.34). Note that the τ dynamics is related to the potential function $U(X,Y)$ and therefore to the path following errors. When the motorcycle follows the desired trajectory, $U(X,Y) = 0$ and $\dot{\tau} = 1$. In this case, τ can be considered as the time variable t. When the path-following errors are large, the progression of desired trajectory (i.e., $\dot{\tau}$) is reduced and the controlled trajectory converges to desired path soon with increased $\lambda_2(X,Y)$. It is noted that $0 < \lambda_1(X,Y) \leq 1$ and $1 \leq \lambda_2(X,Y) < 2$.*

Controller design

For motorcycle control systems design, we combine the EIC-based control approach discussed in the previous section with the above discussed velocity field approach.

The EIC-based trajectory control design consists of two steps; see Fig. 2.6. The velocity vector parameterized by τ, rather than desired trajectory path specified in time t, is used as the reference input to the EIC control. We combine the EIC control and the velocity field design as follows. At any position and on any particular τ, we use (2.63)

and (2.64) to calculate the current velocity vector. Then we construct a special trajectory for the EIC controller as

$$\begin{bmatrix} X_d(\tau) \\ X_d^1(\tau) \\ X_d^{(2,4)}(\tau) \end{bmatrix} = \begin{bmatrix} X(\tau) \\ V_x(\tau) \\ 0 \end{bmatrix}, \quad \begin{bmatrix} Y_d(\tau) \\ Y_d^1(\tau) \\ Y_d^{(2,4)}(\tau) \end{bmatrix} = \begin{bmatrix} Y(\tau) \\ V_y(\tau) \\ 0 \end{bmatrix},$$

where τ is updating by (2.65). The basic design idea is to let velocity vector be the only design components in the desired trajectory space. With this treatment, we can fully inherit the EIC controller design and its properties that are stated in the previous section.

2.6.3 Simulation results

In this section, we demonstrate the control systems design through two examples: one is for a typical "8"-shape trajectory following maneuver and the other for a more agile maneuver. We use the same racing motorcycle and tire profiles in the simulation as these in the previous section.

The first example shows that the motorcycle runs under a regular "8"-shape path following maneuver in which the motorcycle moves along the trajectory with relative large curvatures. The desired parameterized trajectory (see Fig. 2.13(a)) is given by the following equation parameterized by τ

$$\begin{bmatrix} X_d(\tau) \\ Y_d(\tau) \end{bmatrix} = \begin{bmatrix} 25\sin(0.1\pi\tau) \\ 40\cos(0.05\pi\tau) \end{bmatrix} \tag{2.66}$$

Figure 2.13 shows the simulation results. As shown in Fig. 2.13(a), the starting point of motorcycle is $(0, 40)$. We use self-pacing parameter $\beta_2 = 100$ in (2.64), parameter $\beta_1 = 0.0025$ in (2.63), and the initial velocity is 0.1 m/s. In the simulation, we add white noise with standard variations 0.02 m/s, 0.005 m/s^2, 0.3 degs, and 0.6 degs to velocity, acceleration, roll angle, and yaw angle measurements, respectively. By comparing with the desired trajectory, the simulation results show that the

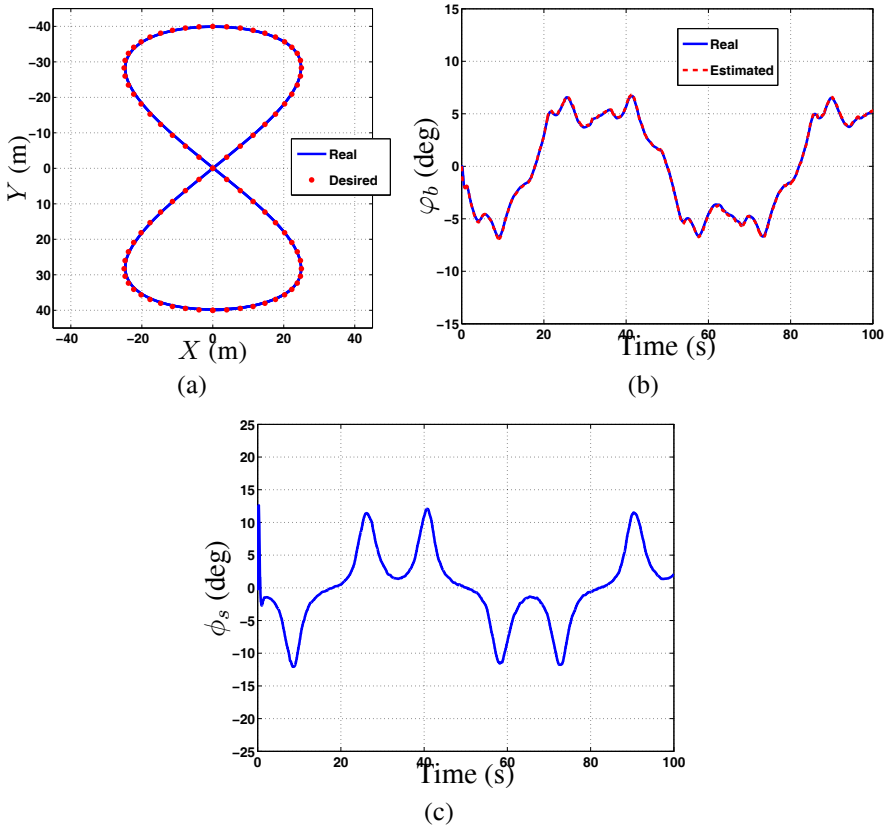

Figure 2.13: (a) Path following. (b) Roll angle φ_b. (c) Steering angle ϕ_s.

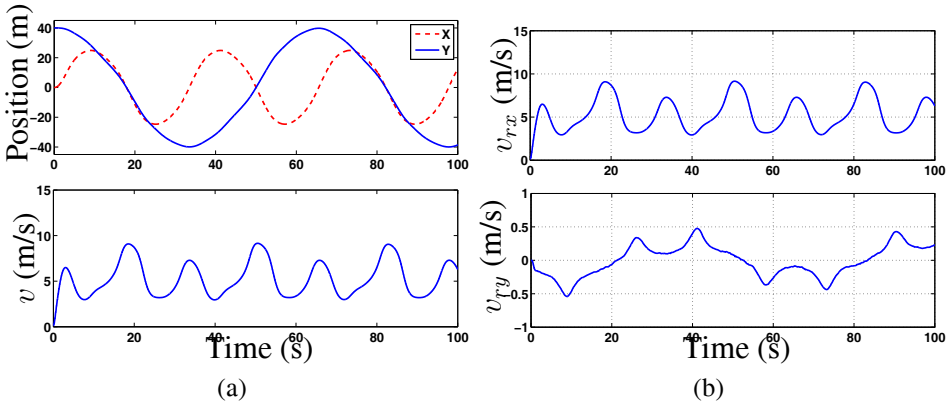

Figure 2.14: A typical motorcycle path-following maneuver. (a) Motorcycle position and velocity (b) Longitudinal velocity v_{rx} and lateral velocity v_{ry}

motorcycle successfully tracks the desired trajectory under the velocity field control. Figure 2.13(b) and 2.13(c) clearly shows the desired and actual motorcycle roll angle φ_b and steering angle ϕ_s, respectively. The roll angle and steering angle are relatively

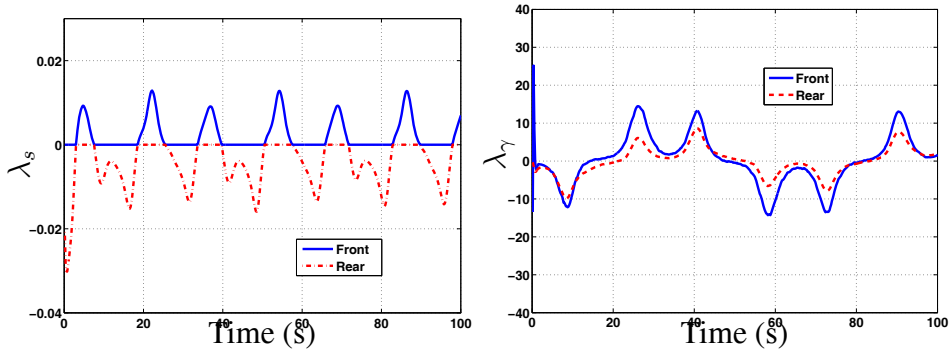

(a) (b)

Figure 2.15: Slip ratios and angles at the front and rear wheels during the "8"-shape trajectory tracking. (a) Slip ratio λ_s. (b) Slip angles γ_γ.

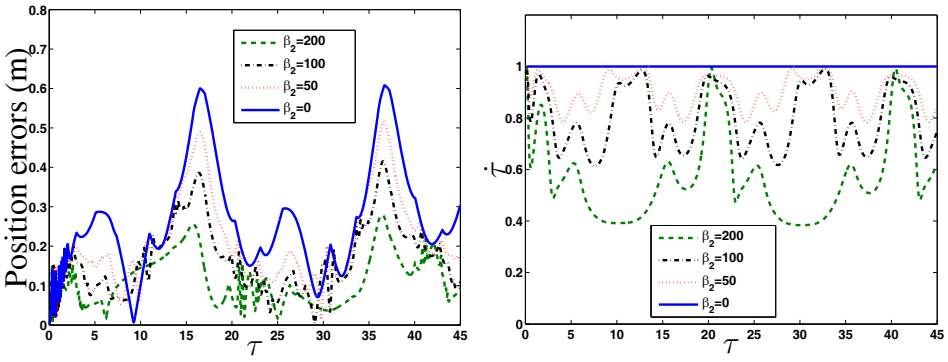

(a) (b)

Figure 2.16: (a) Path-following errors under various values of self-pacing parameter β_2. (b) Progression (i.e., $\dot{\tau}$) under various values of self-pacing parameter β_2.

large when turning at small radius curvatures and small along the straight trajectories.

Figure 2.14 shows the positions, the longitudinal velocity and the lateral velocity of point C_2. From Fig. 2.14(a), the motorcycle spends about 65 s to go through one entire circle. It is quite clear that the motorcycle tunes its own velocity automatically using the self-placing technique. When tuning at a small radius, the tracking errors become large. The motorcycle control system then reduces the rate of the progression in time, namely, its longitudinal velocity, to reduce the errors. Meanwhile, due to the sharply direction change, the lateral velocity is relatively large; see Fig. 2.14(b).

The tire slip ratios and angles during the maneuver are shown in Fig. 2.15. For the front wheel, we see a maximum 15-deg side slip angle while for the rear wheel, the

slip angle reaches almost 6 degs. Figure 2.16(a) shows the tracking error performances of the motorcycle under different values of self-pacing parameter β_2. From this figure, we can see that when self-pacing is increased (i.e., increasing β_2), the tracking errors become smaller, namely, the better path-following performance. When $\beta_2 = 0$, the maximal error is always smaller than 0.3 m. Of course, the better performance is trade-off by the smaller motorcycle velocity. This can be observed by the progression factor $\dot{\tau}$ as shown in Fig. 2.16(b). From Fig. 2.16(b), we see that increasing β_2 will reduce the value of $\dot{\tau}$ in general, which implies that the time has been expanded more. We can clearly see when $\beta_2 = 0$, $\dot{\tau} = 1$ and then the progression always remains at one, which implies no time suspension exists. In this case, the path-following system is the same as time-based trajectory tracking as shown in the previous section. Note that the oscillation of both path-following errors and progression $\dot{\tau}$ are due to the repeated motion trajectory.

In the second example, we show that the motorcycle runs with a more agile "8"-shape path-following maneuver. In this maneuver, the motorcycle will turn sharply at much smaller radii. The desired parameterized trajectory as shown in Fig. 2.17(a) is defined as

$$\begin{bmatrix} X_d(\tau) \\ Y_d(\tau) \end{bmatrix} = \begin{bmatrix} 7.5\sin(0.5\pi\tau) \\ 15\cos(0.25\pi\tau) \end{bmatrix} \tag{2.67}$$

The start point of motorcycle is $(0, 15)$. We choose self-pacing parameter $\beta_2 = 80$ and parameter $\beta_1 = 0.00825$. The initial velocity and noise characteristics are the same as those in the previous example.

From Fig. 2.17(a), we see that even in this extremely tight trajectory case, the motorcycle can still follow the desired trajectory under the velocity field control. From

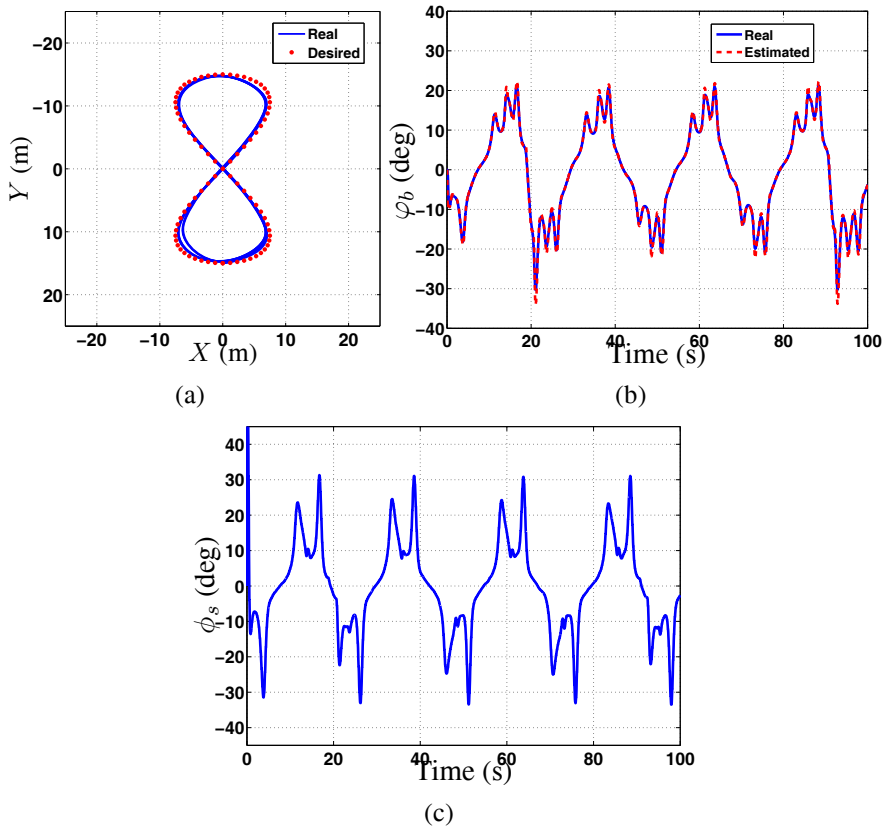

Figure 2.17: Motorcycle agile motion. (a) Path-following performance. (b) Roll angle φ_b. (c) Steering angle ϕ_s.

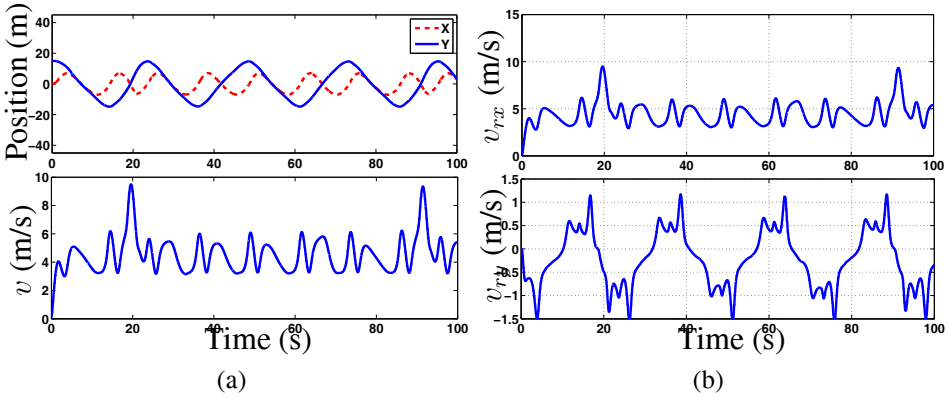

Figure 2.18: Motorcycle agile maneuver. (a) Position and velocity (b) Longitudinal velocity and lateral velocity

Fig. 2.17(b) and 2.17(c), it is clear that the steering angle and roll angle are both obviously larger than those of the previous example due to the much smaller radius curvatures. Figures 2.18(a) and 2.18(b) show the motorcycle position and velocity information for this maneuver. We see a large lateral velocity v_{ry}. Figures 2.19(a) and 2.19(b)

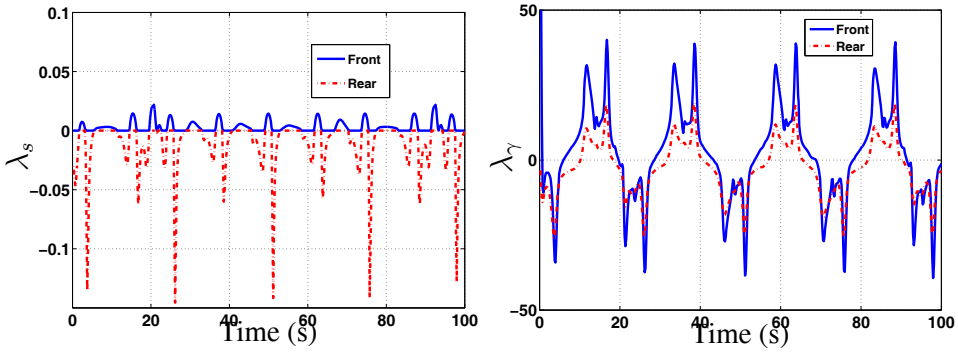

(a) (b)

Figure 2.19: Slip ratios and angles under the agile maneuver. (a) Slip ratio λ_s. (b) Slip angles λ_γ.

show the tire slip ratios and slip angles, respectively. It is noted from Fig. 2.19(a) that the required longitudinal slip ratio of the rear tire nearly reaches 0.15, which is nearly the maximal stable slip ratio of the tire model. From Fig. 2.19(b), we also see the large slip angles in this agile maneuver.

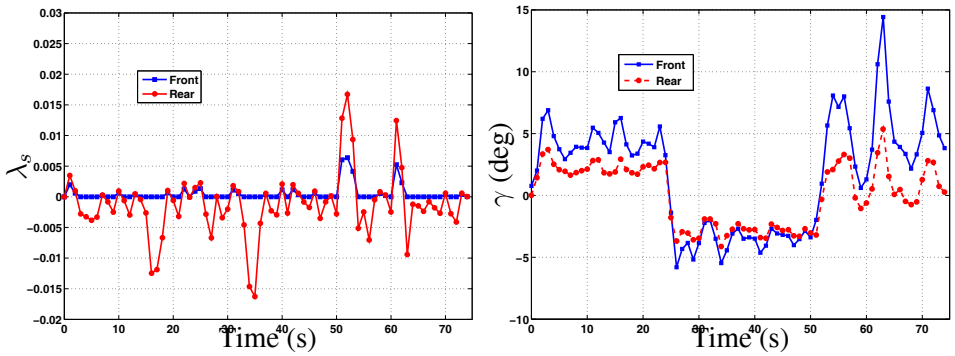

(a) (b)

Figure 2.20: Longitudinal slips and slip angles at the front and rear wheels of the "8"-shape trajectory tracking. (a) Slip ratio λ_{fs} and λ_{rs}. (b) Slip angles γ_f and γ_r.

We clearly see a large side slip angles shown in Fig. 2.20(b). Particularly, for the front wheel, we have seen a 15 degs side slip angle. For the rear wheel, the side slip angle reaches almost 6 degs, which is around the saturation point of the tire characteristics. In other words, the motorcycle rear wheel is starting to slide on the ground. If the side slip angle increases further, the stability of the motorcycle will change significantly. The longitudinal slips are relatively small since the longitudinal acceleration

of the motorcycle is not large and the racing motorcycle tire is stiff. This simulation example demonstrates that the proposed dynamic model and control systems capture the realistic aggressive motorcycle maneuvers.

Comparing with time-based trajectory tracking control design, the simulation results in this section show that the velocity field based path-following design achieves smoother velocity profiles and much smaller tracking errors.

2.7 Conclusion

In this chapter, we presented a new nonlinear dynamic model for autonomous motorcycles for agile maneuvers. The proposed model is obtained through a constrained Lagrange modeling approach. Comparing with the existing riderless motorcycle models, the new features of the proposed motorcycle dynamics model are twofold: First, we relaxed the assumption of zero-lateral-velocity constraints at tire contact points and thus the model can be used for the agile maneuvers when wheels run with large longitudinal slips and lateral side slips. Second, we considered the motorcycle tire models and extended the previously developed motorcycle dynamics. Then a nonlinear control design is proposed with three control inputs: the front wheel steering angle and the angular velocities for the front and rear wheels. The trajectory tracking control design took advantages of the external/internal convertible (EIC) dynamical structure of the motorcycle dynamics, and was extended with three control inputs. Such an extension allowed flexibility in control systems design and therefore simplified the complexity of the final calculation. We demonstrated the trajectory tracking control systems design through two simulation examples using a racing motorcycle prototype. To further improve the tracking performance, we presented a velocity field based pathfollowing control design. A velocity field design was presented to provide a desired velocity profile through a time suspension technique. We then combined the velocity field design

with the previously developed EIC motorcycle controller. The control system automatically tuned the velocity profile based on the tracking errors and trajectory properties. The simulation results of an agile maneuver demonstrated that the velocity field based path-following control design improved the tracking errors.

Chapter 3

Balancing Control of Stationary Riderless Single-Track Vehicle

3.1 Introduction

Balancing control of a stationary riderless bicycle is the main topic of this chapter. The motivation for this study is twofold. First, balance control of stationary bicycle systems is much more challenging than that under a certain velocity. It is known that the two single-track vehicles has "self-balance" ability at high speed. Nevertheless, the stationary single-track vehicles do not possess such property. Only few stationary balancing studies of single-track vehicles have been reported, especially for vehicles under only steering control. Second, understanding the balance capability is important for applications such as the use of bicycle-based rehabilitation device for recovering human postural control for disabilities patients [2].

We will present two balancing control designs. First, we consider the front-wheel steering as the only control input of the system. With only steering control, we show that the balance is maintained within a certain region in the state space. We reveal and explicitly identify this attraction region. We extend the approach in [82] with consideration of steering mechanism for the bicycle systems under a sliding-mode stabilization controller. Second, we use the gyroscopic actuator that is mounted on the rear rack of the bicycle to balance the stationary bicycle. Inspired by the observation that an experienced human rider commonly oscillates his/her body or the front steering mechanism around the equilibria points for balancing a bicycle, we propose an energy-shaping

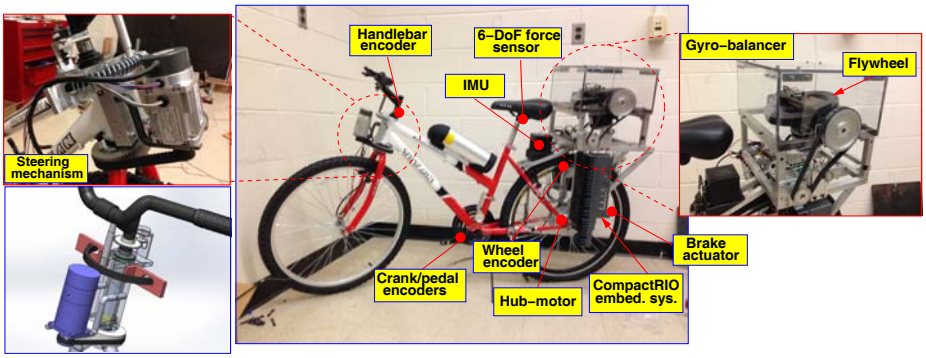

(a)

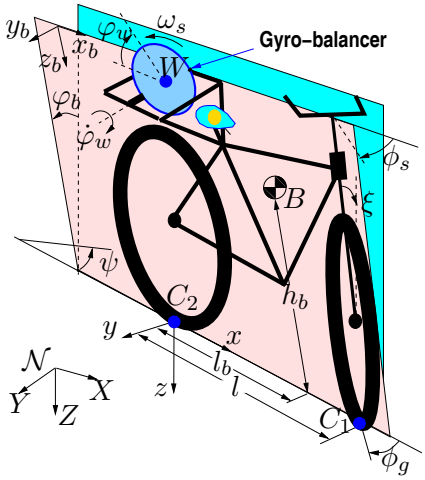

(b)

Figure 3.1: (a) "Bickebot". (b) Schematic of the bicycle system.

based control design to stabilize the bicycle to the orbital trajectory around the vertical equilibrium position. Both the effectiveness and performances of control designs are validated by experiments.

Figure 3.1(a) shows the instrumented bicycle "bikebot" newly developed at Rutgers University. All the stationary balancing experiments are conducted on the the bikebot. The mechanical structure of the bicycle is modified and built on a mountain bicycle with significant modifications. Both the traction/braking and the steering functions are augmented to allow a human rider, the onboard computer, or both to control the unstable platform. A hub motor and a DC motor are used for rear-wheel driving and steering control, respectively. The steering mechanism is modified significantly

such that the handlebar and the actual steering fork are mechanical separated and independently controlled. The rider can turn the handlebar and the human input steering angle is measured by the encoder. The onboard controller then turns the lower-steering mechanism for actual steering angle. Same design is applied to pedaling control of the bicycle moving velocity. A braking actuator is installed on the rear wheel to reduce the moving velocity and is controlled by the onboard computer. To perturb the rider's balancing torque, a single gimbal active controlled gyroscopic actuator is mounted on the back rack of the bicycle as shown in Fig. 3.1. The single gimbal gyroscopic actuator is compact [83] and can generate significant balancing moments to assist or perturb the rider. The values of the bikebot physical parameters are listed in Table 3.1.

3.2 Stationary bicycle balancing with steering control

3.2.1 Steering mechanism and geometric relationships

To facilitate the explanation of the influence of the steering mechanism on bicycle stability, we first assume that the front tire rotates about the fixed axis. Due to the steering mechanism and a caster angle ξ, the height change Δh_B of the center of gravity B is calculated by an estimate of the bicycle frame rotation angle δ. Similar to Chapter 2, the height change Δh_B is then calculated by the following equation

$$\Delta h_B = \delta l_b \, \mathrm{s}_{\varphi_b} = \frac{l_b l_t \, \mathrm{s}_{\varphi_b} \, \mathrm{c}_{\xi}}{l} \beta_g, \tag{3.1}$$

where l_b is the horizontal distance between the rear tire/ground contact point C_2 and the mass center B.

The formulation (3.1) does not consider the movement of the tire/ground contact point C_1 change due to steering. The portion change of C_1 can be negligible for navigation application where only requires small steering angle but not for the stationary balancing. Figure 3.2 illustrates the steering mechanism geometry. As shown in the

Table 3.1: Bikebot physical parameters

m (kg)	I_x (kgm^2)	I_{wx} (kgm^2)	I_{wz} (kgm^2)	h_b (m)	l_b (m)	l (m)	l_t (m)	ξ (deg)	R_t (m)
51	2.5	0.028	0.036	0.64	0.27	1.1	0.06	20	0.33

figure, because the front wheel plane moves from Π_s to Π_s', the change of the height of the center of gravity B is changed from two sources. The first one is the change of height of front tire center point (from O_f to O_f'). We denote the height difference between O_f and O_f' as Δh_{O_f}. The second source comes from the lateral movement of C_1 (to C_1'). We denote the lateral movement distance between C_1 and C_1' as Δy_{c_1}. In the following, we first discuss how to compute Δh_{O_f} and Δy_{c_1} and then revise the formulation of Δh_B in (3.1).

We assume that under steering point C_1 is moving on a circular curve under the effect of tire width. Notice the fact that if the steering angle is 90 degs, the arc length of curve $\widehat{C_1C_1'}$ is equal to $R_t\xi$ [71],where R_t is the tire radius. In this special case, $\phi_g = \frac{\pi}{2}$ and it is straightforward to calculate that $\Delta h_{O_f} = R_t(1-\cos\xi)$. For any general steering angle ϕ_g, we approximate Δh_{O_f} proportionally to that of the special case of $\phi_g = \frac{\pi}{2}$. Therefore, we obtain

$$\Delta h_{O_f} = R_t\left[1-\cos\left(\frac{\phi_g}{\pi/2}\xi\right)\right] = R_t\left[1-\cos\left(\frac{2\phi_g\xi}{\pi}\right)\right],$$

and then we approximate the height change of B as

$$\Delta h_{B1} = R_t\cos\varphi_b\left[1-\cos\left(\frac{2\phi_g\xi}{\pi}\right)\right]\frac{l_b}{l}. \tag{3.2}$$

To calculate Δy_{c_1}, we take the similar approach as calculation Δh_{O_f}. We illustrate the calculation in Fig. 3.2. We denote the contact point as $C_{\pi/2}$ under steering angle $\phi_g = \frac{\pi}{2}$. We assume that the trajectory of $C_1C_{\pi/2}$ is a circular curve with radius $r_s = \frac{R_t\xi}{\pi/2}$ (since the moving length from C_1 to $C_{\pi/2}$ is $R_t\xi$ by the definition of the caster angle ξ). We approximate Δy_{c_1} proportionally to that of steering angle is $\pi/6$,

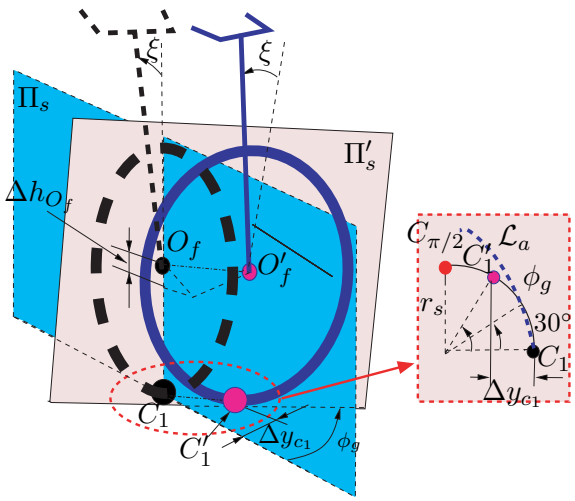

Figure 3.2: Schematic of the front wheel steering mechanism.

namely,

$$\frac{\Delta y_{c_1}}{\phi_g} = \frac{r_s\,(1-\cos\pi/6)}{\pi/6}$$

The above calculation is illustrated in Fig. 3.2 by assuming that the lateral displacement of C'_1 is proportional to that of $\phi_g = \frac{\pi}{6}$. By such an approximation, we obtain

$$\Delta y_{c_1} = \frac{12R_t\xi}{\pi^2}\left(1-\cos\frac{\pi}{6}\right)\phi_g. \tag{3.3}$$

We here choose $\phi_g = \frac{\pi}{6}$ as the reference point mainly for simplicity to obtain a linear relationship between Δy_{c_1} and ϕ_g. Note that by considering the lateral movement of point C_1, we need to deduct an angle of a magnitude of $\frac{\Delta y_{c_1}}{l}$ to revise the calculation of Δh_B in (3.1).

Based on the above discussions with (3.2) and (3.3), we revise the relationship in (3.1) as follows

$$\begin{aligned}\Delta h_B(\phi_s,\varphi_b) = {} & \frac{l_b l_t\,\mathrm{c}_\xi\,\mathrm{s}_{\varphi_b}}{l}\phi_g - \frac{12R_t l_b\xi\,\mathrm{s}_{\varphi_b}}{\pi^2}\left(1-\cos\frac{\pi}{6}\right)\phi_g - \\ & \frac{l_b R_t\,\mathrm{c}_{\varphi_b}}{l}\left[1-\cos\left(\frac{2\xi\phi_g}{\pi}\right)\right].\end{aligned} \tag{3.4}$$

Figure 3.3 shows that the new model is much more accurate than the linear approximation model (3.1).

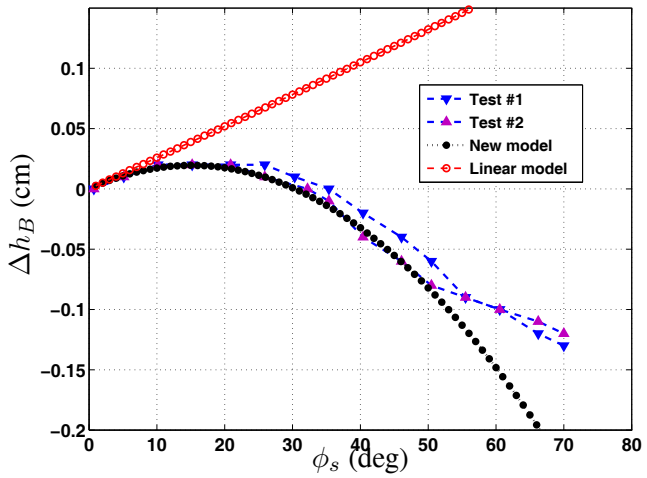

Figure 3.3: Experimental comparison of Δh_B with different model predictions with initial roll angle $\phi = -3.8°$.

3.2.2 Stationary bicycle dynamics

Similar to Chapter 2, we use the Lagrangian equations to obtain the dynamic equation of the motion of a stationary riderless bicycle as follows

$$\ddot{\varphi}_b = \frac{mg\sin\varphi_b}{I_x + mh_b^2}\left(h + \frac{\alpha R_t l_b}{l}\right) + \frac{mgl_b\,\mathrm{c}_{\varphi_b}}{(I_x + mh_b^2)l}\left[l_t\,\mathrm{c}_\xi - \frac{12R_t\xi}{\pi^2}\left(1 - \frac{\sqrt{3}}{2}\right)\right]\phi_g \quad (3.5)$$

where $\alpha := 1 - \cos\left(\frac{2\xi\phi_g}{\pi}\right)$, m is the total mass of the bicycle system, h_b is the height of mass center B, I_x is the mass moment of inertia of the bicycle system along the x-axis, and g is the gravitational constant. Due to the similarity with those in the previous chapter, we neglect the detailed derivation of (3.5). In the model(3.5), we also consider the gyroscopic actuator as a mass point and being included in the total mass.

3.2.3 Balance stability and control design

Roll angle controllable region

We consider the *controllable region* of bicycle systems (3.5) as the maximum roll angle region in which the system is possibly balanced around the vertical position ($\varphi_b = 0$) for *any* given steering control design.

To make the analysis tractable, we assume that: (1) the tire/ground contact is a point rather than a patch; and (2) the two contact points C_1 and C_2 do not move. Under a roll angle φ_b, the lateral movement of the center of gravity B is approximated as $\Delta_{By} = h_b \sin\varphi_b$. Now suppose that we apply a steering angle ϕ_s on the front wheel, the turn of the front wheel will compensate for the lateral movement of point B by distance Δ_{By}^{β} as follows.

$$\Delta_{By}^{\beta} = \frac{l_t l_b \, \mathrm{c}_\xi \, \mathrm{c}_{\varphi_b}}{l} \phi_g. \tag{3.6}$$

To maintain the balance by steering, let $\Delta_{By} - \Delta_{By}^{\beta} = 0$ and thus we obtain

$$\varphi_{bmax} = \tan^{-1}\left(\frac{l_b l_t \, \mathrm{c}_\xi}{h_b l} \beta_g\right). \tag{3.7}$$

It is straightforward to check φ_{bmax} is 4 degree given the parameters in Table 3.1.

Remark 3.1. *From (3.7), we clearly see that the maximum stabilizable roll angle by steering depends on geometric parameters of the bicycle system. Note that the analysis here is based on a simplified static and kinematic calculation and consideration of dynamic effects is ongoing work.*

Control design and domain of attraction (DOA)

We consider the DOA of the bicycle dynamics (3.5) under a particular balance controller. We first specify a controller before analyzing DOA. Using a small angle approximation, we consider $\alpha \approx 0.05$ in the dynamics (3.5) and thus we rewrite (3.5) as

$$\ddot{\varphi}_b = f_1(\varphi_b) + f_2(\varphi_b)\phi_g, \tag{3.8}$$

where

$$f_1(\varphi_b) = \frac{mg\sin\varphi_b}{I_x + m{h_b}^2}\left(h + \frac{0.05 R_t l_b}{l}\right) \quad \text{and}$$
$$f_2(\varphi_b) = \frac{mgl_b \, \mathrm{c}_{\varphi_b}}{(I_x + m{h_b}^2)l}\left[l_t \, \mathrm{c}_\xi - \frac{12 R_t \xi}{\pi^2}\left(1 - \frac{\sqrt{3}}{2}\right)\right].$$

We design a sliding mode control for the dynamic systems (3.8). We first define a sliding surface $s = \varphi_b + \lambda\dot{\varphi}_b$. Then we design the controller

$$\phi_g = \frac{-\dot{\varphi}_b - \lambda f_1(\varphi_b) - Ks}{\lambda f_2(\varphi_b)}, \tag{3.9}$$

where $\lambda > 0$ and $K > 0$ are constants. Plugging (3.9) into (3.8), we obtain

$$\ddot{\varphi}_b = -\frac{K}{\lambda}\varphi_b - \left(\frac{1}{\lambda} + K\right)\dot{\varphi}_b \tag{3.10}$$

as the closed-loop dynamics.

To estimate DOA, we consider the case that the maximum projected steering angle is $\frac{\pi}{3}$, namely, $\phi_g \leq \frac{\pi}{3}$. Combining (3.8) and (3.10), it is straightforward to obtain the DOA estimates given by

$$\left|\frac{-\frac{K}{\lambda}\varphi_b - \left(\frac{1}{\lambda} + K\right)\dot{\varphi}_b - f_1(\varphi_b)}{f_2(\varphi_b)}\right| \leq \frac{\pi}{3}. \tag{3.11}$$

Figure 3.4 shows the DOA estimates with three different sets of control parameters. It is interesting to find that when the controller is aggressive such as $K = 40$, the DOA becomes smaller. This is because that aggressive actions increase the roll angular motion, which is undesirable for the balance control. Figure 3.4 also shows that the DOA estimate under this type of sliding-mode control has a strip shape.

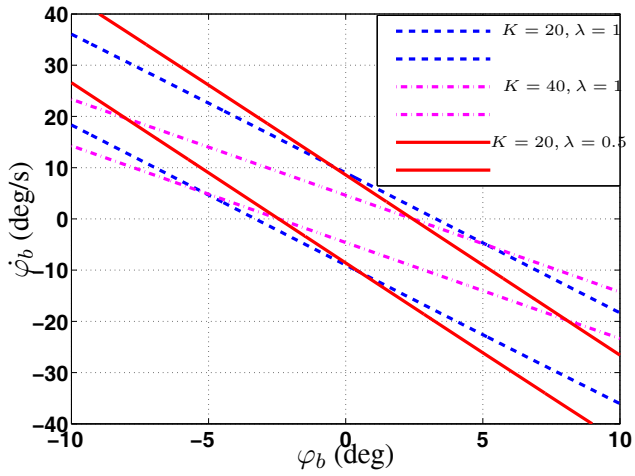

Figure 3.4: DOA estimation under different sliding-mode control designs

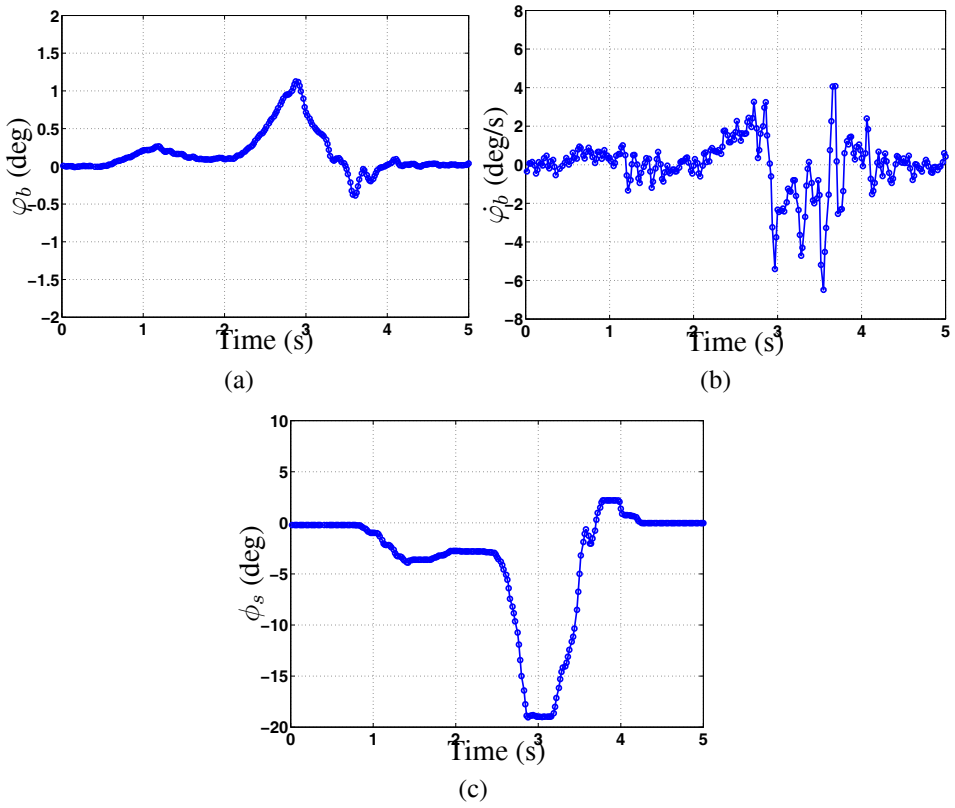

Figure 3.5: Experimental results of the balance controller with $K = 20$ and $\lambda = 1$. (a) Roll angle φ_b. (b) Roll angle rate $\dot{\varphi}_b$. (c) Steering angle ϕ_s.

3.2.4 Experiments

We conducted all experiments using the bikebot shown in Fig. 3.1(a). In experiment, the rear tire is fully locked to achieve zero velocity constraint.

Figure 3.5 shows the experimental results. We release the bicycle from equilibrium position and the controller turned steering immediately. The bicycle was then returned around the equilibrium position finally. We now show a validation of the DOA estimation by two experiments. First, we set up a zero initial roll angular rate. The design parameters of the sliding-mode controller are $K = 20$ and $\lambda = 1$. By calculation, when $\dot{\varphi}_b = 0$ we find the DOA boundary (e.g., curves in Fig. 3.4) is around 2.5 degs. In the first experiment, we use the motorized support jack to setup the bicycle to start at 2.5 degs. In the second experiment, we set the initial roll angle to be slightly larger

than 4 degs. Figure 3.6 shows the experimental roll angle results. The results shown in Fig. 3.6 clearly illustrate that for the first experiment the controller can regulate the roll angle to return back to the equilibrium position, while in the second experiment, the bicycle cannot be balanced and finally supported by the motorized jack. To protect the bicycle from falling down, we set a 6-deg roll angle limit position by the support jack in experiments.

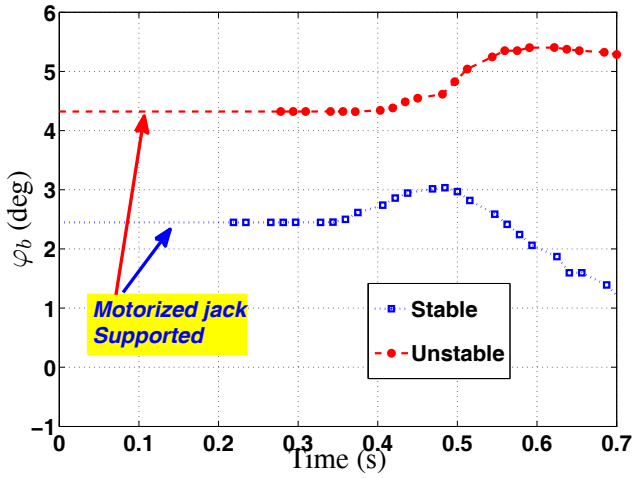

Figure 3.6: Roll angle trajectory of experiments with two different initial roll angle values

3.3 Stationary bicycle balancing with gyroscopic actuator

3.3.1 Bicycle model

In this section, the riderless bicycle is considered as a three-part platform: a rear frame with the gyro-balancer structure and rear wheel, the front wheel and steering mechanism and the gyro-balance flywheel. We consider the following modeling assumptions: (1) the mass center W of the gyro-balancer flywheel and its driving motor is located at the rotating axis and therefore, its translational velocity is along the rear frame; (2) the rear wheel contact point satisfies the nonholonomic constraint, i.e., zero lateral velocity; and (3) the bicycle moves on a flat plane and vertical motion is neglected, namely,

no suspension motion.

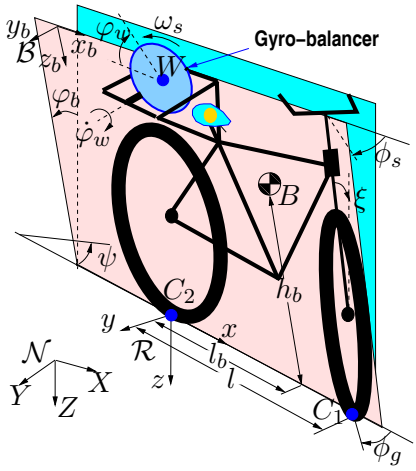

Figure 3.7: Schematic of the bicycle system.

Similar to the previous derivations and using the Lagrange approach, the motion equations of motion of the riderless bicycle with zero steering angle are

$$(mh_b^2 + I_x + I_{wxz}\,\mathrm{s}^2_{\varphi_w})\ddot{\varphi}_b + I_{wxz}\,\mathrm{s}_{2\varphi_w}\,\dot{\varphi}_w\dot{\varphi}_b - mgh_b\,\mathrm{s}_{\varphi_b} + I_{wz}\,\mathrm{c}_{\varphi_w}\,\dot{\varphi}_w\omega_s = 0, \quad (3.12)$$

$$I_{wy}\ddot{\varphi}_w + I_{wxz}\dot{\varphi}_b^2\,\mathrm{c}_{\varphi_w}\,\mathrm{s}_{\varphi_w} - I_{wz}\dot{\varphi}_b\omega_s\,\mathrm{c}_{\varphi_w} = \tau_m, \quad (3.13)$$

where $I_{wxz} = I_{wz} - I_{wx}$ and I represents the inertial of moment,ω_s is the constant rotating speed of flywheel in the gyroscopic actuator.

3.3.2 Stationary bicycle dynamics

The state variable is defined as $\boldsymbol{x} = [x_1 \;\; x_2 \;\; x_3]^T = [\varphi_b \;\; \dot{\varphi}_b \;\; \sin\varphi_w]^T$. For presentation convenience, we also define $\boldsymbol{x}_b = [x_1 \;\; x_2]^T$. It is clear that the bicycle with gyroscopic actuator is an underactuated system under only gyro-balancer control. Since the pivoting motor is controlled through the lower-level embedded control for a given velocity, we consider a velocity control input for pivoting angle x_3. With the defined state variable, we re-write the dynamics equation (3.12) along with the pivoting angular velocity

control as

$$\dot{x}_1 = x_2 \tag{3.14a}$$

$$\dot{x}_2 = f(\boldsymbol{x}) + g_1(\boldsymbol{x})u_1 \tag{3.14b}$$

$$\dot{x}_3 = u_1, \tag{3.14c}$$

where $u_1 = \cos\varphi_w\dot{\varphi}_w$ is the controlled pivoting velocity,

$$f(\boldsymbol{x}) = \frac{mgh_b\,\mathrm{s}_{x_1}}{I_s(\boldsymbol{x})},\ g_1(\boldsymbol{x}) = -\frac{I_{wxz}x_2\,\mathrm{s}_{2x_3} + I_{wz}\omega_s}{I_s(\boldsymbol{x})}, \tag{3.15}$$

and $I_s(\boldsymbol{x}) = mh_B^2 + I_x + I_{wxz}\,\mathrm{s}_{x_3}^2$. Due to the physical constraints, the pivoting angle and angular rate are within a limit. We denote that

$$|x_3| = |\,\mathrm{s}_{\varphi_w}\,| \le \mathrm{s}_{\varphi_w^{\max}} < 1,\ |u| = |\,\mathrm{c}_{\varphi_w}\,\dot{\varphi}_w| \le \omega_w^{\max}, \tag{3.16}$$

where $\varphi_w^{\max}$ and $\omega_w^{\max}$ are the maximum flywheel pivoting angle and angular velocity, respectively. In the following, we present the balancing control design.

3.3.3 Balancing controller

The equilibrium of the dynamics (3.14) is $x_{1e} = x_{2e} = 0$ under $u_{1e} = \dot{\varphi}_{we} = 0$. It is interesting to notice that the flywheel pivoting angle can be any values within $\varphi_w^{\max}$ while the bicycle is balanced.

We now consider how to calculate the gyro-balancer flywheel's pivoting angle $x_3(t)$ for a given profile for roll angle $x_1(t)$. Indeed, (3.12) can be re-written as

$$\frac{d}{dt}\left[(mh_b^2 + I_x)x_2 + I_{wxz}\dot{\varphi}_b x_3^2 + I_{wz}\omega_s x_3\right] = -\frac{\partial}{\partial\varphi_b}\left(mgh_b\,\mathrm{c}_{x_1}\right). \tag{3.17}$$

From the above equation, the bicycle with flywheel satisfies the Hamiltonian dynamics with angular momentum along the x-axis direction

$$p_x(t) = (mh_b^2 + I_x)x_2(t) + I_{wxz}x_2(t)x_3^2(t) + I_{wz}\omega_s x_3(t). \tag{3.18}$$

By integrating (3.17), it is then straightforward to obtain that

$$p_x(t) - p_x(0) = \int_0^t mgh_b \, \mathrm{s}_{x_1(\tau)} \, d\tau. \tag{3.19}$$

From (3.19), we have the following property with a proof given in Appendix E.

Property 3.1. *For a given periodic profile $x_1(t)$ with period T, the profile for the pivoting angle is also periodic with the same period T.*

To further simplify the controller design, from (3.15) and the fact that the flywheel spinning speed $\omega_s \gg |x_2|$, it is noted that $I_{wz}\omega_2 \, \mathrm{c}_{x_3} \gg |I_{wxz}x_2 \, \mathrm{s}_{2x_3}|$. Moreover, $mh_G^2 \gg I_x \gg I_{wxz}$ and therefore, (3.14b) is approximated and reduced to

$$\dot{x}_2 - \frac{g}{h_B} \, \mathrm{s}_{x_1} + \frac{I_{wz}\omega_s}{mh_B^2} u = 0. \tag{3.20}$$

Clearly, for simplified dynamics (3.20), state variable $\boldsymbol{x} \in \mathcal{D} := \mathbb{S} \times \mathbb{R} \times (-1, 1)$.

We consider to regulate roll motion on an orbital trajectory in $\mathcal{D}$. An oscillation orbital trajectory $\mathcal{O}_b$ is selected as given by the following pendulum dynamics.

$$\mathcal{O}_b : \; \dot{x}_2 + \frac{b}{h_b} \, \mathrm{s}_{x_1} = 0, \tag{3.21}$$

where design parameter $b > 0$ is a gravitationally equivalent constant. Plugging (3.21) into the simplified roll dynamics (3.20) to eliminate term s_{x_1}, we obtain

$$\dot{x}_3 = -\frac{(b+g)mh_b^2}{I_{wz}b\omega_s}\dot{x}_2 = -L\dot{x}_2, \tag{3.22}$$

where constant $L = \frac{(g+b)mh_b^2}{I_{wz}b\omega_s}$. Therefore, the corresponding orbital trajectory $\mathcal{O}_w$ for flywheel pivoting angle x_3 is designed as

$$\mathcal{O}_w : \; x_3 = -Lx_2. \tag{3.23}$$

Remark 3.2. *The form of (3.23) is seemingly similar to those of virtual holonomic constraints in orbital stabilization of underactuated mechanical systems in [84, 85]. However, the relationship (3.23) are not the same as the virtual constraints in [84, 85]*

since (3.23) is obtained through the system dynamics (3.20) rather than by design. Moreover, (3.23) represents the torque balance relationship between the controlled flywheel pivoting and the underactuated bicycle roll motion, while the virtual holonomic constraints in [84, 85] capture the displacement relationships among the generalized coordinates.

Once the bicycle roll motion follows the orbit $\mathcal{O}_b$, the total energy $E(\boldsymbol{x}_b)$ is defined as:

$$E(\boldsymbol{x}_b) = \frac{1}{2} m h_b^2 x_2^2 + m h_b b \left(1 - \mathrm{c}_{x_1}\right).$$

When target orbit $\mathcal{O}_b$ reaches the maximum angle x_1^d with $x_2 = 0$, the total energy is $E_d = m h_G b (1 - \mathrm{c}_{x_1^d})$. We define the energy difference $\Delta E = E(\boldsymbol{x}_b) - E_d$. We consider the Lyapunov candidate function $V(\boldsymbol{x})$ as

$$V(\boldsymbol{x}) = \frac{1}{2}\Delta E^2 + \frac{1}{2} k_1 \left(x_3 + L x_2\right)^2,$$

where $k_1 > 0$ is a constant. Obviously, $V(\boldsymbol{x}) \geq 0$ and

$$\dot{V}(\boldsymbol{x}) = \Delta E (m h_b^2 x_2 \dot{x}_2 + m h_b b \, \mathrm{s}_{x_1} x_2) + k_1 (x_3 + L x_2)(\dot{x}_3 + L \dot{x}_2).$$

Using (3.14) and (3.20) and letting

$$u = \frac{Lb}{h_B} \left(\mathrm{s}_{x_1} + v_1\right) = u_{1s} + \frac{Lb}{h_b} v_1, \tag{3.24}$$

where $u_{1s} = \frac{Lb}{h_b} \mathrm{s}_{x_1}$ and v_1 is an auxiliary control input, $\dot{V}(\boldsymbol{x})$ is then reduced to

$$\dot{V}(\boldsymbol{x}) = -m h_b (g + b) \left[\Delta E x_2 + \alpha k_1 \left(x_3 + L x_2\right)\right] v_1, \tag{3.25}$$

where $\alpha = \frac{g}{b I_{wz} \omega_s} > 0$ is a constant.

The control input v is further designed as

$$v_1 = k_2 \left[\Delta E x_2 + \alpha k_1 \left(x_3 + L x_2\right)\right] \tag{3.26}$$

with a positive constant parameter $k_2 > 0$, then we obtain

$$\dot{V}(\boldsymbol{x}) = -m h_b (g + b) k_2 \left[\Delta E x_2 + \alpha k_1 \left(x_3 + L x_2\right)\right]^2 \leq 0.$$

By La'Salle theory [86], the system states asymptotically converge to the invariant set $\mathcal{S}(\boldsymbol{x})$

$$\mathcal{S}(\boldsymbol{x}) = \Big\{ \boldsymbol{x} \in \mathcal{D} \,|\Delta E x_2 + \alpha k_1 \left(x_3 + L x_2\right) = 0 \Big\}. \tag{3.27}$$

The trajectories of the closed-loop dynamics are on orbits $\mathcal{O}_b$ and $\mathcal{O}_w$. Therefore, the origin $\boldsymbol{x}_e = \mathbf{0} \in \mathcal{S}(\boldsymbol{x})$.

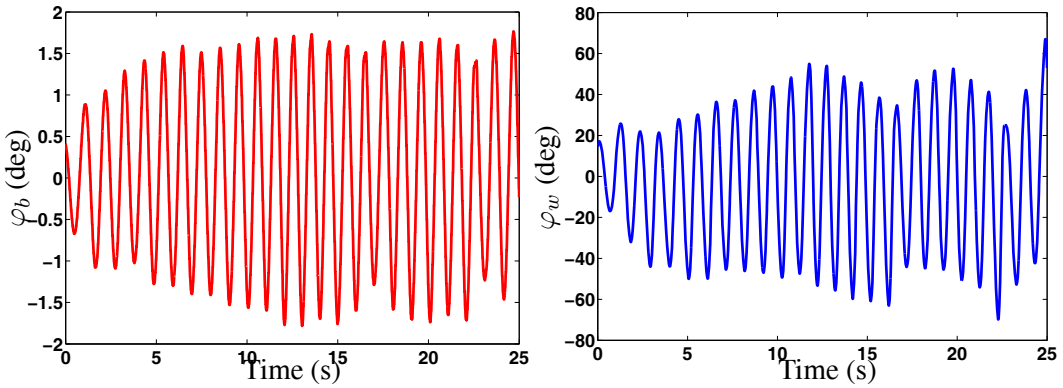

(a) (b)

Figure 3.8: Bicycle self-balancing at zero velocity. (a) Roll angle φ_b. (b) Flywheel pivoting angle φ_w.

3.3.4 Experiments

We demonstrate the self-balancing control of the stationary riderless bicycle in experiments. The balancing controller (3.24) was implemented with parameter $b = 1$ and $k_2 = 1$ and the bicycle was successfully balanced. Figure 3.8 shows the experimental results. The bicycle roll angle is shown in Fig. 3.8(a), and the gyroscopic actuator flywheel pivoting angle is shown in Fig. 3.8(b). Clearly, the trajectories of the bicycle roll angle and the pivoting angle converge to the orbits and are finally synchronized in periodic motion. It is also clear that under the gyroscopic control constraint, the bicycle can be balanced within a small range (i.e., 2-3 degs) around the vertical position.

3.4 Conclusion

In this chapter, we presented two balancing control designs of the stationary riderless bicycle. We first revealed geometric and kinematic relationship of the front wheel steering mechanism of the bicycle system. We presented the analytical estimation of the domain of attraction (DOA) for a sliding mode control by using steering as the only input. We also designed an energy-shaping-based control with a gyroscopic actuator to realize orbital stabilization. Experiments are conducted to validate both the two control designs.

Chapter 4
Modeling and Sensing of Tire-Road Interactions

4.1 Introduction

This chapter is an extension of the tire friction model presented in Chapter 2. In this chapter, a more accurate model of tire deformation and force distributions is presented.

Tire-road interactions play an extremely important role for vehicle operation. However, understanding and modeling of the tire-road interactions are challenging because these interactions are complex, highly nonlinear, and dependent on various tire and road conditions. Further challenges arise because of lack of effective, inexpensive sensing technology to obtain in-situ tire-road contact information [28].

Rubber deformations on the tire-road contact patch generate friction forces. Most empirical friction force models, such as Pacejka "magic" formula [29], capture the phenomenological relationships between total friction forces and tire kinematics (e.g., slip ratios and slip angles etc.) Although the physical and the LuGre dynamic friction models [30–35] try to capture and interpret the total friction forces through rubber deformation distribution, several critical modeling assumptions are made *a prior*. For example, the physical model in [30] uses an assumption of a simple division of adhesion (stick) and sliding (slip) regions of the tire contact patch. The LuGre dynamic models in [32–35] are built on the given normal force distribution to calculate rubber deformation distributions without experimental validation. Although the normal load distribution is discussed in [87,88], few work are reported on analyses and experiments of the rubber deformation and friction force distributions on the contact patch. One of

the main goals of this work is to fill the gap of such knowledge.

Tire-road stick-to-slip transition determines the rubber deformation and friction force distributions. The *stick* contact refers to no locally relative movement between the tire and the road, while in *slip* contact, relative tire-road motion exists locally. Understanding of stick-slip interactions not only provides the fundamentals of the rubber deformation and friction force distributions and their evolutions [89], but also helps build accurate friction models for vehicle dynamic simulation and active safety control [90,91]. Another goal of this work is to present the analysis, modeling and experiments of stick-slip interactions between the stationary tire and the firm road.

Unlike robotic fingertip contact [92–94], the Hertzian contact theory [95] cannot be directly used to obtain the tire-road normal contact force distribution due to the large rubber deformation and the tire's hollow structure. A semi-analytical normal force model for the thin layer-rigid contact [96] is instead used and extended. To obtain the elastic rubber deformation and friction force distributions simultaneously, a beam-spring network model is introduced and employed. Inspired by the discrete mass-spring network models that are used to successfully simulate and compute the deformation of thin layer structures [97, 98], a set of virtual cantilever beams are used to model the rubber's shear effect and a set of virtual springs that connect the beams are introduced to capture the elasticity. The cantilever beam-spring modeling approach not only provide the fundamental information of deformation and force distributions, but also fits well with tire-road dynamic friction models such as the LuGre models in [34, 35]. Therefore, it is naturally convenient to integrate the beam-spring network model with the dynamic tire-road friction model to bridge the local friction force distribution with the total friction force.

To eliminate the influences of tire treads or grooves on the rubber deformation and friction force distributions and to focus on the fundamentals of mechanical contact properties, a tire with a smooth outer surface is used in this study. To validate the

analyses and the models, an embedded, small sensor made of pressure-sensitive, electric conductive rubber (PSECR) is used to extract the multi-directional local friction forces on the tire contact patch [99]. Compared with the other types of the tire sensors (e.g., [36, 40, 44]), the embedded PSECR sensor is capable to extract the local friction forces and their distributions.

The main contribution of the work lies in the force and deformation distribution models, analyses, and sensing for studying stick-slip contacts between a flexible thin layer and a rigid surface. These contact problems include not only the tire-road interactions but also many other applications in mechanical systems, such as robotic grasping and manipulation [100]. Although the presented work focuses on the stick-slip interaction, the results provide new modeling approaches to study the dynamic tire-road interactions. The calculation and modeling of the local contact force distributions will also lead to potentially build relationships among the beam-spring network model, the embedded tire sensor measurements, and the total friction models (e.g., LuGre dynamic friction model). These relationships are particularly useful for using the embedded sensors to estimate the model parameters in the total friction models in real time.

4.2 Tire-road normal contact pressure model

4.2.1 Tire contact patch geometry

Figure 4.1(a) shows the tire-road contact and Fig. 4.1(b) illustrates the schematic of the contact geometry and force generation. A torus-shape motorcycle tire with a smooth outer surface and a circular radial cross section is used in this work. The thickness of the rubber layer is defined as $2h$. A coordinate system is set up with the origin at the center of contact patch $\mathcal{P}$ with a vertical distance of h to the road surface. The x-axis is along the tire center with the positive direction towards the leading edge of $\mathcal{P}$, that

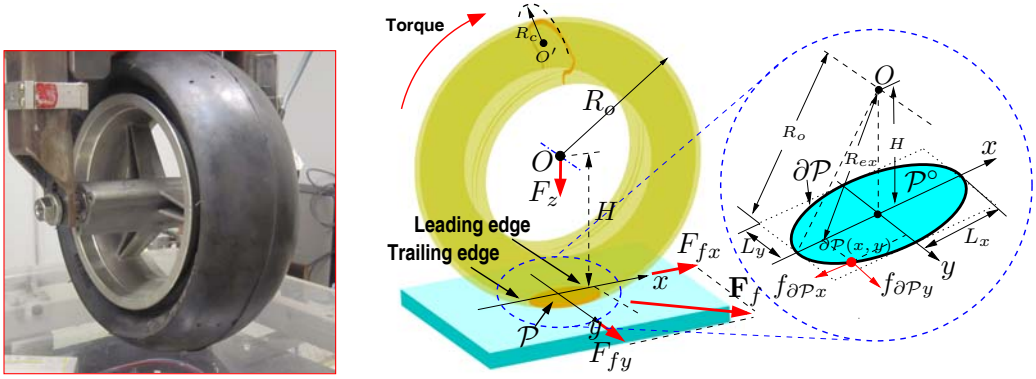

(a) (b)

Figure 4.1: (a) A torus-shape tire-road contact. (b) A schematic of the tire-road contact and the boundary force calculation.

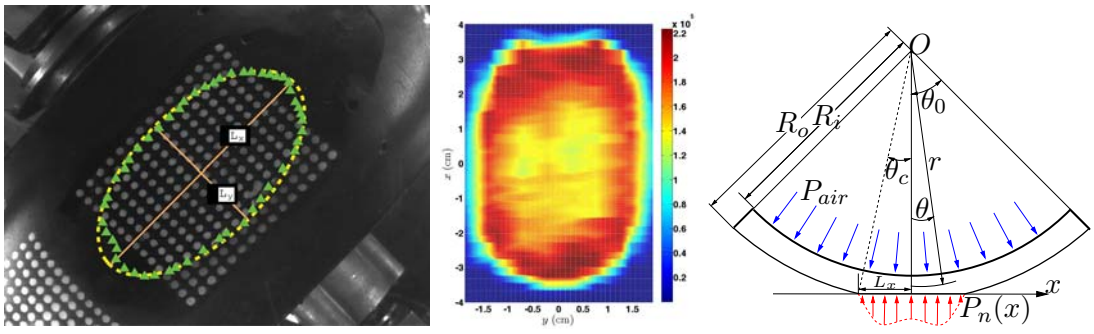

(a) (b) (c)

Figure 4.2: (a) The contact patch geometry. The dashed-line indicates the elliptic model approximation and the triangular line shows the actual contact contour from the images taken by a camera underneath the tire. The white dots painted on the tire surface are used to calculate the rubber deformation distribution. (b) $P_n(x, y)$ distribution (in Pa) under $P_{air} = 69$ kPa and $F_z = 267$ N. (c) Schematic of the one-dimensional tire contact configuration along the center line.

is, the direction where the tire tends to move forward. Total normal force F_z is applied on $\mathcal{P}$ with contact normal pressure distribution $P_n(x, y)$ and inflation air pressure P_{air} Total friction forces $\mathbf{F}_f$ is projected along the x- and y-axis directions as F_{fx} and F_{fy}, respectively. The friction force stress $\mathbf{P}_f(x, y)$ at point $(x, y) \in \mathcal{P}$ is composed by the x- and y-axis components as $P_{fx}(x, y)$ and $P_{fy}(x, y)$, respectively. From the above definitions, it is straightforward to obtain

$$F_z = \int_{\mathcal{P}} P_n(x, y) dS, \quad \mathbf{F}_f = \int_{\mathcal{P}} \mathbf{P}_f(x, y) dS,$$

where dS is an infinitesimal area on $\mathcal{P}$.

Under P_{air} and F_z, $\mathcal{P}$ is in an elliptical shape [101, 102]. To estimate the major radius L_x and the minor radius L_y of $\mathcal{P}$, a series of experiments are conducted under various P_{air} and F_z. An empirical model for L_k, $k = x, y$, is proposed in [102]. In the empirical model, the exponential functions of normal load F_z and tire inflation pressure P_{air} are used to predict L_i, $i = x, y$, as follows.

$$L_i(P_{air}, F_z) = a_i(P_{air}) F_z^{b_i(P_{air})}, \quad i = x, y, \tag{4.1}$$

where $a_i(P_{air}) = e^{a_{i2}P_{air}^2 + a_{i1}P_{air} + a_{i0}}$, $b_i(P_{air}) = b_{i2}P_{air}^2 + b_{i1}P_{air} + b_{i0}$, $i = x, y$, are quadratic functions of p. The values of parameters a_{ij} and b_{ij}, $i = x, y$, $j = 1, 2, 3$, are listed in [102]. The comparison of the model predicted ellipse and the measured $\mathcal{P}$ is shown in Fig. 4.2(a). The prediction matches the actual size of $\mathcal{P}$. With the known L_x and L_y, the distance between the tire center O and $\mathcal{P}$ is calculated as $H = \sqrt{R_o^2 - L_x^2}$. From the geometry in Fig. 4.1(b), the radius of the tire radial cross section is obtained as $R_c = \frac{(R_o - H)^2 + L_y^2}{2(R_o - H)}$.

4.2.2 Normal contact pressure distribution $P_n(x, y)$

Because of its influences on the friction force distribution, the normal contact pressure distribution is discussed in this section. Figure 4.2(b) shows a typical normal contact pressure distribution $P_n(x, y)$ that is obtained from the measurements of a set of PSECR sensor arrays placed on $\mathcal{P}$. It is clear that $P_n(x, y)$ is symmetric with respect to the center of $\mathcal{P}$. Unlike the fingertip contact in which the highest pressure of $P_n(x, y)$ is located around the center [94], the locations of the highest $P_n(x, y)$ form a ring-shaped zone and are close to the edge of $\mathcal{P}$. In [102], an empirical model is presented for $P_n(x, y)$. To provide a better understanding of the normal contact pressure distribution, a semi-analytical model is derived and obtained in this section. In order to capture the fundamental thin layer contacting property and achieve the analytical

model, it is assumed that the tire is only made of rubber without fiber layer in the normal contact pressure model. Note that in the model, the geometry information (i.e, L_x, L_y) of contact patch is assumed known by (4.1).

Due to the symmetry, the analytical model along the tire center line (Fig. 4.1(a)) is presented here. Such a one-dimensional pressure distribution is denoted as $P_n(x)$ and Fig. 4.2(c) illustrates the schematic to calculate $P_n(x)$. The Fourier-Michell solution [103] is used to obtain $P_n(x)$. To satisfy the bi-harmonic condition $\nabla^4\phi(r,\theta)=0$ in polar coordinates [103], the following potential function $\phi(r,\theta)$ is selected [96]

$$\phi(r,\theta) = a_0 r^2 + b_0 \log r + \sum_{n=1}^{\infty}\left(a_n r^{n\pi/\theta_0} + b_n r^{n\pi/\theta_0+2} + c_n r^{-n\pi/\theta_0} + d_n r^{-n\pi/\theta_0+2}\right)\cos\frac{n\pi\theta}{\theta_0}, \quad (4.2)$$

where a_0, b_0, a_n, b_n, c_n and d_n are coefficients to be determined and θ_0 is defined for the cross section where the contacting influence on deflection and shear stress are negligible. In Fig. 4.2(c), contact angle $\theta_c = \sin^{-1}\left(\frac{L_x}{R_o}\right)$. Given the potential function in (4.2), the radial normal stress σ_{rr}, the tangential normal stress $\sigma_{\theta\theta}$ and the shear stresses $\tau_{r\theta}$ in polar coordinates are calculated as follows [103]

$$\sigma_{rr} = \frac{1}{r}\frac{\partial\phi}{\partial r} + \frac{1}{r^2}\frac{\partial^2\phi}{\partial\theta^2},\ \sigma_{\theta\theta} = \frac{\partial^2\phi}{\partial r^2},\ \tau_{r\theta} = -\frac{\partial}{\partial r}\left(\frac{1}{r}\frac{\partial\phi}{\partial\theta}\right). \quad (4.3)$$

For calculation convenience, normalized $\hat{\theta} = \frac{\pi\theta}{\theta_0}$ and $\hat{\theta}_c = \frac{\pi\theta_c}{\theta_0}$ are used in the following calculations. Without confusion, the notations are abused by using θ and θ_c instead of $\hat{\theta}$ and $\hat{\theta}_c$ for brevity.

The normalized boundary conditions are set as

$$\begin{aligned}
&u_\theta = \tau_{r\theta} = 0,\ |\theta| = \pi,\ R_i \le r \le R_o,\\
&\sigma_{rr} = \tau_{r\theta} = 0,\ 0 \le |\theta| < \pi,\ r = R_i,\\
&\sigma_{rr} = \tau_{r\theta} = 0,\ \theta_c \le |\theta| < \pi,\ r = R_o, \text{ and}\\
&\begin{cases} \frac{\partial u_r}{\partial\theta} = \frac{R_o\theta_0^2}{\pi^2}\sin\theta, \\ \tau_{r\theta} = 0, \end{cases} \quad 0 \le |\theta| < \theta_c,\ r = R_o,
\end{aligned} \quad (4.4)$$

where u_r and u_θ are radial and tangential displacements in polar coordinates, respectively. Notice that directly applying the boundary condition $\sigma_{rr} = -P_{air}$ at $r = R_i$ does not provide correct solutions in (4.2) due to the intrinsic limitations of linear elasticity theory. The influence of P_{air} on $P_n(x)$ is temporarily not considered and its effect will be compensated into the $P_n(x)$ model through empirical approach.

Plugging (4.2) and (4.3) with the normalized θ into (4.4), the coefficients in $\phi(r, \theta)$ are solved and obtained. Following the similar derivation in [96], an analytical solution for the normal contact stress at $r = R_o$ is obtained as

$$\sigma_{rr}(R_o, \theta) = \cos\left(\frac{\theta}{2}\right) \int_\theta^{\theta_c} \frac{\varphi(t)dt}{\sqrt{\cos\theta - \cos t}}, \tag{4.5}$$

where φ is an auxiliary function that is found as a Fredholm integral problem of the second kind

$$\varphi(t) + \int_0^{\theta_c} \varphi(s)K(t, s)ds = -\frac{G}{\sqrt{2}(1-\nu)} \left(\frac{\theta_0}{\pi}\right)^2 \sin t \tag{4.6}$$

and the kernel function $K(t, s)$ is defined as

$$K(t,s) = -\frac{1}{2}\sum_{n=1}^{\infty} n\left(1 - \frac{G}{1-\nu}h_n\right)\tan\left(\frac{t}{2}\right)\left\{\left[L_n(\cos s) + L_{n-1}(\cos s)\right]\left[L_n(\cos t) + L_{n-1}(\cos t)\right]\right\}.$$

$L_n(x)$ in the above equation is a Legendre polynomial of order n, $\hat{n} = \frac{n\pi}{\theta_0}$, and parameter $\rho = \frac{R_i}{R_o}$ is the ratio of R_i and R_o and where

$$h_n = \frac{\hat{n}[(2\nu-1)(\rho^{2\hat{n}}-1)^2 + 2\hat{n}(\nu-1)(\rho^{4\hat{n}}-1) - \hat{n}^2\rho^{2\hat{n}-2}(\rho^2-1)(\rho^2+3-4\nu)]}{2G(\hat{n}^2-1)[(\rho^{2\hat{n}}-1)^2 - \hat{n}^2\rho^{2\hat{n}-2}(\rho^2-1)^2]}. \tag{4.7}$$

Considering θ in (4.5) actually represents $\hat{\theta}$, substituting $\hat{\theta} = \frac{\pi\theta}{\theta_0}$ into (4.5) and taking a small angle assumption for θ, $\sigma_{rr}\left(R_o, \frac{\pi x}{\theta_0 R_o}\right)$ is then used to approximate $P_n(x)$ at $x = R_o\theta$.

Remark 4.1. *Although the distribution of* $\sigma_{rr}\left(R_o, \frac{\pi x}{\theta_0 R_o}\right)$ *only along the tire center line is presented, the results are readily extended to the distribution along the* y*-axis direction because the radial cross-section is also in a circular shape. Similar to the approach presented in [102], the two-dimensional model of* $\sigma_{rr}(x, y)$ *distribution on* $\mathcal{P}$ *can be extended and obtained. In here, arguments* R_0 *and other constants are dropped in* σ_{rr} *for explicitness.*

Obviously, the existence of P_{air} also contributes normal contact pressure; see the force equilibrium diagram Fig. 4.2(c). To capture the influence of P_{air}, an empirical approach is proposed by combing the above analytical solution and F_z. Thus, a semi-analytical model of normal contact pressure is calculated as

$$P_n(x, y) = -\sigma_{rr}(x, y) + \frac{F_z - \int_{\mathcal{P}} -\sigma_{rr}(x, y) dS}{S}. \tag{4.8}$$

In (4.8), S is the area on $\mathcal{P}$ and the negative sign follows the convention that a compressive stress is defined as a negative value. The second term in (4.8) captures the partial pressure distribution caused by P_{air}. The uniform influence assumption of P_{air} on $\mathcal{P}$ is taken in (4.8) for simplification and the effectiveness will be validated through real experiments.

Remark 4.2. *The above derivation does not consider the existence of the friction force* $\mathbf{F}_f$ *on* $\mathcal{P}$*. The experimental results show that during the stick-to-slip transition, the peak values of* $P_n(x, y)$ *tend to shift toward the leading edge. However, in contrast to the fingertip contact [92–94], the magnitude of change of* $P_n(x, y)$ *during stick-to-slip transitions is very limited due to the hollow structure and the relatively smaller friction forces than those in dynamic interactions of rotating tires [87]. Therefore, the change of* $P_n(x, y)$ *under* $\mathbf{F}_f$ *is neglected in the rest of the discussions.*

4.3 Stick-slip analysis, modeling and sensing

4.3.1 Beam-spring network modeling

During stick-to-slip transition, some contact points at certain locations on $\mathcal{P}$ begin deforming and slipping while other points remain sticking to the road. The slipping region grows as the applied force increases. It is difficult to obtain a closed-form formulation of the deformation and force distributions. Instead, a beam-spring network approach is used to integrate that integrates the mass-spring model with the cantilever beam model.

Figure 4.3 illustrates the beam-spring network modeling approach. The contact patch $\mathcal{P}$ is partitioned into N virtual cantilever beams and each of them has a height of $2h$ and a square cross-section with dimension $c \times c$, where c is the side length. Virtual linear springs connect each pair of neighboring beams. The following assumptions are considered: (1) for each beam, elongation and compression are ignored and only the bending deformation is considered, and (2) all the cantilever beams are clamped at one end through the tire inlet fiber layer. The fiber layer is flexible to allow deformation. Although the springs connect each pair of neighboring beams, there is no spatial gap among adjacent beams.

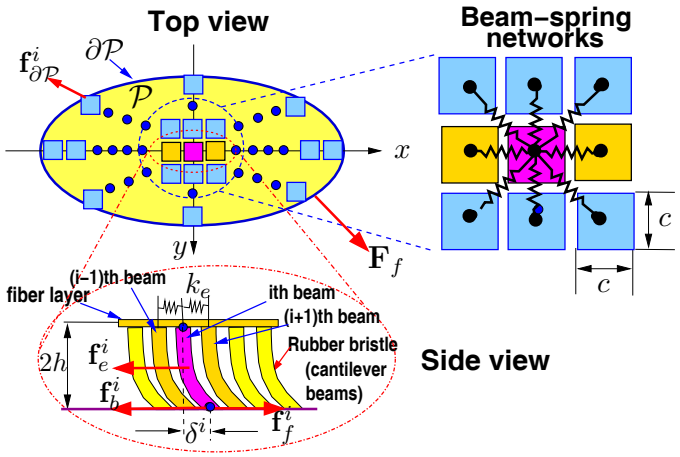

Figure 4.3: A schematic of the hybrid beam-spring network model to capture tire-road stick-slip interaction.

Let $\mathbf{I}_{\mathcal{P}^\circ}$ and $\mathbf{I}_{\partial\mathcal{P}}$ denote the index sets of the beams inside the interior of $\mathcal{P}$ and the beams on the boundary of $\mathcal{P}$, respectively. During stick-to-slip transition, dynamic motions of the beams are negligible. For the ith beam, $i = 1, \cdots, N$, the following force equilibrium is obtained.

$$\begin{cases} \mathbf{f}_f^i + \mathbf{f}_b^i + \mathbf{f}_e^i = 0, & i \in \mathbf{I}_{\mathcal{P}^\circ}, \\ \mathbf{f}_f^i + \mathbf{f}_b^i + \mathbf{f}_e^i + \mathbf{f}_{\partial\mathcal{P}}^i = 0, & i \in \mathbf{I}_{\partial\mathcal{P}}, \end{cases} \tag{4.9}$$

where $\mathbf{f}_f^i$ is the tire contact friction force, $\mathbf{f}_b^i$ is the bending force that captures the shear deformation, $\mathbf{f}_e^i$ is the resultant net elastic force from the connected springs, and $\mathbf{f}_{\partial\mathcal{P}}^i$ is the boundary force from the tire side wall if the beam is on $\partial\mathcal{P}$; see Fig. 4.3. In the following, the calculations of $\mathbf{f}_b^i$, $\mathbf{f}_e^i$, and $\mathbf{f}_{\partial\mathcal{P}}^i$ are presented such that $\mathbf{f}_f^i$ is obtained by (4.9).

Because of relative movements among beams, the resultant elastic force $\mathbf{f}_e^i$ is calculated as

$$\mathbf{f}_e^i = \sum_{j \in \mathcal{N}_i} \mathbf{f}_e^{ij} = \sum_{j \in \mathcal{N}_i} k_e \Delta\mathbf{u}_{ij} = 2Eh \sum_{j \in \mathcal{N}_i} \Delta\mathbf{u}_{ij}, \tag{4.10}$$

where $\mathbf{f}_e^{ij} = k_e \Delta\mathbf{u}_{ij}$ is the spring (elastic) force between the ith beam with its neighboring jth beam, $k_e = 2Eh$ is the spring stiffness coefficient, and $\mathcal{N}_i$ is the index set of all the neighboring beams of the ith beam. Spring deformation

$$\Delta\mathbf{u}_{ij} = (\mathbf{u}_j - \mathbf{u}_i)\left(1 - \frac{\|\mathbf{u}_{j0} - \mathbf{u}_{i0}\|}{\|\mathbf{u}_j - \mathbf{u}_i\|}\right) \tag{4.11}$$

is the relative position change between the ith and the jth beams, where $\mathbf{u}_i$ and $\mathbf{u}_j$ are the position vectors for the ith and jth beams, respectively. In (4.11), $\mathbf{u}_{i0}$ and $\mathbf{u}_{j0}$ are respectively the original position vectors of the ith and jth beams without deformation. Indeed, it is straightforward to obtain

$$\|\mathbf{u}_{j0} - \mathbf{u}_{i0}\| = \begin{cases} \sqrt{2}c & \text{Beams } i \text{ and } j \text{ are diagonal neighbors} \\ c & \text{otherwise.} \end{cases}$$

The virtual cantilever beams are bent under $\mathbf{F}_f$. The tip bending deformation δ_k^i of the ith beam along the k-axis is approximated by [93]

$$\delta_k^i = \frac{P_n^i}{P_n^{ave}} \frac{3\mu F_z}{16 L_k} \frac{2-\nu}{G} \left[1-(1-\psi_k)^{2/3}\right],\ k = x, y, \tag{4.12}$$

where μ is the friction coefficient, P_n^i is the local normal pressure at the ith beam's location, P_n^{ave} is the average normal pressure of $\mathcal{P}$, $\psi_k = \frac{F_{fk}}{\mu F_z}$ is the friction force factor in the k-axis direction. Compared with the model in [93], a normal pressure dependency factor $\frac{P_n^i}{P_n^{ave}}$ is introduced in (4.12) to capture the effect of $P_n(x)$ on δ_k^i. The bending force of the ith beam is then obtained as

$$\mathbf{f}_b^i = k_b \boldsymbol{\delta}^i = \frac{3EI}{(2h)^3} \boldsymbol{\delta}^i, \tag{4.13}$$

where $\boldsymbol{\delta}^i = (\delta_x^i, \delta_y^i)$ is the tip deflection vector of the ith beam, $k_b = \frac{3EI}{(2h)^3}$ is the bending stiffness of the beam.

To compute $\mathbf{f}_f^i$ for $i \in \mathbf{I}_{\mathcal{P}^\circ}$, the Coulomb friction model is adopted. If $|\mathbf{f}_b^i + \mathbf{f}_e^i| < \mu f_z^i$, where $f_z^i = P_n^i c^2$ is the normal force at the tip of the ith beam, the beam is stuck and has no movement. In this case, $\mathbf{f}_f^i$ balances the resultant of $\mathbf{f}_b^i$ and $\mathbf{f}_e^i$. If $|\mathbf{f}_b^i + \mathbf{f}_e^i| \geq \mu f_z^i$, $|\mathbf{f}_f^i| = \mu f_z^i$ cannot fully sustain the resultant of $\mathbf{f}_b^i$ and $\mathbf{f}_e^i$. The beam will slip until the force equilibrium holds again at the new location. $\mathbf{f}_b^i$ is assumed to be saturated when the ith beam slips.

Remark 4.3. *The eight-neighboring-beam topology and the beam's square cross section shown in Fig. 4.3 are chosen because under these configurations, the model represents a structure with an equivalent Poisson's ratio around 0.5 [97], almost the same as the value of rubber $\nu = 0.49$. The number of beams N is important for an accurate beam-spring network model. With a larger N, the model produces more accurate results [97].*

In the above discussion, only the interior beams are considered. For the beams on the boundary $\partial\mathcal{P}$, the same calculation are followed but with additional consideration for boundary force $\mathbf{f}_{\partial\mathcal{P}}^i$. In the next section, the calculation of $\mathbf{f}_{\partial\mathcal{P}}^i$ will be discussed.

4.3.2 Boundary force $\mathbf{f}^i_{\partial\mathcal{P}}$ calculation

By adding all N equations in (4.9) together, the total boundary force $\mathbf{F}_{\partial\mathcal{P}} = \sum_{i\in\mathbf{I}_{\partial\mathcal{P}}} \mathbf{f}^i_{\partial\mathcal{P}}$ is obtained as

$$\mathbf{F}_{\partial\mathcal{P}} = -\mathbf{F}_b - \mathbf{F}_f, \tag{4.14}$$

where

$$\mathbf{F}_b = \sum_{i=1}^{N} \mathbf{f}^i_b \text{ and } \mathbf{F}_f = \sum_{i=1}^{N} \mathbf{f}^i_f, \tag{4.15}$$

where $\mathbf{F}_b$ is total bending force. To obtain (4.14), the fact that total spring force $\mathbf{F}_e = \sum_{i=1}^{N} \mathbf{f}^i_e = \mathbf{0}$ is used since $\mathbf{f}^i_e$s are internal spring forces and their summation is zero.

Figure 4.1(b) illustrates the schematic of the calculation of boundary force $\mathbf{f}^i_{\partial\mathcal{P}}$ of the ith beam at location (x, y) on $\partial\mathcal{P}$. For a given $\mathbf{F}_f$ and F_z, $\mathbf{F}_b$ is calculated by (4.13) and (4.15) and $\mathbf{F}_{\partial\mathcal{P}}$ is then obtained from (4.14). $\mathbf{F}_{\partial\mathcal{P}}$ is further decomposed along the x- and y-axis directions as $F_{\partial\mathcal{P}x}$ and $F_{\partial\mathcal{P}y}$, respectively.

In the following, only the calculation of the x-axis component force $f^i_{\partial\mathcal{P}x}$ of $\mathbf{f}^i_{\partial\mathcal{P}}$ is described and $f^i_{\partial\mathcal{P}y}$ can be obtained similarly. The boundary force $f^i_{\partial\mathcal{P}x}$ is generated through rubber deformation. By symmetry, it is assumed that $F_{\partial\mathcal{P}x}$ is equally distributed on each quarter of the elliptical boundary such that only one quarter of $\partial\mathcal{P}$ with a total boundary force $\frac{1}{4}F_{\partial\mathcal{P}x}$ is considered.

For the boundary point (x, y) shown in Fig. 4.1(b), radius R_{ex} with respect to rotation axis is obtained as $R_{ex} = \sqrt{H^2 + x^2}$. During the stick-to-slip transition, it is assumed that the entire tire/rim structure rotates by an infinitesimal angle $\Delta\theta$. The projected displacement along $\partial\mathcal{P}$ in the xy plane is $\Delta x = R_{ex}\Delta\theta\cos\theta \approx R_{ex}\Delta\theta$ for a small θ. Letting K_s denote the rubber stiffness coefficient, under deformation Δx, the boundary force $f^i_{\partial\mathcal{P}x}$ is then

$$f^i_{\partial\mathcal{P}x} = K_s\Delta x = K_s\Delta\theta\sqrt{H^2 + x^2}. \tag{4.16}$$

Considering that the total boundary force on a quarter of the $\partial\mathcal{P}$ is $\frac{1}{4}F_{\partial\mathcal{P}x}$, it is straightforward to have

$$\frac{1}{4}F_{\partial\mathcal{P}x} = \int_{\partial\mathcal{P}_1} f_{\partial\mathcal{P}x} ds = \int_{\partial\mathcal{P}_1} K_s \Delta\theta \sqrt{H^2 + x^2} ds, \tag{4.17}$$

where s is the arc-length and $\partial\mathcal{P}_1$ is the quarter of $\partial\mathcal{P}$. Noticing that $(ds)^2 = (dx)^2 + (dy)^2$ and that $dy = -\frac{xL_y^2}{yL_x^2}dx$ from the elliptical equation $\frac{x^2}{L_x^2} + \frac{y^2}{L_y^2} = 1$, (4.17) becomes

$$\frac{1}{4}F_{\partial\mathcal{P}x} = \int_0^{L_x} K_s \Delta\theta \sqrt{H^2 + x^2} \sqrt{1 + \left(\frac{xL_y^2}{yL_x^2}\right)^2} dx = K_s \Delta\theta K_x, \tag{4.18}$$

where

$$K_x = \int_0^{L_x} \sqrt{H^2 + x^2} \sqrt{1 + \frac{L_y^2 x^2}{L_x^2(L_x^2 - x^2)}} dx.$$

In the last step of (4.18), the fact that $L_x^2 y^2 = L_y^2(L_x^2 - x^2)$ is used to obtain K_x. Plugging the results (4.18) into (4.16), the final calculation for $f^i_{\partial\mathcal{P}x}$ is obtained as

$$f^i_{\partial\mathcal{P}x} = \frac{\sqrt{H^2 + x^2}}{4K_x} F_{\partial\mathcal{P}x}, \tag{4.19}$$

4.3.3 Computing the deformation and friction force distributions

Using the beam-spring network model, a computational algorithm is presented to simultaneously obtain the tire rubber deformation and the friction force distributions on $\mathcal{P}$. Algorithm 1 illustrates the iteratively computing of deformation distribution $\mathbf{u}$ and friction force $\mathbf{f}_f$ on $\mathcal{P}$. In the algorithm, a variable $\mathbf{A} \in \mathbb{R}^N$ is defined to update the stick ($\mathbf{A}(i) = 1$) or the slip ($\mathbf{A}(i) = 0$) status for the ith beam. An error threshold $E_{thresh} > 0$ is also introduced to terminate the iterations. An updating factor $0 < \eta < 1$ is used to tune the convergence performance. The computation follows the calculations discussed previously and the complexity of the algorithm is $O\left(\frac{1}{\eta}N^2 \log\left(\frac{1}{E_{thresh}}\right)\right)$. Although a Coulomb friction model is used in the algorithm, it can be replaced by other types of friction models to determine the stick-to-slip transition for each beam.

Algorithm 1: Tire stick-slip evolution numerical calculation under $\mathbf{F_f}$.

Initialize: Set normal force f_z^i and original position $\mathbf{u}^i$ for all N beams. Define $\mathbf{A} \in \mathbb{R}^N$ and set $\mathbf{A}(i) = 1$, $\mathbf{F}_f \leftarrow 0$, $\mathbf{f}_b^i \leftarrow 0$, $\mathbf{f}_e^i \leftarrow 0$, $\mathbf{f}_f^i \leftarrow 0$, $i = 1, \cdots, N$;
while $\mathbf{A} \neq \mathbf{0}$ **do**
  $\mathbf{F}_f \leftarrow \mathbf{F}_f + \Delta\mathbf{F}_f$;
  Update $\mathbf{f}_b^i$ and $\mathbf{F}_b$ by (4.13) and (4.15);
  $\mathbf{F}_{\partial\mathcal{P}} \leftarrow -\mathbf{F}_f - \mathbf{F}_b$, update $\mathbf{f}_{\partial\mathcal{P}}^i$ by (4.19);
  Set iteration error indicator $Err \leftarrow 1$;
  while $Err > E_{thresh}$ **do**
    $Err \leftarrow 0$;
    for $i = 1$ *to* N **do**
      Find $\mathcal{N}_i$ and update $\mathbf{f}_e^i$ by (4.10);
      $s_i \leftarrow 0$ if $i \in \mathbf{I}_{\mathcal{P}^\circ}$, or $s_i \leftarrow 1$ if $i \in \mathbf{I}_{\partial\mathcal{P}}$;
      if $\mathbf{A}(i) = 1$ **then**
        if $\|\mathbf{f}_e^i + \mathbf{f}_b^i + s_i\mathbf{f}_{\partial\mathcal{P}}^i\| < \mu f_z^i$ **then**
          $\mathbf{f}_f^i \leftarrow -\mathbf{f}_e^i - \mathbf{f}_b^i - s_i\mathbf{f}_{\partial\mathcal{P}}^i$, $\Delta\mathbf{u}^i \leftarrow 0$;
        else
          $\mathbf{A}(i) \leftarrow 0$, go to Line 9;
        end
      else
        $\mathbf{f}_f^i \leftarrow \mu f_z^i \frac{\mathbf{f}_e^i + \mathbf{f}_b^i + s_i\mathbf{f}_{\partial\mathcal{P}}^i}{\|\mathbf{f}_e^i + \mathbf{f}_b^i + s_i\mathbf{f}_{\partial\mathcal{P}}^i\|}$, $\Delta\mathbf{u}^i \leftarrow \frac{\eta}{4Eh}(\mathbf{f}_e^i + \mathbf{f}_b^i + s_i\mathbf{f}_{\partial\mathcal{P}}^i - \mathbf{f}_f^i)$;
      end
      $\mathbf{u}^i \leftarrow \mathbf{u}^i + \Delta\mathbf{u}^i$, $Err \leftarrow \max(Err, \|\Delta\mathbf{u}^i\|)$;
    end
  end
end

4.4 Embedded tire force sensor

4.4.1 Sensor model

To obtain the multi-directional local friction forces, a PSECR sensor is embedded with a special orientation as shown in Fig. 4.4. If being positioned horizontally, the PSECR sensor is not sensitive to local friction forces on $\mathcal{P}$. Moreover, the PSECR sensor only functions under compressive forces inside the rubber layer and thus, it cannot be placed along the vertical direction since horizontal tensile stresses exist during the stick-to-slip transition. By tilting the sensor at a certain angle, the existence of the

internal compressive normal stress prevents the sensor from exposing to tensile forces.

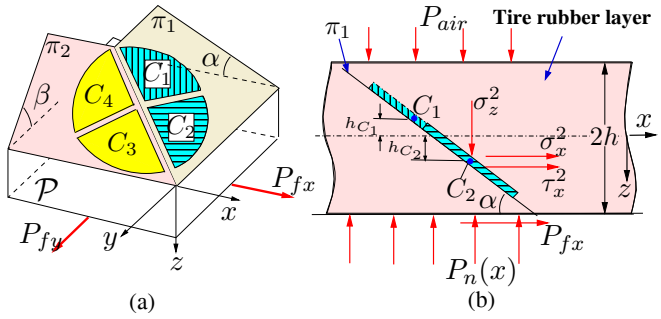

Figure 4.4: Embedded PSECR sensor configuration. (a) Configuration diagrams of the four sensor cells. (b) A side view schematic of the embedded sensor inside the rubber layer.

To extract both the local x- and y-axis directional friction forces, we separate the four sensor cells into two groups: C_1 and C_2 are placed on plane π_1; while C_3 and C_4 lie in plane π_2. The tilting angles of π_1 and π_2 with respect to the x- and y-axis directions are denoted as α and β, respectively.

Let P_{fx} and P_{fy} denote the local friction stresses at location (x, y) on $\mathcal{P}$ along the x- and y-axis directions at the sensor location, respectively; see Fig. 4.4(a). P_{fx} and P_{fy} can be considered as the x- and y-axis components of the spatially normalized friction force $\mathbf{f}_f^i$ given in the beam-spring network model in (4.9); see Fig. 4.3. Due to symmetry of $\mathcal{P}$ and for presentation clarity, we consider locations on $\mathcal{P}$ at the fixed y coordinate (e.g., at the tire center line) and varying x coordinate so that the force variables are only functions of x. Let σ_k^l and τ_k^l denote the normal and shear stresses along the k-axis for C_l, $k = x, y$, $l = 1, 2, 3, 4$, respectively. Note that σ_k^l corresponds to the spring elasticity effect and is considered as the spatially normalized spring force in the beam-spring network model. Similarly, τ_k^l is related to the bending effect at the sensor location. We denote the normal stress along the z-direction at the sensor location as σ_z^l.

Let F_s^l denote the resultant compressive force applied to C_l and V_s^l be its measured output voltage. Then we have $V_s^l = K_l F_s^l$, where K_l, $l = 1, 2, 3, 4$, are the output

gains for sensor cells C_l. The sensor output V_s under P_{fx} and P_{fy} consists of two portions: one portion V_0 is due to the rubber bending and the other portion comes from the existence of σ_k^l and τ_k^l due to the friction forces on $\mathcal{P}$. Thus, output V_s^l can be written as

$$V_s^l = \begin{cases} V_0^l + K_l A_s(-\sigma_x^l + \tau_x^l)\sin\alpha, & l = 1, 2, \\ V_0^l + K_l A_s(-\sigma_y^l + \tau_y^l)\sin\beta, & l = 3, 4, \end{cases} \tag{4.20}$$

where

$$V_0^l = \begin{cases} K_l A_s(-\sigma_z^l \cos\alpha - \sigma_{x0}^l \sin\alpha), l = 1, 2, \\ K_l A_s(-\sigma_z^l \cos\beta - \sigma_{y0}^l \sin\beta), l = 3, 4, \end{cases} \tag{4.21}$$

A_s is the area of each sensor cell, and σ_{x0} and σ_{y0} are the shell-to-plate bending stresses along the x- and y-axis, respectively.

The goal of building a sensor model is to extract P_{fx} and P_{fy} information from measurements V_s^l in (4.20). We first obtain a model for V_0^l. By the assumption of the unchanged length of neutral line during the shell-to-plate bending [103] and considering the thin rubber layer, we estimate

$$\sigma_{x0}^l \approx -\frac{Eh_{C_l}}{R_o - h},\ l = 1, 2, \text{ and } \sigma_{y0}^l \approx -\frac{Eh_{C_l}}{R_c - h},\ l = 3, 4,$$

where h_{C_l} is the z coordinate of cell C_l. To obtain $\sigma_z(z)$, we obtain the following relationship

$$\sigma_z(z) = [P_n(x) - P_{air}]\left(\frac{1}{4h^3}z^3 - \frac{3}{4h}z\right) - \frac{P_n(x) + P_{air}}{2}. \tag{4.22}$$

The derivation of the above equation is given in Appendix D. Combining the above results for σ_{x0}^l, σ_{y0}^l and $\sigma_z^l = \sigma_z(h_{C_l})$ and from (4.21), we obtain V_0^l in (4.20).

We need to build the relationship between σ_k^l, τ_k^l and P_{fx}, P_{fy}. In the following discussion, we only present the development of such relationships for C_1 and C_2 to extract P_{fx} and the similar results can be obtained along the y-axis direction for C_3 and C_4 to obtain P_{fy}.

We denote the spatially normalized net spring force $\mathbf{f}_e^i$ and beam bending force $\mathbf{f}_b^i$ along the x-axis direction as $\sigma_{\mathcal{P}x}$ and $\tau_{\mathcal{P}x}$, respectively. We normalize (4.9) spatially,

take the magnitude of the normalized stress equation along the x-axis direction, and then obtain

$$P_{fx} = \tau_{\mathcal{P}x} + \sigma_{\mathcal{P}x}. \tag{4.23}$$

Notice that $\tau_{\mathcal{P}x}$ corresponds to the shear stress τ_x^l and $\sigma_{\mathcal{P}x}$ is related to the normal stress σ_x^l. Both σ_x^l and τ_x^l can be extracted from the sensor measurements through (4.20) for C_1 and C_2. First, the sensor cells are spatially close each other and in the local area of C_1 and C_2, σ_x^l, $l = 1, 2$, are treated approximately the same because of the small sensor size. Therefore, we have

$$\sigma_x^1 = \sigma_x^2 = \sigma_x. \tag{4.24}$$

To further build the relationship between τ_x^l and $\tau_{\mathcal{P}x}$, we consider that $\tau_{\mathcal{P}x}$ is the boundary shear stress at $z = h$ and τ_x^l, $l = 1, 2$, are the shear stresses at the sensor locations $z_l = h_{C_l}$. We assume that the shear deflection of the rubber layer follows the virtual beam deflection. Using the Euler-Bernoulli beam theory, the deflection $w(z)$ of a cantilever beam under bending force f_{bx} is

$$w(z) = \frac{f_{bx}(z+h)^2(5h-z)}{6EI}$$

and the (maximal) deflection at the tip is $\delta_x = \frac{f_{bx}(2h)^3}{3EI}$. By eliminating f_{bx}, we obtain

$$w(z) = \frac{\delta_x}{16h^3}(-z^3 + 3hz^2 + 9h^2z + 5h^3)$$

and τ_x^l is then calculated by

$$\tau_x^l = G\frac{\partial w(z)}{\partial z}\bigg|_{z=h_{C_l}} = \gamma_l G\frac{\partial w(z)}{\partial z}\bigg|_{z=h} = \gamma_l \tau_{\mathcal{P}x}, \tag{4.25}$$

where $\gamma_l = \frac{1}{4h^2}(-h_{C_l}^2 + 2h_{C_l}h + 3h^2)$, $l = 1, 2$. Eq. (4.25) implies that τ_x^l varies along the z-direction.

Using (4.20), (4.24) and (4.25), we obtain

$$\underbrace{\begin{bmatrix} V_s^1 - V_0^1 \\ V_s^2 - V_0^2 \end{bmatrix}}_{\mathbf{V}} = \underbrace{\begin{bmatrix} -K_1 A_s \sin\alpha & K_1 A_s \gamma_1 \sin\alpha \\ -K_2 A_s \sin\alpha & K_2 A_s \gamma_2 \sin\alpha \end{bmatrix}}_{\mathbf{K}} \underbrace{\begin{bmatrix} \sigma_x \\ \tau_{\mathcal{P}x} \end{bmatrix}}_{\boldsymbol{\sigma}}. \tag{4.26}$$

The coefficient matrix $\mathbf{K}$ is invertible if $\gamma_1 \neq \gamma_2$, that is, C_1 and C_2 are not at the same depth, which is satisfied in the design. σ_x and $\tau_{\mathcal{P}x}$ are then uniquely determined as $\boldsymbol{\sigma} = \mathbf{K}^{-1}\mathbf{V}$. The linear model in (4.26) is derived based on the Euler-Bernoulli beam assumption. Other modeling approaches could lead to the similar conclusion. Instead computing $\mathbf{K}$ in (4.26) from a set of the model parameters, we conduct a calibration process to obtain $\mathbf{K}$ in practice for high accuracy. Therefore, the final results of obtaining coefficient $\mathbf{K}$ are not restricted by knowing the beam model parameters.

We still need to obtain $\sigma_{\mathcal{P}x}$ to calculate P_{fx} by (4.23). We take an empirical approach to calculate $\sigma_{\mathcal{P}x}$: if the sensor lies in the *stick* region, we take the following relationship

$$\sigma_{\mathcal{P}x} = \kappa_x |\sigma_x|^{m_x}, \tag{4.27}$$

where we use the absolute value of σ_x because σ_x can be negative and $\sigma_{\mathcal{P}x}$ is always positive. The coefficients κ_x and m_x are obtained by calibration in experiments. When the sensor lies in the location where the local contact *slips*, $\sigma_{\mathcal{P}x}$ saturates at the value $\sigma^0_{\mathcal{P}x}$. We detect slipping when $\tau_{\mathcal{P}x}$ is saturated and at this moment, we denote $\sigma_x = \sigma^0_x$. Then $\sigma^0_{\mathcal{P}x}$ is calculated by (4.27) for the given σ^0_x.

Summarizing the above discussion, we obtain

$$P_{fx} = \begin{cases} \tau_{\mathcal{P}x} + \sigma_{\mathcal{P}x} & \text{locally stick,} \\ \tau_{\mathcal{P}x} + \sigma^0_{\mathcal{P}x} & \text{locally slip.} \end{cases} \tag{4.28}$$

where $\tau_{\mathcal{P}x}$ and $\sigma_{\mathcal{P}x}$ are respectively obtained by (4.26) and (4.27) with a calibrated PSECR sensor, and $\sigma^0_{\mathcal{P}x} = \kappa_x |\sigma^0_x|^{m_x}$ with σ^0_x is captured by sensor measurements as discussed above.

4.4.2 PSECR sensor calibration and model validation

The sensor calibration processes for the x- and y-direction forces are similar and we here only describe the x-direction case. We first obtain the σ_x measurements right after the sensor is glued on one side inside the tire rubber. We use a force gauge (model FDK

80 from Wagner Inc.) to press on C_1 and C_2 to generate σ_x. Figure 4.6(a) shows the outputs of C_1 and C_2 under various σ_x measurements. The sensor outputs demonstrate a strong linear relationship with σ_x.

After the sensor is completely glued inside the tire, we apply $\tau_{\mathcal{P}x}$ to the local area where the PSECR sensor is embedded using a calibration fixture. The fixture is designed and fabricated with a comparable size to that of the PSECR sensor [102]; see Fig. 4.5. The fixture is directly mounted on the transparent plate of the testing platform; see Fig. 4.11. The use of the calibration fixture guarantees that the friction force lie locally at the location where the sensor is embedded. At this moment, we use a leather coat on the fixture surface to generate high friction forces and prevent the contact from sliding. Therefore, shear force dominates the interaction and we assume that the local friction force P_{fx} is fully contributed by $\tau_{\mathcal{P}x}$. The calibration results with varying $\tau_{\mathcal{P}x}$ are shown in Fig. 4.6(b). A linear relationship between sensor outputs and $\tau_{\mathcal{P}x}$ is clearly obtained, similar to the model prediction by (4.25). Moreover, the results also show that the two sensor cells have different sensitivities to $\tau_{\mathcal{P}x}$, as the model (4.25) predicts due to the different γ_l at locations of C_l, $l = 1, 2$.

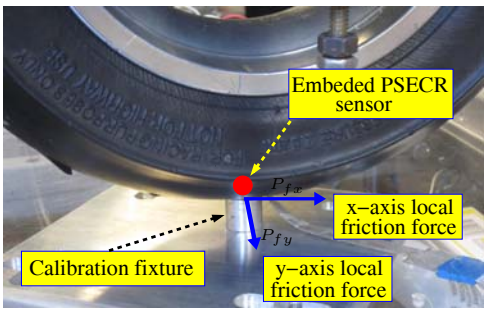

Figure 4.5: The PSECR sensor calibration fixture.

In experiments, multiple repeated calibrations are conducted. Given M_1 measurements of $\boldsymbol{\sigma}_x = (\sigma_x)_{M_1}$ and M_2 measurements of $\boldsymbol{\tau}_{\mathcal{P}x} = (\tau_{\mathcal{P}x})_{M_2}$, we form a stress measurement matrix $\boldsymbol{\sigma}_m \in \mathbb{R}^{2\times(M_1+M_2)}$ and the corresponding sensor output matrix

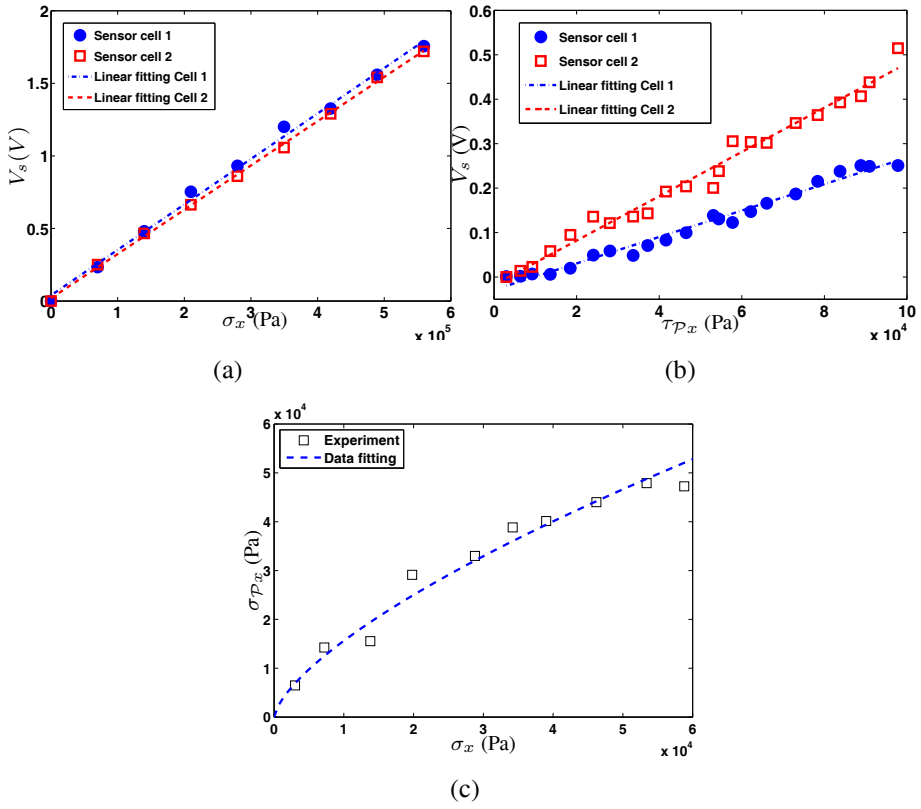

Figure 4.6: Sensor cells C_1 and C_2 calibration results. (a) Sensor output voltage with various σ_x. (b) Sensor output voltage with various $\tau_{\mathcal{P}x}$. (c) Gain κ_x (between $\sigma_{\mathcal{P}x}$ and σ_x) calibration.

$\mathbf{V}_m \in \mathbb{R}^{2\times(M_1+M_2)}$ respectively as

$$\boldsymbol{\sigma}_m = \begin{bmatrix} \boldsymbol{\sigma}_x & \mathbf{0}_{M_2} \\ \mathbf{0}_{M_1} & \boldsymbol{\tau}_{\mathcal{P}x} \end{bmatrix} \text{ and } \mathbf{V}_m = \begin{bmatrix} \boldsymbol{V}_s^1 - \boldsymbol{V}_0^1 \\ \boldsymbol{V}_s^2 - \boldsymbol{V}_0^2 \end{bmatrix},$$

where $\mathbf{0}_M \in \mathbb{R}^{1\times M}$ is the zero row vector. From the relationship $\mathbf{V} = \mathbf{K}\boldsymbol{\sigma}$ in (4.26), we estimate $\mathbf{K}$ in x-direction as

$$\hat{\mathbf{K}}_x = \mathbf{V}_m\boldsymbol{\sigma}_m^+ = \mathbf{V}_m\boldsymbol{\sigma}_m^T(\boldsymbol{\sigma}_m\boldsymbol{\sigma}_m^T)^{-1}, \tag{4.29}$$

where $\boldsymbol{\sigma}_m^+ = \boldsymbol{\sigma}_m^T(\boldsymbol{\sigma}_m\boldsymbol{\sigma}_m^T)^{-1}$ is the pseudo-inverse of $\boldsymbol{\sigma}_m$. The calibration value and

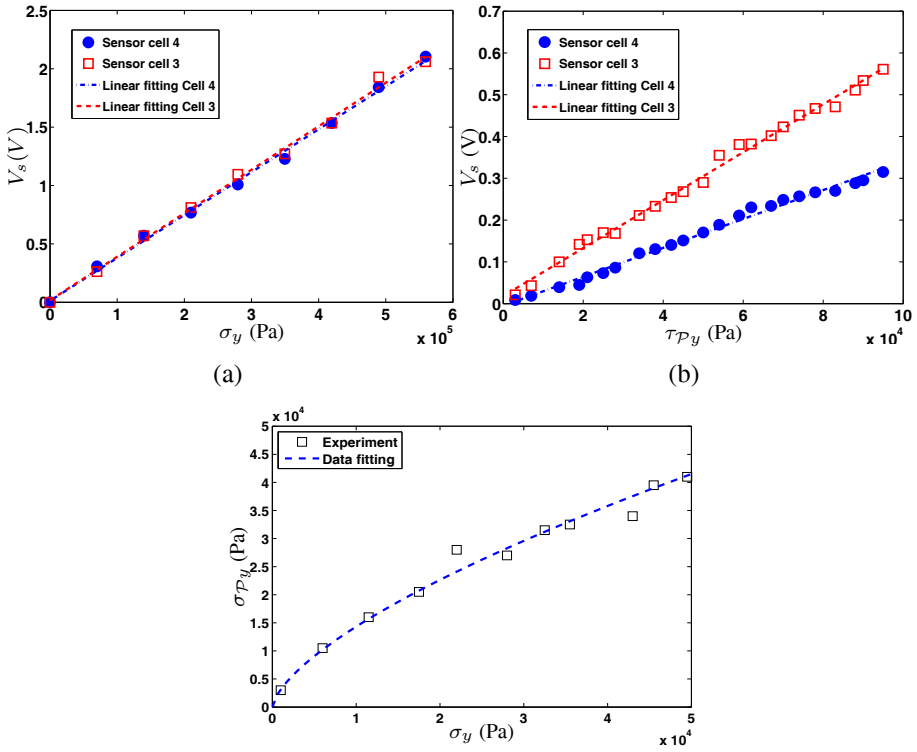

Figure 4.7: Sensor cells C_3 and C_4 calibration results. (a) Sensor output voltage with various σ_y. (b) Sensor output voltage with various $\tau_{\mathcal{P}y}$. (c) Gain κ_y (between $\sigma_{\mathcal{P}y}$ and σ_y) calibration.

the standard error of the estimated $\mathbf{K}_x$ are respectively as

$$\hat{\mathbf{K}}_x = \begin{bmatrix} -3.01 & 2.73 \\ -3.02 & 4.84 \end{bmatrix} \text{ V/MPa}$$

and

$$\hat{\boldsymbol{\sigma}}_{\mathbf{K}_x} = \begin{bmatrix} 0.09 & 0.18 \\ 0.10 & 0.23 \end{bmatrix} \text{ V/MPa.}$$

By substituting $\hat{\mathbf{K}}_x$ into the sensor output model, we then calibrate coefficients κ_x and m_x in (4.27) with measurements σ_x and $\sigma_{\mathcal{P}x}$, where $\sigma_{\mathcal{P}x} = P_{fx} - \tau_{\mathcal{P}x}$ and P_{fx} is obtained again from the calibration fixture without the leather coat; See Fig. 4.5. Fig. 4.6(c) shows the calibration curve. The calibration values of estimated κ_x and m_x

are $\hat{\kappa}_x = 29.74$ and $\hat{m}_x = 0.68$, respectively. The standard errors of estimated κ_x and m_x are $\hat{\sigma}_{\kappa_x} = 1.97$ and $\hat{\sigma}_{m_x} = 0.01$, respectively.

Similar calibration process is conducted for the y-direction force sensor cells C_3 and C_4. The calibration results are shown in Fig. 4.7 and the calibration coefficients in the y-direction are

$$\hat{\mathbf{K}}_y = \begin{bmatrix} -3.32 & 2.97 \\ -3.33 & 5.03 \end{bmatrix} \text{ V/MPa}, \ \hat{\kappa}_y = 32.40 \ \text{ and } \ \hat{m}_y = 0.66,$$

respectively. The standard errors for estimated $\mathbf{K}_y$, κ_y and m_y are respectively as

$$\hat{\boldsymbol{\sigma}}_{\mathbf{K}_y} = \begin{bmatrix} 0.13 & 0.22 \\ 0.11 & 0.24 \end{bmatrix} \text{ V/MPa}, \ \hat{\sigma}_{\kappa_y} = 1.91 \ \text{ and } \ \hat{\sigma}_{m_y} = 0.01.$$

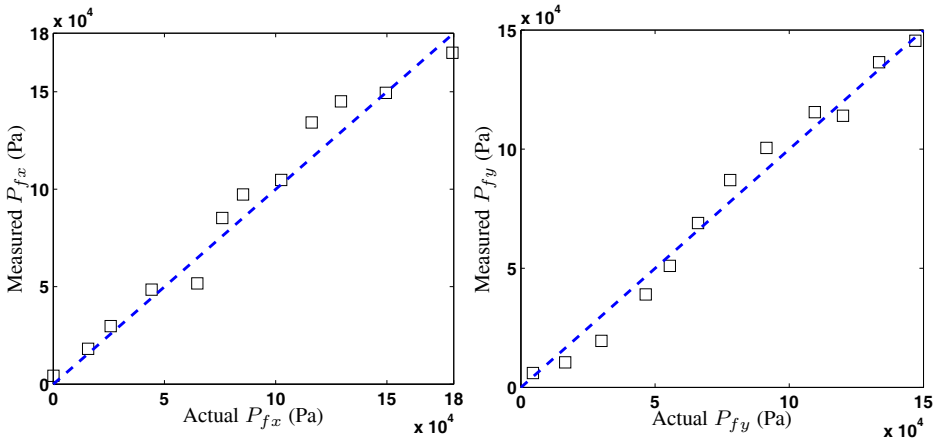

(a) (b)

Figure 4.8: Friction force measurement validations. (a) P_{fx} measurements. (b) P_{fy} measurements.

To validate the sensor model, we conduct multiple repeated validation tests by varying P_{fx} and P_{fy} at the sensor location and then compare with the sensor measurements. Figure 4.8 shows the comparison results for both P_{fx} and P_{fy} in one validation test. The root mean square differences are 1.1×10^4 Pa (for the x-direction stress) and 0.9×10^4 Pa (for the y-direction stress). Figure 4.9 shows the statistical errors of the

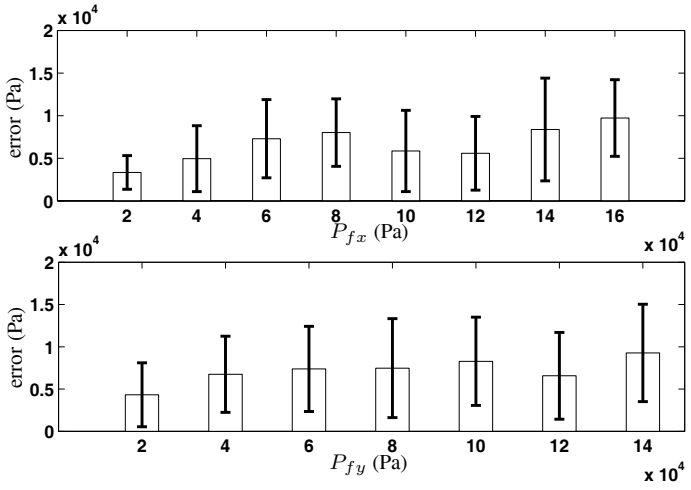

Figure 4.9: The statistical mean errors and their standard deviations of sensor measurements.

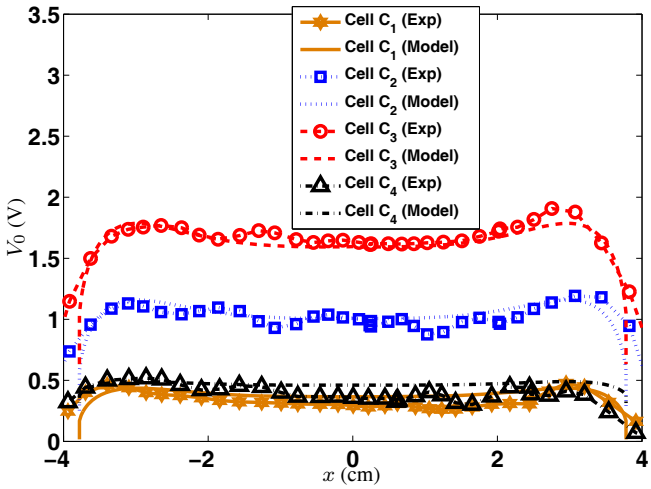

Figure 4.10: Comparison of the prediction of the static bending stress (represented by V_0) with the experiments.

multiple validation tests. The maximum errors are consistently less than 1.5×10^4 Pa in both the x- and y-directions. We also compare the measured voltage V_0 with the model prediction (4.21) as shown in Fig. 4.10. The values for the V_0 model parameters are listed in Table 4.2. The model predictions show a clear agreement with the experiments for V_0.

Table 4.1: PSECR sensor and tire parameters

E(MPa)	R_o(m)	h(mm)	A_s(cm^2)	K_1(V/N)	K_2(V/N)	K_3(V/N)	K_4(V/N)
11.7	0.128	3.5	0.16	0.56	0.54	0.53	0.53

4.5 Experiments

In this section, the experiments are presented to demonstrate the models and analysis of tire-road stick-slip interactions discussed in the previous sections.

4.5.1 "Smart tire" test platform

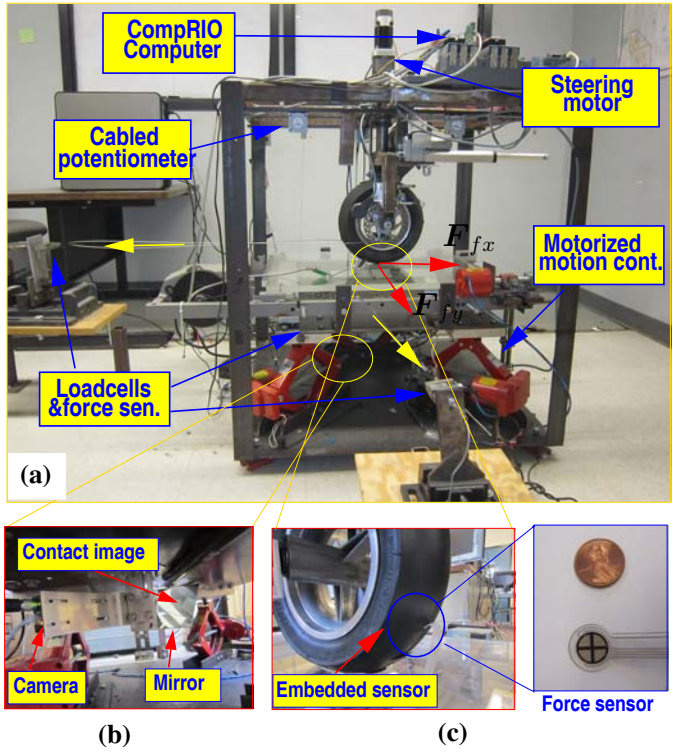

Figure 4.11: "Smart tire" test platform prototype with embedded force sensors and vision-based tire deformation measurement systems. (a) The entire system. (b) Camera system setup for deformation measurement. (c) Embedded tire force sensor.

Figure 4.11 shows the "smart tire" test platform developed at Rutgers University. A treadmill is modified to act as a support foundation for the testing tire in the design.

The treadmill belt is removed and replaced by a thick transparent plate to represent the road surface. The plate is supported by three individually computer-controlled electric jacks. Three cable potentiometers (from Celesco Transducer Products, Inc.) are used to feedback the positions and the tilting angles of the plate. Three load cells (from Transducer Techniques Inc.) are positioned under the supporting plate to measure the total normal load between the tire and the plate. A feedback controller is designed to take the load cell's readings and regulate the normal load by raising/lowering the motorized jacks. To generate friction forces along the x- and y-axis directions, the tire and the plate are respectively pulled by two steel cables, one for the longitudinal (x-axis) direction and the other for the lateral (y-axis) direction. The total friction forces F_{fx} and F_{fy} are measured respectively by two force sensors (from Transducer Technique Inc.) as shown in Fig. 4.11.

The PSECR sensor (from Pongpara Codan Rubber Technology Company, Thailand) is shown in Fig. 4.11(c). The circular PSECR sensor is around 12-mm in diameter and is flexible. To measure the tire rubber deformation on the contact patch, we use a high-resolution camera (CM-080GE camera from Teledyne DALSA Inc., 1032 $\times$ 778 pixels, 30 fps) to capture images of white dots (Fig. 4.2(a)) painted on the tire surface through the transparent supporting plate; see Fig. 4.11(b). The image acquisition, camera calibration, and image processing are implemented through the National Instrument (NI) Vision Development Module (VDM). The entire system is controlled through a real-time NI CompactRIO embedded system. More details about the setup can be found in [102].

4.5.2 Tire contact normal pressure experiments

A set of the PSECR sensors are placed on the treadmill surface to measure $P_n(x)$ along the tire center line. Figure 4.12 shows comparison results between the prediction of the model and the experimental data. The parameters used in the model are listed

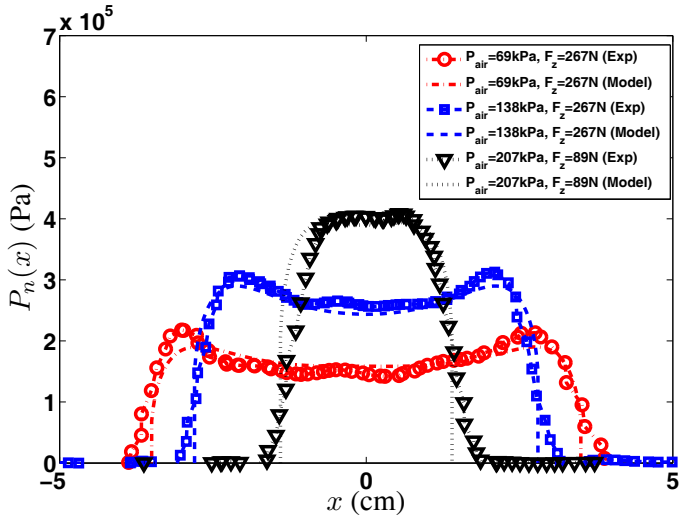

Figure 4.12: Comparison of the model prediction and experiments of the tire-road contact normal load distribution $P_n(x)$.

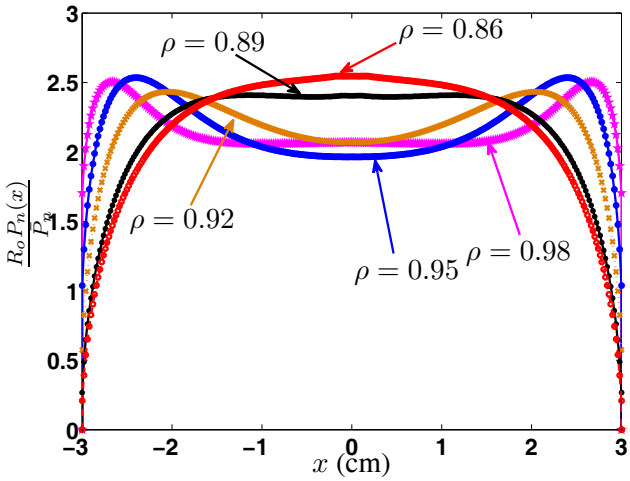

Figure 4.13: Normalized contact pressure distribution $P_n(x)$ with respect to $\bar{P}_n = \int_{-L_x}^{L_x} P_n(x)dx$ under various tire rubber layer thicknesses ρ, P_{air}=69 kPa.

in Table 4.2. Parameter θ_0 in the normal pressure model cannot be directly measured and it is tuned empirically. The model predications match experiments under various P_{air} and F_z. It is noted that although the simple torus-shape tire is used in this study, as shown in Fig. 4.12 and in [102], the normal contact pressure distribution follows the similar pattern as those obtained by using actual automobile tires reported in [87, 88].

One advantage of the analytical model over the empirical model in [102] is that

the former can be used to predict $P_n(x)$ under variations of physical parameters, while the empirical model cannot. For example, Fig. 4.13 shows the normalized $P_n(x)$ under varying tire rubber layer thicknesses. For tires with a thin rubber layer, $\rho = R_i/R_o \to 1$ and a thick layer, ρ is small. It is clearly shown in Fig. 4.13 that for tires with thin rubber layers (e.g., $\rho > 0.9$), the bending effect dominates the pressure distribution and the pressure peaks lie close to the contact edge, while for tires with thick rubber layers (e.g., $\rho = 0.86$), $P_n(x)$ follows the Hertzian contact with the highest pressure around the center of $\mathcal{P}$. These results explain the observed differences between the tire-road contact and these in fingertip contact reported in [92–94].

Table 4.2: Beam-spring tire model parameters

E (MPa)	G (MPa)	ν	μ	θ_0 (deg)	R_o (m)	c (cm)	h (cm)	N
11.7	3.9	0.49	0.7	45	0.128	0.2	0.35	591

4.5.3 Stick-to-slip transition experiments

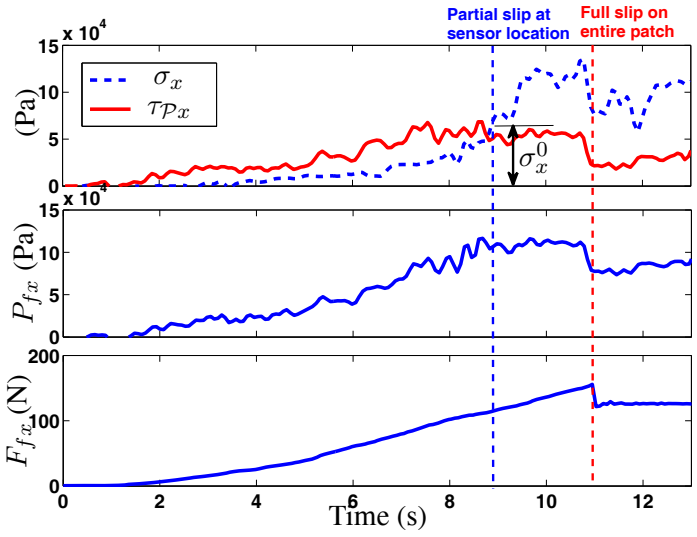

Figure 4.14: The PSECR sensor measurements and stress estimation at the sensor location during the stick-to-slip transition.

To observe stick-to-slip transition and friction force evolutions for the points on $\mathcal{P}$,

the tire is rotated and the sensor is placed at around the middle point between the trailing edge and the center of $\mathcal{P}$. An increasing F_{fx} is generated until the tire completely slips at around $F_{fx} = 160$ N. Figure 4.14 shows the local friction force measurements at the PSECR sensor location during the stick-to-slip transition. Shear stress $\tau_{\mathcal{P}x}$ starts to increase with the increasing F_{fx}. Once the partial slip at the sensor location starts around $t = 8.8$ s, $\tau_{\mathcal{P}x}$ stops increasing and keeps constant. This observation agrees with the previously discussed friction model in which P_{fx} saturates when the partial slip starts. The observation of the saturated $\tau_{\mathcal{P}x}$ is used to predict the moment when the partial slip happens at the sensor location. We estimate $\sigma_x^0 = 6 \times 10^4$ Pa and therefore, $\sigma_{\mathcal{P}x}^0 = \kappa_x |\sigma_x^0|^{m_x} = 5.27 \times 10^4$ Pa.

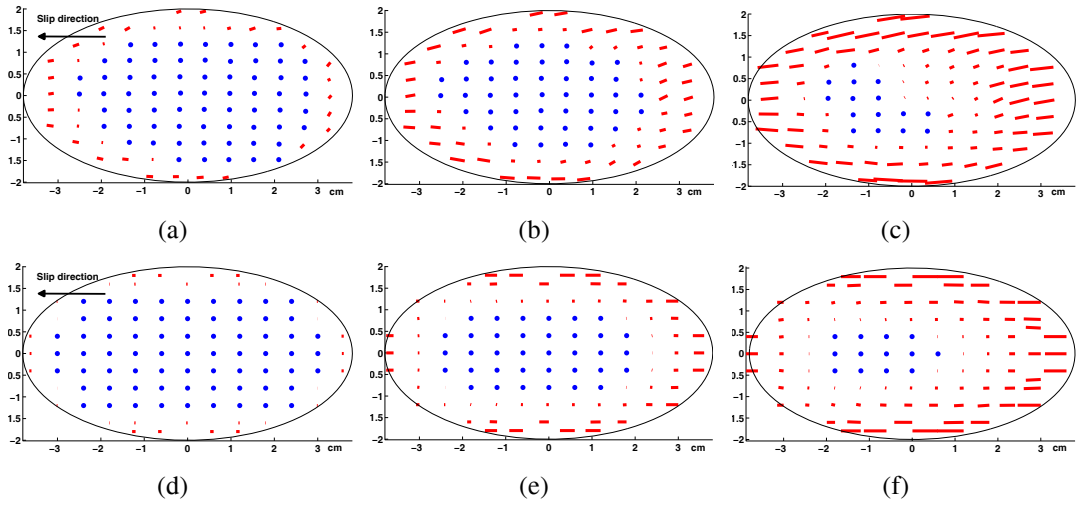

Figure 4.15: Deformation distribution (in cm) on $\mathcal{P}$ with various friction forces F_{fx}. The blue dots indicate stick point and the red bars indicate slipping displacements. The elliptical contour indicates the contact patch $\mathcal{P}$ and the plotting deformations are magnified five times for clear presentation. Vision-based experiments: (a) $F_{fx} = 44.5$ N. (b) $F_{fx} = 89$ N. (c) $F_{fx} = 133.5$ N. Numerical computation: (d) $F_{fx} = 44.5$ N. (e) $F_{fx} = 89$ N. (f) $F_{fx} = 133.5$ N.

After the partial slip starts, σ_x keeps increasing with the increasing F_{fx} and the slip region moves towards the interior area of $\mathcal{P}$. The middle plot of Fig. 4.14 shows the local friction stress P_{fx} from the calibrated PSECR sensor. When the full slip of the entire patch starts around $t = 11$ s, $\tau_{\mathcal{P}x}$ and P_{fx} drop rapidly. The timing ($t = 8.8$

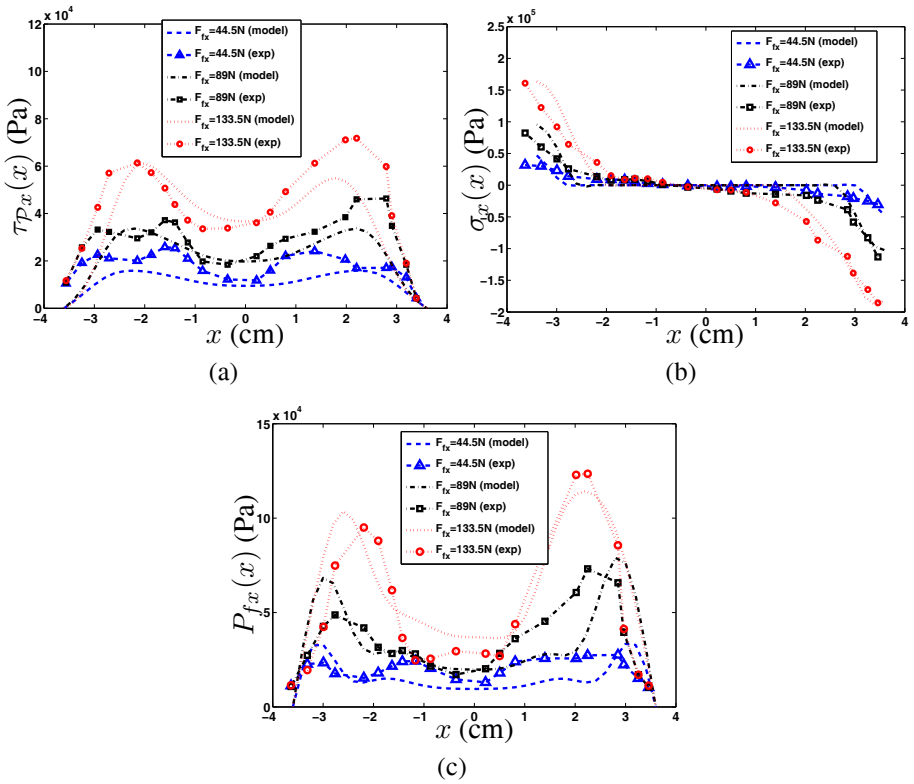

Figure 4.16: Comparison results between model prediction and sensor measurements of stress distributions on $\mathcal{P}$ under various friction forces F_{fx}. (a) $\tau_{\mathcal{P}x}(x)$. (b) $\sigma_x(x)$. (c) $P_{fx}(x)$.

s) to determine the partial slip depends on the relative sensor location on $\mathcal{P}$, while the timing of the full slip of $\mathcal{P}$ ($t = 11$ s) is determined by the magnitude of F_{fx}. These observations fit the previously discussed analysis.

4.5.4 Rubber deformation and friction force distributions

The experiments of obtaining rubber deformation and friction force distributions are conducted under $P_{air} = 69$ kPa and $F_z = 267$ N. The camera image is used to obtain the rubber deformation on $\mathcal{P}$. Figure 4.15 shows the rubber deformation distribution results under F_{fx}. In the figure, the blue dots indicate the sticking points and the red bars represent the displacements of slipping points on $\mathcal{P}$. Both the vision-based

experiments and the computational results show consistent trends. During the stick-to-slip transition, the rubber deformations grow with the increasing F_{fx}. The points on $\partial\mathcal{P}$ start slipping first and then the slipping region propagates to the center portion of $\mathcal{P}$. It is interesting to note that the last portion to slip is not exactly the geometry center of $\mathcal{P}$ but the location close to the trailing edge.

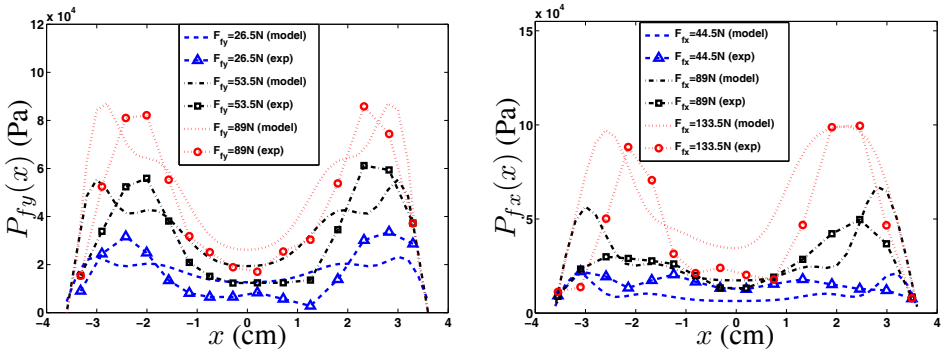

Figure 4.17: (a) Comparison results between model prediction of $P_{fy}(x)$ distribution and sensor measurements under various friction forces F_{fy} along the center line. (b) Comparison of friction force distribution $P_{fx}(x)$ under a combined F_{fx} and $F_{fy} = 89$N.

To study the local friction force distributions during the stick-slip transition, scanning experiments are conducted by moving the embedded sensor at various locations along the tire center line (i.e., fixed $y = 0$). At a given location x, both the local longitudinal and lateral friction stresses $P_{fx}(x)$ and $P_{fy}(x)$ exist. The first set of scanning experiments are conducted under only F_{fx} and in this case, $P_{fy}(x) = 0$ along the center line due to the symmetry. Figs. 4.16(a) and 4.16(b) show the comparison results between the model predictions and the experiments for $\tau_{\mathcal{P}x}(x)$ and $\sigma_x(x)$, respectively. The results demonstrate a clear agreement between the model predictions and the experiments. As shown in Fig. 4.16(a), the distribution of $\tau_{\mathcal{P}x}(x)$ is not uniform on $\mathcal{P}$ and indeed has a similar pattern to the distribution of $P_n(x)$. The results in Fig. 4.16(b) show that $\sigma_x(x)$ has larger values close to $\partial\mathcal{P}$ than those around the center of $\mathcal{P}$. The sign of $\sigma_x(x)$ has changed: at the leading edge the rubber is under compression (i.e.,

negative $\sigma_x(x)$), while at the trailing edge portion it is under elongation (i.e., positive $\sigma_x(x)$). This phenomenon also matches the rubber deformation distribution shown in Fig. 4.15. Figure 4.16(c) shows the matching friction stress $P_{fx}(x)$ along the center line of $\mathcal{P}$ between the model predictions and the experiments.

Figure 4.17(a) shows the consistently matching results between the model predictions and the experiments for $P_{fy}(x)$ along the center line of $\mathcal{P}$ under only friction force F_{fy}. Similar to $P_{fx}(x)$ under F_{fx}, the results of $P_{fy}(x)$ under F_{fy} show a two-peak distribution pattern. Finally, the experiments are conducted to obtain the local fricton force distribution $P_{fx}(x)$ along the x-axis direction under the existence of both F_{fx} and F_{fy}. Figure 4.17(b) shows the comparison results of $P_{fx}(x)$. In the scanning experiments, constant $F_{fy} = 89$ N are applied. These results confirm a similar distribution pattern to that under only applying F_{fx}.

4.5.5 Discussions

The distributions $P_{fx}(x)$ and $P_{fy}(x)$ in Figs. 4.16(c) and 4.17 demonstrate a similar two-peak trend as $P_n(x)$ shown in Fig. 4.12 for the case of $P_{air} = 69$ kPa and $F_z = 267$ N. To determine whether the friction force distribution completely follows the distribution of $P_n(x)$, $P_{fx}(x)$ is computed under a single-peak $P_n(x)$ distribution by using parameter $\rho = 0.86$. Figure 4.18 shows the evolution of $P_{fx}(x)$ distributions under increasing F_{fx}. It is interesting to see that with increasing F_{fx}, the evolution of the distribution of $P_{fx}(x)$ changes its shape: at the beginning of the stick-to-slip transition, the $P_{fx}(x)$ distributions show a two-peak pattern; see the case of $F_{fx} = 40, 80$, or 110 N. However, when the full slip starts on $\mathcal{P}$, that is, the case of $F_{fx} = 135$ N, $P_{fx}(x)$ follows the single-peak shape, similar to that of $P_n(x)$.

From the above comparison results, it is concluded that the local friction force distribution is indeed a resultant of both the tire thin layer structure and the normal force

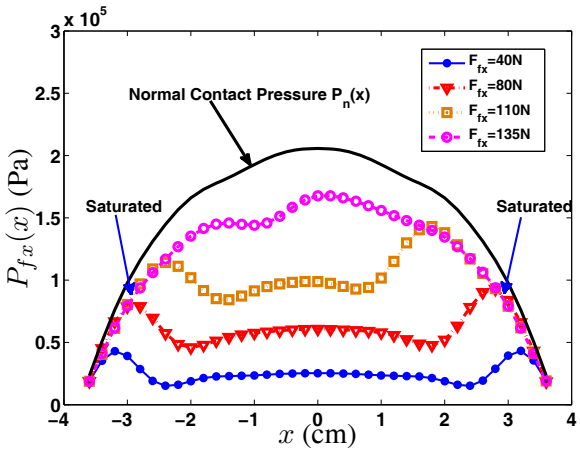

Figure 4.18: Friction force distribution $P_{fx}(x)$ along the tire center line under a single-peak normal force distribution $P_n(x)$.

distribution. Because of the thin layer structure, when F_{fx} is small, the boundary portion of $\mathcal{P}$ starts slipping and $P_{fx}(x)$ reaches their saturation values. That is the reason why a two-peak shape of $P_{fx}(x)$ distribution appears at the beginning of the partial slip stage. With an increasing F_{fx}, the entire patch is about to slip, and the $P_{fx}(x)$ distribution follows the $P_n(x)$ distribution due to the kinetic friction relationship, i.e., $P_{fx}(x) = \mu P_n(x)$ at $-L_x \leq x \leq L_x$. Therefore, during the stick-to-slip transition, the friction force distribution evolutes from the two-peak shape to the shape of the normal pressure distribution.

Compared with the experimental results, some discrepancies exist in the prediction results of both the normal contact pressure model and the stick-slip model. These differences mainly come from several sources: first, the tire-road contact is more complicated than what the models capture in this work. The imperfect models leads to some prediction errors. For example, the rubber has the hyper-elasticity property and both the normal pressure model and stick-slip model do not incorporate such characteristics. In stick-slip experiments, due to the physical constraints, the sensor is not installed at the optimal orientation for superior sensitivity [99]. Finally, the limited force measurement accuracy of the low-cost PSECR sensor also lead to measurement errors [99].

4.6 Conclusion

In this chapter, modeling, analysis and sensing of tire-road stick-slip interactions were presented. The presented modeling and analyses were validated through the developed "smart tire" test platform with the embedded PSECR tire force sensor. A beam-spring network model was proposed to capture the evolution of the complex stick-to-slip transition on the tire contact patch. The predictions of the model showed good agreements with the experiments for both the rubber deformation and the local friction force distributions. The results demonstrated that the rubber deformation propagates from the boundary to the center of the contact patch during the stick-to-slip transition. Moreover, the local friction force distribution on the contact patch was determined by both the normal force distribution and the thin layer structure properties.

Chapter 5

Rider-Bicycle Pose Estimation with Fusion of Force/Inertial Sensors

5.1 Introduction

From this chapter on, we take the rider's effect in consideration in the HME modeling and control frame. We first propose a pose estimation scheme of the rider-bicycle system based on the fusion for force/inertial sensors. Pose and gait estimation not only benefits clinical analysis and diagnosis [104], but also provides tools to understand human sensorimotor mechanisms and their interactions within HME systmes. Human pose estimation in physical human-machine interactions such as bicycling is challenging because of the highly-dimensional human movement and the dynamic interactions with machines. Further challenges arise in lack of effective, non-intrusive motion sensors in natural environment.

Existing motion capture systems, such as optical-, acoustic-, or magnetic-based tracking systems, are limited to indoor usage within a confined space and cannot be used for tracking human movement in natural environment. Wearable sensors have been extensively used for human pose and gait estimation [105]. For example, estimations of human upper-limb orientations were discussed in [50, 55, 106, 107]. The work in [56, 57, 108–110] discuss the lower-limb pose estimation. Some other work discuss general human segment pose measurement [49, 52–54]. Most of the abovementioned work focus on human walking, standing, or reaching activities, and there is few work that discusses the human motion and pose estimation in highly-skilled human-machine

interactions such as bicycling. The goal of this work is to develop an estimation scheme for the rider trunk pose and the bicycle roll angle using inertial and force sensors.

Human bicycling motor skill is chosen as a pose estimation application for several reasons. Unlike commonly studied walking or stance where the human-environment interaction is only through the ground contact, the rider-bicycle interactions are through multiple contacts at the handlebar, the seat and the pedals. The multi-contact interactions bring complexity but also provide new features for pose estimation. Sitting on the unstable platform, riders have to actively react to the sensory feedback through body movement for balancing. Bicycles provide a unique platform for studying coupled human sensorimotor functions with machines. Finally, the recent clinical studies demonstrate promising results of treating Parkinson's disease patients through bicycle riding [2–4]. Bicycles can be further developed and used as a postural rehabilitation device.

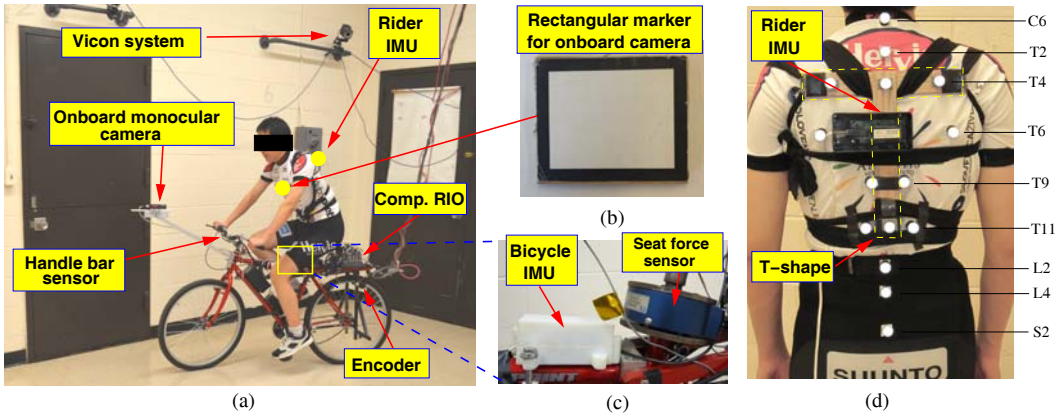

Figure 5.1: (a) The instrumented bicycle. (b) Rectangular marker for outdoor use. (c) Bicycle IMU and seat force sensor. (d) Locations of the IMU and optical markers mounted on rider trunk.

Because of small size, low cost and low power consumption, MEMS-based inertial sensors such as accelerometers, gyroscopes, or inertial measurement units (IMU) are widely used as wearable sensors for human motion and gait estimation. The orientation or the position of a body segment can be obtained by integration of gyroscope or

acceleration signals. However, the results of such strapdown IMU integration have severe drifting problem due to the sensor measurement biases and noises. To overcome this problem, other complementary sensors are usually fused with inertial sensors to eliminate the drifting effect. For example, inclinations are estimated by accelerometer measurements and then integrated with gyroscope measurements in [49, 50]. In [51], ultrasonic sensors are attached on human body to provide positioning information. In [52–54], magnetic sensors are used as an attitude reference to constrain the drift growth and to provide the initial estimates in the filter design. However, the above-mentioned sensor fusion schemes have various limitations. Accelerometer-based inclination can generate large measurement errors for dynamic activities, ultrasonic sensors potentially suffer from the line-of-sight restriction, and magnetic sensors are vulnerable to magnetic disturbances in environment. Human anatomical constraints are also used to enhance the fusion accuracy [55]. In [56], multiple accelerometers are used to estimate the gait without directly integrating IMU measurements. For walking gait estimation, a "resetting" technique is used in [57, 58] to initialize the integration at the beginning of each stride.

In this chapter, we fuse the force sensors with the IMUs to overcome the drifting issue in integration of the inertial measurements. Unlike magnetic and ultrasonic sensors, the force sensors are reliable and robust to environmental disturbances and do not have the line-of-sight restriction. The fusions of force and inertial sensors have been used to measure the interaction kinetics between human and environment [111–114]. However, the work in [111–114] use the force and inertial sensors to obtain kinetic measurements and none of them uses the force measurements to enhance the pose estimation. Unlike in walking or stance, pose estimation in bicycling has different features. The rider sits on a moving platform and the measurements from wearable IMUs contain motion information of both the rider and the bicycle. Multiple IMUs are needed and analyses have to be conducted to decouple the IMU measurements. A trunk-bicycle

dynamic model is used to reveal the underlying dynamic relationship between the inertial and force measurements. We present extensive experiments to demonstrate the drift-free and robust performance of the pose estimation design.

The main contributions of this work are twofold. First, the pose estimation scheme relies only on the wearable sensors and the onboard sensors and therefore, it aims for human pose and gait studies in daily surroundings rather than in restrictive indoor environment. The use of the inertial/force sensors fusion is novel and provides reliable and robust estimates of human pose under dynamic motions. Second, the new dynamic model captures the rider-bicycle motion characteristics and bridges the human motion kinematics with the driving force measurements. The modeling framework provides a new approach to potentially study other types of human-machine interactions.

5.2 Instrumented bicycle and riding experiments

Figure 5.1(a) shows the instrumented bicycle. The bicycle is modified from a commercial mountain bike and equipped with various sensors. The bicycle is designed for both indoor and outdoor experiments. A force/torque sensor (from JR3 Inc.) is installed along the seat supporting rod to measure the 3-axis hip-seat forces and torques; see Fig. 5.1(c). Three load cells are installed inside the customly-built bicycle seat to measure the sitting force distribution (Fig. 5.3). An optical encoder is used to measure the bicycle speed. A set of stain gauges are installed on the bicycle handlebar to measure the handlebar forces. A real-time embedded system (CompactRIO 9074 from National Instruments Inc.) samples and stores all sensor measurements at the frequency of 50 Hz, a maximum sampling frequency that can be achieved by the given hardware capability.

Two IMU units (model 605 from Motion Sense Inc. [1]) are used: one IMU is

[1] http://www.motionsense.com/.

mounted to the bicycle frame (Fig. 5.1(c)) and the other one is rigidly attached to a T-shape fixture at level T6 on the back of the rider trunk. The T-shape fixture spans levels T4 to T11; see Fig. 5.1(d). Each IMU consists of a tri-axial gyroscope and a tri-axial accelerometer. Similar to [115–117], we assume the rigid-body movement of the trunk and we will discuss this assumption in Section 5.8. The direction of the spinal segment from levels T4 to T11 is used to represent the human trunk orientation.

For indoor experiments, a vision-based motion capture system (from Vicon Inc.) is used to provide the ground truth for the trunk and bicycle poses. The Vicon system includes 8 Botina cameras, MX Giganet module, and a workstation computer with Nexus 1.6 motion capture software. For outdoor experiments, the ground truth of the bicycle attitude angles is obtained by a high accuracy IMU (model 800 from Motion Sense Inc., 0.3-degree attitude accuracy). The trunk pose with respect to the bicycle is obtained by an onboard high-resolution monocular camera with a rectangular-shape feature marker; see Fig. 5.1(b). The camera (Manta G-145 from Allied Vision Technologies, 1392$\times$1040 pixels, 16 fps) is mounted on an extended rod that is rigidly connected to the bicycle frame. The details of the camera-based pose calculation are given in [118]. The motion capturing systems are synchronized with the onboard sensors through the wireless network connections.

In experiments, the subjects are asked to ride the bicycle at their own riding styles. For indoor experiments, due to spatial constraints, the subjects are asked to ride the bicycle for a circular trajectory (with radius around 2.5 m). For outdoor experiments, the subjects arbitrarily ride the bicycle in an area of a size of 50$\times$40 m^2. The ground is paved with bricks in outdoor experiment.

5.3 IMU model

Figure 6.1 illustrates a schematic of the kinematic rider-bicycle interactions. The rider's trunk is modeled as an inverted pendulum in the three-dimensional (3D) space.

The bicycle roll and yaw angles are denoted as φ_b and ψ, respectively.

The IMU on the bicycle frame is tilted by angle α with respect to the x_b-axis. Let $\mathcal{I}_h$ and $\mathcal{I}_b$ denote the rider and bicycle IMU frames, respectively. The orientation of the trunk is defined by three Euler angles with the X-Y-X ordered rotation from $\mathcal{R}$ to $\mathcal{N}_h$: roll angle φ_h around the x-axis, angle θ around the y-axis, and finally self-spinning angle ϕ around the x-axis. The generalized coordinates for the trunk and the bicycle are denoted as $\boldsymbol{q}_h = [\varphi_h\ \theta\ \phi]^T$ and $\boldsymbol{q}_b = [\varphi_b\ \psi]^T$, respectively. We also define $\boldsymbol{q} = [\boldsymbol{q}_h^T\ \boldsymbol{q}_b^T]^T$.

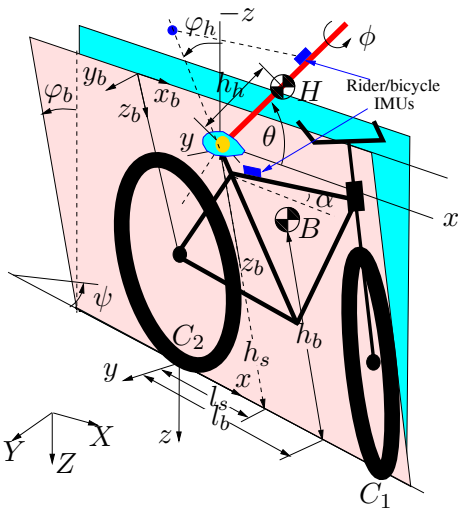

Figure 5.2: Schematic of the rider-bicycle system.

5.3.1 Gyroscope model

The bicycle IMU gyroscope measurements $\boldsymbol{\omega}_b = [\omega_{bx}\ \ \omega_{by}\ \ \omega_{bz}]^T$ are calculated as

$$\boldsymbol{\omega}_b = \boldsymbol{R}_y^T(\alpha)\boldsymbol{R}_x^T(\varphi_b)\begin{bmatrix}0\\0\\\dot{\psi}\end{bmatrix} + \boldsymbol{R}_y^T(\alpha)\begin{bmatrix}\dot{\varphi}_b\\0\\0\end{bmatrix}, \tag{5.1}$$

where $\boldsymbol{R}_i(\beta)$ represents the 3D rotational matrix around the i-axis with angle β, $i = x, y, z$ [2]. To obtain the rider IMU gyroscope model, we consider the transformation from $\mathcal{R}$ to $\mathcal{I}_h$ and the rider IMU gyroscope measurements $\boldsymbol{\omega}_h = [\omega_{hx} \;\; \omega_{hy} \;\; \omega_{hz}]^T$ are then calculated as

$$\boldsymbol{\omega}_h = \boldsymbol{R}_x^T(\phi)\boldsymbol{R}_y^T(\theta)\begin{bmatrix}\dot{\varphi}_h\\0\\0\end{bmatrix} + \boldsymbol{R}_x^T(\phi)\begin{bmatrix}0\\\dot{\theta}\\0\end{bmatrix} + \begin{bmatrix}\dot{\phi}\\0\\0\end{bmatrix}$$
$$+\boldsymbol{R}_x^T(\phi)\boldsymbol{R}_y^T(\theta)\boldsymbol{R}_x^T(\varphi_h)\begin{bmatrix}0\\0\\\dot{\psi}\end{bmatrix}. \tag{5.2}$$

Combining (5.1) and (5.2) and solving for $\dot{\boldsymbol{q}}_b$ and $\dot{\boldsymbol{q}}_h$, we obtain

$$\dot{\boldsymbol{q}}_b = \boldsymbol{e}(\boldsymbol{q}_b;\boldsymbol{\omega}_b) = \begin{bmatrix}\mathrm{c}_\alpha & 0 & \mathrm{s}_\alpha\\ -\frac{\mathrm{s}_\alpha}{\mathrm{c}_{\varphi_b}} & 0 & \frac{\mathrm{c}_\alpha}{\mathrm{c}_{\varphi_b}}\end{bmatrix}\boldsymbol{\omega}_b, \tag{5.3}$$

$$\dot{\boldsymbol{q}}_h = \boldsymbol{f}(\boldsymbol{q};\boldsymbol{\omega}_h,\boldsymbol{\omega}_b) = \begin{bmatrix}0 & \frac{\mathrm{s}_\phi}{\mathrm{s}_\theta} & \frac{\mathrm{c}_\phi}{\mathrm{s}_\theta}\\ 0 & \mathrm{c}_\phi & -\mathrm{s}_\phi\\ 1 & -\frac{\mathrm{c}_\theta}{\mathrm{s}_\theta}\mathrm{s}_\phi & -\frac{\mathrm{c}_\theta}{\mathrm{s}_\theta}\mathrm{c}_\phi\end{bmatrix}\boldsymbol{\omega}_h + \begin{bmatrix}\frac{\mathrm{s}_\alpha\,\mathrm{c}_\theta\,\mathrm{c}_{\varphi_h}}{\mathrm{c}_{\varphi_b}\,\mathrm{s}_\theta} & 0 & -\frac{\mathrm{c}_\alpha\,\mathrm{c}_\theta\,\mathrm{c}_{\varphi_h}}{\mathrm{c}_{\varphi_b}\,\mathrm{s}_\theta}\\ \frac{\mathrm{s}_\alpha\,\mathrm{s}_{\varphi_h}}{\mathrm{c}_{\varphi_b}} & 0 & -\frac{\mathrm{c}_\alpha\,\mathrm{s}_{\varphi_h}}{\mathrm{c}_{\varphi_b}}\\ -\frac{\mathrm{s}_\alpha\,\mathrm{c}_{\varphi_h}}{\mathrm{c}_{\varphi_b}\,\mathrm{s}_\theta} & 0 & \frac{\mathrm{c}_\alpha\,\mathrm{c}_{\varphi_h}}{\mathrm{c}_{\varphi_b}\,\mathrm{s}_\theta}\end{bmatrix}\boldsymbol{\omega}_b \tag{5.4}$$

where notations $\mathrm{c}_{\varphi_h} = \cos\varphi_h$, $\mathrm{s}_{\varphi_h} = \sin\varphi_h$ are used for angle φ_h and any other angles.

[2] The details of the definition and formulation of the standard rotational matrices can be found in [119] (e.g., p. 31) and we omit here.

$$\boldsymbol{a}_b = \begin{bmatrix} \mathrm{c}_\alpha\,\dot{v}_b + (\mathrm{c}_\alpha\,\mathrm{c}_{\varphi_b}\,p_z - \mathrm{s}_\alpha\,\mathrm{c}_{\varphi_b}\,p_x)\dot{\psi}\dot{\varphi}_b + (\mathrm{s}_\alpha\,\mathrm{s}^2_{\varphi_b}\,p_z - \mathrm{c}_\alpha\,p_x)\dot{\psi}^2 + \mathrm{s}_\alpha\,p_z\dot{\varphi}_b^2 \\ +(\mathrm{c}_\alpha\,\mathrm{s}_{\varphi_b}\,p_z + \mathrm{s}_\alpha\,\mathrm{s}_{\varphi_b}\,p_x)\ddot{\psi} - \mathrm{s}_\alpha\,\mathrm{c}_{\varphi_b}\,g, \\ \mathrm{c}_{\varphi_b}\,\mathrm{s}_{\varphi_b}\,p_z\dot{\psi}^2 + \mathrm{c}_{\varphi_b}\,p_x\ddot{\psi} - p_z\ddot{\varphi}_b + \mathrm{s}_{\varphi_b}\,p_x\dot{\psi}\dot{\varphi}_b + \mathrm{s}_{\varphi_b}\,g, \\ \mathrm{s}_\alpha\,\dot{v}_b + (\mathrm{s}_\alpha\,\mathrm{c}_{\varphi_b}\,p_z + \mathrm{c}_\alpha\,\mathrm{c}_{\varphi_b}\,p_x)\dot{\psi}\dot{\varphi}_b - (\mathrm{c}_\alpha\,\mathrm{s}^2_{\varphi_b}\,p_z + \mathrm{s}_\alpha\,p_x)\dot{\psi}^2 - \mathrm{s}_\alpha\,p_z\dot{\varphi}_b^2 + \\ (\mathrm{s}_\alpha\,\mathrm{s}_{\varphi_b}\,p_z - \mathrm{c}_\alpha\,\mathrm{s}_{\varphi_b}\,p_x)\ddot{\psi} + \mathrm{c}_\alpha\,\mathrm{c}_{\varphi_b}\,g \end{bmatrix} \tag{5.6}$$

5.3.2 Accelerometer model

The position of the bicycle IMU in $\mathcal{B}$ is denoted as $\boldsymbol{r}_{bI} = [p_x \quad 0 \quad -p_z]^T$, where p_x and p_z are the horizontal and vertical distances from the IMU to C_2, respectively. Considering the nonholonomic constraint at C_2, the acceleration of C_2 in $\mathcal{R}$ is ${}^{\mathcal{R}}\dot{\boldsymbol{v}}_{C_2} = [\dot{v}_b \quad 0 \quad g]^T$, where g is the gravitational constant and v_b is the bicycle velocity. The angular velocity of the bicycle in $\mathcal{R}$ is ${}^{\mathcal{R}}\boldsymbol{\omega}_b = [\dot{\varphi}_b \quad 0 \quad \dot{\psi}]^T$. The bicycle IMU accelerometer measurements $\boldsymbol{a}_b = [a_{bx} \;\; a_{by} \;\; a_{bz}]^T$ in $\mathcal{I}_b$ are then calculated as

$$\boldsymbol{a}_b = {}^{\mathcal{R}}_{\mathcal{I}_b}\boldsymbol{R}^T \left[{}^{\mathcal{R}}\dot{\boldsymbol{v}}_{C_2} + {}^{\mathcal{R}}\boldsymbol{\omega}_b \times {}^{\mathcal{R}}\boldsymbol{\omega}_b \times {}^{\mathcal{R}}_{\mathcal{B}}\boldsymbol{R}\boldsymbol{r}_{bI} + {}^{\mathcal{R}}\dot{\boldsymbol{\omega}}_b \times {}^{\mathcal{R}}_{\mathcal{B}}\boldsymbol{R}\boldsymbol{r}_{bI} \right], \tag{5.5}$$

where ${}^{\mathcal{R}}_{\mathcal{B}}\boldsymbol{R} = \boldsymbol{R}_x(\varphi_b)$ and ${}^{\mathcal{R}}_{\mathcal{I}_b}\boldsymbol{R}^T = \boldsymbol{R}_y^T(\alpha)\boldsymbol{R}_x^T(\varphi_b)$ are the rotational matrices from $\mathcal{R}$ to $\mathcal{B}$ and $\mathcal{I}_b$, respectively. The calculation of $\boldsymbol{a}_b$ is given in (5.6) on the top of this page. Notice that the coefficients of $\ddot{\psi}$ in a_{bx} and a_{bz} are near zero when φ_b is around zero. We take an approximation that during typically bicycle riding, the average value of $\ddot{\varphi}_b$ is around zero, i.e., $\ddot{\varphi}_b \approx 0$. From a_{by} in (5.6), we then obtain

$$\ddot{\psi} = \frac{a_{by}}{p_x\,\mathrm{c}_{\varphi_b}} - \frac{\mathrm{s}_{\varphi_b}\,p_z}{p_x}\dot{\psi}^2 - \frac{\mathrm{s}_{\varphi_b}}{\mathrm{c}_{\varphi_b}}\dot{\psi}\dot{\varphi}_b - \frac{\mathrm{s}_{\varphi_b}\,g}{\mathrm{c}_{\varphi_b}\,p_x}. \tag{5.7}$$

Let $\boldsymbol{r}_s = [l_s \;\; 0 \;\; -h_s]^T$ denote the seat position in $\mathcal{B}$, where l_s and l_s are the horizontal and vertical distances from the seat to C_2, respectively; see Fig. 6.1. To make calculation tractable, the angular velocity of rider's trunk in $\mathcal{R}$ is approximated as ${}^{\mathcal{R}}\boldsymbol{\omega}_h = [\dot{\varphi}_h \;\; \mathrm{c}_{\varphi_h}\,\dot{\theta}\;\dot{\psi} + \mathrm{s}_{\varphi_h}\,\dot{\theta}]^T$. Let $\boldsymbol{r}_{hI} = [h \;\; 0 \;\; 0]^T$ denote the position of the rider

$$\begin{bmatrix} \ddot{\varphi}_h \\ \ddot{\theta} \end{bmatrix} = \begin{bmatrix} \frac{1}{\mathrm{s}_\theta\, h} a_{hy} + \mathrm{s}_{\varphi_h}\, \mathrm{c}_{\varphi_h}\, \dot{\psi}^2 + \mathrm{c}_{\varphi_h}\, \dot{\psi}\dot{\theta} - \mathrm{s}_{\varphi_h}\, \frac{\mathrm{c}_\theta}{\mathrm{s}_\theta} \dot{\varphi}_h \dot{\psi} - \frac{\mathrm{c}_\theta}{\mathrm{s}_\theta} \dot{\varphi}_h \dot{\theta} - \mathrm{c}_{\varphi_h}\, \frac{\mathrm{c}_\theta}{\mathrm{s}_\theta} \ddot{\psi} - \frac{\mathrm{c}_{\varphi_h}}{\mathrm{s}_\theta\, h} a_{sy} \\ -\frac{\mathrm{s}_{\varphi_h}}{\mathrm{s}_\theta\, h} a_{sz} \\ -\frac{a_{hz}}{h} - \mathrm{c}_{\varphi_h}\, \dot{\varphi}_h \dot{\psi} + 2\, \mathrm{c}_{\varphi_h}\, \mathrm{c}_\theta^2\, \dot{\varphi}_h \dot{\psi} - \mathrm{s}_\theta\, \mathrm{c}_\theta\, \mathrm{c}_{\varphi_h}^2\, \dot{\psi}^2 + \mathrm{s}_\theta\, \mathrm{c}_\theta\, \dot{\varphi}_h^2 - \mathrm{s}_{\varphi_h}\, \ddot{\psi} + \frac{\mathrm{s}_\theta\, a_{sx}}{h} \\ -\frac{\mathrm{c}_\theta\, \mathrm{s}_{\varphi_h}\, a_{sy}}{h} + \frac{\mathrm{c}_{\varphi_h}\, a_{sz}\, \mathrm{c}_\theta}{h} \end{bmatrix} \tag{5.8}$$

IMU in $\mathcal{I}_h$ with respect to the seat, where h is the distance from the rider IMU to the seat. Similar to (5.5), we obtain the seat acceleration ${}^{\mathcal{R}}\boldsymbol{a}_s = [a_{sx} \;\; a_{sy} \;\; a_{sz}]^T$ in $\mathcal{R}$ and the rider IMU accelerometer measurements $\boldsymbol{a}_h = [a_{hx} \;\; a_{hy} \;\; a_{hz}]^T$ are then calculated using ${}^{\mathcal{R}}\boldsymbol{a}_s$. Similar to (5.7), we obtain the attitude acceleration formulation in (5.8) on the top of this page by using acceleration $\boldsymbol{a}_h$.

With the results in (5.7) and (5.8), the IMU accelerometer measurements $\boldsymbol{a}_h$ and $\boldsymbol{a}_b$ are used to provide the attitude accelerations $\ddot{\varphi}_h$, $\ddot{\theta}$ and $\ddot{\psi}$ in the EKF design in Section 5.6.

5.4 Rider-bicycle dynamic model

Let $\boldsymbol{\rho}_B = [l_b \;\; 0 \;\; -h_b]^T$ denote the position of bicycle mass center B in $\mathcal{B}$, where l_b and h_b are the horizontal and the vertical distances from C_2 to B, respectively. The trunk mass is denoted as m_h at H; see Fig. 6.1. The distance between H and the seat is denoted as h_h. Using the Lagrange's equations, we obtain the human driving torque

$$\boldsymbol{\tau}_h = \begin{bmatrix} \tau_{\varphi_h} \\ \\ \tau_\theta \end{bmatrix} = \boldsymbol{M}\ddot{\boldsymbol{q}}_h + \boldsymbol{C}(\boldsymbol{q}, \dot{\boldsymbol{q}}, \ddot{\boldsymbol{q}}_b) + \boldsymbol{G}, \tag{5.9}$$

where τ_{φ_h} and τ_θ are the driving torques along the x-axis (φ_h) and the y'-axis (θ) directions in $\mathcal{R}$, respectively. The y'-axis is obtained from the y-axis by rotating φ_h about the x-axis. A brief derivation of (5.9) and matrices $\boldsymbol{M}$, $\boldsymbol{C}(\boldsymbol{q}, \dot{\boldsymbol{q}}, \ddot{\boldsymbol{q}}_b)$ and $\boldsymbol{G}$ are

given in Appendix F.

5.5 Force/torque sensor model

We designed and fabricated a special seat as shown in Fig. 5.3. Three load cells are used to calculate the location of the center of pressure (CoP) of the hip-seat interaction force. In this section, we discuss how to use the force sensor measurements to obtain driving torque $\boldsymbol{\tau}_h$ in (5.9).

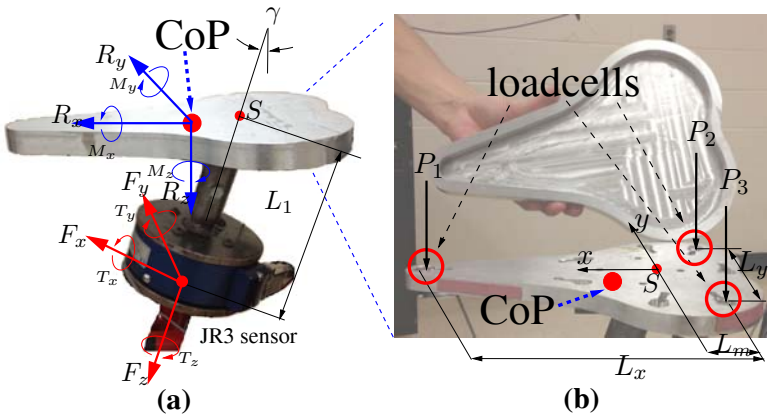

Figure 5.3: (a) A schematic of bicycle seat forces/torques and the transformation. (b) The CoP calculations through three load cell-measured forces.

A seat frame $\mathcal{S}_t$ is defined as the same orientation of $\mathcal{B}$ with the origin S at the intersection of seat rod and the seat surface; see Fig. 5.3(a). Let $\boldsymbol{R}_h = [R_x \ R_y \ R_z]^T$ and $\boldsymbol{M}_h = [M_x \ M_y \ M_z]^T$ denote the hip-seat forces (acting at the CoP) and torques in $\mathcal{S}_t$, respectively. Let $\boldsymbol{F}_s = [F_x \ F_y \ F_z]^T$ and $\boldsymbol{T}_s = [T_x \ T_y \ T_z]^T$ denote the forces and torques measured by the JR3 sensor in sensor frame $\mathcal{S}_r$, respectively. Considering the transformation between frames $\mathcal{S}_t$ and $\mathcal{S}_r$, we obtain

$$\begin{bmatrix} \boldsymbol{R}_h \\ \boldsymbol{M}_h \end{bmatrix} = \begin{bmatrix} {}^{\mathcal{S}_t}_{\mathcal{S}_r}\boldsymbol{R} & \boldsymbol{0} \\ \boldsymbol{S}({}^{\mathcal{S}_t}\boldsymbol{r}_c){}^{\mathcal{S}_t}_{\mathcal{S}_r}\boldsymbol{R} & {}^{\mathcal{S}_t}_{\mathcal{S}_r}\boldsymbol{R} \end{bmatrix} \begin{bmatrix} \boldsymbol{F}_s \\ \boldsymbol{T}_s \end{bmatrix}, \tag{5.10}$$

where ${}^{\mathcal{S}_t}_{\mathcal{S}_r}\boldsymbol{R} = \boldsymbol{R}_y(\gamma)$ is the rotational matrix from frames $\mathcal{S}_t$ to $\mathcal{S}_r$ and γ is the tilting angle of the supporting rod. The skew-symmetric matrix $\boldsymbol{S}({}^{\mathcal{S}_t}\boldsymbol{r}_c)$ is defined by ${}^{\mathcal{S}_t}\boldsymbol{r}_c =$

$[-x_C + L_1\,\mathrm{s}_\gamma \quad -y_C \quad L_1\,\mathrm{c}_\gamma]^T$ (the position vector of the force sensor with respect to the CoP in $\mathcal{S}_t$), L_1 is the distance between S and the JR3 sensor, and (x_C, y_C) is the coordinate of the CoP in $\mathcal{S}_t$. Letting P_i, $i = 1, 2, 3$, denote the measurements of the three load cells, (x_C, y_C) is then calculated by

$$x_C = \frac{P_1}{P_1 + P_2 + P_3} L_x - L_m,\ y_C = \frac{P_2 - P_3}{2(P_1 + P_2 + P_3)} L_y,$$

where L_x and L_y are the x- and y-axis directional distances between the front and rear load cells, respectively, and L_m is the x-axis distance between S and rear two load cells.

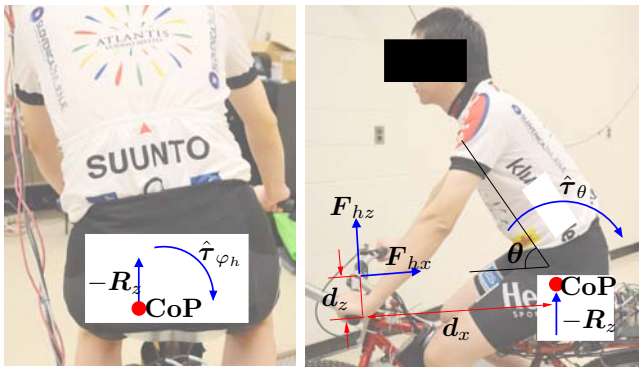

(a) (b)

Figure 5.4: Rider trunk driving forces and torques. (a) τ_{φ_h} calculation. (b) τ_θ calculation.

Table 5.1: Model parameters in inertial/force sensors fusion

α (deg)	γ (deg)	g (m/s^2)	l_s (m)	h_s (m)	l_b (m)	h_b (m)	p_x (m)	p_z (m)	L_1 (m)	L_x (m)	L_y (m)	L_m (m)
10	20	9.8	0.26	0.38	0.45	0.66	0.37	0.71	0.13	0.2	0.12	0.043

To capture the sitting position variations among different riders, we define the CoP location $\boldsymbol{r}_V = [x_V, y_V]^T$ in $\mathcal{S}_t$ when the trunk is upright. Vector $\boldsymbol{r}_V$ is obtained for each subject in experiments. As shown in Fig. 5.4(a), along the φ_h direction the torque applied on the trunk is the sum of the measured M_x and the torque generated by the

reacting force R_z. Thus, we obtain the estimate of τ_{φ_h} as

$$\hat{\tau}_{\varphi_h} = -M_x - R_z(y_C - y_V). \tag{5.11}$$

Along the θ direction, the handlebar forces also contribute to torque τ_θ that drives the trunk motion (Fig. 5.4(b)). Neglecting the arms dynamics, the estimated torque $\hat{\tau}_\theta$ is approximated as

$$\hat{\tau}_\theta = \frac{-M_y + F_{hx}d_z + F_{hz}d_x - R_z(x_C - x_V)}{\mathrm{c}_{\varphi_b - \varphi_h}}, \tag{5.12}$$

where F_{hx} and F_{hz} are the resultant handlebar reaction forces along the x_b-axis and the z_b-axis directions, respectively, and d_x and d_z are the the horizontal and vertical distances from the handlebar to the seat, respectively. Finally, similar to the results in [117], bicycle roll angle φ_b is estimated as

$$\hat{\varphi}_b = \tan^{-1}\left(\frac{R_y}{R_z}\right). \tag{5.13}$$

5.6 Extended Kalman filter (EKF) design

Figure 5.5 illustrates the EKF design structure. The EKF system equations are built on the IMU gyroscope model with a bias model that will be discussed later in this section. The rider-bicycle dynamic model is used as output equations to bridge the EKF state variables with the force sensor model. The IMU accelerometer model provides the attitude acceleration calculations to the rider-bicycle dynamic model.

A first-order random walk is considered for modeling the measurement bias only for the rider IMU gyroscope. If we consider the bias model for the both IMU gyroscopes, the EKF system becomes unobservable and the EKF convergence cannot be guaranteed. Let $\boldsymbol{n}_h$ and $\boldsymbol{n}_b$ denote the measurement noises for the rider and bicycle IMU gyroscopes, respectively. Then, we have the noise model [120]

$$\boldsymbol{n}_h = \boldsymbol{c_h} + \boldsymbol{b} + \boldsymbol{\nu}_h,\ \boldsymbol{n}_b = \boldsymbol{c_b} + \boldsymbol{\nu}_b, \tag{5.14}$$

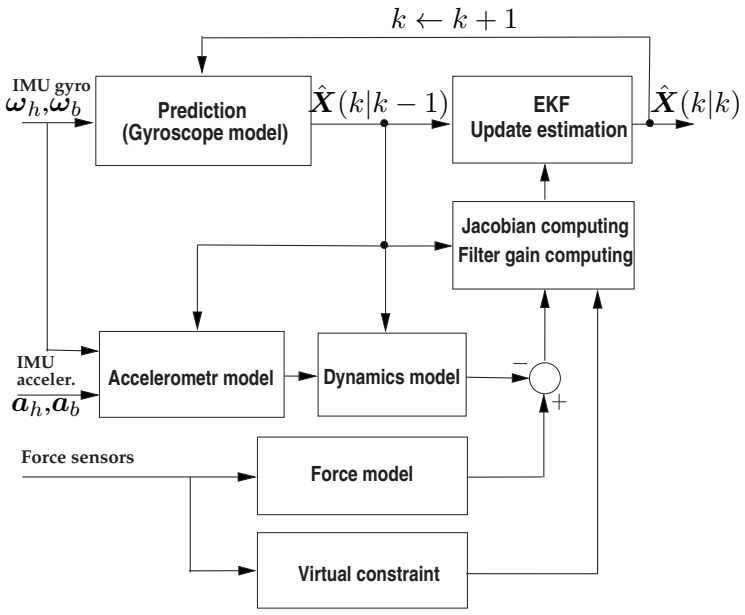

Figure 5.5: The structural and information flow diagram of the EKF design.

where $\boldsymbol{c}_h$ and $\boldsymbol{c}_b$ are the constant offset biases and obtained in experiments, and $\boldsymbol{\nu}_h$ and $\boldsymbol{\nu}_b$ are assumed to be the zero-mean white noise vectors. Vector $\boldsymbol{b} = [b_x \; b_y \; b_z]^T$ is the random walk bias with the model

$$\dot{b}_i = -\frac{1}{\tau_i} b_i + \sqrt{\frac{2 f_s \sigma_i^2}{\tau_i}} w_i, \quad i = x, y, z, \tag{5.15}$$

where τ_i are the time constants, f_s is the sampling frequency, $\sigma_i^2 = E[b_i^2]$, and $w_i \sim \mathcal{N}(0, 1)$ are zero-mean white noises with unit variances.

We define the discrete-time EKF state variables as

$$\boldsymbol{X}(k) = [\varphi_h(k) \; \theta(k) \; \phi(k) \; \varphi_b(k) \; b_x(k) \; b_y(k) \; b_z(k)]^T$$

and

$$\boldsymbol{f}_x(\boldsymbol{X}(k), \boldsymbol{u}(k)) = \begin{bmatrix} \boldsymbol{f}(\boldsymbol{q}(k); \boldsymbol{u}(k)) \\ e_1(\boldsymbol{X}(k); \boldsymbol{\omega}_b(k)) \\ -\frac{1}{\tau_x} b_x(k) \\ -\frac{1}{\tau_y} b_y(k) \\ -\frac{1}{\tau_z} b_z(k) \end{bmatrix},$$

where $\boldsymbol{u}(k) = [\boldsymbol{\omega}_h^T(k) \;\; \boldsymbol{\omega}_b^T(k)]^T$ are the IMU gyroscope measurements at the kth step, $\boldsymbol{f}(\boldsymbol{q}(k); \boldsymbol{u}(k)) = \boldsymbol{f}(\boldsymbol{q}(k); \boldsymbol{\omega}_h(k) - \boldsymbol{b}(k) - \boldsymbol{c}_h, \boldsymbol{\omega}_b(k) - \boldsymbol{c}_b)$ is given in (5.4) and $e_1(\boldsymbol{X}(k); \boldsymbol{\omega}_b(k))$ is the first element of $\boldsymbol{e}(\boldsymbol{q}_b; \boldsymbol{\omega}_b)$ in (5.3). We obtain the EKF state dynamics

$$\boldsymbol{X}(k) = \boldsymbol{X}(k-1) + \Delta T \boldsymbol{f}_x \left(\boldsymbol{X}(k-1), \boldsymbol{u}(k-1) \right), \tag{5.16}$$

where $\Delta T = 20$ msec is the sampling period. The values of the rider-bicycle systems and the bias model parameters are listed in Table 5.1.

For EKF outputs, we obtain the estimated torques $\hat{\tau}_{\varphi_h}$ and $\hat{\tau}_\theta$ in (5.11) and (5.12) and the estimated bicycle roll angle $\hat{\varphi}_b$ in (5.13). Moreover, the experiments show that the rider always tries to keep his/her shoulder level during bicycle riding. Therefore, a level-shoulder constraint among the trunk orientation angles is then used as a virtual measurement, namely,

$$s_c = \mathrm{s}_{\varphi_h} \mathrm{c}_\phi + \mathrm{c}_{\varphi_h} \mathrm{c}_\theta \mathrm{s}_\phi = 0. \tag{5.17}$$

Thus, including the above physical and virtual measurements, we have the EKF output

equation

$$\boldsymbol{y}(k) = \boldsymbol{h}(\boldsymbol{X}(k)) + \boldsymbol{n}_y(k) = \begin{bmatrix} \tau_{\varphi_h}(k) \\ \tau_\theta(k) \\ \varphi_b(k) \\ s_c(k) \end{bmatrix} + \boldsymbol{n}_y(k). \tag{5.18}$$

The first two elements of $\boldsymbol{h}(\boldsymbol{X}(k))$ are calculated by (5.9) and $\boldsymbol{n}_y(k) \sim \mathcal{N}(\boldsymbol{0}, \boldsymbol{\Sigma}_y)$ is the white noise vector with variance matrix $\boldsymbol{\Sigma}_y$.

An EKF design is applied to the system (5.16) and (5.18). For the state dynamics (5.16), we obtain the Jacobian matrix $\boldsymbol{F}(k)$ as

$$\boldsymbol{F}(k) = \boldsymbol{I}_7 + \Delta T \boldsymbol{F}_X(k),$$

where $\boldsymbol{I}_n$ is $n \times n$ identity matrix and $\boldsymbol{F}_X(k) = \left.\frac{\partial \boldsymbol{f}_x}{\partial \boldsymbol{X}}\right|_{\boldsymbol{X}(k),\boldsymbol{u}(k)}$. The final result for $\boldsymbol{F}_X(k)$ is given as

$$\boldsymbol{F}_X(k) = \begin{bmatrix}
\frac{\mathrm{c}_\theta\, \mathrm{s}_{\varphi_h}(-\mathrm{s}_\alpha\, \omega_{bx} + \mathrm{c}_\alpha\, \omega_{bz})}{\mathrm{s}_\theta\, \mathrm{c}_{\varphi_b}} & \frac{\dot{\phi} - \omega_{hx}}{\mathrm{s}_\theta} & \frac{\mathrm{c}_\phi\, \omega_{hy} - \mathrm{s}_\phi\, \omega_{hz}}{\mathrm{s}_\theta} & \frac{\mathrm{s}_{\varphi_b}\, \mathrm{c}_\theta\, \mathrm{c}_{\varphi_h}(\mathrm{s}_\alpha\, \omega_{bx} - \mathrm{c}_\alpha\, \omega_{bz})}{\mathrm{c}^2_{\varphi_b}\, \mathrm{s}_\theta} & 0 & -\frac{\mathrm{s}_\phi}{\mathrm{s}_\theta} & \frac{\mathrm{c}_\phi}{\mathrm{s}_\theta} \\
\frac{\mathrm{c}_{\varphi_h}(\mathrm{s}_\alpha\, \omega_{bx} - \mathrm{c}_\alpha\, \omega_{bz})}{\mathrm{c}_{\varphi_b}} & 0 & -\mathrm{s}_\phi\, \omega_{hy} - \mathrm{c}_\phi\, \omega_{hz} & \frac{\mathrm{s}_{\varphi_b}\, \mathrm{s}_{\varphi_h}(\mathrm{s}_\alpha\, \omega_{bx} - \mathrm{c}_\alpha\, \omega_{bz})}{\mathrm{c}^2_{\varphi_b}} & 0 & -\mathrm{c}_\phi & \mathrm{s}_\phi \\
\frac{\mathrm{s}_{\varphi_h}(\mathrm{s}_\alpha\, \omega_{bx} - \mathrm{c}_\alpha\, \omega_{bz})}{\mathrm{c}_{\varphi_b}\, \mathrm{s}_\theta} & \frac{\dot{\varphi}_h}{\mathrm{s}_\theta} & -\frac{\mathrm{c}_\theta(\mathrm{c}_\phi\, \omega_{hy} - \mathrm{s}_\phi\, \omega_{hz})}{\mathrm{s}_\theta} & -\frac{\mathrm{s}_{\varphi_b}\, \mathrm{c}_{\varphi_h}(\mathrm{s}_\alpha\, \omega_{bx} - \mathrm{c}_\alpha\, \omega_{bz})}{\mathrm{c}^2_{\varphi_b}\, \mathrm{s}_\theta} & -1 & \frac{\mathrm{c}_\theta\, \mathrm{s}_\phi}{\mathrm{s}_\theta} & \frac{\mathrm{c}_\theta\, \mathrm{c}_\phi}{\mathrm{s}_\theta} \\
0 & 0 & 0 & 0 & 0 & 0 & 0 \\
0 & 0 & 0 & 0 & -\frac{1}{\tau_x} & 0 & 0 \\
0 & 0 & 0 & 0 & 0 & -\frac{1}{\tau_y} & 0 \\
0 & 0 & 0 & 0 & 0 & 0 & -\frac{1}{\tau_z}
\end{bmatrix}. \tag{5.19}$$

Similarly, the Jacobian matrix $\boldsymbol{H}(k) = \left.\frac{\partial \boldsymbol{h}}{\partial \boldsymbol{X}}\right|_{\boldsymbol{X}(k),\boldsymbol{u}(k)}$ is obtained for the outputs (5.18)

as

$$\boldsymbol{H}(k) = \begin{bmatrix} H_{11} & H_{12} & 0 & H_{14} & 0 & 0 & 0 \\ H_{21} & H_{22} & 0 & H_{24} & 0 & 0 & 0 \\ 0 & 0 & 0 & 1 & 0 & 0 & 0 \\ H_{41} & H_{42} & H_{43} & 0 & 0 & 0 & 0 \end{bmatrix},$$

where elements of $\boldsymbol{H}(k)$ are given as follows

$$\begin{aligned}
H_{11} &= -m_h h_h (l_s \, \mathrm{s}_{\varphi_h} \, \mathrm{s}_\theta + h_h \, \mathrm{s}_{\varphi_h} \, \mathrm{s}_\theta \, \mathrm{c}_\theta) \ddot{\psi} + m_h h_s h_h \, \mathrm{c}_{\varphi_b - \varphi_h} \, \mathrm{s}_\theta \, \dot{\varphi}_b^2 + 2 m_h h_h^2 \, \mathrm{s}_{\varphi_h} \, \mathrm{s}_\theta^2 \, \dot{\theta} \dot{\psi} + \\
&\quad m_h h_h (-h_h \, \mathrm{c}_{2\varphi_h} \, \mathrm{s}_\theta^2 + h_s \, \mathrm{s}_{\varphi_b} \, \mathrm{s}_{\varphi_h} \, \mathrm{s}_\theta) \dot{\psi}^2 - m_h h_h \, \mathrm{s}_{\varphi_h} \, \mathrm{s}_\theta \, v_b \dot{\psi} - m_h g h_h \, \mathrm{c}_{\varphi_h} \, \mathrm{s}_\theta, \quad (5.20a) \\
H_{12} &= 2 m_h h_h^2 \, \mathrm{s}_\theta \, \mathrm{c}_\theta \, \ddot{\varphi}_h + m_h h_h (l_s \, \mathrm{c}_{\varphi_h} \, \mathrm{c}_\theta + h_h \, \mathrm{c}_{\varphi_h} \, \mathrm{c}_{2\theta}) \ddot{\psi} + 2 m_h h_h^2 \, \mathrm{c}_{2\theta} \, \dot{\theta} \dot{\varphi}_h \\
&\quad - m_h h_s h_h \, \mathrm{s}_{\varphi_b - \varphi_h} \, \mathrm{c}_\theta \, \dot{\varphi}_b^2 - 2 m_h h_h^2 \, \mathrm{c}_{\varphi_h} \, \mathrm{s}_{2\theta} \, \dot{\theta} \dot{\psi} \\
&\quad - m_h h_h (h_h \, \mathrm{s}_{\varphi_h} \, \mathrm{c}_{\varphi_h} \, \mathrm{s}_{2\theta} + h_s \, \mathrm{s}_{\varphi_b} \, \mathrm{c}_{\varphi_h} \, \mathrm{c}_\theta) \dot{\psi}^2 \\
&\quad + m_h h_h \, \mathrm{c}_{\varphi_h} \, \mathrm{c}_\theta \, v_b \dot{\psi} - m_h g h_h \, \mathrm{s}_{\varphi_h} \, \mathrm{c}_\theta, \quad (5.20b) \\
H_{21} &= (m_h l_s h_h \, \mathrm{c}_\theta \, \mathrm{c}_{\varphi_h} + m_h h_h^2 \, \mathrm{c}_{\varphi_h}) \ddot{\psi} - 2 m_h h_h^2 \, \mathrm{s}_\theta^2 \, \mathrm{s}_{\varphi_h} \, \dot{\varphi}_h \dot{\psi} - m_h h_s h_h \, \mathrm{s}_{\varphi_b - \varphi_h} \, \mathrm{c}_\theta \, \dot{\varphi}_b^2 - \\
&\quad m_h h_h (h_h \, \mathrm{s}_{2\varphi_h} \, \mathrm{s}_\theta \, \mathrm{c}_\theta + h_s \, \mathrm{s}_{\varphi_b} \, \mathrm{c}_{\varphi_h} \, \mathrm{c}_\theta) \dot{\psi}^2 + m_h h_h \, \mathrm{c}_{\varphi_h} \, \mathrm{c}_\theta \, v_b \dot{\psi} - m_h g h_h \, \mathrm{s}_{\varphi_h} \, \mathrm{c}_\theta, \quad (5.20c) \\
H_{22} &= (m_h h_s h_h \, \mathrm{s}_{\varphi_b} \, \mathrm{c}_\theta - m_h l_s h_h \, \mathrm{s}_\theta \, \mathrm{s}_{\varphi_h}) \ddot{\psi} - m_h h_h \, \mathrm{c}_\theta \, \dot{v}_b + 2 m_h h_s h_h \, \mathrm{c}_{\varphi_b} \, \mathrm{c}_\theta \, \dot{\varphi}_b \dot{\psi} \\
&\quad + 2 m_h h_h^2 \, \mathrm{s}_{2\theta} \, \mathrm{c}_{\varphi_h} \, \dot{\varphi}_h \dot{\psi} + m_h h_s h_h \, \mathrm{c}_{\varphi_b - \varphi_h} \, \mathrm{s}_\theta \, \dot{\varphi}_b^2 \\
&\quad - m_h h_h (h_h \, \mathrm{s}_{\varphi_h}^2 \, \mathrm{c}_{2\theta} - h_s \, \mathrm{s}_{\varphi_b} \, \mathrm{s}_{\varphi_h} \, \mathrm{s}_\theta - l_s \, \mathrm{c}_\theta) \dot{\psi}^2 \\
&\quad - m_h h_h \, \mathrm{s}_{\varphi_h} \, \mathrm{s}_\theta \, v_b \dot{\psi} - m_h h_h^2 \, \mathrm{c}_{2\theta} \, \dot{\varphi}_h^2 + m_h h_h^2 \, \mathrm{c}_{2\theta} \, \dot{\psi}^2 - m_h g h_h \, \mathrm{c}_{\varphi_h} \, \mathrm{s}_\theta, \quad (5.20d) \\
H_{24} &= m_h h_s h_h \, \mathrm{c}_{\varphi_b} \, \mathrm{s}_\theta \, \ddot{\psi} - 2 m_h h_s h_h \, \mathrm{s}_{\varphi_b} \, \mathrm{s}_\theta \, \dot{\varphi}_b \dot{\psi} + m_h h_s h_h \, \mathrm{s}_{\varphi_b - \varphi_h} \, \mathrm{c}_\theta \, \dot{\varphi}_b^2 \\
&\quad - m_h h_h h_s \, \mathrm{c}_{\varphi_b} \, \mathrm{s}_{\varphi_h} \, \mathrm{c}_\theta \, \dot{\psi}^2, \quad (5.20e) \\
H_{14} &= -2 m_h h_s h_h \, \mathrm{s}_{\varphi_b - \varphi_h} \, \mathrm{s}_\theta \, \dot{\varphi}_b, \;\; H_{41} = \mathrm{c}_{\varphi_h} \, \mathrm{c}_\phi - \mathrm{s}_{\varphi_h} \, \mathrm{c}_\theta \, \mathrm{s}_\phi, \;\; H_{42} = -\mathrm{s}_\theta \, \mathrm{c}_{\varphi_h} \, \mathrm{s}_\phi, \quad (5.20f) \\
H_{43} &= -\mathrm{s}_{\varphi_h} \, \mathrm{s}_\phi + \mathrm{c}_{\varphi_h} \, \mathrm{c}_\theta \, \mathrm{c}_\phi \, . \quad (5.20g)
\end{aligned}$$

With these Jacobian matrices, the EKF implementation for the systems is written as

a prediction step ($\hat{\boldsymbol{X}}(k|k-1)$) and a correction step ($\hat{\boldsymbol{X}}(k|k)$) recursively as follows

$$\hat{\mathbf{X}}(k|k-1) = \hat{\mathbf{X}}(k-1|k-1) + \Delta T \mathbf{f}(\hat{\mathbf{X}}(k-1|k-1), \mathbf{u}(k-1)) \tag{5.21a}$$

$$\mathbf{P}(k|k-1) = \mathbf{F}(k)\mathbf{P}(k|k-1)\mathbf{F}^T(k) + \mathbf{Q}(k) \tag{5.21b}$$

$$\hat{\mathbf{X}}(k|k) = \hat{\mathbf{X}}(k|k-1) + \mathbf{W}(k)\left[\mathbf{y}(k) - \mathbf{H}(k)\hat{\mathbf{X}}(k|k-1)\right] \tag{5.21c}$$

$$\mathbf{W}(k) = \mathbf{P}(k|k-1)\mathbf{H}^T(k)\mathbf{S}^{-1}(k) \tag{5.21d}$$

$$\mathbf{S}(k) = \mathbf{H}(k)\mathbf{P}(k|k-1)\mathbf{H}^T(k) + \mathbf{R} \tag{5.21e}$$

$$\mathbf{P}(k|k) = (\mathbf{I}_9 - \mathbf{W}(k)\mathbf{H}(k))\mathbf{P}(k|k-1)(\mathbf{I}_9 - \mathbf{W}(k)\mathbf{H}(k))^T + \mathbf{W}(k)\mathbf{R}\mathbf{W}^T(k). \tag{5.21f}$$

In (5.21b), the symmetric positive definite matrix $\mathbf{Q}$ is used as a tuning parameter for the EKF performance [121].

5.7 Experiments

We recruited five healthy and experienced bicycle riders (four male and one female with age: 27 $\pm$ 3 years, height: 176 $\pm$ 4 cm, and weight: 70 $\pm$ 7 kg) to conduct both the indoor and the outdoor experiments. The duration for each riding experiment run was around 2 minutes. When riding the bicycle, the subjects were asked to arbitrarily change the bicycle speed and trajectory and to freely move their upper bodies. In outdoor experiments, the maximum bicycle speed was around 22 km/h. All the subjects gave their informed consent before being tested using a protocol approved by the Institutional Review Board (IRB) at Rutgers University.

Figure 5.6 shows the indoor pose estimation results for Subject #1. The subject rode the bicycle by his own riding style. Figs. 5.6(a)-(c) show the estimates of the trunk pose angles and Fig. 5.6(d) shows the estimates of the bicycle roll angle. For clarity, we only show truncated estimates during the time period between 45 to 70 s. For comparison purposes, the estimates by the direct strapdown IMU integration are

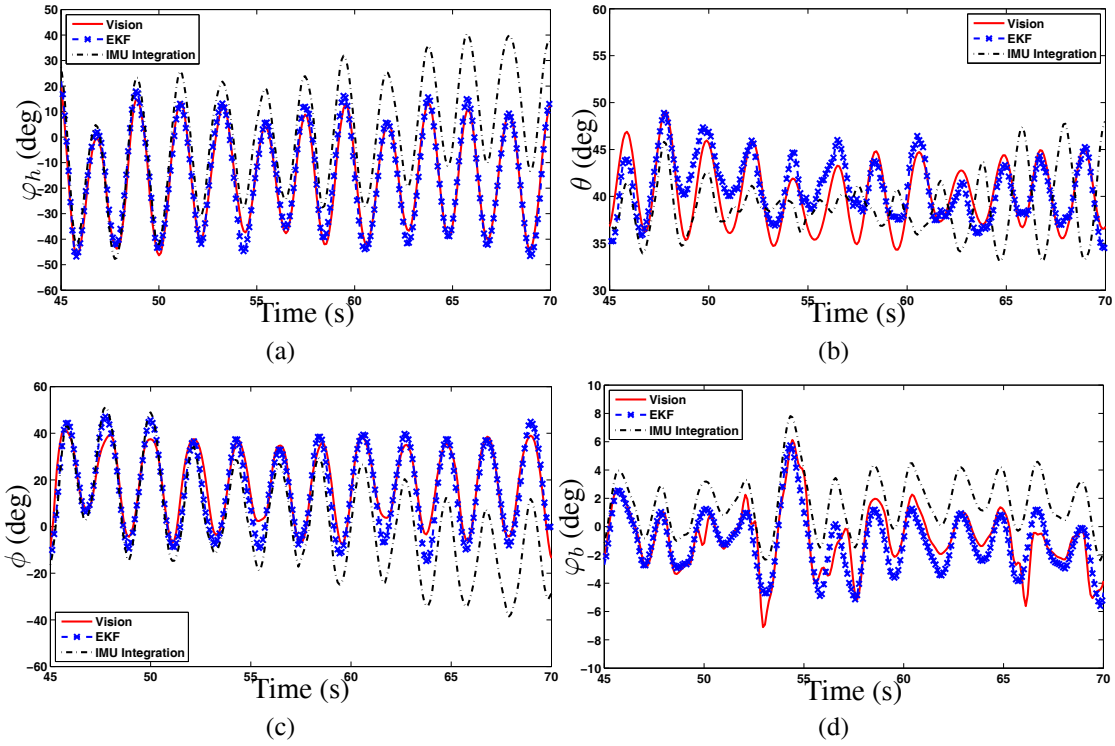

Figure 5.6: Indoor comparison results of the estimated poses by the Vicon motion capturing systems, the EKF estimates, and the integrations of IMU measurements for Subject #1. (a) φ_h. (b) θ. (c) ϕ. (d) φ_b.

also plotted in these figures. For the direct IMU integration results, the offset biases (i.e., $\boldsymbol{c}_h$ and $\boldsymbol{c}_b$ in the noise model (5.14)) are measured and their effects are eliminated in calculation. The subject tried to move his trunk aggressively in the experiment. Balancing the bicycle for a counter-clockwise circular trajectory, the subject tilted his trunk toward the center of the trajectory. Thus, the average value of φ_h is around -20 deg. The EKF-based estimation results clearly demonstrate a superior tracking performance than those by the direct strapdown IMU integration. The estimates by the direct IMU integration diverge after 50 s as shown in Figs. 5.6(a)-(c), while the EKF-based pose estimates consistently match the ground truth. Figure 5.7 shows the indoor estimation performance for Subject #2. Comparing with Subject #1, this subject moved his trunk arbitrarily. For example, as shown in Fig. 5.7, the subject moved his trunk aggressively before 48 s, then mildly and slightly from 48 to 66 s, and finally aggressively again.

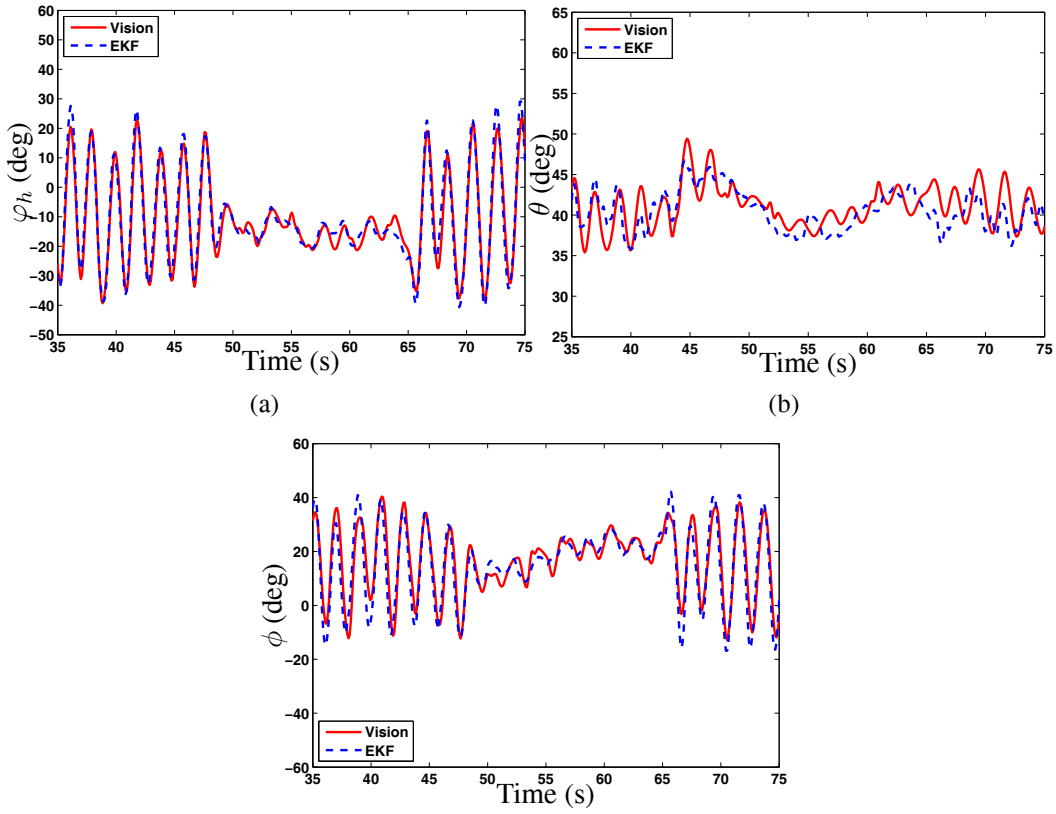

Figure 5.7: Indoor comparison results of the estimated poses by the Vicon vision capturing systems, the EKF estimates for Subject #2. (a) φ_h. (b) θ. (c) ϕ.

In this experiment, the EKF-based pose estimation also demonstrates matching performance. The pose estimation performance of the outdoor experiments demonstrates similar results as those of the indoor experiments.

Table 5.2: The mean and standard deviation (SD) of Root-mean-square (RMS) errors with and without the bias model (BM)

Experiment type		φ_h (deg)	θ (deg)	ϕ (deg)	φ_b (deg)
Indoor	With BM	3.42 ± 1.34	1.62 ± 1.06	5.56 ± 1.45	0.82 ± 0.31
	No BM	3.73 ± 1.46	1.84 ± 1.09	5.81 ± 1.42	0.84 ± 0.33
Outdoor	With BM	4.46 ± 1.62	4.01 ± 1.61	6.18 ± 2.43	2.31 ± 0.89
	No BM	4.42 ± 1.75	4.18 ± 1.63	6.24 ± 2.39	2.30 ± 0.88

To further demonstrate the performance of the EKF-based design, we compute the

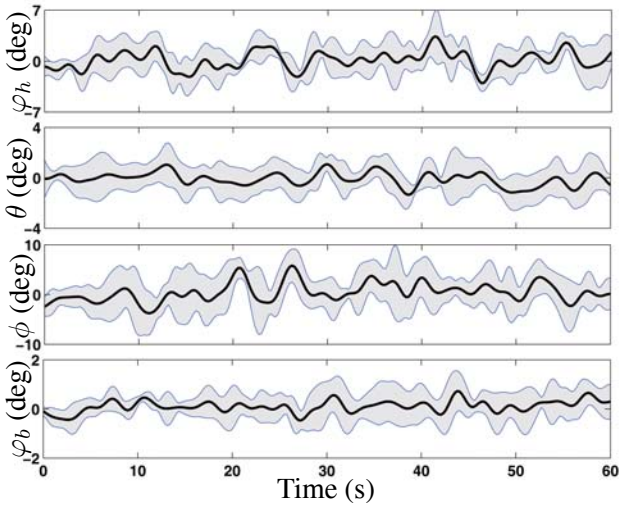

(a)

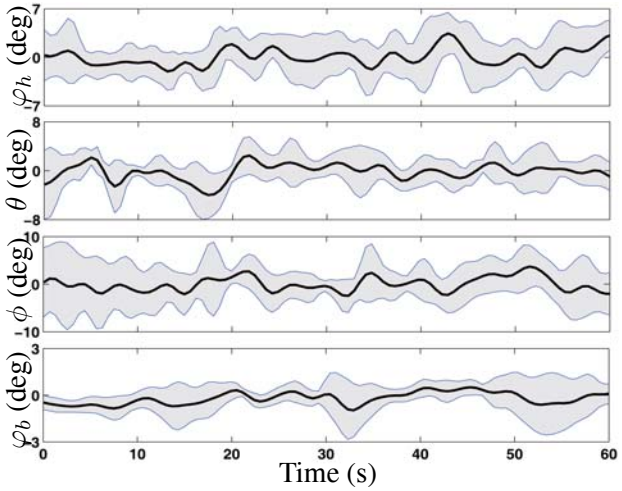

(b)

Figure 5.8: Pose estimation errors from the EKF-based design. The solid lines indicate the mean values of the errors of all subjects and the dashed lines are one-standard deviation (SD) bounds. (a) Indoor experiments. (b) Outdoor experiments.

statistics of the pose estimation errors for all subjects. Table 5.2 shows the accuracy performance in terms of the mean and standard deviation (SD) of root mean square (RMS) errors for all subjects for both the indoor and the outdoor tests. Figure 5.8 shows the calculated statistic errors over time for all subjects. For all experiments, the estimation errors are around zero and do not grow over time. The results shown in Table 5.2 and Fig. 5.8 confirm the consistently robust performance of the estimated trunk and bicycle poses by the EKF-based sensing fusion.

5.8 Discussions

In [54], the fusion of inertial and magnetic sensors shows the mean RMS errors of 2.4 to 3.2 degs for different body segments orientations. The approach in [49] demonstrates a 2.8 degs mean RMS error in the orientation estimation by using inclination in the Kalman filter design. In [51], the fusion of inertial and ultrasonic sensors demonstrates the mean RMS errors ranging from 5.7 to 6.6 degs. All the above results are obtained in the laboratory conditions. Compared with those results, our indoor experiment results are on the same accuracy level. Although our outdoor experiments show slightly large errors, the accuracy is still comparable to those by the other fusion approaches in literature.

From the results shown in Table 5.2 and Fig. 5.8, we notice that the estimation errors are not at the same level among the four estimated angles. In general, estimates of φ_b have the least errors, while the estimates of ϕ have the largest errors. These differences are due to several reasons. First, during typical bicycle riding, the change of the bicycle roll angle φ_b is relatively small. The performance of the IMU-based estimation within a small range is better than those with a large range such as for the trunk angles. Second, there is no direct measurement for angle ϕ in the EKF design and the constraint (5.17) of ϕ is coupled with the other two angles. Therefore, the estimation of ϕ has the maximal error. Moreover, for different riding styles, the performances of the EKF-based estimation design are not the same. For example, for a rider with an aggressively riding style, the EKF-based estimation scheme produces relatively larger errors than those with a mild riding style.

To quantify the improvement of the usage of the random-walk bias model in the EKF design, we compare the estimation errors with and without the inclusion of the bias model. As shown in Table 5.2, the results confirm that the use of the bias model

improves the overall estimation performance. For outdoor experiments, the improvement is not significant due to the large ground truth errors provided by the on board camera. We shall emphasize that, with or without using the bias model, the EKF-based fusion always achieves the non-drifting results, unlike the strapdown IMU integration approach.

The estimation errors are mainly due to the imperfect models for the IMU measurement noises, the interaction forces, and the complicated rider-bicycle interactions. For example, the calculated torques $\hat{\tau}_{\varphi_h}$ and $\hat{\tau}_\theta$ in (5.11) and (5.12) do not consider the articulated arm dynamics and the interactions between the legs and the trunk (e.g., pedaling effect). During the normal riding, we found the influences from the articulated arm dynamics and the pedaling effects are not significant for trunk pose estimation. Therefore, we ignore them in the rider-bicycle dynamic model for simplicity. Another error source might come from the measurement errors by the Vicon motion capture system. We estimated and found a maximum 0.8-deg accuracy for the trunk pose angles and 0.3-deg accuracy for the bicycle roll angle measurements by the Vicon motion capture system. For the outdoor experiments, the vibration of the camera mounting base due to uneven road surface also contributes to the ground truth errors.

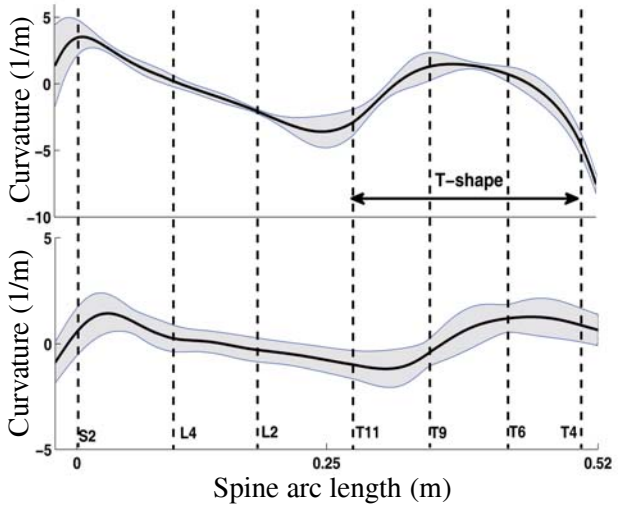

Figure 5.9: The mean values and one standard deviation (SD) bounds of the spine curvatures in the sagittal plane (top) and in the coronal plane (bottom).

Human trunk is flexible and its orientation is difficult to define and measure. In [115–117], the trunk is modeled as a rigid one-link inverted pendulum in walking, stance and bicycling balance studies. To validate this rigid-body modeling assumption in bicycle riding, we placed a set of optical markers along the spine to observe the characteristics of trunk motion; see Fig. 5.1(d). Figure 5.9 shows the means and the standard deviations of the spine curvature calculations in the sagittal plane and the coronal plane during one aggressively indoor riding experiment. The results shown in the figure confirm that the trunk maintains rigid-body motions in bicycle riding since the variations of the spinal curvatures are small. The curvatures at the level T4-T11 region, where the rider IMU is attached, are small. This implies a straight line-shape spine. Especially, in the coronal plane the curvature of the entire spine is around zero. Therefore, the rigid pendulum seems a valid model for capturing the trunk motion in bicycle riding.

The force measurements at the seat and handlebar contain motion information about the rider-bicycle pose angles and their dynamics, as shown in (5.9). The use of the IMU measurements facilitates the EKF design to calculate the pose information from the force measurements by (5.9). Therefore, the fusion of the force/inertial measurements in the EKF design provides a more restrictive constraint than that of the velocity constraints such as those in [120, 122]. This is the main reason why the drifts by the strapdown IMU integration are eliminated. Unlike the approaches in [49, 50] to build an empirical acceleration model to enhance pose estimation accuracy, the use of force measurements is built on the system dynamics and thus, the obtained estimation results are reliable under dynamic motions. The robust estimation results shown in Fig. 5.8 confirm such an observation.

Unlike some inertial sensor-based schemes in which the ground-truth pose information is needed to initialize the estimation design [58], the force/inertial fusion design is robust to the choice of the initial state values. For example, Fig. 5.10 shows the EKF-based estimate of φ_h in the first few seconds. Although the initial value is set by more

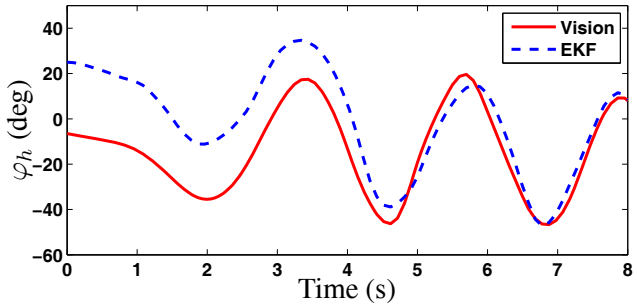

Figure 5.10: The initialization and convergence of the EKF-based estimation design (only shown for φ_h).

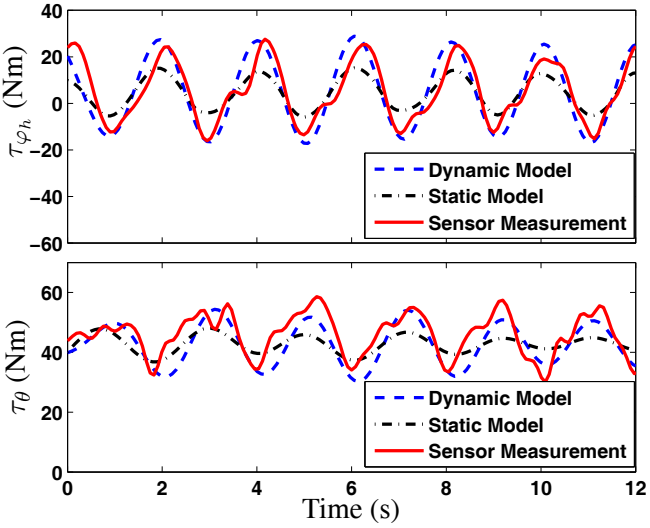

Figure 5.11: Comparison results among the dynamic model-based, the static model-based, and the sensor measured τ_{φ_h} and τ_θ.

than 30 deg different from its actual value, the estimates of φ_h converge to the ground truth within around 6 s. Of course, it is preferable to use a set of initial values that are near their true values for a fast convergence. We used the static force measurements to calculate the initial values for the state variables [117]. The static model assumes zero derivatives in (5.9). Figure 5.11 shows the comparison of the estimated torques by the dynamic model, the static model, and the sensor measurements. Clearly, the dynamic model-based torque calculations match well with the measurements, while the magnitudes of the static model-based calculations are much smaller than those of the measurements because of the neglected dynamic effects. The results in Fig. 5.11 also indirectly validate the rider-bicycle dynamic model (5.9).

As one design limitation, the force/inertial sensor fusion design is not capable to identify and estimate the bicycle yaw angle ψ because none of the onboard sensors provides the absolute yaw motion information. The used inverted pendulum model is valid only for typical bicycle riding in which the rider always sits on the seat. The pose estimation will not perform well in the cases of uncommonly riding styles, such as acrobatic bicycle riding in which the rider stands on the pedals and does not sit on the seat.

5.9 Conclusion

In this chapter, we presented a rider-bicycle pose estimation scheme using the inertial and force sensors. The pose estimation scheme was built on the attractive properties of the robust force measurements and the motion-sensitive responses of the inertial sensors. A rider-bicycle dynamic model was developed to provide the underlying dynamic relationship between the pose angles and the human body driving forces. By incorporating the rider-bicycle dynamics into the design, the pose estimation results did not drift over time even under highly dynamic motions. We demonstrated and validated the pose estimation scheme through both the indoor and the outdoor bicycle riding experiments. The results showed superior performance than those by using the direct strapdown IMU integration method and the estimation performances were also comparable with the other fusion methods reported in literature. Since the pose estimation approach uses only onboard sensors, it is particularly useful for outdoor applications and also potentially for other types of human-machine interactions.

Chapter 6
Control of Rider-Bicycle Systems

6.1 Introduction

An accurate pose estimation of ride-bicycle system is already obtained in Chapter 5, the chapter we mainly present the balancing control and perturbation for rider-bicycle system.

In the first part of the chapter, we present a dynamic modeling and balance control of stationary rider-bicycle system. We consider the human as an inverted pendulum connected to the moving bicycle platform. When the bicycle is at stationary, the dynamics of the rider-bicycle systems are shown similar to these of double-link inverted pendulum systems. If we consider the human motion is a disturbance, the rider-bicycle system is an underactuated system like an acrobot or a pendubot. It is known that such dynamic systems are controllable [123]. Several control approaches are reported for acrobot or pendubot, such as hybrid-based [124] or passivity-based control laws [125]. However, these control designs do not work for the rider-bicycle control because no cyclic swing motion is allowed before the system reaches the attraction basin around the unstable equilibria. We take a hierarchical sliding-model control (SMC) approach in [126, 127] to design the balancing controller. A nonlinear disturbance observer (NDOB) [128, 129] is used to estimate the human turning torque. We show that the integrated hierarchical SMC and the NDOB design is asymptotically stable. The control systems design is illustrated through simulation examples.

In the second part of this chapter, we consider to use rider-bicycle interactions as

a new paradigm to examine a sensorimotor theory for modeling and shaping human-robot interactions. Humans with trained motor skills can flexibly interact with machines. Many efficient human-robot interactions are unstable [130, 131]. The recent study in [60] demonstrates that human neuro-control has different, complementary sensitivities of balancing stability between riding the bicycle and quiet stance. Although studying interactions between the rider and the passive bicycle is reported in recent years [60, 132–134], the bikebot platform provides active perturbation to break rider's sensorimotor feedback mechanism through actively controlled steering, velocity, and balancing. Sitting on the bicycle, riders have to actively react to the sensory feedback through body movements (i.e., steering, pedaling and upper-body leans) for balancing and navigation. Compared to other motor skills such as quiet stance [135], riding the bicycle requires the coordinated control of multi-limb and body movements following the sensorimotor cues. Therefore, the bikebot offers an new platform for studying sensorimotor human-robot interactions.

6.2 Balance control of rider-bicycle system

6.2.1 Rider-bicycle dynamics

General motion dynamics

Figure 6.1(a) shows the schematic rider/bicycle system. The system is considered as a three-part platform: a rear frame, a steering mechanism, and human body. We consider the following assumptions: (1) the rider trunk is modeled as a point mass; (2) the wheel/ground is a point contact and thickness and geometry of the motorcycle tire are neglected; (3) The motorcycle body frame is considered a point mass; and (4) the motorcycle moves on a flat plane and vertical motion is neglected, namely, no suspension motion.

Similar to the previous chapters, we use the constrained Lagrangian method to

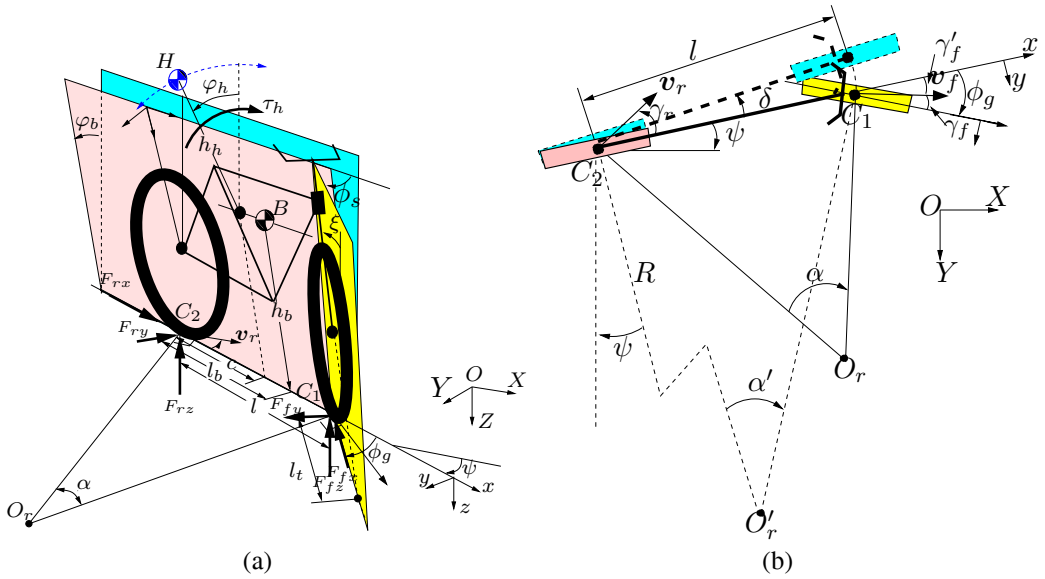

Figure 6.1: Schematic of the rider-bicycle systems. (a) Side view. (b) Top view.

obtain the dynamics equation of the rider-bicycle motion. We consider the motorcycle as three parts: one rear frame with mass m, one steering mechanism with the mass moment of inertia J_s, and the human rider with mass m_h. Let $\dot{\boldsymbol{q}} := [\dot{\varphi}_b \ \dot{\varphi}_h \ v_{rx} \ v_{ry}]^T$ denote the generalized velocity of the motorcycle, where φ_h is the trunk roll angle and v_{ry} is the lateral velocity of C_2 in the body frame. Following the similar approach and calculation in [11], we obtain the motion equations

$$\mathbf{M}\ddot{\boldsymbol{q}} = \mathbf{K} + \mathbf{B}\boldsymbol{u}\,, \tag{6.1}$$

where $\boldsymbol{u} := \begin{bmatrix} \omega_\sigma & \tau_h & F_{fx} & F_{fy} & F_{rx} & F_{ry} \end{bmatrix}^T$, $\omega_\sigma := \dot{\sigma}$, τ_h is the human turning torque, F_{fi}, F_{ri}, $i = x, y$, are the front/rear tire frictional forces. Matrices $\mathbf{M}$, $\mathbf{K}$, and $\mathbf{B}$ are given in (6.2b) to (6.2c), respectively. C_d is the aerodynamic drag coefficient, and parameters

$$M := m + m_h, \quad M_{bh} := \frac{l_b m + c m_h}{l},$$
$$M_x := m + m_h \, \mathrm{s}^2_{\varphi_b - \varphi_h}, \quad H_s := h_b \, \mathrm{s}_{\varphi_b} + h_h \, \mathrm{s}_{\varphi_h}\,.$$

In (6.2b), we have

$$M_{rx} := m\left[(1 - h_b\sigma \, \mathrm{s}_{\varphi_b}/l)^2 + {l_b}^2\sigma^2/l^2\right] + m_h\left[(1 - \sigma H_s/l)^2 + c^2\sigma^2/l^2\right],$$

in (6.2c)

$$K_3 := -2\left[m\left(1-\frac{h_b\sigma\,\mathrm{s}_{\varphi_b}}{l}\right)\left(-\frac{h_b\sigma\,\mathrm{c}_{\varphi_b}}{l}\right)+m_h\left(1-\frac{H_s\sigma}{l}\right)\left(-\frac{H_s\sigma}{l}\right)\right]\dot{\varphi}_b v_{rx}$$
$$+2m_h\left(1-\frac{\sigma H_s}{l}\right)\left(\frac{\sigma h_h\,\mathrm{c}_{\varphi_h}}{l}\right)\dot{\varphi}_h v_{rx}+M_{bh}h_b\sigma\,\mathrm{s}_{\varphi_b}\,\dot{\varphi}_b^2+m_h\frac{c\sigma h_h\,\mathrm{s}_{\varphi_h}}{l}\dot{\varphi}_h^2,$$

and in (6.2c)

$$B_\omega = -\left\{2m\left[\left(1-\frac{h_b\sigma\,\mathrm{s}_{\varphi_b}}{l}\right)\left(-\frac{h}{l}\,\mathrm{s}_{\varphi_b}\right)+\frac{b^2\sigma}{l^2}\right]\right.$$
$$\left.+2m\left[\left(1-\frac{h_b\sigma\,\mathrm{s}_{\varphi_b}}{l}\right)\left(-\frac{h}{l}\,\mathrm{s}_{\varphi_b}\right)+\frac{c^2\sigma}{l^2}\right]\right\}v_{rx}-M_{bh}v_{ry}-M_{bh}h_b\,\mathrm{c}_{\varphi_b}\,\dot{\varphi}_b$$
$$-\frac{m_h c h_h}{l}\,\mathrm{c}_{\varphi_b}\,\dot{\varphi}_b.$$

Remark 6.1. *In this chapter, in order to have a closed-form design for the controller, simplifications are used in modeling process. Comparing with the steering mechanism presented in Chapter 3, we consider the simple model developed in Chapter 2 to make the calculation tractable. Simplification is also taken to the rider trunk modeling. So we only consider rider roll angle and not include the rider trunk pitch angle.*

System dynamics at zero velocity

We consider the balancing control of the rider/bicycle system when the system is stationary. Letting $v_{rx} = v_{ry} = 0$, dynamic equations (6.1) are reduced to

$$M_{11}\ddot{\boldsymbol{q}}_s + \mathbf{C}_s(\boldsymbol{q}_s, \dot{\boldsymbol{q}}_s)\dot{\boldsymbol{q}}_s + \mathbf{G}(\boldsymbol{q}_s) = \boldsymbol{u}_s\,, \tag{6.3}$$

$$\mathbf{M} = \left[\begin{array}{c:c} M_{11} & M_{12} \\ \hdashline M_{21} & M_{22} \end{array}\right] \tag{6.2a}$$

$$= \left[\begin{array}{cc:cc} Mh_b^2 & m_h h_b h_h \, \mathrm{c}_{(\varphi_b-\varphi_h)} & M_{bh}\sigma h_b \, \mathrm{c}_{\varphi_b} & Mh_b \, \mathrm{c}_{\varphi_b} \\ m_h h_b h_h \, \mathrm{c}_{(\varphi_b-\varphi_h)} & m_h h_h^2 & \dfrac{m_h c h_h \sigma \, \mathrm{c}_{\varphi_b}}{l} & m_h h_h \, \mathrm{c}_{\varphi_h} \\ \hdashline M_{bh}\sigma h_b \, \mathrm{c}_{\varphi_b} & \dfrac{m_h c h_h \sigma \, \mathrm{c}_{\varphi_h}}{l} & M_{rx} & M_{bh}\sigma \\ Mh_b \, \mathrm{c}_{\varphi_b} & m_h h_h \, \mathrm{c}_{\varphi_h} & M_{bh}\sigma & M \end{array}\right], \tag{6.2b}$$

$$\mathbf{K} = \begin{bmatrix} (Mh_b \, \mathrm{s}_{\varphi_b} + m_h h_h \, \mathrm{s}_{\varphi_h}) \frac{h_b \sigma^2}{l^2} \, \mathrm{c}_{\varphi_b} \, v_{rx}^2 - m_h h_b h_h \dot{\varphi}_h^2 \, \mathrm{s}_{(\varphi_b-\varphi_h)} \\ + Mg \left(h_b \, \mathrm{s}_{\varphi_b} + \frac{l_t b \, \mathrm{c}_\xi \, \sigma \, \mathrm{c}_{\varphi_b}}{l} \right) \\ -m_h \left[1 - \frac{\sigma H_s}{l}\right] \frac{\sigma h_h \, \mathrm{c}_{\varphi_h}}{l} v_{rx}^2 + m_h h_b h_h \dot{\varphi}_b^2 \, \mathrm{s}_{(\varphi_b-\varphi_h)} + m_h g h_h \, \mathrm{s}_{\varphi_h} \\ K_3 \\ Mh_b \, \mathrm{s}_{\varphi_b} \, \dot{\varphi}_b^2 + m_h h_h \, \mathrm{s}_{\varphi_b} \, \dot{\varphi}_h^2 \end{bmatrix},$$

$$\mathbf{B} = \begin{bmatrix} -M_{bh} h_b \, \mathrm{c}_{\varphi_b} \, v_{rx} & 0 & 0 & 0 & 0 & 0 \\ -\frac{m_h \sigma h_h \, \mathrm{c}_{\varphi_h} \, v_{rx}}{l} & 1 & 0 & 0 & 0 & 0 \\ B_\omega & 0 & -\frac{1}{\sqrt{1+\sigma^2}} & -\frac{\sigma}{\sqrt{1+\sigma^2}} & 1 & 0 \\ -M_{bh} v_{rx} & 0 & -\frac{\sigma}{\sqrt{1+\sigma^2}} & \frac{1}{\sqrt{1+\sigma^2}} & 0 & -1 \end{bmatrix}. \tag{6.2c}$$

---

where $\boldsymbol{q}_s = [\varphi_b \;\; \varphi_h]$, $\boldsymbol{u}_s = [\frac{Mgl_t b \, \mathrm{c}_\xi^2}{l} \tan\phi \;\; \tau_h]^T$, and

$$M_{11} = \begin{bmatrix} Mh_b^2 & m_h h_b h_h \, \mathrm{c}_{\varphi_b-\varphi_h} \\ m_h h_b h_h \, \mathrm{c}_{\varphi_b-\varphi_h} & m_h h_h^2 \end{bmatrix},$$

$$\mathbf{C_s} = \begin{bmatrix} 0 & m_h h_b h_h \dot{\varphi}_h \, \mathrm{s}_{(\varphi_b-\varphi_h)} \\ -m_h h_b h_h \dot{\varphi}_b \, \mathrm{s}_{(\varphi_b-\varphi_h)} & 0 \end{bmatrix},$$

$$\mathbf{G_s} = \begin{bmatrix} -Mgh_b \, \mathrm{s}_{\varphi_b} \\ -m_h g h_h \, \mathrm{s}_{\varphi_h} \end{bmatrix}.$$

Let $\boldsymbol{x} := [x_1 \;\; x_2 \;\; x_3 \;\; x_4]^T = [\varphi_b \;\; \dot{\varphi}_b \;\; \varphi_h \;\; \dot{\varphi}_h]$ be the state variable and we rewrite (6.3) as

$$\begin{cases} \dot{x}_1 = x_2 \\ \dot{x}_2 = f_1(\boldsymbol{x}) + b_1(\boldsymbol{x})u + b_{1w}(\boldsymbol{x})d_w \\ \dot{x}_3 = x_4 \\ \dot{x}_4 = f_2(\boldsymbol{x}) + b_2(\boldsymbol{x})u + b_{2w}(\boldsymbol{x})d_w, \end{cases} \tag{6.4}$$

where $u := \frac{Mgl_t b\, \mathrm{c}_\xi^2}{l} \tan\phi$ is the steering angle input, $d_w = \tau_h$ is the disturbance, and

$$f_1(\boldsymbol{x}) = \frac{1}{M_x h_b h_h}\left[(M\,\mathrm{s}_{x_1} - m_h\,\mathrm{s}_{x_3}\,\mathrm{c}_{x_1-x_3})gh_h - (h_b x_2^2\,\mathrm{c}_{x_1-x_3} + h_h^2 x_4^2)m_h h_h\,\mathrm{s}_{x_1-x_3}\right],$$

$$f_2(\boldsymbol{x}) = \frac{1}{M_x h_b h_h}\left[(\mathrm{s}_{x_3} - \mathrm{s}_{x_1}\,\mathrm{c}_{x_1-x_3})Mgh_b + (Mh_b x_2^2 + m_h h_h x_4^2\,\mathrm{c}_{x_1-x_3})h_b\,\mathrm{s}_{x_1-x_3}\right],$$

$$b_1(\boldsymbol{x}) = \frac{1}{M_x h_b^2},\; b_2(\boldsymbol{x}) = b_{1w}(\boldsymbol{x}) = -\frac{\mathrm{c}_{x_1-x_3}}{M_x h_b h_h},$$

$$b_{2w}(\boldsymbol{x}) = \frac{M}{m_h M_x h_h^2}.$$

Systems (6.4) are considered for balance controller design.

6.2.2 Balancing control design

We are now ready to design balance control by only steering the front wheel. We assume that the human rider turning torque $d_w = \tau_h$ is unknown. For systems (6.4), the desired trajectories are $x_{1d} = \varphi_{bd} = 0$ and $x_{3d} = \varphi_{hd} = 0$. Therefore, we define the following two sliding surfaces

$$s_1 = c_1 x_1 + x_2, \quad s_2 = c_2 x_3 + x_4, \tag{6.5}$$

where $c_1 > 0$ and $c_2 > 0$ are constants. We define the coupled surface $S = \lambda s_1 + s_2$, where λ is a constant. To estimate the disturbance d_w, we take the dynamics of the bicycle (e.g., the first two equations in (6.4)), and using the similar design in [128,129],

we propose the following disturbance observer

$$\begin{cases} \dot{z} = -l(\boldsymbol{x}_b)b_{1w}(\boldsymbol{x})z - l(\boldsymbol{x}_b)\Big[b_{1w}(\boldsymbol{x})p(\boldsymbol{x}_b) + f_1(\boldsymbol{x}) + b_1(\boldsymbol{x})u\Big], \\ \hat{d}_w = z + p(\boldsymbol{x}_b), \end{cases} \tag{6.6}$$

where $\boldsymbol{x}_b = [x_1 \;\; x_2]^T$, $l(\boldsymbol{x}_b) = \frac{\partial p(\boldsymbol{x}_b)}{\partial \boldsymbol{x}_b}$, and $p(\boldsymbol{x}_b)$ is a function to be designed. Letting $\tilde{d}_w = d_w - \hat{d}_w$, it has been shown that the error dynamics of the NDOB is

$$\dot{\tilde{d}}_w + \beta(\boldsymbol{x}_b)\tilde{d}_w = 0, \tag{6.7}$$

where $\beta(\boldsymbol{x}_b) := l(\boldsymbol{x}_b)b_{1w}(\boldsymbol{x}) > 0$ by the choice of $p(\boldsymbol{x}_b)$.

For the balance control of each subsystems in (6.4), we introduce nominal control inputs

$$u_1 = -\frac{1}{b_1(\boldsymbol{x})}\left[f_1(\boldsymbol{x}) + c_1 x_2\right],\; u_2 = -\frac{1}{b_2(\boldsymbol{x})}\left[f_2(\boldsymbol{x}) + c_2 x_4\right] \tag{6.8}$$

to compensate their desired trajectories assuming zero disturbance. Finally, we design the control input as

$$u = u_1 + u_2 + u_c, \tag{6.9}$$

where u_c will be determined as in the following theorem.

Theorem 6.1. *For the rider-bicycle system (6.3) with the NDOB design (6.6) and the coupled SMC (6.9) with*

$$u_c = \frac{-1}{b_2(\boldsymbol{x}) + \lambda b_1(\boldsymbol{x})}\Bigg\{ KS + b_2(\boldsymbol{x})u_1 + \lambda b_1(\boldsymbol{x})u_2 + \left[b_{2w}(\boldsymbol{x}) + \lambda b_{1w}(\boldsymbol{x})\right]\hat{d}_w + \frac{S\left[b_{2w}(\boldsymbol{x}) + \lambda b_{1w}(\boldsymbol{x})\right]^2}{\beta(\boldsymbol{x}_b)}\Bigg\}, \tag{6.10}$$

where $K > 0$, the balance control and the NDOB errors asymptotically converge to zero.

Proof. We consider the Lyapunov function

$$V = \frac{1}{2}S^2 + \frac{1}{2}\tilde{d}_w^2. \tag{6.11}$$

Taking the derivative of V and using the systems dynamics (6.4) and NDOB error dynamics (6.7), we obtain

$$\begin{aligned}
\dot{V} &= S\left[\lambda\left(\dot{x}_2 + c_1\dot{x}_1\right) + c_2\dot{x}_3 + \dot{x}_4\right] - \beta(\boldsymbol{x}_b)\tilde{d}_w^2 \\
&= S\left\{b_2(\boldsymbol{x})u_1 + \lambda b_1(\boldsymbol{x})u_2 + \left[b_2(\boldsymbol{x}) + \lambda b_1(\boldsymbol{x})\right]u_c + \left[b_{2w}(\boldsymbol{x}) + \lambda b_{1w}(\boldsymbol{x})\right]d_w\right\} \\
&\quad -\beta(\boldsymbol{x}_b)\tilde{d}_w^2.
\end{aligned}$$

By control design (6.10), the above equation becomes

$$\begin{aligned}
\dot{V} &= S\left\{-KS + \left[b_{2w}(\boldsymbol{x}) + \lambda b_{1w}(\boldsymbol{x})\right]\tilde{d}_w - \frac{S\left[b_{2w}(\boldsymbol{x}) + \lambda b_{1w}(\boldsymbol{x})\right]^2}{\beta(\boldsymbol{x}_b)}\right\} - \beta(\boldsymbol{x}_b)\tilde{d}_w^2 \\
&= -KS^2 - \frac{S^2\left[b_{2w}(\boldsymbol{x}) + \lambda b_{1w}(\boldsymbol{x})\right]^2}{\beta(\boldsymbol{x}_b)} + S\left[b_{2w}(\boldsymbol{x}) + \lambda b_{1w}(\boldsymbol{x})\right]\tilde{d}_w - \beta(\boldsymbol{x}_b)\tilde{d}_w^2 \\
&\leq -KS^2 - \left[\sqrt{\beta(\boldsymbol{x}_b)}\tilde{d} - \frac{S|b_{2w}(\boldsymbol{x}) + \lambda b_{1w}(\boldsymbol{x})|}{\sqrt{\beta(\boldsymbol{x}_b)}}\right]^2 \\
&\leq -KS^2 \leq 0.
\end{aligned} \tag{6.12}$$

Therefore, the stability of the equilibria $S = 0$ and $\tilde{d}_w = 0$ is obtained. To see the asymptotic stability, we use Barbalat's lemma by showing the uniformly continuity of $\dot{V}$. This completes the proof. □

To implement the control and the NDOB design, we need to choose the function $p(\boldsymbol{x}_b)$. For the rider-bicycle system, we use $p(\boldsymbol{x}_b) = -\gamma x_2$ and $l(\boldsymbol{x}_b) = [-\gamma\ \ 0]^T$, and thus $\beta(\boldsymbol{x}_b) > 1$. In implementation, we choose a large γ value for rapidly changing disturbances.

Similar to [126], we need to be careful to design parameter λ. It may be shown that by an appropriate choice of λ, we can guarantee the asymptotic stability of sliding surfaces s_1 and s_2 around the unstable equilibria.

Theorem 6.2. *For the control design given in Theorem 6.1, if we choose* λ

$$\lambda = \begin{cases} \lambda_0 & s_1 s_2 \geq 0 \\ -\lambda_0 & s_1 s_2 < 0, \end{cases} \tag{6.13}$$

where $\lambda_0 > 0$*, then the sliding surfaces* s_1 *and* s_2 *are both asymptotic stable.*

Proof. We consider the same Lyapunov function (6.11). By the controller design, we have $\dot{V} = S\dot{S} - \beta(\boldsymbol{x}_b)\tilde{d}_w^2 < 0$ and $V(t) = \frac{1}{2}S^2 + \frac{1}{2}\tilde{d}_w^2 < V(0) < \infty$. Hence $|S| < \infty$ is obtained. Due to $\lambda s_1 s_2 \geq 0$, it's straightforward to obtain that $|s_1| < \infty$ and $|s_2| < \infty$.

From (6.5), we obtain

$$\dot{s}_1 = c_1\dot{x}_1 + \dot{x}_2 = c_1 x_2 + f_1(\boldsymbol{x}) + b_1(\boldsymbol{x})u + b_{1w}(\boldsymbol{x})d_w.$$

Since all terms on the right-hand side of the above equation are bounded (u is bounded due to the physical actuation limitation), we obtain $|\dot{s}_1| < \infty$. Similarly, we obtain $|\dot{s}_2| < \infty$. Taking integration on both sides of (6.12), we obtain $\int_0^\infty S^2 dt < \infty$. Thus, by (6.13), we have

$$0 < \int_0^\infty (\lambda^2 s_1^2 + s_2^2)dt \leq \int_0^\infty (\lambda^2 s_1^2 + 2\lambda s_1 s_2 + s_2^2)dt = \int_0^\infty S^2 dt < \infty,$$

namely,

$$0 < \int_0^\infty s_1^2 dt < \infty, \quad 0 < \int_0^\infty s_2^2 dt < \infty.$$

Using Barbalat's lemma, we can show that

$$\lim_{t\to\infty} s_1 = 0, \quad \lim_{t\to\infty} s_2 = 0.$$

Therefore, sliding surfaces s_1 and s_2 are asymptotically stable. This completes the proof. □

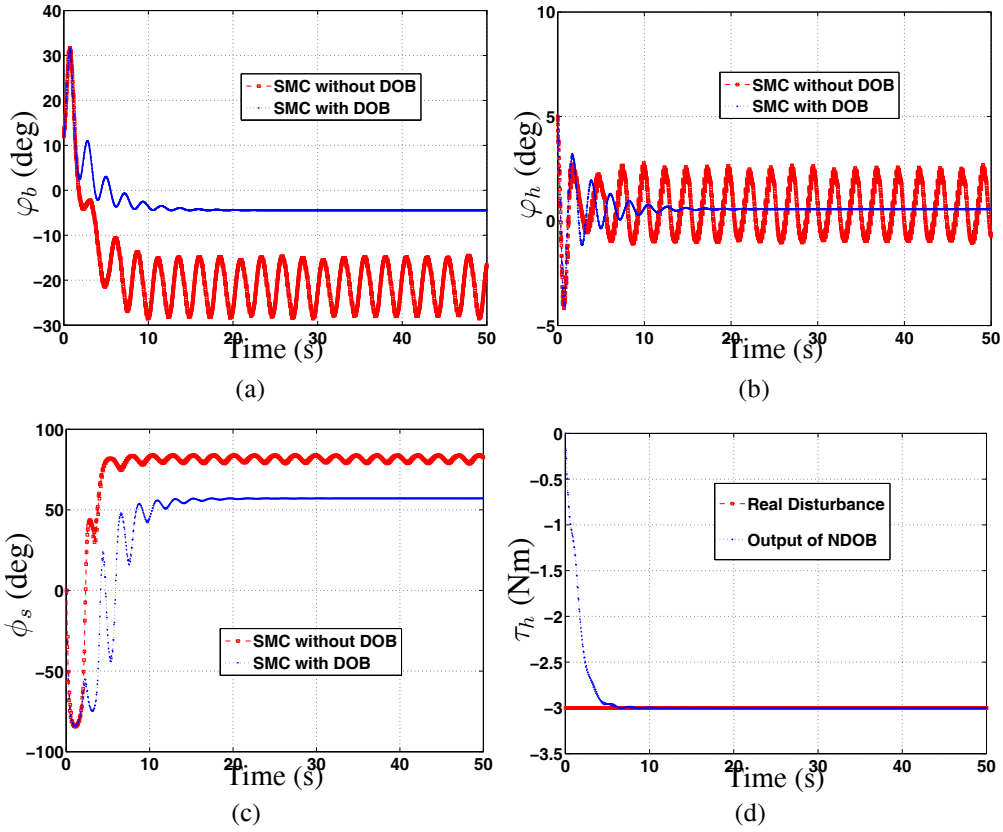

Figure 6.2: Balance control of rider-bicycle system under a constant disturbance human motion torque. (a) Bicycle roll angle. (b) Human roll angle. (c) Steering angle. (d) Actual and estimated disturbances.

6.2.3 Simulation results

We demonstrate the control system design through two numerical examples. In each example, we compare the results of the proposed control design (6.9) with the NDOB and of the regular hierarchical SMC without NDOB design. The physical parameters of the rider-bicycle systems are listed in Table 6.1. These parameters are based on the Rutgers' "smart bicycle" prototype. The control systems parameters with the NDOB design are $\lambda_0 = 0.4$, $c_1 = 0.4$, $c_2 = 1$, and $K = 25$. For comparison purposes, we use the same set of the parameters in hierarchical sliding-model controller. In simulation, the initial state values are $\boldsymbol{x}_0 = \begin{bmatrix} 0.21 & 0 & 0.087 & 0 \end{bmatrix}^T$, namely, the bicycle is released from rest with an initial roll angle of 12 degrees and the human has an initial roll angle of 5 degrees.

Table 6.1: Rider/bicycle system parameters

m (kg)	m_h (kg)	h_b (m)	h_h (m)	l (m)	l_t (m)	l_b (m)	c (m)	ξ (rad)
13.13	65	0.38	0.47	0.97	0.05	0.41	0.34	0.33

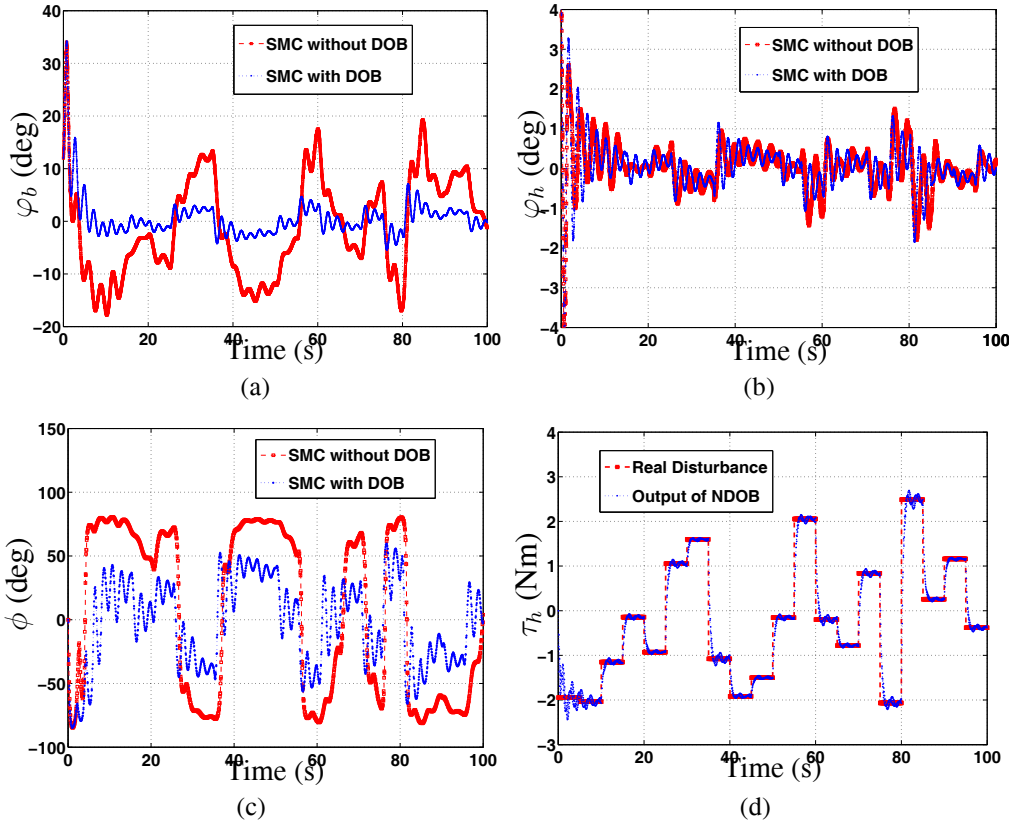

Figure 6.3: Balance control of rider-bicycle system under a random disturbance human motion torque. (a) Bicycle roll angle. (b) Human roll angle. (c) Steering angle. (d) Actual and estimated disturbances.

In the first example, we assume a constant human body turning torque $\tau_h = 3$ Nm. We use $\gamma = -3$ in the NDOB design. Figure 6.2 shows the simulation results. It is clearly to see that the roll angles of the bicycle and human are smaller when the proposed NDOB is applied. From Fig. 6.2(c), we see that the steering angle input is also smaller with the NDOB design comparing with the controller without the NDOB design. The NDOB successfully estimates the disturbance τ_h as shown in Fig. 6.2(d). We can see that the NDOB design can accurately estimate the constant disturbance after 5 s. Note that there is always a bias in roll and steering angles from their desired

equilibria (e.g., vertical positions) at steady-state. Such biases are coming from the existence of the constant disturbance. The rider-bicycle system tries to overcome the constant disturbance by using a non-zero steering angle as shown in Fig. 6.2(c).

In the second example, we assume that the disturbance τ_h is randomly changing. The magnitude of disturbance is varying periodically around every 5 s. Figure 6.3 shows the simulation results. We use $\gamma = -10$ in the NDOB design. The exact disturbance is shown in Fig. 6.3(d). When only the coupled SMC is used, the performance of the rider-bicycle systems is changing abruptly and a large control input is needed to balance the platform. From Fig. 6.3(d), we can see that the NDOB can catch up the time-varying disturbance in a very short time due to using a large γ value. The rapidly changing disturbance in this example makes the NDOB convergence challenging. From Fig. 6.3, we clearly see the superior performance by using the NDOB design.

6.3 Human sensorimotor control in rider-bicycle interaction

6.3.1 Experiments

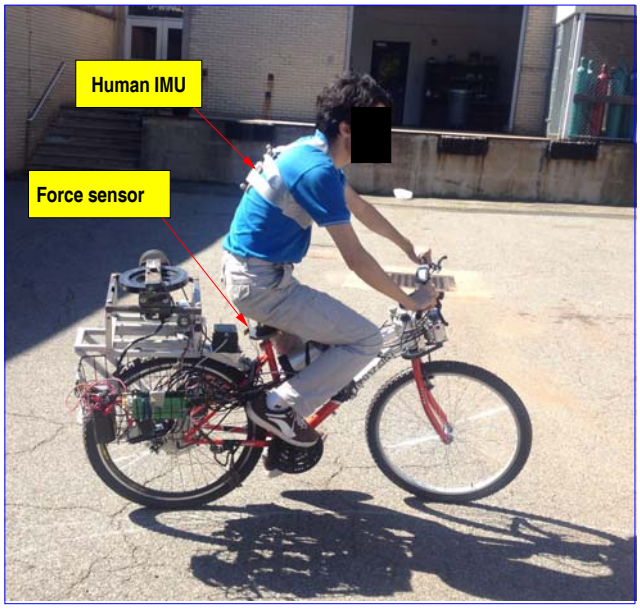

Figure 6.4: Human outdoor riding experiments.

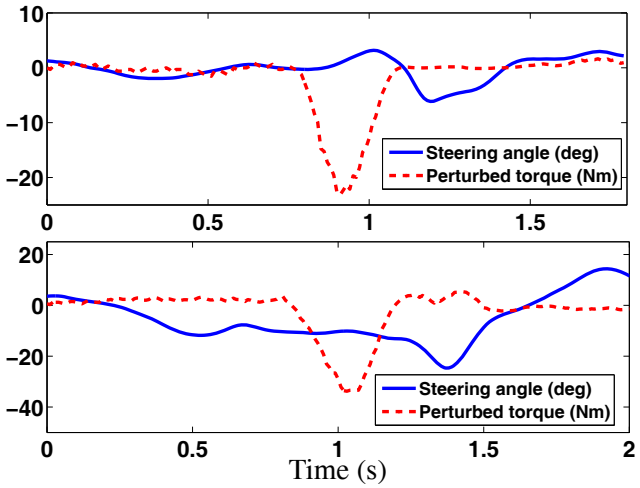

Figure 6.5: Steering angle and a single perturbed torque disturbance. Top: Bikebot riding following a straight-line. Bottom: Bicycle riding following a circle.

To demonstrate the feasibility of the use of the bikebot to perturb the human motor control and coordination and study the human sensorimotor control, we conduct a set of human riding experiments. A young male experienced bicycle riding subject was recruited to ride the bicycle in outdoor environment; see Fig. 6.4. The subject was asked to ride the bicycle by tuning the driving motor control and steering handlebar, the same as his regular bicycle riding style. Both a straight-line riding (for a distance of 50 m) and a circular riding (about a radius of 3 m) were conducted in experiments. After the subject got used to ride the bicycle comfortably, we turned on the gyro-balancer to perturb the riding and measured the rider's responses to the generated torque disturbances. The subject gave his informed consent before being tested using a protocol approved by the Institutional Review Board (IRB) at Rutgers University.

We first perturbed the riding by a step torque disturbance suddenly applied without notifying the rider. Figure 6.5 shows the rider steering angle responses and the perturbed torques for both the straight-line and circular bicycle riding experiments. It is clearly shown in these plots that under a perturbation, the rider uses the steering as a motion strategy to keep balancing the unstable platform. The responses also confirm

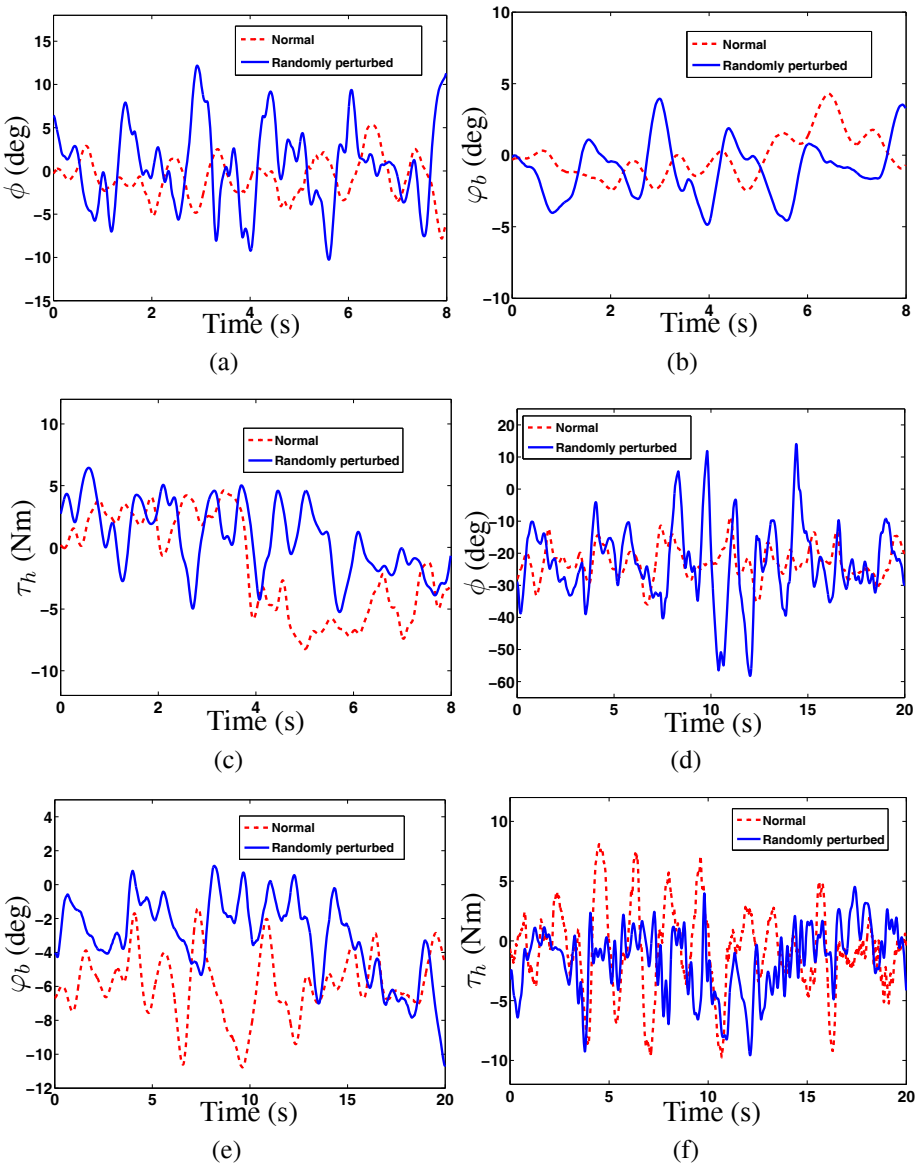

Figure 6.6: Rider-bicycle responses under typical riding and randomly perturbation by the gyro-balancer for the straight-line (top row) and circular (bottom row) trajectories. (a) Steering angle ϕ_s for straight-line. (b) Bicycle roll angle φ_b for straight-line. (c) Gyroscopic perturbed torque for straight-line. (d) Steering angle ϕ_s for straight-line. (e) Bicycle roll angle φ_b for straight-line. (f) Gyroscopic perturbed torque for straight-line.

the so-called "counter-steering" strategy (turning the steering toward the same direction as falling trend), a bicycle-riding motor skill that is obtained through training.

To further demonstrate that riders use steering as an effective strategy, rather than other motor strategies such as upper body motions, we conduct riding experiments

under randomly generated torques. We compare the riding responses in these perturbed experiments with responses from normally riding experiments without any disturbances. Figure 6.6 shows the comparison results of the rider-bicycle interactions under a normal and a perturbed experiment. Figure 6.6(a)-(c) shows the rider's steering angle responses, bicycle roll angle, and the perturbed torque for straight-line riding and Fig. 6.6(d)-(f) shows the profiles of the same variables for circular riding experiments. The rider responded to the random perturbation by actively turning the handlebar and using steering to balance the platform in experiments. This can be clearly observed by the comparison with normal riding behavior shown in Fig. 6.6(a) and 6.6(d). On the other hand, the comparison of the bicycle roll angle profiles shown in Fig. 6.6(b) and 6.6(e) does not clearly demonstrate significant difference. Although not being presented here, the comparison results of the rider's body movement do not show significant difference between normal and perturbed bicycle riding, either. These results and observations confirm that the bicycle platform can be used to study dynamic postural human motor skills.

6.4 Conclusion

In this chapter, we first presented a dynamic modeling and balance control of stationary rider-bicycle system. We considered the human as an inverted pendulum and treated the human actuation torque as an unknown disturbance. The balance control was designed by using a coupled two sliding-mode surface approach and the controller was integrated with a nonlinear disturbance observer. We proved the asymptotic stability of the integrated control and disturbance observer design. The performance of the control system was demonstrated through simulation results. In the second part of the chapter, we mainly demonstrate the possibility to use the bikebot to study the human sensorimotor skill. We conclude that the human rider uses steering as the first priority way to

maintain the bicycle balance when he/she feels large external disturbances.

Chapter 7
Conclusions and Future Work

7.1 Conclusions

The dissertation proposed a modeling and control framework of the single-track vehicles from the human-machine-environment (HME) interactions perspective. We thoroughly investigated the HME interactions from three aspects: the navigation and stationary balancing of an autonomous motorcycle, the tire-road interactions and the rider-bicycle interactions. The newly developed Rutgers instrumented bicycle "bikebot" was also presented in the dissertation.

For the autonomous motorcycle navigation, we relaxed the lateral zero velocity constraint and considered the tire-road interactions in the modeling of riderless single-track vehicles. EIC-based nonlinear controllers were designed to realize the trajectory tracking and the path following, respectively. The simulation results demonstrated that autonomous motorcycle can even achieve the agile maneuvers which only belong to professional riders with such the significant improvements in modeling process. We also investigated the challenging balancing problem of a riderless stationary bicycle. Two different controllers were designed based on the steering control and the gyroscopic actuator control, respectively. Experiments were conducted to validate the effectiveness of the two controller designs.

To study the tire-road interactions, a new high-fidelity tire model was proposed to predict the deformation and friction force distributions on the tire contact patch in stick-slip transition. An in-situ sensing technique by using a new PSECR sensor was

developed to directly measure the friction force distribution and validate the new tire model. The new model not only extends the current knowledge of tire-road interaction, but also can be used to potentially guide the future tire sensing development.

For the ride-bicycle interactions, a new dynamic model was first proposed to capture the physical interactions for rider-bicycle system. A novel sensor fusion scheme was presented based on the dynamic model to measure the system motion in real time. The sensor fusion approach combined both the advantages of inertial sensors and force sensors. Drift-free performance was achieved in both the indoor and outdoor experiments. The new pose estimation approach benefits the future studies for rider-bicycle interactions, especially in outdoor environment. A hierarchical sliding mode control was then designed to control the rider-bicycle system via steering control. Simulation results showed that the rider-bicycle system can converge to the equilibrium position under such the control. Finally, some experiments were conducted to show the possibility to use the "bikebot" to study the human sensorimotor skill. The experimental results showed that the human rider mainly uses steering angle to keep the system balance.

The outcomes of the dissertation in terms of the modeling, sensing and control of HME interactions of single-track vehicles not only lay down a theoretical and experimental foundation for the HME interactions of single-track vehicles, but also provide methodologies and enabling experimental platforms to study the HME interactions in other mechanical and robotic systems.

7.2 Future Work

Following the research developments in this dissertation, there are quite a few research directions and continuation work in future. For the study of autonomous single-track

vehicles, a piece of natural extension work is to experimentally realize the riderless bicycle or motorcycle navigation for both the trajectory tracking and path following. The work can be conducted on the newly developed Rutgers instrumented bicycle "bike-bot". Second, the orbital stabilization of the stationary bicycle can be further investigated for both the steering control and gyroscopic balancer control. Besides the energy shaping-based control design presented in the dissertation, other approaches, such as virtual-constraint-based control design, sliding mode control, dynamics inversion-based tracking, can be also used to potentially design a controller to reach the orbital stabilization. Furthermore, the problem of gyroscopic balancer control of stationary bicycle can be even generalized for the control of a class of underactuated dynamic systems where the subsystems are coupled through torque or force interaction. The hybrid control of combining the steering control and gyroscopic balancer control is another interesting research topic. With the hybrid control, we believe that the maximal domain of attraction can be obtained in the stationary bicycle balancing case. The third future research direction is to design a control system for the stationary balancing-navigation transition of the autonomous single-track vehicles, which is critical for the real application for bicycle-like robots.

For the tire-road interactions, we shall further investigate the friction force distribution of the dynamic rotating tire. We are currently modifying the tire platform to prepare for such an objective. The beam-spring model can be integrated with LuGre model to calculate the deformation and friction force distributions.

For the rider-bicycle interaction, the whole body motion pose estimation is obviously necessary for the further studies of rider-bicycle system. The whole body motion pose estimation can be achieved by using multiple wearable inertial sensors with enhancements by fusing vision measurement from onboard camera or geometry constraints. A thorough study of human sensorimotor control is also needed for the rider-bicycle interactions. The stability analysis of the rider-bicycle system should be

developed using the new results of the human sensorimotor control that can be obtained through experiments.

Finally, extension of the modeling and control framework to study other types of unstable HME interactions would be interestingly explored in future.

References

[1] R. S. Sharp, S. Evangelou, and D. J. N. Limbeer, "Advances in the modelling of motorcycle dynamics," *Multibody Syst. Dyn.*, vol. 12, pp. 251–283, 2004.

[2] C.-G. Song, J.-Y. Kim, and N.-G. Kim, "A new postural balance control system for rehabilitation training based on virtual cycling," *IEEE Trans. Inform. Technol. Biomed.*, vol. 8, no. 2, pp. 200–207, 2004.

[3] M. B. Aerts, W. F. Abdo, and B. R. Bloem, "The "bicycle sign" for atypical Parkinsonism," *Lancet*, vol. 377, no. 9760, pp. 125–126, 2011.

[4] A. H. Snijders and B. R. Bloem, "Cycling for dreezing of gait." *New Engl. J. Med.*, vol. 362, 2010, p.e46.

[5] J. Meijaard, J. Papadopoulos, A. Ruina, and A. Schwab, "Linearized dynamics equations for the balance and steer of a bicycle: A benchmark and review," *Proc. Royal Soc. A*, vol. 463, pp. 1955–1982, 2007.

[6] J. Moore, "Human control of a bicycle," Ph.D. dissertation, Dept. Mech. and Aero. Eng., Univ. Calif., Davis, CA, 2012.

[7] S. Timoshenko and D. H. Young, *Advanced Dynamics*. New York: McGraw-Hill, 1948.

[8] D. Karnopp, *Vehicle Stability*. Marcel Dekker, Inc., 2004.

[9] K. J. Astr, R. E. Klein, and A. Lennartsson, "Bicycle dynamics and control," *IEEE Control Syst. Mag.*, vol. 25, no. 4, pp. 26–47, 2005.

[10] F. J. W. Whipple, "The stability of the motion of a bicycle," *Quart. J. of Pure and Appl. Math.*, vol. 30, pp. 312–348, 1899.

[11] J. Yi, Y. Zhang, and D. Song, "Autonomous motorcycles for agile maneuvers: Part I: Dynamic modeling," in *Proc. IEEE Conf. Decision Control*, Shanghai, China, 2009, pp. 4613–4618.

[12] M. Defoort and T. Murakami, "Sliding-mode control scheme for an intelligent bicycle," *IEEE Trans. Ind. Electron.*, vol. 56, no. 9, pp. 3357–3368, 2009.

[13] R. Sharp, "The stability and control of motorcycles," *J. Mech. Eng. Sci.*, vol. 13, no. 5, pp. 316–329, 1971.

[14] ——, "Stability, control and steering responses of motorcycles," *Veh. Syst. Dyn.*, vol. 35, no. 4-5, pp. 291–318, 2001.

[15] V. Cossalter and R. Lot, "A motorcycle multi-body model for real time simulations based on the natural coordinates approach," *Veh. Syst. Dyn.*, vol. 37, no. 6, pp. 423–447, 2002.

[16] V. Cossalter, A. Doria, R. Lot, N. Ruffo, and M. Salvador, "Dynamic properties of motorcycle and scooter tires: Measurement and comparison," *Veh. Syst. Dyn.*, vol. 39, no. 5, pp. 329–352, 2003.

[17] V. Cossalter and A. Doria, "The relation between contact patch geometry and the mechanical properties of motorcycle tyres," *Veh. Syst. Dyn.*, vol. 43, no. Suppl., pp. 156–167, 2005.

[18] J. Grizzle, M. Di Benedetto, and F. Lamnabhi-Lagarrigue, "Necessary conditions for asymptotic tracking in nonlinear systems," *IEEE Trans. Automat. Contr.*, vol. 39, no. 9, pp. 1782–1794, 1994.

[19] K. Åström, R. Klein, and A. Lennartsson, "Bicycle dynamics and control," *IEEE Control Syst. Mag.*, vol. 25, no. 4, pp. 26–47, 2005.

[20] A. Beznos, A. Formal'sky, E. Gurfinkel, D. Jicharev, A. Lensky, K. Savitsky, and L. Tchesalin, "Control of autonomous motion of two-wheel bicycle with gyroscopic stabilisation," in *Proc. IEEE Int. Conf. Robot. Autom.*, Leuven, Belgium, 1998, pp. 2670–2675.

[21] N. Getz, "Dynamic inversion of nonlinear maps with applications to nonlinear control and robotics," Ph.D. dissertation, Dept. Electr. Eng. and Comp. Sci., Univ. Calif., Berkeley, CA, 1995.

[22] A. Saccon, "Maneuver regulation of nonlinear systems: The challenge of motorcycle control," Ph.D. dissertation, Dept. Informat. Eng., Univ. Padova, Padova, Italy, 2006.

[23] S. Lee and W. Ham, "Self-stabilzing strategy in tracking control of unmanned electric bicycle with mass balance," in *Proc. IEEE/RSJ Int. Conf. Intell. Robot. Syst.*, Lausanne, Switzerland, 2002, pp. 2200–2205.

[24] Y. Tanaka and T. Murakami, "Self sustaining bicycle robot with steering controller," in *Proc. 2004 IEEE Adv. Motion Contr. Conf.*, Kawasaki, Japan, 2004, pp. 193–197.

[25] ——, "A study on straight-line tracking and posture control in electric bicycle," *IEEE Trans. Ind. Electron.*, vol. 56, no. 1, pp. 159–168, 2009.

[26] J. Yi, D. Song, A. Levandowski, and S. Jayasuriya, "Trajectory tracking and balance stabilization control of autonomous motorcycles," in *Proc. IEEE Int. Conf. Robot. Autom.*, Orlando, FL, 2006, pp. 2583–2589.

[27] M. Defoort and T. Murakami, "Second order sliding mode control with disturbance observer for bicycle stabilization," in *Proc. IEEE/RSJ Int. Conf. Intell. Robot. Syst.*, Nice, France, 2008, pp. 2822–2827.

[28] APOLLO Consortium, "Intelligent tyre systems - State of the art and potential technologies," Technical Research Centre of Finland (VTT), APOLLO Deliverable D7 for Project IST-2001-34372. Also available at http://www.vtt.fi/apollo., 2003.

[29] H. B. Pacejka, *Tire and Vehicle Dynamics*, 2nd ed. Warrendale, PA: SAE International, 2006.

[30] G. Gim and P. Nikravesh, "An analytical model of pneumatic tyres for vehicle dynamic simulations. Part I: Pure slips," *Int. J. Veh. Des.*, vol. 11, no. 6, pp. 589–618, 1990.

[31] J. Svendenius, "Tire modeling and friction estimation," Ph.D. dissertation, Dept. Automat. Contr., Lund Inst. Tech., Lund, Sweden, 2007.

[32] J. Yi, L. Alvarez, X. Claeys, and R. Horowitz, "Tire/road friction estimation and emergency braking control using a dynamic friction model," *Veh. Syst. Dyn.*, vol. 39, no. 2, pp. 81–97, 2003.

[33] J. Deur, J. Asgari, and D. Hrovat, "A 3D brush-type dynamic tire friction model," *Veh. Syst. Dyn.*, vol. 42, no. 3, pp. 133–173, 2004.

[34] W. Liang, J. Medanic, and R. Ruhl, "Analytical dynamic tire model," *Veh. Syst. Dyn.*, vol. 46, no. 3, pp. 197–227, 2008.

[35] J. Li, Y. Zhang, and J. Yi, "A hybrid physical/dynamic tire/road friction model," *ASME J. Dyn. Syst., Meas., Control*, vol. 135, no. 1, 2013, Article #011007.

[36] O. Yilmazoglu, M. Brandt, J. Sigmund, E. Genc, and H. Hartnagel, "Integrated InAs/GaSb 3D magnetic field sensors for "the intelligent tire"," *Sens. Actuators, A*, vol. 94, pp. 59–63, 2001.

[37] S. Gruber, M. Semsch, T. Strothjohann, and B. Breuer, "Elements of a mechatronic vehicle corner," *Mechatronics*, vol. 12, no. 8, pp. 1069–1080, 2002.

[38] A. Pohl, R. Steindl, and L. Reindl, "The "intelligent tire" utilizing passive saw sensors – measurement of tire friction," *IEEE Trans. Instrum. Meas.*, vol. 48, no. 6, pp. 1041–1046, 1999.

[39] R. Matsuzaki and A. Todoroki, "Passive wireless strain monitoring of actual tire using capacitance-resistance change and multiple spectral features," *Sens. Actuators, A*, vol. 126, pp. 277–286, 2006.

[40] ——, "Wireless flexible capacitive sensor based on ultra-flexible epoxy resin for strain measurement of automobile tires," *Sens. Actuators, A*, vol. 140, pp. 32–42, 2007.

[41] F. Braghin, M. Brusarosco, F. Cheli, A. Cigada, S. Manzoni, and F. Mancosu, "Measurement of contact forces and patch features by means of accelerometers fixed inside the tire to improve future car active control," *Veh. Syst. Dyn.*, vol. 44, no. Suppl., pp. 3–13, 2006.

[42] S. Savaresi, M. Tanelli, P. Langthaler, and L. Del Re, "New regressors for the direct identification of tire deformation in road vehicles via "in-tire" accelerometers," *IEEE Trans. Contr. Syst. Technol.*, vol. 16, no. 4, pp. 769–780, 2008.

[43] M. Palmer, C. C. Boyd, J. McManus, and S. Meller, "Wireless smart-tires for road friction measurement and self state determination," in *Proc. 43rd AIAA/ASME/ASCE/AHS Struct., Struct. Dyn., and Mat. Conf.*, Denver, CO, 2002.

[44] J. Yi, "A piezo-sensor based "smart tire" system for mobile robots and vehicles," *IEEE/ASME Trans. Mechatronics*, vol. 13, no. 1, pp. 95–103, 2008.

[45] G. Erdogan, L. Alexander, and R. Rajamani, "Estimation of tire-road friction coefficient using a novel wireless piezoelectric tire sensor," *IEEE Sensors J.*, vol. 11, no. 2, pp. 267–279, 2011.

[46] J. Yi and H. Liang, "A PVDF-based deformation and motion sensor: Modeling and experiments," *IEEE Sensors J.*, vol. 8, no. 4, pp. 384–391, 2008.

[47] D. Limebeer and R. Sharp, "Bicycles, motorcycles, and models," *IEEE Control Syst. Mag.*, vol. 26, no. 5, pp. 34–61, 2006.

[48] T. Katayama, A. Aoki, and T. Nishimi, "Control behavior of motorcycle riders," *Veh. Syst. Dyn.*, vol. 17, no. 4, pp. 211–229, 1988.

[49] H. J. Luinge and P. H. Veltink, "Measuring orientation of human body segments using miniature gyroscopes and accelerometers," *Med. Biol. Eng. Comput.*, vol. 43, no. 2, pp. 273–282, 2005.

[50] H. Zhou and H. Hu, "Reducing drifts in the inertial measurements of wrist and elbow positions," *IEEE Trans. Instrum. Meas.*, vol. 59, no. 3, pp. 575–585, 2010.

[51] D. Vlasic, R. Adelsberger, G. Vannucci, J. Barnwell, M. Gross, W. Matusik, and J. Popović, "Practical motion capture in everyday surroundings," *ACM Trans. Graph.*, vol. 26, no. 3, 2007, article 35.

[52] R. Zhu and Z. Zhou, "A real-time articulated human motion tracking using tri-axis inertial/magnetic sensors package," *IEEE Trans. Neural Syst. Rehab. Eng.*, vol. 12, no. 2, pp. 295–302, 2004.

[53] A. M. Sabatini, "Quaternion-based extended kalman filter for determining orientation by inertial and magnetic sensing," *IEEE Trans. Biomed. Eng.*, vol. 53, no. 7, pp. 1346–1356, 2006.

[54] D. Roetenberg, P. J. Slycke, and P. H. Veltink, "Ambulatory position and orientation tracking fusing magnetic and inertial sensing," *IEEE Trans. Biomed. Eng.*, vol. 54, no. 5, pp. 883–890, 2007.

[55] H. J. Luinge, P. H. Veltink, and C. T. M. Baten, "Ambulatory measurement of arm orientation," *J. Biomech.*, vol. 40, no. 1, pp. 78–85, 2007.

[56] K. Liu, Y. Inoue, K. Shibata, and E. Cao, "Ambulatory estimation of knee-joint kinematics in anatomical coordinate system using accelerometers and magnetometers," *IEEE Trans. Biomed. Eng.*, vol. 58, no. 2, pp. 435–442, 2011.

[57] A. M. Sabatini, C. Martelloni, S. Scapellato, and F. Cavallo, "Assessment of walking features from foot inertial sensing," *IEEE Trans. Biomed. Eng.*, vol. 52, no. 3, pp. 486–494, 2005.

[58] Q. Li, M. Young, V. Naing, and J. M. Donelan, "Walking speed estimation using a shank-mounted inertial measurement unit," *J. Biomech.*, vol. 43, no. 8, pp. 1640–1643, 2010.

[59] S. M. Cain, "An experimental investigation of human/bicycle dynamics and rider skill in children and adults," Ph.D. dissertation, Dept. Bio. Eng., Univ. Michigan, Ann Arbor, MI, 2013.

[60] J. Yi, D. Soudbakhsh, Y. Zhang, and Y. Zhang, "Why some Parkinson's disease patients cannot stand or walk but can ride a bicycle – A control system-based analysis," in *Proc. ASME Dyn. Syst. Control Conf.*, Ft. Lauderdale, FL, 2012, Paper # DSCC2012-8735.

[61] A. L. Schwab and J. P. Meijaard, "A review on bicycle dynamics and rider control," *Vehicle System Dynamics*, vol. 51, no. 7, pp. 1059–1090, 2013.

[62] A. Levandowski, A. Schultz, C. Smart, A. Krasnov, H. Chau, B. Majusiak, F. Wang, D. Song, J. Yi, H. Lee, and A. Parish, "Ghostrider: Autonomous motorcycle," in *Proc. IEEE Int. Conf. Robot. Autom. (Video)*, Orlando, FL, 2006.

[63] F. Bullo and A. Lewis, *Geometric Control of Mechanical Systems: Modeling, Analysis, and Design for Simple Mechanical Control Systems*. New York, NY: Springer, 2004.

[64] S. Sastry, *Nonlinear Systems: Analysis, Stability, and Control*. New York, NY: Springer, 1999.

[65] J. Hauser and R. Hindman, "Maneuver regulation from trajectory tracking: Feedback linearizable systems," in *Proc. IFAC Symp. Nonlinear Contr. Syst. Design*, Tahoe City, CA, 1995, pp. 638–643.

[66] S. Al-Hiddabi and N. McClamroch, "Tracking and maneuver regulation control for nonlinear nonminimum phase systems: Application to flight control," *IEEE Trans. Contr. Syst. Technol.*, vol. 10, no. 6, pp. 780–792, 2002.

[67] R. Skjetne, T. Fossen, and P. Kokotović, "Robust output maneuvering for a class of nonlinear systems," *Automatica*, vol. 40, pp. 373–383, 2004.

[68] A. Aguiar, J. Hespanda, and P. Kokotović, "Path-following for nonminimum phase systems removes performance limitations," *IEEE Trans. Automat. Contr.*, vol. 50, no. 2, pp. 234–239, 2005.

[69] A. Aguiar and J. Hespanda, "Trajectory-tracking and path-following of underactuated autonomous vehicles with parametric modeling uncertainty," *IEEE Trans. Automat. Contr.*, vol. 52, no. 8, pp. 1362–1379, 2007.

[70] P. Y. Li and R. Horowitz, "Passive velocity field control (PVFC): Part II – Application to contour following," *IEEE Trans. Automat. Contr.*, vol. 46, no. 9, pp. 1360–1371, 2001.

[71] V. Cossalter, *Motorcycle Dynamics*. Greendale, WI: Race Dynamics, 2002.

[72] A. Bloch, *Nonholonomic Mechanics and Control*. New York, NY: Springer, 2003.

[73] Y. Zhang, J. Li, J. Yi, and D. Song, "Balance control and analysis of stationary riderless motorcycles," in *Proc. IEEE Int. Conf. Robot. Autom.*, Shanghai, China, 2011, pp. 3018–3023.

[74] J. Hauser and A. Saccon, "Motorcycle modeling for high-performance maneuvering," *IEEE Control Syst. Mag.*, vol. 26, no. 5, pp. 89–105, 2006.

[75] D. Jones, "The stability of the bicycle," *Phys. Today*, vol. 23, no. 4, pp. 34–40, 1970.

[76] J. Lowell and H. McKell, "The stability of bicycles," *Amer. J. Phys.*, vol. 50, no. 12, pp. 1106–1112, 1982.

[77] J. Fajans, "Steering in bicycles and motorcycles," *Amer. J. Phys.*, vol. 68, no. 7, pp. 654–659, 2000.

[78] A. Isidori, *Nonlinear Control Systems*, 3rd ed. London, UK: Springer-Verlag, 1995.

[79] J. C. Gerdes and E. J. Rossetter, "A unified approach to driver assistance systems based on artificial potential fields," *ASME J. Dyn. Syst., Meas., Control*, vol. 123, no. 3, pp. 431–438, 2001.

[80] D. Song, H.-L. Lee, J. Yi, and A. Levandowski, "Vision-based motion planning for an autonomous motorcycle on ill-structured roads," *Auton. Robots*, vol. 23, no. 3, pp. 197–212, 2007.

[81] M. Corno, S. M. Savaresi, M. Tanelli, and L. Fabbri, "On optimal motorcycle braking," *Contr. Eng. Pract.*, vol. 16, pp. 644–657, 2008.

[82] B. Roy and H. H. Asada, "Nonlinear feedback control of a gravity-assisted underactuated manipulator with application to aircraft assembly," *IEEE Trans. Robotics*, vol. 25, no. 5, pp. 1125–1133, 2009.

[83] N. Townsend and R. Shenoi, "Gyrostabilizer vehicular technology," *Appl. Mech. Rev.*, vol. 64, no. 2, pp. 010 801–1–010 801–14, 2011.

[84] A. S. Shiriaev, J. W. Perram, and C. Canudas-de-Wit, "Constructive tool for orbital stabilization of underactuated nonlinear systems: Virtual constraints approach," *IEEE Trans. Automat. Contr.*, vol. 50, no. 8, pp. 1164–1176, 2005.

[85] A. S. Shiriaev, L. B. Freidovich, A. Robertsson, R. Johansson, and A. Sandberg, "Virtual-holonomic-constraints-based design of stable oscillations of Furuta pendulum: Theory and experiments," *IEEE Trans. Robotics*, vol. 23, no. 4, pp. 827–832, 2007.

[86] H. K. Khalil, *Nonlinear Systems*, 2nd ed. Upper Saddle River, NJ: Prentice Hall, 1996.

[87] H. Shiobara, T. Akasaka, and S. Kagami, "Two-dimensional contact pressure distribution of a radial tire in motion," *Tire Sci. Technol.*, vol. 24, no. 4, pp. 294–320, 1996.

[88] S. Kim, P. Nikravesh, and G. Gim, "A two-dimensional tire model on uneven roads for vehicle dynamic simulations," *Veh. Syst. Dyn.*, vol. 46, no. 10, pp. 913–930, 2008.

[89] C. Melchiorri, "Slip detection and control using tactile and force sensors," *IEEE/ASME Trans. Mechatronics.*, vol. 5, no. 3, pp. 235 –243, 2000.

[90] J. Yi, L. Alvarez, and R. Horowitz, "Adaptive emergency brake control with underestimation of friction coefficient," *IEEE Trans. Contr. Syst. Technol.*, vol. 10, no. 3, pp. 381–392, 2002.

[91] L. Alvarez, J. Yi, L. Olmos, and R. Horowitz, "Adaptive emergency braking control with observer-based dynamic tire/road friction model and underestimation of friction coefficient," *ASME J. Dyn. Syst., Meas., Control*, vol. 127, no. 1, pp. 22–32, 2005.

[92] T. Maeno, T. Kawamura, and S.-C. Cheng, "Friction estimation by pressing an elastic finger-shaped sensor againest a surface," *IEEE Trans. Robot. Automat.*, vol. 20, no. 2, pp. 222–228, 2004.

[93] J. Ueda, A. Ikeda, and T. Ogagawara, "Grip-force control of an elastic object by vision-based slip-margin feedback during the incipient slip," *IEEE Trans. Robotics*, vol. 21, no. 6, pp. 1139–1147, 2005.

[94] V.-A. Ho, D. V. Dao, and S. Hirai, "Development and analysis of a sliding tactile soft fingertip embedded with a microforce/moment sensor," *IEEE Trans. Robotics*, vol. 27, no. 3, pp. 411–424, 2011.

[95] K. L. Johnson, *Contact Mechanics*. Cambridge, UK: Cambridge University Press, 1987.

[96] J. M. Block and L. M. Keer, "Partial plane contact of an elastic curved beam pressed by a flat surface," *ASME J. Tribol.*, vol. 129, no. 1, pp. 60–64, 2007.

[97] T. Omori1, T. Ishikawa, D. Barthés-Biesel, A.-V. Salsac, J. Walter, Y. Imai, and T. Yamaguchi, "Comparison between spring network models and continuum constitutive laws: Application to the large deformation of a capsule in shear flow," *Phys. Rev. E*, vol. 83, no. 4, p. 041918, 2011.

[98] B. S. Mahal, D. E. R. Clark, and J. E. L. Simmons, "Mass-spring simulation of deformation in elastic sheet structures," *Presence: Teleoper. Virtual Environ.*, vol. 10, no. 3, pp. 331–342, 2001.

[99] Y. Zhang, J. Yi, and T. Liu, "Embedded flexible force sensor for in-situ tire-road interaction measurements," *IEEE Sensors J.*, vol. 13, no. 5, pp. 1756–1765, 2013.

[100] L. Beccai, S. Roccella, L. Ascari, P. Valdastri, A. Sieber, M. Carrozza, and P. Dario, "Development and experimental analysis of a soft compliant tactile microsensor for anthropomorphic artificial hand," *IEEE/ASME Trans. Mechatronics.*, vol. 13, no. 2, pp. 158 –168, 2008.

[101] Y. Q. Wang, R. Gnadler, and R. Schieschke, "Two-dimensional contact area of a pneumatic tire subjected to a lateral force," *Veh. Syst. Dyn.*, vol. 23, pp. 149–163, 1994.

[102] Y. Zhang, A. W. Allen, J. Yi, and T. Liu, "Understanding tire/road stick-slip interactions with embedded rubber force sensors," in *Proc. IEEE/ASME Int. Conf. Adv. Intell. Mechatronics*, Kaohsiung, Taiwan, 2012, pp. 550–555.

[103] S. P. Timoshenko, *Theory of Elasticity*. New York, NY: McGraw-Hill, 1970.

[104] S. R. Simon, "Quantification of human motion: gait analysis - benefits and limitations to its application to clinical problems," *J. Biomech.*, vol. 37, no. 12, pp. 1869 – 1880, 2004.

[105] P. Bonato, "Wearable sensors and systems from enabling technology to clinical applications," *IEEE Eng. Med. Biol. Mag.*, vol. 29, no. 3, pp. 25–36, 2010.

[106] R. A. Hyde, L. P. Ketteringham, S. A. Neild, and R. J. S. Jones, "Estimation of upper-limb orientation based on accelerometer and gyroscope measurements," *IEEE Trans. Biomed. Eng.*, vol. 55, no. 2, pp. 746–754, 2008.

[107] Z.-Q. Zhang, W.-C. Wong, and J.-K. Wu, "Ubiquitous human upper-limb motion estimation using wearable sensors," *IEEE Trans. Inform. Technol. Biomed.*, vol. 15, no. 4, pp. 513–521, 2011.

[108] H. Dejnabadi, B. M. Jolles, E. Casanova, P. Fua, and K. Aminian, "Estimation and visualization of sagittal kinematics of lower limbs orientation using body-fixed sensors," *IEEE Trans. Biomed. Eng.*, vol. 53, no. 7, pp. 1385–1393, 2006.

[109] H. M. Schepers, H. F. J. M. Koopman, and P. H. Veltink, "Ambulatory assessment of ankle and foot dynamics," *IEEE Trans. Biomed. Eng.*, vol. 54, no. 5, pp. 895–902, 2007.

[110] K. J. O'Donovan and R. Kamnik and D. T. O'Keeffe and G. M. Lyons, "An inertial and magnetic sensor based technique for joint angle measurement," *J. Biomech.*, vol. 40, no. 12, pp. 2604–2611, 2007.

[111] H. Rouhani, J. Favre, X. Crevoisier, and K. Aminian, "Ambulatory measurement of ankle kinetics for clinical applications," *J. Biomech.*, vol. 44, pp. 2712–2718, 2011.

[112] P. H. Veltink, C. Liedtke, E. Droog, and H. van der Kooij, "Ambulatory measurement of ground reaction forces," *IEEE Trans. Neural Syst. Rehab. Eng.*, vol. 13, no. 3, pp. 423–427, 2005.

[113] H. M. Schepers, E. H. F. van Asseldonk, J. H. Buurke, and P. H. Veltink, "Ambulatory estimation of center of mass displacement during walking," *IEEE Trans. Biomed. Eng.*, vol. 56, no. 4, pp. 1189–1195, 2009.

[114] P. H. Veltink, H. Kortier, and H. M. Schepers, "Sensing power transfer between the human body and the environment," *IEEE Trans. Biomed. Eng.*, vol. 56, no. 6, pp. 1711–1718, 2009.

[115] A. D. Goodworth and R. J. Peterka, "Influence of bilateral vestibular loss on spinal stabilization in humans," *J. Neurophysiol.*, vol. 103, no. 4, pp. 1978–1987, 2010.

[116] J. H. van der Spek, P. H. Veltink, H. J. Hermens, B. F. J. M. Koopman, and H. B. K. Boom, "A model-based approach to stabilizing crutch supported paraplegic standing by artificial hip joint stiffness," *IEEE Trans. Neural Syst. Rehab. Eng.*, vol. 11, no. 4, pp. 443–451, 2003.

[117] Y. Zhang, F. Liu, M. Trkov, and J. Yi, "Rider/bicycle pose estimation with IMU/seat force measurements," in *Proc. IEEE/ASME Int. Conf. Adv. Intell. Mechatronics*, Kaohsiung, Taiwan, 2012, pp. 604–609.

[118] X. Lu, Y. Zhang, K. Yu, J. Yi, and J. Liu, "Upper limb pose estimation in rider-bicycle interactions with an un-calibrated monocular camera and wearable gyroscopes," in *Proc. ASME Dyn. Syst. Control Conf.*, Stanford, CA, 2013, moBT2.1.

[119] R. Murray, Z. Li, and S. Sastry, *A Mathematical Introduction to Robotic Manipulation*. Boca Raton, FL: CRC Press, 1994.

[120] C. C. Ward and K. Iagnemma, "A dynamic-model-based wheel slip detector for mobile robots on outdoor terrain," *IEEE Trans. Robotics*, vol. 24, no. 4, pp. 821–831, 2008.

[121] M. Boutayeb and D. Aubry, "A strong tracking extended Kalman observer for nonlinear discrete-time systems," *IEEE Trans. Automat. Contr.*, vol. 44, no. 8, pp. 1550–1556, 1999.

[122] J. Yi, H. Wang, J. Zhang, D. Song, S. Jayasuriya, and J. Liu, "Kinematic modeling and analysis of skid-steered mobile robots with applications to low-cost inertial-measurement-unit-based motion estimation," *IEEE Trans. Robotics*, vol. 25, no. 5, pp. 1087–1097, 2009.

[123] K. Kobayashi and T. Yoshikawa, "Controllability of under-actuated planar manipulators with one unactuated joint," *Int. J. Robot. Res.*, vol. 21, no. 5-6, pp. 555–561, 2002.

[124] M. Zhang and T.-J. Tarn, "Hybrid control of the pendubot," *IEEE/ASME Trans. Mechatronics.*, vol. 7, no. 1, pp. 79–86, 2002.

[125] I. Fantoni and R. Lozano and M. W. Spong, "Energy based control of pendubot," *IEEE Trans. Automat. Contr.*, vol. 45, no. 4, pp. 725–729, 2000.

[126] W. Wang, J. Yi, D. Zhao, and D. Liu, "Design of a stable sliding-mode controller for a class of second-order underactuated systems," *IEE Proc. - Control Theory Appl.*, vol. 151, no. 6, pp. 683–690, 2004.

[127] M.-S. Park and D. Chwa, "Swing-up and stabilization control of inverted-pendulum systems via coupled sliding-mode control method," *IEEE Trans. Ind. Electron.*, vol. 56, no. 9, pp. 3541–3555, 2009.

[128] W.-H. Chen, D. J. Ballance, P. J. Gawthrop, and J. O'Reilly, "A nonlinear disturbance observer for robotic manipulators," *IEEE Trans. Ind. Electron.*, vol. 47, no. 4, pp. 932–938, 2000.

[129] M. Chen and W.-H. Chen, "Sliding mode control for a class of uncertain nonlinear system based on disturbance observer," *Int. J. Adapt. Control Signal Process.*, vol. 24, pp. 51–64, 2010.

[130] C. Yang, G. Ganesh, S. Haddadin, S. Parusel, A. Albu-Schaeffer, and E. Burdet, "Human-like adaptation of force and impedance in stable and unstable interactions," *IEEE Trans. Robotics*, vol. 27, no. 5, pp. 918–930, 2011.

[131] S. Ikemoto, H. Amor, T. Minato, B. Jung, and H. Ishiguro, "Physical human-robot interaction: mutual learning and adaptation," *IEEE Robot. Automat. Mag.*, vol. 19, no. 4, pp. 24–35, 2012.

[132] Y. Zhang and J. Yi, "Dynamic modeling and balance control of human/bicycle systems," in *Proc. IEEE/ASME Int. Conf. Adv. Intell. Mechatronics*, Montreal, Canada, 2010, pp. 1385–1390.

[133] K. Chen, Y. Zhang, and J. Yi, "Modeling of rider-bicycle interactions with learned dynamics on constrained embedding manifolds," in *Proc. IEEE/ASME Int. Conf. Adv. Intell. Mechatronics*, Wollongong, Australia, 2013, pp. 442–447.

[134] Y. Zhang, K. Chen, and J. Yi, "Rider trunk and bicycle pose estimation with fusion of force/inertial sensors," *IEEE Trans. Biomed. Eng.*, vol. 60, no. 9, pp. 2541 – 2551, 2013.

[135] H. van der Kooij, R. Jocob, B. Koopman, and H. Grootenboer, "A multisensory integration model of human stance control," *Biol. Cybern.*, vol. 80, pp. 299–308, 1999.

Appendix A

Calculation of M_s

We consider the front wheel center O_1 and the projected steering axis point C_3 on the ground surface. Since the frictional moment is independent of the coordinate system. We setup a local coordinate system $x_f y_f z_f$ by rotating the coordinate system xyz around the z-axis with an angle ϕ_g (origin at contact point C_1). Let $(\boldsymbol{i}_f, \boldsymbol{i}_f, \boldsymbol{i}_f)$ denote the unit vectors along the x_f, y_f, z_f-axis directions, respectively.

In the new coordinate system, the coordinates of O_1 and C_3 are $(0, r\,\mathrm{s}_{\varphi_f}, -r\,\mathrm{c}_{\varphi_f})$ and $(l_t, 0, 0)$, respectively. We write the front wheel friction force vector $\boldsymbol{F}_f$ as

$$\boldsymbol{F}_f = -F_{tx}\boldsymbol{i}_f - F_{ty}\boldsymbol{j}_f - F_{tz}\boldsymbol{k}_f$$

and the vector $\boldsymbol{r}_{C_3C_1} = -l_t\boldsymbol{i}_f$. The directional vector $\boldsymbol{n}_{O_1C_3}$ of the steering axis O_1, C_3 is then

$$\boldsymbol{n}_{O_1C_3} = \frac{l_t\boldsymbol{i}_f - r\,\mathrm{s}_{\varphi_f}\boldsymbol{j}_f + r\,\mathrm{c}_{\varphi_f}\boldsymbol{k}_f}{\sqrt{l_t^2 + r^2}}.$$

Therefore, the friction moment M_s about the steering axis is calculated as

$$M_s = (\boldsymbol{r}_{C_3C_1} \times \boldsymbol{F}_f) \cdot \boldsymbol{n}_{O_1C_3} = \frac{l_t}{\sqrt{1 + (l_t/r)^2}} \left(F_{ty}\,\mathrm{c}_{\varphi_f} - F_{tz}\,\mathrm{s}_{\varphi_f}\right).$$

Appendix B

Calculation of acceleration $\dot{\boldsymbol{v}}_B$

Taking the time derivative of the mass center velocity $\boldsymbol{v}_G$ and considering the moving frame xyz's angular velocity $\boldsymbol{\omega} = \dot{\varphi}_b \boldsymbol{i} + \dot{\psi}\boldsymbol{k}$, we obtain

$$\begin{aligned}
\dot{\boldsymbol{v}}_B = \frac{\delta \boldsymbol{v}_B}{\delta t} + \boldsymbol{\omega} \times \boldsymbol{v}_B &= (\dot{v}_{rx} - h_b\ddot{\psi}\,\mathrm{s}_{\varphi_b} - h_b\dot{\psi}\dot{\varphi}_b\,\mathrm{c}_{\varphi_b})\boldsymbol{i} + (\dot{v}_{ry} + l_b\ddot{\psi} + h_b\ddot{\varphi}_b\,\mathrm{c}_{\varphi_b} \\
&\quad - h_b\dot{\varphi}_b^2\,\mathrm{s}_{\varphi_b})\boldsymbol{j} + (h_b\ddot{\varphi}_b\,\mathrm{s}_{\varphi_b} + h\dot{\varphi}_b^2\,\mathrm{c}_{\varphi_b})\boldsymbol{k} + (\dot{\varphi}_b\boldsymbol{i} + \dot{\psi}\boldsymbol{k}) \times \boldsymbol{v}_B \\
&= (\dot{v}_{rx} - v_{ry}\dot{\psi} - h_b\ddot{\psi}\,\mathrm{s}_{\varphi_b} - l_b\dot{\psi}^2 - 2h_b\dot{\psi}\dot{\varphi}_b\,\mathrm{c}_{\varphi_b})\boldsymbol{i} \\
&\quad + (\dot{v}_{ry} + v_{rx}\dot{\psi} + l_b\ddot{\psi} + h_b\ddot{\varphi}_b\,\mathrm{c}_{\varphi_b} - h_b\dot{\psi}^2\,\mathrm{s}_{\varphi_b} - 2h_b\dot{\varphi}_b^2\,\mathrm{s}_{\varphi_b})\boldsymbol{j} \\
&\quad + (v_{ry}\dot{\varphi}_b + h_b\ddot{\varphi}_b\,\mathrm{s}_{\varphi_b} + l_b\dot{\psi}\dot{\varphi}_b + 2h_b\dot{\varphi}_b^2\,\mathrm{c}_{\varphi_b})\boldsymbol{k},
\end{aligned}$$

where $\frac{\delta \boldsymbol{v}_B}{\delta t}$ denotes the derivative of $\boldsymbol{v}_B$ by treating the xyz-coordinate as a fixed frame.

Appendix C

Calculation of the Lie derivatives

The calculation of $\bar{L}_{\mathbf{N}_{\text{ext}}} u_{rx}^{\text{ext}}$ and $\bar{L}_{\mathbf{N}_{\text{ext}}} u_{ry}^{\text{ext}}$ is obtained by taking the Lie derivative along the nominal external vector field (2.51) and the control input (2.53). The calculation are shown in (C.1) and (C.2).

$$
\begin{aligned}
\bar{L}_{\mathbf{N}_{\text{ext}}} u_{rx}^{\text{ext}} = & \begin{bmatrix} -\,\mathrm{s}_\psi & \mathrm{c}_\psi \end{bmatrix} \dot{\psi} \left(-\mathbf{U} + \boldsymbol{u}^{\text{ext}} \right) + \begin{bmatrix} \mathrm{c}_\psi & \mathrm{s}_\psi \end{bmatrix} \\
& \left(- \begin{bmatrix} -2u_{rx}^{\text{ext}}\,\mathrm{s}_\psi - 2u_{ry}^{\text{ext}}\,\mathrm{c}_\psi - 3\dot{v}_{rx}\dot{\psi}\,\mathrm{c}_\psi + 3\dot{v}_{ry}\dot{\psi}\,\mathrm{s}_\psi + \ddot{\psi}\left(v_{rx}\,\mathrm{s}_\psi + v_{ry}\,\mathrm{c}_\psi\right) \\ 2u_{rx}^{\text{ext}}\,\mathrm{c}_\psi - 2u_{ry}^{\text{ext}}\,\mathrm{s}_\psi - 3\dot{v}_{rx}\dot{\psi}\,\mathrm{s}_\psi - 3\dot{v}_{ry}\dot{\psi}\,\mathrm{c}_\psi - \ddot{\psi}\left(v_{rx}\,\mathrm{c}_\psi - v_{ry}\,\mathrm{s}_\psi\right) \end{bmatrix} \dot{\psi} \right. \\
& \left. + \begin{bmatrix} \bar{L}_{\mathbf{N}_{\text{ext}}} u_X^{\text{ext}} \\ \bar{L}_{\mathbf{N}_{\text{ext}}} u_Y^{\text{ext}} \end{bmatrix} \right) \\
= & \dot{v}_{rx}\dot{\psi}^2 + \left(2u_{ry}^{\text{ext}} - u_X^{\text{ext}}\,\mathrm{s}_\psi + u_Y^{\text{ext}}\,\mathrm{c}_\psi\right)\dot{\psi} + \bar{L}_{\mathbf{N}_{\text{ext}}} u_X^{\text{ext}}\,\mathrm{c}_\psi \\
& + \bar{L}_{\mathbf{N}_{\text{ext}}} u_Y^{\text{ext}}\,\mathrm{s}_\psi, \qquad \text{(C.1)} \\
\bar{L}_{\mathbf{N}_{\text{ext}}} u_{ry}^{\text{ext}} = & \dot{v}_{ry}\dot{\psi}^2 - \left(2u_{rx}^{\text{ext}} + u_X^{\text{ext}}\,\mathrm{c}_\psi + u_Y^{\text{ext}}\,\mathrm{s}_\psi\right)\dot{\psi} - \bar{L}_{\mathbf{N}_{\text{ext}}} u_X^{\text{ext}}\,\mathrm{s}_\psi \\
& + \bar{L}_{\mathbf{N}_{\text{ext}}} u_Y^{\text{ext}}\,\mathrm{c}_\psi\,. \qquad \text{(C.2)}
\end{aligned}
$$

In these equations, we have

$$
\begin{bmatrix} \bar{L}_{\mathbf{N}_{\text{ext}}} u_X^{\text{ext}} \\ \bar{L}_{\mathbf{N}_{\text{ext}}} u_Y^{\text{ext}} \end{bmatrix} = \begin{bmatrix} X_d^{(4)}(t) \\ Y_d^{(4)}(t) \end{bmatrix} - b_3 \begin{bmatrix} u_X^{\text{ext}} - X_d^{(3)}(t) \\ u_Y^{\text{ext}} - Y_d^{(3)}(t) \end{bmatrix} - \sum_{i=1}^{2} b_i \begin{bmatrix} X^{(i)} - X_d^{(i)}(t) \\ Y^{(i)} - Y_d^{(i)}(t) \end{bmatrix}.
$$

Similarly, we calculate $\bar{L}^2_{\mathbf{N}^{\text{ext}}} \varphi_e$ by directly taking a directional derivative of $\bar{L}_{\mathbf{N}_{\text{ext}}} \varphi_e$

along the vector field $\mathbf{N}_{\text{ext}}$. From (2.59), we have

$$\bar{L}^2_{\mathbf{N}_{\text{ext}}}\varphi_e = \left(h_b\dot{\psi}\,\mathrm{c}_{\varphi_e} + g\sec^2\varphi_e\right)^{-1}\left[\frac{gl_bl_t\,\mathrm{c}_\xi}{h_b}\left(\frac{\dot{\psi}u^{\text{ext}}_{rx}}{v^2_{rx}} - \frac{2\dot{v}^2_{rx}\dot{\psi}}{v^3_{rx}}\right) + \dot{\psi}u^{\text{ext}}_{rx} + \right.$$

$$\left. \bar{L}_{\mathbf{N}_{\text{ext}}}u^{\text{ext}}_{ry} + \left(h_b\dot{\psi}\,\mathrm{s}_{\varphi_e} - 2g\sec^2\varphi_e\tan\varphi_e\right)\left(\bar{L}_{\mathbf{N}_{\text{ext}}}\varphi_e\right)^2\right]. \tag{C.3}$$

Appendix D

Calculation of $\sigma_z(z)$ inside the rubber layer

Figure 4.4(b) illustrates the configuration of the tire rubber layer. We first decompose $P_n(x)$ by a Fourier series.

$$P_n(x) = P_0 + \sum_{m=1}^{\infty} A_m \sin(\lambda x) + \sum_{n=1}^{\infty} B_m \cos(\lambda x), \tag{D.1}$$

where P_0 is the constant term and $\lambda = \frac{m\pi}{L_x}$ and L_x is the major axis length of the elliptical $\mathcal{P}$. By superposition, we consider the contribution of each term in (D.1) to the internal stress $\sigma_z(z)$. The particular solution of $\sigma_z(z)$ when P_{air} and P_0 are applied on each side of the tire rubber layer is given by (page 41 of [103])

$$\sigma_z^s(z) = \frac{P_0 - P_{air}}{4h^3} z^3 - \frac{3(P_0 - P_{air})}{4h} z - \frac{P_0 + P_{air}}{2}.$$

To calculate the contribution of the first harmonic term $A_m \sin(\lambda x)$ in (D.1) to $\sigma_z(z)$, we introduce an Airy function $\phi_m(x,z) = \sin(\lambda x) f_m(z)$ in the form of the Fourier series [103]. Plugging $\phi_m(x,z)$ into bi-harmonic condition $\nabla^4 \phi_m(x,z) = 0$, we obtain

$$\lambda^4 f_m(z) - 2\lambda^2 f_m''(z) + f_m^{(4)}(z) = 0.$$

The general solution for $f_m(z)$ is

$$f_m(z) = D_1 \operatorname{ch}(\lambda z) + D_2 \operatorname{sh}(\lambda z) + D_3 z \operatorname{ch}(\lambda z) + D_4 z \operatorname{sh}(\lambda z), \tag{D.2}$$

where $\operatorname{sh}(x) := \sinh(x)$ and $\operatorname{ch}(x) := \cosh(x)$ for x.

Considering that $\sigma_z = \frac{\partial^2 \phi_m}{\partial x^2}$ and $\tau_{xz} = \frac{\partial^2 \phi_m}{\partial x \partial z}$ and the boundary conditions: $\tau_{xz} = 0$, $\sigma_z = -A_m \sin \lambda x$ for $z = h$, and $\tau_{xz} = 0$ and $\sigma_z = 0$ for $z = -h$, we obtain

coefficients D_i in (D.2). Therefore, the contribution of the term $A_m \sin(\lambda x)$ in (D.1) for $P_n(x)$ is given by σ_s^m shown in (D.3). Similarly, for the term $B_m \cos(\lambda x)$ in (D.1) for $P_n(x)$, the contribution to the stress distribution is given by σ_s^m in (D.4).

$$\sigma_s^m = -A_m \sin(\lambda x)\left(\frac{[\lambda h \operatorname{ch}(\lambda h) + \operatorname{sh}(\lambda h)]\operatorname{ch}(\lambda z) - \lambda z \operatorname{sh}(\lambda z)\operatorname{sh}(\lambda h)}{\operatorname{sh}(2\lambda h) + 2\lambda h} + \frac{[\lambda h \operatorname{sh}(\lambda h) + \operatorname{ch}(\lambda h)]\operatorname{sh}(\lambda z) - \lambda z \operatorname{ch}(\lambda z)\cos(\lambda h)}{\operatorname{sh}(2\lambda h) - 2\lambda h}\right) \tag{D.3}$$

$$\sigma_c^m = -B_m \cos(\lambda x)\left(\frac{[\lambda h \operatorname{ch}(\lambda h) + \operatorname{sh}(\lambda h)]\operatorname{ch}(\lambda z) - \lambda z \operatorname{sh}(\lambda z)\operatorname{sh}(\lambda h)}{\operatorname{sh}(2\lambda h) + 2\lambda h} + \frac{[\lambda h \operatorname{sh}(\lambda h) + \operatorname{ch}(\lambda h)]\operatorname{sh}(\lambda z) - \lambda z \operatorname{ch}(\lambda z)\cos(\lambda h)}{\operatorname{sh}(2\lambda h) - 2\lambda h}\right) \tag{D.4}$$

For $L_x \gg h$, using the approximations $\operatorname{sh}(x) \approx x + \frac{x^3}{6} + \frac{x^5}{120}$ and $\operatorname{ch}(x) \approx 1 + \frac{x^2}{2} + \frac{x^4}{24}$ for small x, Eqs. (D.3) and (D.4) are reduced respectively to

$$\sigma_s^m \approx A_m \sin(\lambda x)\left(\frac{1}{4h^3}z^3 - \frac{3}{4h}z - \frac{1}{2}\right) \quad \text{and}$$
$$\sigma_c^m \approx B_m \cos(\lambda x)\left(\frac{1}{4h^3}z^3 - \frac{3}{4h}z - \frac{1}{2}\right).$$

By superposition, we add all the above calculated stress terms together and using (D.1), we obtain

$$\begin{aligned}\sigma_z(z) &= \sigma_z^s(z) + \sum_{m=1}^{\infty}\sigma_s^m + \sum_{m=1}^{\infty}\sigma_c^m \\ &= [P_n(x) - P_{air}]\left(\frac{1}{4h^3}z^3 - \frac{3}{4h}z\right) - \frac{P_n(x) + P_{air}}{2},\end{aligned}$$

for a given x. This completes the calculation of (4.22). The above derivation is readily extended to the two-dimensional case (i.e., including stress along the y-axis direction) if $L_y \gg h$.

Appendix E

Proof of Property 3.1

For a periodic profile $x_1(t+T) = x_1(t)$ for any t, $x_2(t) = \dot{x}_1(t)$ is also periodic with period T, i.e., $x_2(t+T) = x_2(t)$. From (3.19), we obtain

$$p_x(t+T) - p_x(0) = \int_0^{t+T} mgh_G \, \mathrm{s}_{x_1(\tau)} \, d\tau.$$

Taking the difference of the above equation with (3.19), we obtain

$$p_x(t+T) - p_x(t) = \int_0^{T} mgh_G \, \mathrm{s}_{x_1(\tau)} \, d\tau. \tag{E.1}$$

Using the fact that both $x_1(t)$ and $x_2(t)$ are periodic functions with period T and $\int_0^T \mathrm{s}_{x_1(\tau)} \, d\tau = 0$, using (3.18), (E.1) reduces to

$$[x_3(t+T) - x_3(t)] \, [I_{wz}\omega_s + I_{wxz}(x_3(t+T) + x_3(t))] = 0.$$

Thus, $x_3(t+T) = x_3(t)$ and the flywheel's pivoting angle is periodic with period T. This completes the proof.

Appendix F

Rider-bicycle dynamic model

The rider-bicycle dynamic model is obtained by the Lagrangian approach. The Lagrangian of the rider-bicycle system is obtained as

$$\mathcal{L} = \frac{1}{2} m {}^{\mathcal{R}}\boldsymbol{v}_B \cdot {}^{\mathcal{R}}\boldsymbol{v}_B + \frac{1}{2} m_h^{\mathcal{R}} \boldsymbol{v}_H \cdot {}^{\mathcal{R}}\boldsymbol{v}_H - g \Big[m h_b \, \mathrm{c}_{\varphi_b} + m_h \left(h_s \, \mathrm{c}_{\varphi_b} + h_h \, \mathrm{c}_{\varphi_h} \, \mathrm{s}_\theta \right) \Big],$$

where ${}^{\mathcal{R}}\boldsymbol{v}_B$ and ${}^{\mathcal{R}}\boldsymbol{v}_H$ are the linear velocities for the bicycle and the trunk, respectively. We obtain ${}^{\mathcal{R}}\boldsymbol{v}_B = [v_b \quad 0 \quad 0]^T +^{\mathcal{R}} \boldsymbol{\omega}_b \times \boldsymbol{\rho}_B$. Similarly, we obtain the seat velocity ${}^{\mathcal{R}}\boldsymbol{v}_s$ and ${}^{\mathcal{R}}\boldsymbol{v}_H$ is then calculated as ${}^{\mathcal{R}}\boldsymbol{v}_H =^{\mathcal{R}} \boldsymbol{v}_s +^{\mathcal{R}} \boldsymbol{\omega}_h \times \boldsymbol{\rho}_H$, where $\boldsymbol{\rho}_H = [h_h \, \mathrm{c}_\theta \quad h_h \, \mathrm{s}_{\varphi_h} \, \mathrm{s}_\theta \quad -h_h \, \mathrm{c}_{\varphi_h} \, \mathrm{s}_\theta]^T$. Finally, using Lagrange's equations, matrices $\boldsymbol{M}$ and $\boldsymbol{G}$ are obtained as

$$\boldsymbol{M} = \begin{bmatrix} m_h h_h^2 \, \mathrm{s}_\theta^2 & 0 & 0 \\ 0 & m_h h_h^2 & 0 \end{bmatrix}, \; \boldsymbol{G} = \begin{bmatrix} -m_h g h_h \, \mathrm{s}_{\varphi_h} \, \mathrm{s}_\theta \\ m_h g h_h \, \mathrm{c}_{\varphi_h} \, \mathrm{c}_\theta \end{bmatrix}$$

and $\boldsymbol{C}(\boldsymbol{q}, \dot{\boldsymbol{q}}, \ddot{\boldsymbol{q}}_b)$ is given in (F.1).

$$\boldsymbol{C}(\boldsymbol{q}, \dot{\boldsymbol{q}}, \ddot{\boldsymbol{q}}_b) =$$
$$\begin{bmatrix} m_h h_h (l_s \, \mathrm{c}_{\varphi_h} \, \mathrm{s}_\theta + h_h \, \mathrm{c}_{\varphi_h} \, \mathrm{s}_\theta \, \mathrm{c}_\theta) \ddot{\psi} + m_h h_s h_h \, \mathrm{c}_{\varphi_b - \varphi_h} \, \mathrm{s}_\theta \, \ddot{\varphi}_b + m_h h_h^2 \, \mathrm{s}_{2\theta} \, \dot{\theta} \dot{\varphi}_h \\ -m_h h_s h_h \, \mathrm{s}_{\varphi_b - \varphi_h} \, \mathrm{s}_\theta \, \dot{\varphi}_b^2 - 2 m_h h_h^2 \, \mathrm{c}_{\varphi_h} \, \mathrm{s}_\theta^2 \, \dot{\theta} \dot{\psi} - m_h h_h (h_h \, \mathrm{s}_{\varphi_h} \, \mathrm{c}_{\varphi_h} \, \mathrm{s}_\theta^2 + h_s \, \mathrm{s}_{\varphi_b} \, \mathrm{c}_{\varphi_h} \, \mathrm{s}_\theta) \dot{\psi}^2 \\ + m_h h_h \, \mathrm{c}_{\varphi_h} \, \mathrm{s}_\theta \, v_b \dot{\psi} \\ \cdots\cdots\cdots\cdots\cdots\cdots\cdots\cdots\cdots\cdots\cdots\cdots \\ (m_h h_s h_h \, \mathrm{s}_{\varphi_b} \, \mathrm{s}_\theta + m_h l_s h_h \, \mathrm{c}_\theta \, \mathrm{s}_{\varphi_h} + m_h h_h^2 \, \mathrm{s}_{\varphi_h}) \ddot{\psi} - m_h h_s h_h \, \mathrm{s}_{\varphi_b - \varphi_h} \, \mathrm{c}_\theta \, \ddot{\varphi}_b \\ -m_h h_h \, \mathrm{s}_\theta \, \dot{v}_b + 2 m_h h_s h_h \, \mathrm{c}_{\varphi_b} \, \mathrm{s}_\theta \, \dot{\varphi}_b \dot{\psi} + 2 m_h h_h^2 \, \mathrm{s}_\theta^2 \, \mathrm{c}_{\varphi_h} \, \dot{\varphi}_h \dot{\psi} - m_h h_s h_h \, \mathrm{c}_{\varphi_b - \varphi_h} \, \mathrm{c}_\theta \, \dot{\varphi}_b^2 \\ -m_h h_h (h_h \, \mathrm{s}_{\varphi_h}^2 \, \mathrm{s}_\theta \, \mathrm{c}_\theta + h_s \, \mathrm{s}_{\varphi_b} \, \mathrm{s}_{\varphi_h} \, \mathrm{c}_\theta - l_s \, \mathrm{s}_\theta) \dot{\psi}^2 + m_h h_h \, \mathrm{s}_{\varphi_h} \, \mathrm{c}_\theta \, v_b \dot{\psi} \\ -m_h h_h^2 \, \mathrm{s}_\theta \, \mathrm{c}_\theta \, \dot{\varphi}_h^2 + m_h h_h^2 \, \mathrm{s}_\theta \, \mathrm{c}_\theta \, \dot{\psi}^2 \end{bmatrix}. \tag{F.1}$$